## *Ultracold Molecules for Quantum Science: Theories of Molecule Formation*

ROBERT CHADWICK BIRD

# Ultracold Molecules for Quantum Science: Theories of Molecule Formation

**Robert Chadwick Bird**

---

A thesis presented for the degree of

Doctor of Philosophy

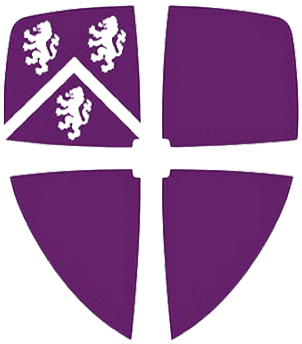

Department of Chemistry
Durham University
December 2024

**Ultracold Molecules for Quantum Science:**

**Theories of Molecule Formation**

**Robert Chadwick Bird**

---

The formation of ultracold molecules is the overarching focus of this thesis. We undertake a number of calculations to explore a variety of systems and the different techniques that can be used to produce them at ultracold temperatures.

Magnetoassociation is routinely used to associate pairs of alkali-metal atoms together to produce alkali-metal dimers. Magnetoassociation exploits the zero-energy magnetically tuneable Feshbach resonances that exist in ultracold atomic and molecular collisions. We study the near-threshold bound states that cause Feshbach resonances in ultracold $^{39}$K + $^{133}$Cs collisions. In order to generate an accurate model of the interatomic $^{39}$K$^{133}$Cs potential we undertake an interactive non-linear least-squares fit to a number of experimental measurements.

Using Feshbach resonances to control the interactions between atoms and molecules at ultracold temperatures is an important avenue of research. Coupled-channel calculations are used to investigate resonances in Rb+CaF collisions. The quantity, and characteristics, of these resonances are determined by the atom-molecule interaction potential, which is yet to be modeled accurately. We utilize a number of representative potentials to explore what the spectrum of Feshbach resonances may look like.

Mergoassociation is a new way of making molecules at ultracold temperatures. We develop a theory for pairs of nonidentical nonspherical traps and a coupled-channel approach for the relative motion of the two atoms. We study mergoassociation for pairs of cylindrically symmetrical traps as a function of their anisotropy. We also develop a basis-set method for the relative and center-of-mass motions of the two atoms. We consider the example of RbCs and then extend the treatment to other systems where mergoassociation may be effective, namely RbSr, RbYb and CsYb.

# Contents

**Abstract** **i**

**List of Figures** **x**

**List of Tables** **xii**

**Declaration** **xiii**

**Acknowledgements** **xiv**

**1 Introduction** **1**

1.1 Ultracold Atomic Gasses . . . . . 2

1.2 Formation of Ultracold Molecules . . . . . 5

1.3 Applications of Ultracold Molecules . . . . . 7

1.4 Research Frontiers . . . . . 9

1.5 Outline . . . . . 12

**2 Quantum Scattering Theory and Bound States** **14**

2.1 Structureless Particles . . . . . 16

2.2 Multichannel Problem . . . . . 20

2.3 Low-Temperature Scattering . . . . . 24

**3 Collisions of K and Cs** **28**

3.1 Introduction . . . . . 29

3.2 Theoretical Background and Methods . . . . . 31

3.2.1 Monomer States and Pair States . . . . . 31

3.2.2 Calculations of Bound States and Scattering . . . . . 38
3.2.3 $^{39}K^{133}Cs$ Interaction Potential . . . . . 40
3.2.4 Scattering Observables and the Interaction Potential . . . . . 42
3.2.5 Least-Squares Fitting . . . . . 45
3.3 Results and Discussion . . . . . 48
3.3.1 Part I: Near-threshold Bound States and Scattering Resonances 49
3.3.2 Part II: Fitting the Interaction Potential . . . . . 61
3.4 Conclusions . . . . . 71

**4 Resonances in collisions of Rb and CaF 73**

4.1 Introduction . . . . . 74
4.2 Theory . . . . . 76
4.2.1 Monomer Hamiltonians and Levels . . . . . 76
4.2.2 Calculations of Bound States and Scattering . . . . . 79
4.2.3 The Interaction Operator . . . . . 81
4.2.4 Thresholds . . . . . 83
4.2.5 Near-threshold Levels . . . . . 83
4.3 Bound States and Resonances in the Absence of Anisotropy . . . . . 84
4.3.1 Bound States Below the Lowest Threshold . . . . . 84
4.3.2 Resonances . . . . . 88
4.4 The Role of CaF Rotation . . . . . 89
4.5 Potential Effects of Chaos . . . . . 92
4.6 Conclusions . . . . . 93
4.7 Recent Perspectives . . . . . 95

**5 Mergoassociation with Optical Tweezers: Part I 98**

5.1 Introduction . . . . . 99
5.2 Separation of Relative and Center-of-Mass Motion . . . . . 102
5.2.1 Spherical Traps . . . . . 102
5.2.2 Nonspherical Traps . . . . . 103

5.3 Coupled-Channel Formulation for Relative Motion . . . . . 104
5.3.1 The Trap Potential . . . . . 104
5.3.2 The Interaction Potential . . . . . 107
5.3.3 Coupled-channel Equations . . . . . 108
5.3.4 Solution of Coupled Equations . . . . . 109
5.4 Coupled-Channel Results . . . . . 112
5.5 Approximate Model . . . . . 116
5.5.1 Errors in Approximations to $\Omega_{\text{eff}}$ . . . . . 123
5.6 Conclusions . . . . . 131

**6 Mergoassociation with Optical Tweezers: Part II 133**

6.1 Introduction . . . . . 134
6.2 Theoretical Methods . . . . . 135
6.2.1 Direct-Product Approach . . . . . 136
6.2.2 Shifted-Molecule Approach . . . . . 138
6.3 Effects of Coupling Between Relative and Center-of-Mass Motion . . 141
6.3.1 Weak Coupling . . . . . 145
6.3.2 Intermediate and Strong Coupling . . . . . 146
6.3.3 Mergoassociation for Other Systems . . . . . 150
6.3.4 Trap Anisotropy . . . . . 153
6.3.5 Logic Gates . . . . . 155
6.4 Conclusions . . . . . 156

**7 Conclusions 159**

**A Matrix Elements for Mergoassociation Basis Set Method 163**

A.1 Relative motion . . . . . 164
A.2 Center-of-mass motion . . . . . 165
A.3 Coupling between relative and center-of-mass motions . . . . . 167
A.4 Shifted-molecule basis set . . . . . 168

# List of Figures

3.1 Energies of the $^{39}$K (left-hand panel) and $^{133}$Cs (right-hand panel) hyperfine states as a function of magnetic field. Energies are shown relative to the hyperfine ground state at $B = 0$ G. Values of $|m_f|$ are color-coded as shown in the legend. Solid (and dashed) lines are used for positive (and negative) values of $m_f$. . . . . 32

3.2 $^{39}$K+$^{133}$Cs pair states with $m_F = 4, 3$, and 2 as a function of magnetic field. The color of the pair states encodes their singlet fractions. Pink corresponds to $F_s = 0.5$ and red corresponds to $F_s = 0.0$, as is shown in the inset. . . . . 35

3.3 $^{39}$K+$^{133}$Cs pair states with $m_F = 1, 0$, and $-1$ as a function of magnetic field. The color of the pair states encodes their singlet fractions. Pink corresponds to $F_s = 0.5$ and red corresponds to $F_s = 0.0$ as is shown by the inset in Figure 3.2. . . . . 36

3.4 $^{39}$K+$^{133}$Cs pair states with $m_F = -2, -3$, and $-4$ as a function of magnetic field. The color of the pair states encodes their singlet fractions. Pink corresponds to $F_s = 0.5$ and red corresponds to $F_s = 0.0$ as is shown by the inset in Figure 3.2. . . . . 37

3.5 Energies of bound states with $m_F = 4$ (lower panel) and the scattering length (upper panel) for the a+a threshold. Singlet fractions of deeply bound states are printed in the lower panel. . . . . 53

3.6 Square of the radial channel functions that constitute the multichannel wavefunctions of the states that appear in Figure 3.5. Panel (a) corresponds to the state in Figure 3.5 with a singlet fraction of 0.378 and panel (b) corresponds to the state with a singlet fraction of 0.482. 54

3.7 Energies of bound states with $m_F = 3$ (lower panel), the real part of scattering length for the a+b and b+a thresholds (middle panel), and the imaginary part of the scattering length with the loss coefficient at limitingly low energy (upper panel). Singlet fractions of deeply bound states are printed in lower panel. . . . . 55

3.8 Energies of bound states with $m_F = 2$ (lower panel), the real part of scattering length for the a+c, b+b, and c+a thresholds (middle panel), and the imaginary part of the scattering length with the loss coefficient at limitingly low energy (upper panel). Singlet fractions of deeply bound states are printed in lower panel. . . . . 56

3.9 Energies of bound states with $m_F = 1$ (lower panel), the real part of scattering length for the a+d, b+c, c+b, and d+a thresholds (middle panel), and the imaginary part of the scattering length with the loss coefficient at limitingly low energy (upper panel). Singlet fractions of deeply bound states are printed in lower panel. . . . . 57

3.10 Energies of bound states with $m_F = 0$ (lower panel), the real part of scattering length for the a+e, b+d, c+c, and d+b thresholds (middle panel), and the imaginary part of the scattering length with the loss coefficient at limitingly low energy (upper panel). Singlet fractions of deeply bound states are printed in lower panel. . . . . 58

3.11 Energies of KCs near-threshold bound-states with $M_F$ = 4, 3, 2, 1, and 0. . . . . 59

3.12 Bound-state energy measurements (blue crosses) in the vicinity of the Feshbach resonance at the a+a threshold. The bound-state energies calculated with the G2017 (black line) and B2024 (red line) potential are shown. . . . . 66

3.13 $L = 0$ and $L = 2$ bound states calculated in the vicinity of the resonance at the a+a threshold. The positions of avoided crossings between different states are included on the figure as are the strengths of these avoided crossings. . . . . 70

4.1 Energies as a function of magnetic field for (a) $^{87}$Rb atom in ground $^2$S state; (b) Lowest two rotational levels of CaF, with expanded views of $n = 0$ and 1 in (c) and (d), respectively; (e) Scattering thresholds of $^{87}$Rb+CaF, with expanded views of $(f_{\mathrm{Rb}}, n) = (1, 0)$, (2,0), (1,1) and (2,1) in (f) and (g), (h) and (i), respectively. All level energies are shown relative to the ground state at zero field and are color-coded as shown in the legend according to $m_{f,\mathrm{Rb}}$, $m_{f,\mathrm{CaF}}$ or $M_F = m_{f,\mathrm{Rb}} + m_{f,\mathrm{CaF}}$, as appropriate; negative values are indicated by dashed lines. . . . . 77

4.2 Near-threshold levels of Rb+CaF with $M_F = 1$, neglecting anisotropy, shown relative to the energy of the lowest threshold, for four representative combinations of the singlet and triplet scattering lengths. Solid black lines show results from coupled-channel calculations. Dashed (dot-dashed) lines show uncoupled states parallel to thresholds with $f_{\mathrm{Rb}} = 1$ (2). Values of $m_{s,\mathrm{CaF}}$ are encoded with red (blue) for $\frac{1}{2}$ $(-\frac{1}{2})$, with darker (lighter) colors for $m_{i,\mathrm{F}} = \frac{1}{2}$ $(-\frac{1}{2})$. $m_{f,\mathrm{Rb}}$ is given by $M_F - m_{s,\mathrm{CaF}} - m_{i,\mathrm{F}}$. Above each plot of energies is the corresponding plot of scattering length, with Feshbach resonances where states cross threshold. . . . . 85

5.1 Schematic representation of the energy levels involved in mergoassociation, as a function of trap separation $z_0$. The molecular level (approximately quadratic as a function of $z_0$) has avoided crossings with motional states of the atom pair (approximately horizontal at large $z_0$). Mergoassociation occurs when an atom pair in the lowest motional state is transferred into the molecular state by adiabatic passage over the lowest avoided crossing. . . . . 100

5.2 (a) Coordinate system for relative motion. The ellipsoid is a schematic representation of the shape of the trap potential for relative motion, and the Cartesian axes are aligned along its principal axes. (b) A cut through the potential for relative motion for $y = 0$, showing the contours of the harmonic trap centered at $\boldsymbol{R}_0$ (green) and a shorter-range atom-atom potential centered at the origin (blue). . . . . 105

5.3 Energies of two atoms in separate tweezers as a function of trap separation, obtained from coupled-channel calculations. Each panel is for a different aspect ratio $A_x$, for $\beta_{\mathrm{rel},z} = \beta_{\mathrm{rel},y} \approx 677\ a_0$, corresponding to $\omega_{\mathrm{rel},z} = \omega_{\mathrm{rel},y} = 150$ kHz. The grey dotted lines correspond to the spherical case with $A_x = A_y = 1$. . . . . 111

5.4 Effective matrix element $\Omega_{\mathrm{eff}}$ for the lowest avoided crossing, from coupled-channel calculations, as a function of aspect ratio $A_x$ for $A_y = 1$ and various values of $\beta_{\mathrm{rel},z}$. . . . . 115

5.5 Energies of two atoms in separate tweezers as a function of trap separation for $A_x = 2.1$. Black lines show the results of coupled-channel calculations, while orange and blue dashed lines show basis-set calculations with $n_x, n_y, n_z \leq 2$ and 10, respectively. Other parameters are as in Fig. 5.3. . . . . 119

5.6 Effective matrix element for the lowest avoided crossing as a function of aspect ratio $A_x$ for $A_y = 1$ and two values of $\beta_{\mathrm{rel},z}$; results shown are $\Omega_{\mathrm{eff}}$ from coupled-channel calculations (black), $|\langle a|V_{\mathrm{int}}(\boldsymbol{R})|000\rangle|$ from Eq. 5.53 (dotted), and $|\Omega_{\mathrm{eff}}^{2\times2}|$ from Eq. 5.55 (dashed). . . . . 121

5.7 LHS: bound state spectra for $a = 250.0$ a$_0$, $\beta_{\mathrm{rel,z}} = 500$ a$_0$, and a series of different aspect ratios. Eigenvalues from $2\times2$ (black) and $397\times397$ (grey) calculation are shown. RHS: terms featuring in 5.56. The blue solid (dashed) line is $E_{\mathrm{b}}$ ($\langle a|\hat{V}_{\mathrm{harm}}|a\rangle$). Black dot is the 'actual' shift of molecular state due to the trap. . . . . 126

5.8 LHS: bound state spectra for $a = 645.0$ a$_0$, $\beta_{\mathrm{rel,z}} = 500$ a$_0$, and a series of different aspect ratios. Eigenvalues from $2\times2$ (black) and $397\times397$ (grey) calculation are shown. RHS: terms featuring in 5.56. The blue solid (dashed) line is $E_{\mathrm{b}}$ ($\langle a|\hat{V}_{\mathrm{harm}}|a\rangle$). Black dot is the 'actual' shift of molecular state due to the trap. . . . . 128

5.9 Comparison of eigenvalues obtained with $2 \times 2$ (red) and $397 \times 397$ (black) Hamiltonian for different combinations of $A_a$ and $A_x$. Dashed vertical lines show approximation of $z_0^X$ obtained with Equation 5.35 130

6.1 Levels of Rb and Cs atoms in separated spherical traps as a function of separation $z_0$, with $\omega_{\mathrm{Rb}} = 100$ kHz and $\omega_{\mathrm{Cs}} = 60$ kHz. Solid green lines show the levels for pure relative motion, while dashed green lines show levels excited in the center-of-mass coordinate but neglecting coupling between relative and center-of-mass motions. Black lines show the results of the full coupled calculation using a direct-product basis set (444)(444). Only levels with EE symmetry are shown. . . . . 137

6.2 Levels of Rb and Cs atoms in separated spherical traps, as in Fig. 6.1, using different approaches. Black lines show results using a large shifted-molecule basis set (444)(444). Blue (or red) lines show results with smaller basis sets (444)(222) using the direct-product (or shifted-molecule) approach. . . . . 140

6.3 Levels of Rb and Cs atoms in separated spherical traps as a function of separation $z_0$, with $\omega_{\mathrm{Rb}} = 110$ kHz and $\omega_{\mathrm{Cs}} = 90$ kHz. Levels of EE, EO, OE, and OO symmetry are shown, but those of EO and OE symmetry are degenerate for spherical traps. . . . . 142

6.4 Levels of Rb and Cs in separated spherical traps as a function of separation $z_0$, with small differences between $\omega_1$ and $\omega_2$. Only levels of EE symmetry are shown. . . . . 144

6.5 Levels of Rb and Cs in separated spherical traps as a function of separation $z_0$, with moderate differences between $\omega_1$ and $\omega_2$. Only levels of EE symmetry are shown. . . . . 147

6.6 The strength of avoided crossings A to D as a function of $\omega_{\mathrm{Cs}} - \omega_{\mathrm{Rb}}$, with $\omega_{\mathrm{Rb}} + \omega_{\mathrm{Cs}}$ held constant at 200 kHz. The black lines show the crossing strengths from the shifted-molecule approach. The grey dashed lines show interpolations through regions where a $2 \times 2$ treatment breaks down, obtained as described in the text. The blue dashed line in (a) shows the result from Eq. 55 of ref. of the previous chapter. 149

6.7 Level crossing diagrams for $^{87}$Rb$^{87}$Sr, $^{133}$Cs$^{176}$Yb and $^{87}$Rb$^{174}$Yb for $\hbar\omega_1 = 2.5|E_a|$ and $\hbar\omega_2 = 1.5|E_a|$. This corresponds to $(\omega_1, \omega_2) = (51.4, 30.9)$, (94.0, 56.4) and (100.5, 60.3) kHz for the three systems, respectively. . . . . 152

6.8 Levels of Rb and Cs atoms in separated anisotropic traps as a function of separation $z_0$, with $\{\omega_{\mathrm{Rb},x}, \omega_{\mathrm{Rb},y}, \omega_{\mathrm{Rb},z}\} = \{144, 24, 144\}$ kHz and $\{\omega_{\mathrm{Cs},x}, \omega_{\mathrm{Cs},y}, \omega_{\mathrm{Cs},z}\} = \{96, 16, 96\}$ kHz. Levels with EE, EO, OE, and OO symmetry are shown. The atom-pair states are labeled with quantum numbers $\{n_{\mathrm{Rb},x}, n_{\mathrm{Rb},y}, n_{\mathrm{Rb},z}, n_{\mathrm{Cs},x}, n_{\mathrm{Cs},y}, n_{\mathrm{Cs},z}\}$. . . . . 154

# List of Tables

3.1 Available basis sets for alkali-metal atom + alkali-metal atom calculations in BOUND, FIELD, and MOLSCAT. . . . . 38

3.2 Feshbach resonance positions used by Gröbner et al. in 2017 to refine the KCs interaction potential. The threshold at which the resonance occurred, the position of the resonance as measured in experiment, and the singlet fraction of the state that causes the resonance are given. 44

3.3 $B_{\mathrm{res}}$ (B), $\Delta$ (G), and $a_{\mathrm{bg}}$ ($a_0$) for the s-wave Feshbach resonances caused by states with low singlet fractions. The thresholds these resonances occur at are given. . . . . 60

3.4 $B_{\mathrm{res}}$ (B), $\Delta$ (G), and $a_{\mathrm{bg}}$ ($a_0$) for s-wave Feshbach resonances caused by states with $n = -1$. The thresholds at which these resonances occur are given. . . . . 61

3.5 Agreement between measured Feshbach resonance positions and those predicted with the B2024 potential. The thresholds these resonances occur at are given. The uncertainty of the measurement included in our fit and the $2\sigma$ value calculated from our fit are included.

67

3.6 Broad resonances at lowest scattering thresholds characterized with $L = 0$ scattering calculations. . . . . 68

4.1 Feshbach resonance positions, widths and background scattering lengths for different combinations of $a_s$ and $a_t$. The approximate quantum numbers of the uncoupled state that causes the resonance are given in each case. Asterisks indicate cases where this uncoupled state is substantially mixed with the least-bound state in the incoming channel where it crosses threshold. . . . . 90

# Declaration

I confirm that no part of the material contained in this thesis has previously been submitted by myself for a degree in this or any other University. Where material has been generated through joint work, the work of others has been indicated.

# Acknowledgements

Firstly, I would like to thank my supervisor, Professor Jeremy Hutson, whose vision and drive made the work presented in this thesis possible. I am hugely grateful for his patience, attention, and guidance over the previous three years.

I would like to thank all the members of the Hutson Group for their expertise and friendship; Dr German Sinuco, Dr Bijit Mukherjee, Dr Matthew Frye, Dr Ruth Le Sueur, Dr Joy Dutta, and Dr James Croft. I'd like to thank Ruth in particular for the important contributions she made to the $^{39}K^{133}Cs$ and mergoassociation projects.

The work presented in this thesis was born out of several collaborations with experimental groups. I would like to thank Charly Beulenkamp, Krzysztof Zamarski, Dr Yi Zeng, Dr Manuele Landini, and Professor Hanns Christoph Nägerl for their contributions to the $^{39}K^{133}Cs$ project. I'd like to thank Professor Mike Tarbutt for his insights into atom-molecule collisions. I'd like to thank Dr Daniel Ruttley, Dr Stefan Spence, Dr Alexander Guttridge, and Professor Simon Cornish for their insights into optical tweezers and their work on mergoassociation.

Before moving away from the professional, I would like to acknowledge that many people played a role in my early academic career. I was lucky to have wonderful chemistry teachers in my last two years at school, and I was able to work with a series of great PhD students, post-docs, and academics during my undergraduate studies. Special thanks are due to Professor Katharine Reid – the summer I spent in her research group inspired me to do a PhD.

I have met many lovely people during my time in Durham. My sincere thanks go

to the members of the Durham Quantum Light and Matter research section and the members of the Wilson, Miller, and Tozer groups, all of whom have been unfailingly friendly.

The friends I have made while in Durham have been wonderful. I am deeply grateful for Frankie, Cath, Alex, Charles, Eoin, and Josh. Over the last three years their company, humour, support, and friendship have been a large part of my life.

I would like to take this opportunity to thank Rose, Pond, and Tasha for their enduring and close friendship. It has been invaluable.

Finally, I would like to thank my family – Mum, Dad, Harry, Hannah, Jess, Luke, Sarah, Paul, Granny, Marcus, Ashley, Nicola, Hugh, Andrew, and Farmor. Mum and Dad, in particular, continue to be an endless source of love and support.

# Chapter 1

# Introduction

## 1.1 Ultracold Atomic Gasses

During the 20$^{\text{th}}$ century experimental and theoretical physicists worked to resolve the structure of atoms and simple molecules. The development of atomic, molecular, and optical (AMO) physics was intimately related with the development of quantum theory. Progress made in these research fields marked a huge step forward in humanity's fundamental understanding of matter. One vein of contemporary AMO physics, ultracold physics, stemmed from attempts to study atomic gasses at increasingly low temperatures. At ultracold temperatures, typically accepted as those beneath 1 mK, quantum mechanics plays a dominant role in determining the behavior of matter [1–3]. Physicists' mission to reach increasingly low temperatures was partly motivated by the potential discovery of novel physics far removed from our classical world. At these temperatures physicists are also afforded exquisite control over the motions of and interactions between atoms and molecules. The experimental realization of Bose-Einstein condensation in ultracold atomic gasses of Na and Rb, at 2 $\mu$K and 170 nK, in 1995 was a landmark in the development of ultracold AMO physics [4, 5]. This seminal achievement was recognised with the 2001 Nobel Prize in Physics, which spoke to the many exciting, and potentially revolutionary, possibilities of experiments performed with atomic gasses at ultracold temperatures [6, 7].

A Bose-Einstein condensate is an exotic state of matter in which an ensemble of bosons have entered the same quantum state. The first Bose-Einstein condensates, that were produced in ultracold atomic gasses, offered model systems with which to explore more elusive quantum phenomena and effects [6, 8]. Some of the many exciting discoveries made with these condensates are reviewed here in order to illustrate the excitement around ultracold physics at the turn of the 21$^{\text{st}}$ century. The Na condensate was used to study the quantum interference of matter waves and vortex lattices, the manifestation of quantized rotational motion in macroscopic quantum systems. These studies were key to further understanding phenomena such as superfluidity and superconductivity. The Na condensate also played a central role

in early studies of the zero-energy magnetically tuneable Feshbach resonances that exist in the collisions between ultracold atoms [9]. The Rb condensate was used to study excitations of Bose-Einstein condensates and the dynamics of two-component condensates [7]. These resonances occur when the energy of two colliding atoms is equal to the energy of a bound state supported by the atom-atom interaction potential [10]. These resonances play an important and enduring role in ultracold AMO physics as they allow physicists to control the interactions between atoms with a magnetic field.

A variety of applications beyond Bose-Einstein condensation have been found for ultracold atomic gasses. Cold and ultracold atomic gasses have been used as platforms for precision measurement. Transitions between atomic states are used as absolute reference frequencies in atom clocks and cold atoms have been used to measure magnetic and optical fields as well as forces such as gravity [11]. Many discoveries were made with ultracold gasses of fermionic atoms. The first experimental evidence of a Fermi gas was observed at 300 nK [12]. The pairing of fermions and the BCS-BEC crossover have been studied with these gasses [13]. Gasses of ultracold dipolar atoms, such as Cr, Dy, and Er, have allowed the study of quantum fluids and offered a model system for exploring quantum chaos in ultracold collisions [14].

Before we discuss the production of ultracold atomic gasses we take the opportunity to explore the important role theoretical physicists have played in ultracold AMO physics. At the turn of the century theoretical physicists were contributing to ultracold AMO physics in two different ways. Condensed matter physicists focused on elucidating the properties of macroscopic quantum systems and the many-body physics that could be investigated with ultracold atomic gasses such as Superfluid-Mott insulator transitions and the BCS-BEC crossover [15]. Molecular physicists were less concerned with the macroscopic sample itself and instead focused on the microscopic interactions between the constituent particles of an ultracold gas. Advanced theoretical methods were developed to explain the scattering dynamics of ultracold atoms that were inspired by earlier theories of atomic and molecular scat-

tering [16–19]. Numerous properties of ultracold atomic gasses were consequently resolved, for example why certain BECs were stable and others were not [20]. By understanding how the interaction of particles in an ultracold gas could be controlled new physics could be studied, such as the controlled collapse of a BEC [21]. Controlling atomic interactions in an ultracold atomic gas relied on tuning a magnetic field across the zero-energy Feshbach resonances mentioned previously. A general introduction to the theory of quantum scattering is given in Section 2 of this thesis. A detailed discussion of Feshbach resonances is given in Section 2.3.

Thus far we have considered the physics studied with ultracold atomic gasses. In the next section we shall begin to explore ultracold molecules, the formation of which is the central topic of this thesis. Before moving ahead, however, we shall address the production of ultracold atomic gasses. Laser light is used to cool atoms and confine them in space [22–24]. The development of these cooling and trapping techniques were awarded the 1997 Nobel Prize in Physics and many of them are still used in experiments today.

Laser cooling encompasses a number of techniques that exploit the various forces electromagnetic radiation exerts on particles. Doppler cooling, the most simple laser cooling technique, and Zeeman slowing, a cooling technique that remains widely popular, are discussed here. Both techniques have been used in ultracold experiments to cool particles in an atomic beam prior to trapping and further cooling. In Doppler cooling, atoms are irradiated with counter-propagating photons. These photons are red-detuned from an electronic transition within the atom. Due to the Doppler effect only atoms whose momenta oppose the momenta of the photons can absorb a photon. An atom's velocity is reduced when it absorbs a counter propagating photon. When many photons have been absorbed and re-emitted the velocity of the atom is on average lower. The efficiency of Doppler cooling is limited because the atom's excited electronic state can decay to different hyperfine states in the ground electronic state. Furthermore, as atoms are cooled their velocities reduce and the frequency of the cooling light becomes off-resonant with the atomic transition due to

the Doppler effect. Zeeman slowing uses a magnetic field to impose more stringent selection rules on the atom-photon interaction, by conserving the projection of the system's total angular momentum, thereby reducing the states the excited state can decay to, and to tune the energies of the atomic states such that the photons used for cooling do not become off-resonant with the relevant atomic transition.

The force exerted on atoms by laser light is also the basis of many traps. Optical molasses use six counter propagating laser beams to generate an overall force on atoms that opposes their motion, thereby trapping them. The magneto-optical trap (MOT) is a key feature of most ultracold experiments and uses a magnetic field in addition to counter-propagating laser beams in order to trap and cool atoms simultaneously [25]. Certain traps relied on the dipole force generated by electromagnetic radiation rather than the scattering force [26]. The induced dipole moment of an atom in a light field is subject to a potential energy well in 3D space. The minimum of this potential exists where the intensity of light is greatest. The dipole force is proportional to the derivative of this potential; as the particle moves away from the center of the trap the force exerted on the particle increases and opposes its velocity. This physics underpinned some of the first traps for cold atoms, which were made with a single focused laser beam, and the more recent tweezer traps that are an important topic in this thesis. Many of the techniques outlined here were used in the first BEC experiments and still constitute the basic features of most ultracold experiments developed today [27].

## 1.2 Formation of Ultracold Molecules

The field of ultracold molecules has grown rapidly over the past two decades [28]. The rich physics of diatomic molecules has underpinned significant scientific and technological innovation at ultracold temperatures. The field is explored in the remainder of Section 1. We begin by discussing the various methods used to generate ultracold molecules.

Substantial progress has been made with respect to making molecules at ultra-

cold temperatures. The methods employed are categorized as direct or indirect. Direct methods cool 'hot' molecules to ultracold temperatures. Indirect methods make molecules at ultracold temperatures from ultracold atoms. Magnetoassociation is an indirect method used to make ultracold molecules. A magnetic field is tuned across a Feshbach resonance sufficiently slowly such that two colliding atoms are converted into a loosely-bound molecule. Magnetoassociation produces molecular gasses with high phase space densities at ultracold temperatures and is therefore the preferred indirect method for making ultracold molecules. Magnetoassociation, and other indirect approaches, are typically followed by Stimulated Raman Adiabatic Passage (STIRAP) which transfers the vibrationally excited molecule to the absolute ground state [29]. The first ultracold gas of molecules produced with magnetoassociation and STIRAP was $^{40}$K$^{87}$Rb in 2008 [30]. Since then a large number of bi-alkali molecules have been made with similar methods including $^{87}$Rb$^{133}$Cs [31], $^{23}$Na$^{39}$K [32], $^{23}$Na$^{40}$K [8], $^{23}$Na$^{133}$Cs [33], $^{23}$Na$^{6}$Li [34], $^{23}$Na$^{87}$Rb [35], $Rb_2$ [36], and $Cs_2$ [37]. Theoretical molecular physicists were intimately involved with the development of magnetoassociation as a standard technique for the formation of ultracold molecules [38, 39]. There is the potential for more exotic molecules containing alkaline-earth metal atoms [40], d-block elements [41], and highly magnetic atoms [42] to be magnetoassociated. At present no such molecules have been produced in their absolute ground states, however.

An alternative method of making molecules is direct laser cooling. The same mechanisms which were relied upon to cool atoms (Section 1.1.1) to ultracold temperatures are employed with molecules. Laser cooling is very effective for molecules with diagonal Frank Condon factors. Examples of such molecules include the alkaline earth monoflourides and oxides such as YbF [43], SrF [44], CaF [45, 46], and YO [47]. At present experiments with CaF have achieved temperatures of 5 $\mu$K. Some success has been achieved with polyatomic molecules as well, for example linear triatomics such as SrOH, although this is still an emerging area of research [48].

## 1.3 Applications of Ultracold Molecules

The production of a variety of molecules at cold and ultracold temperatures has enabled researchers to make important discoveries in a number of fields. In this section we review some of the applications of ultracold molecules and try to capture their variety.

New insights into fundamental chemical processes have been gained with ultracold molecules. The molecular beam techniques used in reaction dynamics experiments are often unable to reach temperatures where the translational motion of the reaction partners is quantised [49]. Bimolecular KRb collisions have been studied at 500 nK [50, 51]. Theories of statistical quantum mechanics for chemical reactions were tested by analysing the rotational state distribution of the collision products. Molecule-molecule collisions in ultracold molecular gasses pose a number of challenges for researchers. These are discussed in depth in Section 1.4. Interrogating collisional processes at these temperatures is an important avenue of research. Chemical reactions can occur at cold temperatures in nature. For example, the interstellar medium has temperatures of a few K. Cold and ultracold molecules allow chemical processes to be studied at these temperatures [52, 53].

Laser-cooled molecules at ultracold temperatures are bridging the gap to seemingly unrelated fields such as nuclear physics, particle physics, and cosmology due to their possible use in testing theories of fundamental physics [54]. The Standard Model is unable to explain a number of observations made about the universe. It cannot account for the matter-antimatter asymmetry in the universe, explain why the expansion of the universe is accelerating, or how gravity fits in relation to other fundamental forces [55]. Fundamental physics is typically investigated with exceptionally expensive high-energy particle colliders. Ultracold molecules offer a platform for cheaper table-top experiments that are able to probe some of the pressing questions in fundamental physics relating to our theories of nature and the universe. Ultracold molecules may be used to investigate the violation of time-reversal symmetry with measurements of the electron's electric dipole moment. Molecules would

be a particularly good platform for these studies because they can be strongly polarized with low, and easily controllable, electric fields. These measurements would be used to assess various theories that go beyond the Standard Model [56].

Ultracold molecules are increasingly discussed in the context of more technological and applied areas of research such as quantum simulation and quantum computation [57]. Quantum simulation has been a long-sought goal, imagined alongside the quantum computer, as a method to probe the quantum nature of many-body systems [58]. Ultracold polar molecules are useful for simulating key phenomena in condensed matter physics for a number of reasons. Polar molecules interact with one another via long-range dipole-dipole interactions, which can be tuned with external fields [59]. These interactions are stronger than the dipole-dipole interactions that exist between magnetic atoms and are weaker than those that exist between Rydberg atoms. Rydberg atoms, however, are usually short lived. Ground-state molecules in optical lattices and tweezer arrays at ultracold temperatures have long lifetimes and a large number of states that can be easily populated and controlled by physicists with external fields. There have been proposals for using polar molecules as the hardware in quantum simulators studying Hubbard models [60], quantum-phase transitions [61], topological order [62], and quantum magnetism [63]. Quantum simulation is an important avenue of research due the importance of various topics in many-body physics. For example, Hubbard models are used to describe the behavior of low-energy bosons or fermions in periodic potentials, as such they offer insight into phenomena such as the high-temperature superconductivity of cuprates [64]. Implementing a Hubbard model with ultracold molecules in a lattice and then taking measurements of various observables allows comparison with the 'real' system. This procedure allows theories and models to be ruled out, confirmed, and/or adapted [65].

Quantum computation is an approach to information processing that is fundamentally different from classical computation. It exploits the basic principles of quantum mechanics to improve the speed and efficiency of calculations. Quan-

tum computers will be able to undertake tasks that are impossible for conventional computers. There are many different areas of research that underpin the creation of quantum computers such as the development of quantum algorithms, proposing systems to use as qubits (quantum bits) and qudits (computational unit with more than two dimensions), and finally engineering and building the computers [66]. Molecular physicists and materials scientists are primarily concerned with identifying systems to use as qubits and qudits. Several different physical systems are being explored, one of which is ultracold molecules. Several proposals have been published studying the energy-level structure of different ultracold molecules, such as CaF and RbCs, with a view to identifying what manifolds of states would make effective qubits. Qudits could feasibly be implemented with ultracold molecules [67]. Designing methods to entangle states and perform operations on states, so called quantum-logic gates, is a key objective that needs to be achieved if molecules are to be a possible architecture for quantum computers. One such example would be using dipolar-exchange interactions between molecules in different rotational states to mix different hyperfine states [68].

## 1.4 Research Frontiers

Thus far this section has explored the development of, and achievements in, the field of ultracold molecules. Substantial challenges remain, however, and our attention now turns to sketching the landscape of research with ultracold molecules in the present day.

Ultracold molecular gasses are subject to high levels of loss, which places serious limits on the density and lifetimes achieved in state-of-the-art experiments. Researchers' understanding of the processes underpinning the losses in different experiments is still incomplete. There are two dominant routes by which molecules are lost; direct collisions and sticky collisions. Intermolecular complexes do not form during direct collisions. The collision products are ejected from whatever trap is used in the experiment if they gain sufficient kinetic energy during an inelastic or

reactive process [69]. The challenge lies in understanding this particular loss mechanism. At present theoretical calculations simply cannot manage the basis-set size needed to describe a bimolecular collision at ultracold temperatures. Sticky collisions are typically associated with the non-reactive collisions between bi-alkali molecules occupying their ground rovibrational and hyperfine states [70]. The term sticky collision is derived from some of the first theories exploring the loss of molecules from ultracold molecular gasses. These theories suggested that when two molecules get close enough such that their dynamics are governed by the short-range region of the interaction potential the molecules form a long-lived complex, subject to the statistical RRKM theory [71, 72]. The existence of these complexes has been verified experimentally [73]. Their role in the loss of molecules from experiments is, however, clouded by a series of conflicting theoretical and experimental results. There also remains some ambiguity as to whether sticky collisions and direct collisions both contribute to the loss, or if one dominates over the other [74]

At present there are a large number of different ultracold molecule experiments in operation around the world. As would be expected these experiments are all at different stages and therefore face different challenges. Experiments that are yet to produce ultracold molecules in their absolute ground state require expertise and research in atom-atom scattering. Molecule formation via indirect methods for certain systems are just now being investigated, therefore questions pertinent to magnetoassociation and STIRAP remain relevant. On the other hand, many experiments are starting to utilize new experimental techniques and address the issue of loss we just introduced. The remainder of Section 1.4 explores some of these new experimental techniques.

One particularly exciting technology, which a large portion of this thesis is related to, is optical tweezer traps which were briefly mentioned in Section 1.1. Optical tweezer traps, which use focused laser beams to trap particles in space, allow the positions of atoms and molecules to be controlled and arrays of particles to be constructed. Making molecules in optical tweezers and investigating their applications

has progressed very quickly in the last 5-10 years. Some highlights include the photoassociation of NaCs in a tweezer [75], the formation of a loosely bound molecule in a tweezer with magnetoassociation [33], transferring the loosely-bound molecule to the rovibronic ground state [76], and current work constructing optical tweezer arrays [77].

A series of new experimental techniques, so-called shielding techniques, are being developed to address the challenge of loss in experiments. Shielding relies on external fields to engineer long-range barriers in the interaction potentials of two molecules, therefore preventing molecules from interacting via short-range processes that induce loss. Current proposals for molecule-molecule shielding use optical fields [78], microwave fields [79], and electric fields [80].

Another avenue of research being pursued in a number of experiments is how to address the challenge of dephasing. Experiments in the area of quantum simulation and quantum computation use molecules prepared in specific quantum states. When these state-selected molecules interact with their environment they can dephase and the state that was needed for the application is lost. New proposals are being developed to reduce this dephasing such as numerous magic trapping techniques [81, 82].

A recent and exceptionally important landmark in the field of ultracold physics was the observation of Bose-Einstein condensation in an ultracold molecular gas [83]. NaCs molecules were cooled to temperatures of 6 nK after microwave shielding was used to reduce loss. The NaCs molecule has a dipole moment that can be tuned between the weak and strong dipolar regimes. This versatility cannot be achieved with other dipolar particles, such as dipolar atoms or Rydberg atoms, thereby illustrating ultracold molecules' emerging appeal to physicists and their bright future.

In the preceding discussion we have traced the field of ultracold molecules from its inception, out of the seminal work on ultracold atomic gasses, to the challenges the field faces in the present day. Part of this discussion reviewed the exciting appli-

cations that ultracold molecules have found in the fields of chemistry, fundamental particle physics, condensed matter physics, and information processing.

## 1.5 Outline

This thesis is the result of many different collaborations and research projects. These projects, and by extension this thesis, are connected by the theme of molecule formation in contemporary ultracold AMO experiments. The methods used to make molecules that are addressed here include magnetoassociation and mergoassociation with optical tweezer traps. From Section 1.2 it is clear that magnetoassociation is a well-established technique for making molecules. We explore the physics behind magnetoassociation in the context of $^{39}$K + $^{133}$Cs collisions. We then explore the possibility of controlling atom-molecule collisions with magnetic fields and the prospect of magnetoassociating triatomic molecules. The latter half of this thesis is devoted to mergoassociation. Mergoassociation is a novel approach to molecule formation that has been observed in the previous two years.

Many of the chapters in this thesis are adapted from previously published scientific papers. References to these papers are given below, in the outline to this thesis, and at the start of the relevant chapter.

The thesis is structured as follows. Chapter 2 is a guide to the theory of atomic and molecular scattering. Single-channel, multichannel, and near-threshold scattering are introduced. The numerical propagation techniques we use in the BOUND and MOLSCAT program packages to solve the coupled-channel Schrödinger equation are discussed [84, 85]. Chapter 3 details our efforts to improve our understanding of the near-threshold bound states of $^{39}$K$^{133}$Cs. These results were used to help our collaborators in the Nägerl Group (University of Innsbruck) undertake a series of measurements that would allow us to refine the $^{39}$K + $^{133}$Cs interaction potential. We were able to refine the interaction potential. Details of our refitting and the new potential are included here. Chapter 4 considers the magnetically tunable Feshbach resonances that may exist in ultracold mixtures of CaF molecules and

Rb atoms. The existence of these resonance will be crucial for forming RbCaF molecules by magnetoassociation. Chapter 4 is a reproduction of [86]. Chapter 5 develops coupled-channel and basis set approaches for solving the relative motion Schrödinger equation for two atoms contained in two separate optical tweezer traps. We study the effects of trap strength and trap anisotropy. Chapter 5 is a reproduction of [87]. Chapter 6 includes our extension to the work presented in Chapter 5. We develop a theoretical method that accounts for the coupling between the relative motion and center-of-mass motion for two atoms contained in two separate traps and consider its consequences for mergoassociation. Chapter 6 is a reproduction of a paper currently under review [88]. Chapter 7 presents the conclusions drawn from this thesis.

# Chapter 2

# Quantum Scattering Theory and Bound States

Collisions occur in the ultracold atomic and molecular gasses discussed in the Introduction. Atomic and molecular scattering theory, which we introduce in this chapter, is needed to describe and understand these collisions. In Section 2.1 key concepts in the theory of molecular scattering are illustrated with the model problem of two structureless particles interacting via a central potential. The description offered in this section is based on Hutson [89], Friedrich [90], and Child [91]. The scattering of structured particles is considered in Section 2.2. The work of Child [91], Hutson [89], and Quéméner [92] proved useful in the development of this section. In this thesis the notation and conventions selected by Le Sueur and Hutson will be used [84, 85].

Before proceeding we introduce the differential and integral cross sections. The differential cross section is defined as

$$\frac{d}{d\Omega}\sigma_{ij} = I_{ij}(\Theta, \Phi). \tag{2.1}$$

The subscripts $i$ and $j$ label the internal states of the collision partners before and after the collision, $\Theta$ and $\Phi$ are the deflection angles, $I_{ij}(\Theta, \Phi)$ is the flux of particles in state $j$ after the collision normalized by the flux of the incident particles in state $i$ before the collision, and $d\Omega$ is an element of solid angle. The integral cross section,

$$\sigma_{ij} = \int_0^{2\pi} \int_0^{\pi} I_{ij}(\Theta, \Phi) \sin\Theta d\Theta d\Phi, \tag{2.2}$$

is independent of angle and quantifies the probability of the collision driving a transition between states $i$ and $j$. The total cross section is the sum of the cross sections for all possible final states.

## 2.1 Structureless Particles

The Hamiltonian that describes the relative motion of two interacting and structureless quantum particles,

$$-\frac{\hbar^2}{2\mu}\nabla^2 + V(R), \tag{2.3}$$

is derived from the canonical quantization of the classical two-body Hamiltonian. $\nabla^2$ is the Laplacian and $V(R)$ is the potential energy function that governs the interaction of the particles. In the case of a central potential the interaction potential is isotropic. The angular terms in the Laplacian are equal to the square of the collision pair's orbital angular momentum, $\hat{L}^2$, which we refer to as the end-over-end angular momentum. The Hamiltonian is written more explicitly as

$$-\frac{\hbar^2}{2\mu}\frac{1}{R}\left(\frac{\partial^2}{\partial R^2}\right)R + \frac{\hbar^2}{2\mu R^2}\hat{L}^2 + V(R). \tag{2.4}$$

By convention the dissociation limit of the potential is zero. This Hamiltonian is applicable in studies of bound states with discrete energies, $E_n < 0$, and the continuum of scattering states with $E > 0$. We explore the scattering states before discussing bound states.

In the asymptotic limit the wavefunction is comprised of an incoming plane wave along $Z$ and an outgoing spherical wave, the magnitude of which varies with deflection angle $\Theta$. This is expressed as

$$\Psi(R,\Theta) \overset{R\to\infty}{\sim} e^{ikz} + f(\Theta)\frac{e^{ikR}}{R}, \tag{2.5}$$

where $f(\Theta)$ is the scattering amplitude. Equation 2.5 constitutes an important ansatz for, and boundary condition of, the wavefunction describing the scattering of two quantum particles.

It is possible to expand the total wavefunction in a basis of radial functions,

$\psi_L(R)$, and Legendre polynomials, $P_L(\cos\Theta)$, as

$$\Psi(R,\Theta) = \frac{1}{R}\sum_L \psi_L(R) P_L(\cos\Theta). \tag{2.6}$$

The $R^{-1}$ term has been introduced to simplify the radial kinetic energy operator in Equation 2.4. The Legendre polynomials are eigenfunctions of $\hat{L}^2$. The end-over-end angular momentum, $L$, is a good quantum number i.e. the Hamiltonian contains no terms that can couple states of different $L$ and the matrix representation of the Hamiltonian is therefore diagonal in $L$. This simplifies any attempt to develop a more detailed description of the wavefunction as each angular momentum state can be considered independently to one another. This rational forms the foundations of the partial wave analysis. Restricting $L$ to a single value and substituting the wavefunction, Equation 2.6, into the Schrödinger equation, along with the Hamiltonian, Equation 2.4, gives the radial equation,

$$\left(-\frac{\hbar^2}{2\mu}\frac{d^2}{dR^2} + \frac{\hbar^2}{2\mu R^2}L\left(L+1\right) + V(R) - E\right)\psi_L(R) = 0. \tag{2.7}$$

The solutions of Equation 2.7 depend on the potential $V(R)$. For realistic interaction potentials, and simple models such as Lennard-Jones potentials, one cannot derive analytic expressions for $\psi_L(R)$ or key scattering observables, such as the differential cross section. Numerical methods are intimately related with quantum scattering theory and are introduced later in this Section.

To gain insight into $\psi_L(R)$ we consider Equation 2.7 in the regions of $R$ where the centrifugal term dominates over $V(R)$. As $V(R) \to 0$ the form of Equation 2.7 is that of a Riccati-Bessel differential equation, and

$$\psi_L(R) = A_L kR j_L(kR) + B_L kR n_L(kR), \tag{2.8}$$

where $A_L$ and $B_L$ are constants, $k^2 = 2\mu E/\hbar^2$, $j_L$ is the spherical Bessel function of the first kind, and $n_L$ is the spherical Bessel function of the second kind [93]. In the

limit of $R \to \infty$, Equation 2.8 reduces to

$$\psi_L(R) \overset{R\to\infty}{\sim} \sin(kR - \frac{L\pi}{2} + \delta_L), \tag{2.9}$$

where $\delta_L$ is the phase shift which quantifies the effect of the potential on the scattering wavefunction in the infinite limit. The phase shift is related to the coefficients $A_L$ and $B_L$ in Equation 2.8 by $\delta_L = \tan^{-1}(B_L/A_L)$. Euler's formula can be applied to Equation 2.9 to get an expression for $\psi_L(R)$ that lends itself to the concept of incoming and outgoing waves. Equation 2.9, in tandem with Equation 2.6, allows us to understand that the states of the time-independent scattering Schrödinger Equation are a potentially infinite sum of spherical waves, each of which supports an incoming and outgoing radial component. The outgoing component in each partial wave is shifted in phase to a different extent by the potential.

A detailed expression for the scattering amplitude, featuring the phase shift, can be derived. If the scattering amplitude in Equation 2.5 is expanded as $\sum_L f_L P_L(\cos\Theta)$, and the plane wave is expanded using Rayleigh's formula, then in the limit of $R \to \infty$, Equation 2.5 matches Equation 2.6 when the expression for $\psi_L(R)$ in Equation 2.8 has been substituted. Consequently, expressions for $A_L$ and $B_L$ can be found, that contain the term $f_L$, and the scattering amplitude is expressed as

$$f(\Theta) = \sum_L \frac{(2L+1)}{k} e^{i\delta_L} \sin(\delta_L)\, P_L \cos\Theta. \tag{2.10}$$

The square of the modulus of the scattering amplitude, $|f(\Theta)|^2$, if generalized to be a function of $\Theta$ and $\Phi$, is equal to $I_{i,j}(\Theta, \Phi)$ in the differential cross section, Equation 2.1.

To obtain a value of $\delta_L$, for a given potential, Equation 2.7 must be solved using numerical methods. We typically elect to use numerical propagation [17, 89]. The principles of these methods are closely related to more simple numerical methods for ordinary differential equations such as the Numerov method [94]. Single-channel scattering is a perfect example with which to introduce some features of numerical

propagation. Regions of $R$ for which $V(R) > E$ are termed classically forbidden regions. Regions of $R$ for which $V(R) < E$ are classically allowed regions. Numerical propagation uses a grid of points between $R_{\text{min}}$, placed in the classically forbidden region, and $R_{\text{max}}$, placed well into the classically allowed region. Various different propagation methods exist that rely on propagating different mathematical functions. Perhaps most simply the wavefunction can be propagated although this is disadvantageous so far as propagating the wavefunction is numerically unstable in classically forbidden regions. Johnson developed more complex propagation procedures such as the renormalized Numerov and log-derivative methods [95]. The latter propagates the log derivative of the wavefunction,

$$Y(R) = \frac{1}{\psi_L(R)}\psi_L(R)', \tag{2.11}$$

where $\psi_L(R)'$ denotes the derivative of $\psi_L(R)$ with respect to $R$. We use the example of $\psi_L(R)$ to define $Y(R)$ to be consistent with Equation 2.6 and our present discussion. Having obtained the wavefunction, the phase shift is obtained by comparing the value and derivative of the numerical solution to the analytic expression for the asymptotic behavior of the free particle, $\sin(kR - L\pi/2)$.

Bound states supported by $V(R)$ are subject to two boundary conditions; $\psi(0) = 0$ and $\psi(\infty) = 0$. The bound states of $V(R)$ exist at discrete energies, $E_n$.

Numerical propagation is also used for the calculation of bound-state eigenvalues and eigenfunctions. Compared to the scattering problem there are two classically forbidden regions and a single classically allowed region. Propagation into a classically forbidden region is typically unstable and best avoided, so the simple procedure of propagation from $R_{\text{min}}$ to $R_{\text{max}}$ is not appropriate. Two propagations are undertaken, one out from $R_{\text{min}}$ and one in from $R_{\text{max}}$ to a matching point in the classically allowed region, $R_{\text{match}}$. An accurate eigenvalue will correspond to an eigenfunction that is continuous and has a continuous derivative. A matching function can be

defined with the log-derivative of the wavefunction,

$$Y^{+}(R_{\text{match}}) - Y^{-}(R_{\text{match}}) = 0, \tag{2.12}$$

which will be zero when the eigenvalue is found. $Y^{+}$ constitutes the outwards propagation and $Y^{-}$ constitutes the inwards propagation. The algorithms used to find eigenvalues are usually made of two steps. Firstly, bisection is used with a specified trial energy to obtain a small energy range the state is known to exist in. The node count of the state being investigated is used in this bisection procedure [17, 96]. Once a region of energy has been found that is sufficiently precise then propagation is used to obtain a value of the matching function. The eigenvalue is then found by iterating towards a zero of the matching function.

## 2.2 Multichannel Problem

In Section 2.1 key concepts in atomic and molecular scattering theory, such as partial waves, phase shifts, bound states, and numerical propagation, were introduced with the simple example of structureless particles. Section 2.2 discusses the theoretical treatment of structured particles.

The channels that govern the collision dynamics of structured particles are the asymptotic states of the collision pair. We use a general subscript, $j$, in the following discussion to label each scattering channel. If the energy of a given channel, $E_j$, exceeds the collision energy, $E$, the channel is closed. If the energy of a given channel, $E_j$, lies beneath the collision energy, $E$, the channel is open. If there is a single open channel only elastic collisions are possible. If there are multiple open channels inelastic and reactive processes are possible and the collision may populate any of the open channels.

The relative motion Hamiltonian for the collision of two structured particles is

$$\hat{H} = -\frac{\hbar^2}{2\mu}\left(R^{-1}\frac{d^2}{dR^2}R\right) + \frac{\hbar^2}{2\mu R^2}\hat{L}^2 + \hat{H}_{\text{intl}}(\xi) + \hat{V}(R,\xi) \tag{2.13}$$

where $\xi$ encompasses all dimensions excluding the coordinate $R$, $\hat{H}_{\text{intl}}(\xi)$ is composed of the internal Hamiltonians of the collision partners, and $\hat{V}(R,\xi)$ is the potential energy operator that is a function of the internal coordinates of the particles. For the example of two alkali-metal atoms colliding in a magnetic field $\xi$ encompasses the electron spin and nuclear spin of each atom and the end-over-end angular momentum of the complex. A basis encompassing all possible states of the collision pair is needed to span the space of the Hamiltonian in Equation 2.13. An obvious route forward is to expand the wavefunction in a basis that is the direct product of functions that span the space of $\hat{H}_{\text{intl}}(\xi)$ and $\hat{L}^2$ and therefore describes the scattering channels at $R \to \infty$,

$$\Psi(R,\xi) = \frac{1}{R}\sum_j \psi_j(R)|j(\xi)\rangle. \tag{2.14}$$

The wavefunction expansion includes radial channel functions, $\psi_j(R)$, which can be thought of, at a given value of $R$, as the expansion coefficients describing how much a given channel contributes to the wavefunction describing the collision pair. By substituting Equations 2.13 and 2.14 into the Schrödinger Equation, taking the braket product with $\langle j'(\xi)|$, and rearranging the result, we arrive at a series of coupled differential equations, expressed in matrix notation as,

$$\left(-\frac{\hbar^2}{2\mu}\frac{d^2}{dR^2} - E\right)\boldsymbol{\psi} + \bar{\boldsymbol{W}}\boldsymbol{\psi} = 0. \tag{2.15}$$

$\boldsymbol{\psi}$ is a wavefunction vector, the elements of which are the radial channel functions, and $\bar{\boldsymbol{W}}$ is the coupling matrix which quantifies the coupling between each channel and every other channel. The elements of $\bar{\boldsymbol{W}}$, $W_{j'j}$, are equal to

$$\langle j'|\left(\frac{\hbar^2}{2\mu R^2}\hat{L}^2 + \hat{H}_{\text{intl}}(\xi) + V(\boldsymbol{R},\xi)\right)|j\rangle. \tag{2.16}$$

The above constitutes a diabatic formulation of a multichannel scattering problem. An alternative adiabatic formulation is possible. Before proceeding we discuss these different formalisms. Whereas in the diabatic formulation the wavefunction

is expanded in a set of orthonormal functions that span the space of $\hat{H}_{\text{intl}}(\xi)$ and $\hat{L}^2$ the adiabatic formulation relies on the expansion of the wavefunction in a basis that diagonalizes $\hat{H}_{\text{intl}}(\xi)$, $\hat{L}^2$, and $\hat{V}(R,\xi)$ [97]. In the adiabatic formulation the wavefunction is expanded in functions that depend parametrically on the internuclear separation and diagonalize $\hat{V}(R,\xi)$ at every value of the internuclear separation. The result of this difference is where the couplings between scattering channels emerge. In the adiabatic formulation the radial kinetic energy operator is non-diagonal and therefore couples different channels to one another. In the diabatic formulation the couplings between channels can be found in the potential energy matrix. The work throughout this thesis uses a diabatic formulation. Concepts from adiabatic formulations are occasionally used in order to interpret and discuss various results.

Our attention now turns to solving the coupled-channel scattering problem presented in Equation 2.15 and describing how we obtain the scattering $\boldsymbol{S}$ matrix. We elect to use numerical propagation and the MOLSCAT program package [85]. Basis sets can be used for the internuclear coordinate, although this approach is more computationally expensive than propagation [98]. We propagate the log-derivative of the wavefunction matrix from short range to the asymptotic region at long range. It is uncommon to propagate a wavefunction vector, $\boldsymbol{\psi}$, or some function of $\boldsymbol{\psi}$, because the $N$ radial channel functions in the expansion of $\Psi(R,\xi)$ gives rise to $N$ linearly independent solutions of the Schrödinger Equation, all of which meet the boundary condition $\psi_j(R) \to 0$ at short range. The wavefunction matrix, $\boldsymbol{\Psi}$, is constructed by stacking the $N$ linearly independent solution vectors $\boldsymbol{\psi}$ side-by-side. In the asymptotic region, where $\hat{V}(R,\xi) \to 0$, the wavefunction matrix can be matched to $\boldsymbol{J}(R) + \boldsymbol{N}(R)\boldsymbol{K}$, the solution of Equation 2.13 when $\hat{V}(R,\xi) = 0$. For open channels $\boldsymbol{J}(R)$ and $\boldsymbol{N}(R)$ contain Ricatti-Bessel functions. For closed channels $\boldsymbol{J}(R)$ and $\boldsymbol{N}(R)$ contain modified spherical Bessel functions [85, 93]. The open-open

submatrix of $\boldsymbol{K}$, $\boldsymbol{K}_{\mathrm{oo}}$, is used to obtain the scattering matrix,

$$\boldsymbol{S} = (\boldsymbol{I} + i\boldsymbol{K}_{\mathrm{oo}})^{-1}(\boldsymbol{I} - i\boldsymbol{K}_{\mathrm{oo}}). \tag{2.17}$$

The scattering matrix is an exceptionally important construct in the theory of scattering as it contains information about the probability of inelastic transitions between channels and is related to the scattering observables that are frequently measured in experiments.

Our attention now turns to the calculation of bound-state eigenvalues in the multichannel problem [17, 84, 89]. In analogy with Equation 2.14 the wavefunction of the $n^{\mathrm{th}}$ bound state is expanded as

$$\Psi^n(R,\xi) = \frac{1}{R}\sum_j \psi_j^n(R)|j(\xi)\rangle. \tag{2.18}$$

The desired solution of the bound-state Schrödinger Equation that contains the Hamiltonian in Equation 2.13 is a column vector $\boldsymbol{\psi}$. $\boldsymbol{\psi}$ is continuous, has a continuous derivative, meets the boundary conditions that $\boldsymbol{\psi}(0) = 0$ and $\boldsymbol{\psi}(\infty) = 0$, and exists at a discrete energy. Similarly to the single-channel case an inwards propagation, from $R_{\mathrm{max}}$ in the outer classically forbidden region, and outwards propagation, from $R_{\mathrm{min}}$ in the inner classically forbidden region, are undertaken to a matching point, $R_{\mathrm{match}}$, in the classically allowed region. For bound-state problems propagators in BOUND and FIELD exclusively use the log-derivative of the wavefunction.

For an energy that is an eigenvalue of the problem, $E_n$, the condition that

$$\bar{\boldsymbol{Y}}^+(R_{\mathrm{match}})\boldsymbol{\psi}^+(R_{\mathrm{match}}) = \bar{\boldsymbol{Y}}^-(R_{\mathrm{match}})\boldsymbol{\psi}^-(R_{\mathrm{match}}) \tag{2.19}$$

will be fulfilled. This condition codifies the requirement that the wavefunction and its derivative are continuous at $R_{\mathrm{match}}$. From the matching condition, and the definition of a log-derivative matching matrix $\Delta\bar{\boldsymbol{Y}} = \bar{\boldsymbol{Y}}^+(R_{\mathrm{match}}) - \bar{\boldsymbol{Y}}^-(R_{\mathrm{match}})$, it is clear that the wavefunction vector of the $n^{\mathrm{th}}$ bound state is also an eigenfunction of

the log-derivative matching matrix with a zero eigenvalue. To find $E_n$ BOUND uses bisection and the multichannel node count [96] to identify ranges of energy that contain one state. In each energy range bisection and the VWDB algorithm [99] are used to find the energy at which $\Delta \boldsymbol{Y}$ has a zero eigenvalue. The bound-state wavefunction, $\Psi^n(R, \xi)$, can then be found with the method of Thornley and Hutson [100].

## 2.3 Low-Temperature Scattering

In Sections 2.1 and 2.2 we introduced single-channel and multichannel scattering theory. In the current section we focus on scattering in the ultracold temperature regime.

Collisions at ultracold temperatures are dominated by the $L = 0$ partial wave. In the limit of $E \to 0$ and $R \to \infty$ the $L = 0$ radial equation reduces to

$$\frac{d^2}{dR^2}\psi_0(R) = 0, \tag{2.20}$$

and the scattering wavefunction is linear with $R$. At short range the wavefunction will rapidly oscillate. Extrapolating the linear region of the wavefunction to $\psi_0(R) = 0$ returns the zero-energy scattering length, $a(0)$. The scattering length is an energy-dependent quantity and is related to the $L = 0$ phase shift;

$$a(k) = -\frac{1}{k}\tan\delta_0. \tag{2.21}$$

As $k \to 0$ $a(k)$ becomes constant and is equal to $a(0)$. Correction terms to $a(0)$ are given by the effective range theory [101],

$$a(k) = a(0) + \frac{1}{2}k^2 r_{\text{eff}} a(0)^2 + ..., \tag{2.22}$$

where $r_{\text{eff}}$ is the effective range.

In the remainder of this thesis we use $a$ to refer to the zero-energy s-wave scat-

tering length. The scattering length is an imaginary quantity, $a = \alpha - i\beta$, when inelastic processes are possible. In the absence of inelastic processes $\beta = 0$ and the scattering length is a real quantity. The scattering length can be used to obtain expressions for the s-wave contribution to the elastic scattering cross section,

$$\sigma_{ii}(k) = \frac{4\pi|a|^2}{1 + k^2|a|^2 + 2k\beta}, \tag{2.23}$$

and the s-wave contribution to the total inelastic scattering cross section

$$\sigma_{\text{inel}}^{\text{tot}}(k) = \frac{4\pi\beta}{k(1 + k^2|a|^2 + 2k\beta)}. \tag{2.24}$$

Note that Eq. 2.23 can be modified by setting $\beta = 0$ in order to obtain an expression for the scattering cross section in the absence of any inelastic processes.

Gribakin and Flambaum used the semi-classical approximation and a model interatomic potential to study the s-wave scattering length [102]. At long range the potential is proportional to a leading term and a coefficient,

$$V(r) \approx -\frac{C_n}{r^n}. \tag{2.25}$$

For two alkali-metal atoms $n = 6$ and at long range $V(R)$ depends on the $C_6$ parameter. Gribakin and Flambaum defined a mean scattering length,

$$\bar{a} = \cos\left(\frac{\pi}{n-2}\right)\left(\frac{\gamma}{n-2}\right)^{\frac{2}{n-2}} \frac{\Gamma\left(\frac{n-2}{n-2}\right)}{\Gamma\left(\frac{n-1}{n-2}\right)}, \tag{2.26}$$

where $\gamma^2 = 2\mu C_n/\hbar^2$, and found that

$$a = \bar{a}\left(1 - \tan\left(\frac{\pi}{n-2}\right)\tan\left(\Phi - \frac{\pi}{2(n-2)}\right)\right). \tag{2.27}$$

$\Phi$ is the phase shift calculated with semiclassical approximation. The phase of the potential is significant because it determines the number of bound states supported by the potential. As $\Phi$ changes the position and number of the bound states changes.

When

$$\Phi - \frac{\pi}{2(n-2)} = N\pi + \frac{\pi}{2}, \tag{2.28}$$

where $N$ is an integer, the least-bound state has zero energy and the scattering length has infinite value.

Ultracold atomic scattering is universal in the sense that several key constants of a given system determine the collision properties of that system. Gao's analytical solutions to $R^{-6}$ potentials allow us to make, to a good approximation, further quantitative predictions of the energies of the near-threshold bound states of a given potential [103–106]. We regularly deploy the concept of energy bins to explain patterns of near-threshold bound states and derive labels for the different states we see in bound-state spectra. Bins are well-defined energy ranges that a bound state must exist in. For example, the least-bound state lies within $36\bar{E}$ of the threshold where $\bar{E} = \hbar^2/2\mu\bar{a}^2$. Each subsequent bound state lies within its own bin.

Feshbach resonances occur when a bound state is coupled to, and becomes resonant with, a scattering state. Any field can, in principle, be used to tune the energy of the bound state into resonance. In ultracold scattering the Feshbach resonances we refer to are zero-energy magnetic Feshbach resonances. Feshbach resonances occur in both elastic and inelastic scattering, although the behavior is markedly more simple when there is no inelasticity.

A simple elastic Feshbach resonance displays a pole in the scattering length and follows

$$a(B) = a_{\mathrm{bg}}\left(1 - \frac{\Delta_B}{B - B_{\mathrm{res}}}\right), \tag{2.29}$$

where $B_{\mathrm{res}}$ is the field at which the energy of the bound state is equal to the threshold energy and $\Delta_B$ is the resonance width. The scattering length changes because the phase in the wavefunction of the scattering state increases by $\pi$ as it is tuned from beneath the resonance to above the resonance. The phase shift contains a background and resonant component.

The scattering length is an imaginary quantity in inelastic scattering. The mag-

nitude of $\beta$ is indicative of how strongly coupled the open channel is to lower channels that it can decay to. The scattering length behaves as

$$a(B) = a_{\rm bg} + \frac{a_{\rm res}}{2(B - B_{\rm res})(\Gamma_B^{\rm inel})^{-1} + i}, \tag{2.30}$$

where $a_{\rm bg} = \alpha_{\rm bg} - i\beta_{\rm bg}$ and $a_{\rm res} = \alpha_{\rm res} - i\beta_{\rm res}$. To characterize the resonances in this thesis we use the algorithms of Frye and Hutson [107]. Frye and Hutson treated elastic resonances, resonances with weak background inelasticity, and resonances with strong background inelasticity. Resonances with weak background inelasticity show an oscillation in $\alpha$ and a sharp symmetric peak in $\beta$. The maximum in the oscillation of $\alpha$ is $a_{\rm res}/2$ above $a_{\rm bg}$ and the maximum in $\beta$ is at $a_{\rm res}$. $\beta_{\rm bg} = 0$ and $\beta_{\rm res} = 0$ when there is weak background inelasticity. Resonances with strong background inelasticity also show an oscillation in $\alpha$ but the background inelasticity is high and the peak in $\beta$ is asymmetric. $\beta_{\rm bg}$ and $\beta_{\rm res}$ are non zero.

# Chapter 3

# Collisions of K and Cs

## 3.1 Introduction

This chapter details recent advancements in our understanding of ultracold $^{39}$K + $^{133}$Cs collisions. We have explored the near-threshold bound states that can cause Feshbach resonances at the lowest collision thresholds. We have developed a more accurate model of the KCs interaction potential using an interactive non-linear least-squares analysis and the results from a series of experiments undertaken by the Nägerl Group (University of Innsbruck). Details of our new potential (B2024) are included in this chapter. The results and analysis presented here will support future theoretical and experimental studies of $^{39}$K$^{133}$Cs.

Bialkali molecules have a rich history in the field of ultracold physics. Their production via magnetoassociation and their many applications in quantum science and technology have been reviewed in the Introduction. The specific history of ultracold $^{39}$K$^{133}$Cs is detailed here. Ultracold $^{39}$K$^{133}$Cs molecules have, at present, not been produced in their rovibrational ground state. The Nägerl Group has succeeded in producing an ultracold mixture of $^{39}$K and $^{133}$Cs and has characterized several zero-energy magnetic Feshbach resonances that exist in the collisions between these atoms. Three key papers were published in 2013, 2014 and 2017. Ferber et al. used Fourier-transform spectroscopy to study the near-dissociation vibrational levels of KCs in the ground-electronic state [108]. Ferber et al. used their results to develop models of the $X^1\Sigma^+$ and $a^3\Sigma^+$ potentials (F2013). Patel et al. used the F2013 potential in coupled-channel calculations to assess the prospect of producing loosely bound states of $^{39}$K$^{133}$Cs, $^{40}$K$^{133}$Cs, and $^{41}$K$^{133}$Cs with magnetoassociation [109]. Several years later Gröbner et al. presented the results of a joint experimental and theoretical study of the Feshbach resonances in $^{39}$K + $^{133}$Cs collisions [110]. They found that the F2013 potential gave an error of $\approx 20$ G in Patel et al.'s calculations of Feshbach resonance positions and a systematic overestimation of the resonances' widths. Consequently, Gröbner et al. developed a new interaction potential (G2017). They were able to develop a new model of the triplet curve but did not attempt to develop a model of the singlet curve. We discuss the F2013 and G2017 potentials

in more detail in Section 3.2.3.

The aim of experimentalists working on the ultracold $^{39}$K+$^{133}$Cs gas is to produce $^{39}$K$^{133}$Cs molecules in the absolute-ground state. Magnetoassociation and Stimulated Raman Adiabatic Passage (STIRAP) will be used to achieve this [111]. For STIRAP and the production of ground-state $^{39}$K$^{133}$Cs molecules to be efficient, an intermediate state that has a strong transition between the loosely bound state and the rovibrational-ground state must be identified [29]. Theory is invaluable when assessing different STIRAP schemes, and accurate models of the potential that support the Feshbach molecule are vital. It is possible that the most efficient scheme will not involve the state populated during magnetoassociation. It is important to have an accurate picture of the loosely bound states that can be populated by exploiting the avoided crossings between different states. The energies of bound states and their variation with magnetic field are determined by the interaction potential.

This chapter is structured as follows. Section 3.2.1 discusses the hyperfine structure of $^{39}$K and $^{133}$Cs, and the structure and properties of the $^{39}$K+$^{133}$Cs pair states. Section 3.2.2 gives details of our calculations using BOUND, FIELD, and MOLSCAT. In Section 3.2.3 a discussion of the mathematical functions used in models of alkali+alkali interaction potentials is given. We discuss the F2013 and G2017 potentials in more depth. The relation between the parameters in these models and various scattering observables in analyzed in Section 3.2.4. In Section 3.2.5 the theory of non-linear least-squares analysis is summarized. In Section 3.3.1 we analyze the near-threshold bound states that can cross the lowest thresholds and cause Feshbach resonances. We also characterize the resonances that would be most advantageous to measure for refitting the potential. Section 3.3.2 discusses our fit to obtain the B2024 potential, its uncertainty, and the predictions we can make from it.

## 3.2 Theoretical Background and Methods

### 3.2.1 Monomer States and Pair States

The Hamiltonian of an alkali-metal atom in its $^2$S state is

$$\hat{h}_A = \zeta_{\mathrm{A}} \hat{\boldsymbol{i}}_{\mathrm{A}} \cdot \hat{\boldsymbol{s}}_{\mathrm{A}} + \left( g_{s,\mathrm{A}} \hat{s}_{\mathrm{A},z} + g_{i,\mathrm{A}} \hat{i}_{\mathrm{A},z} \right) \mu_{\mathrm{B}} B, \tag{3.1}$$

where $\hat{\boldsymbol{i}}_{\mathrm{A}}$ and $\hat{\boldsymbol{s}}_{\mathrm{A}}$ are vector operators for the nuclear and electron spins, and their components along the $z$-axis defined by the magnetic field, $B$, are $\hat{i}_{\mathrm{A},z}$ and $\hat{s}_{\mathrm{A},z}$. $\zeta_{\mathrm{A}}$ is the hyperfine coupling constant, which gives rise to a hyperfine splitting $A_{\mathrm{hfs}} = \zeta_{\mathrm{A}}(i_{\mathrm{A}} + 1/2)$, and $g_{s,\mathrm{A}}$ and $g_{i,\mathrm{A}}$ are the gfactors for the electron and nuclear spins. $\zeta_{^{39}\mathrm{K}} \approx 0.2309$ GHz, $g_{s,\mathrm{K}} = 2.002$, and $g_{i,\mathrm{K}} = -1.419 \times 10^{-4}$ [112]. $\zeta_{^{133}\mathrm{Cs}} \approx 2.298$ GHz, $g_{s,\mathrm{Cs}} = 2.003$, and $g_{i,\mathrm{Cs}} = -3.989 \times 10^{-4}$ [113].

At $B = 0$ G the total angular momentum, $f_{\mathrm{K}}$, is either 1 or 2 as $i_{\mathrm{K}} = 3/2$ and $s_{\mathrm{K}} = 1/2$. For $B > 0$ G the degeneracies of the different $m_f$ states are lifted and states of different $f_{\mathrm{K}}$ interact with one another. The left panel of Figure 3.1 shows that for $B < 200$ G the hyperfine states of $^{39}$K are well described by the labels ($f_{\mathrm{K}}$, $m_{f,K}$). For $B > 200$ G the projection of the electron and nuclear spins, $m_s$ and $m_i$, are more appropriate labels and the electron and nuclear spins are more strongly coupled to the external field than they are to one another. The lower (and upper) groups of states correspond to $m_s = -1/2$ (and $m_s = 1/2$). Within each group the states are distinguished by their value of $m_i$, which for $^{39}$K can be $-3/2$, $-1/2$, $1/2$, or $3/2$, and is equal to $m_i = m_f - m_s$. $s_{\mathrm{Cs}} = 1/2$ and $i_{\mathrm{Cs}} = 7/2$ such that $f_{\mathrm{Cs}} = 3$ or 4. For Caesium the total angular momentum and its projection along the magnetic field axis remain appropriate labels for all $B < 600$ G. This is evident in the right panel of Figure 3.1 and is due to Caesium's large hyperfine coupling constant which keeps the electron and nuclear spins strongly coupled to one another.

The different possible combinations of the atomic hyperfine states give rise to the $^{39}\mathrm{K} + {}^{133}\mathrm{Cs}$ pair states. These pair states label the collision thresholds at long range. In the presence of a magnetic field the thresholds are separable in the projection of

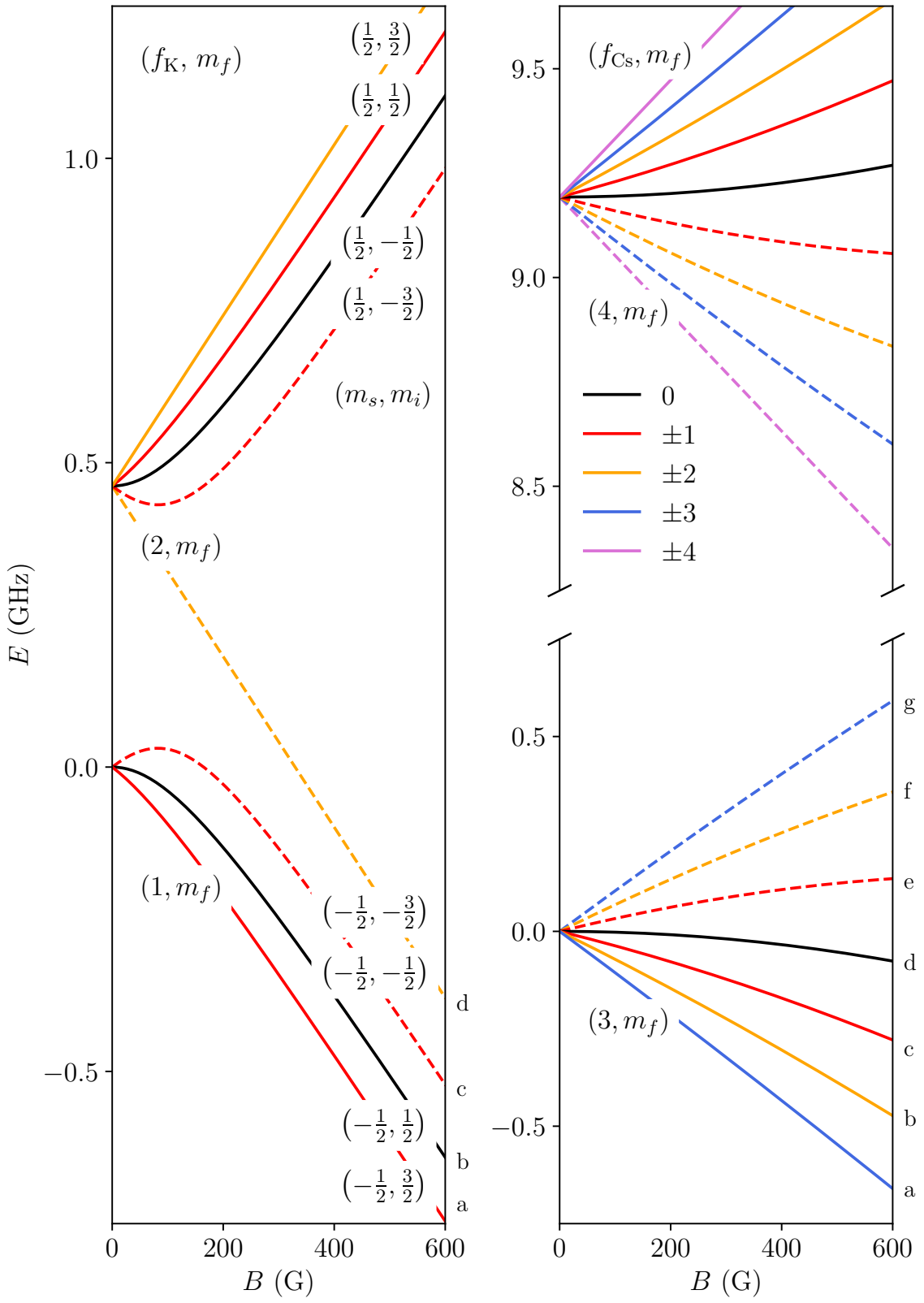


Figure 3.1: Energies of the $^{39}$K (left-hand panel) and $^{133}$Cs (right-hand panel) hyperfine states as a function of magnetic field. Energies are shown relative to the hyperfine ground state at $B = 0$ G. Values of $|m_f|$ are color-coded as shown in the legend. Solid (and dashed) lines are used for positive (and negative) values of $m_f$.

the total angular momentum, $m_F = m_{f,\mathrm{K}} + m_{f,\mathrm{Cs}}$, that can take all integer values between $-6$ and 6. The pair states can be labelled by their constituent atomic states. At low fields, when $^{39}$K has not reached the high-field limit, appropriate labels are ($f_\mathrm{K}$, $m_{f,\mathrm{K}}$, $f_\mathrm{Cs}$, $m_{f,\mathrm{Cs}}$). The fields of interest in this work are typically $> 200$ G so the labels ($m_{s,\mathrm{K}}$, $m_{i,\mathrm{K}}$, $f_\mathrm{Cs}$, $m_{f,\mathrm{Cs}}$) are used throughout this chapter. Irrespective of the appropriate representation the labels can be shortened substantially by labelling the different hyperfine states for each atom according to a, b, c, ... in increasing order of energy. These labels are included in Figure 3.1 for the lowest manifolds of states. If, for example, we were discussing the lowest threshold with $m_F = 4$, which is ($m_{s,\mathrm{K}} = -1/2$, $m_{i,\mathrm{K}} = 3/2$, $f_\mathrm{Cs} = 3$, $m_{f,\mathrm{Cs}} = 3$), we would use the label a + a.

It is advantageous to build an understanding of the singlet fractions of the $^{39}$K + $^{133}$Cs pair states. We have extensively studied the singlet/triplet fractions of the near-threshold bound states and use the approximation that a near-threshold bound state is supported by a single collision threshold to interpret our results. If a bound state runs approximately parallel to a threshold it is likely to have the character of that threshold. We have calculated the singlet fraction of a pair of alkali-metal atoms' singlet fraction as a function of magnetic field. Consider a single alkali-metal atom in a non-spin-stretched state. Two hyperfine states will have the $m_f$ value of that state. Their interaction with one another is determined by Equation 3.1. Each state is expanded in a basis of two functions, $|s, \pm 1/2\rangle|i, m_f \mp 1/2\rangle$, such that

$$\psi_1 = \cos\theta|1/2, 1/2\rangle|i, m_f - 1/2\rangle + \sin\theta|1/2, -1/2\rangle|i, m_f + 1/2\rangle \tag{3.2}$$

and

$$\psi_2 = -\sin\theta|1/2, 1/2\rangle|i, m_f - 1/2\rangle + \cos\theta|1/2, -1/2\rangle|i, m_f + 1/2\rangle, \tag{3.3}$$

where $\theta$ is

$$\theta = \frac{1}{2}\tan^{-1}\left(\frac{\zeta\left((i+1/2)^2 - m_f^2\right)^{1/2}}{\zeta m_f + g\mu_\mathrm{B}B}\right). \tag{3.4}$$

When $\theta$ has been obtained for each atom it is possible to calculate the singlet amplitude of the pair,

$$A_{\mathrm{s}} = \frac{1}{\sqrt{2}} \left( \cos\theta_1 \sin\theta_2 \mp \sin\theta_1 \cos\theta_2 \right), \tag{3.5}$$

of a given pair state. Equation 3.5 can be derived by expanding $\psi_1\psi_2$, coupling $|s_1, \pm 1/2\rangle$ and $|s_2, \pm 1/2\rangle$ to give a resultant $|S, M_S\rangle$, and summing the coefficients of the singlet states. The singlet fraction, $F_{\mathrm{s}} = A_{\mathrm{s}}^2$, is obtained from the singlet amplitude.

Figure 3.2 shows the pair states, and $L = 0$ thresholds, with $m_F = 4, 3$, and 2. A color map, included as an inset in the bottom left corner of Figure 3.2, has been used to encode the singlet fractions of these pair states. For each $m_F$ the various pair states have a singlet fraction that varies from 0 to 0.5. Most pair states with high singlet fractions have small values of $dE/dB$. The singlet fractions of pair states with $M_F = 1, 0, -1, -2, -3$, and $-4$ are included in Figures 3.2.1 and 3.2.1. It is clear from these figures that as $M_F$ reduces the variety of states' singlet fractions reduces.

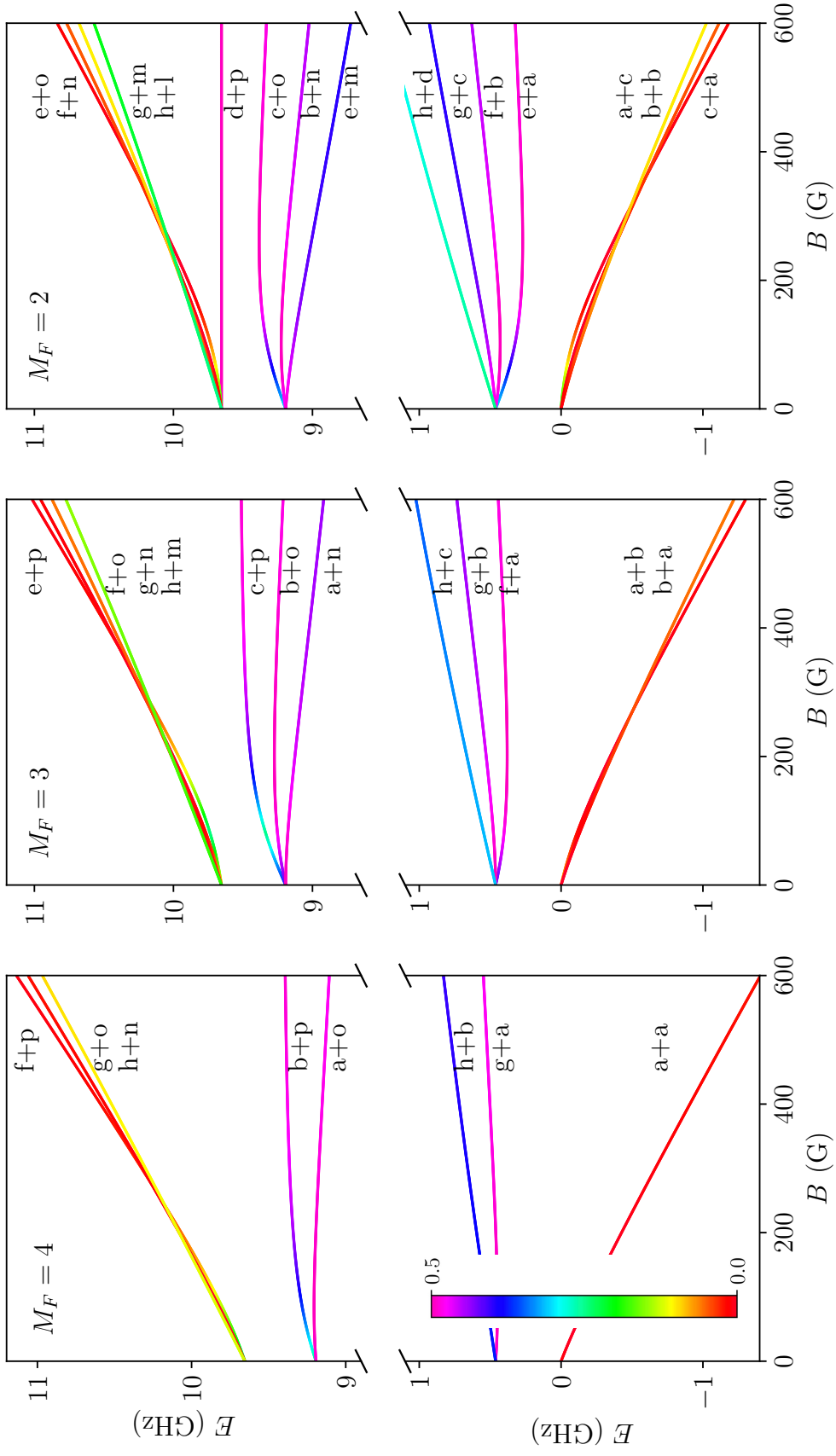


Figure 3.2: $^{39}$K+$^{133}$Cs pair states with $m_F = 4, 3$, and 2 as a function of magnetic field. The color of the pair states encodes their singlet fractions. Pink corresponds to $F_s = 0.5$ and red corresponds to $F_s = 0.0$, as is shown in the inset.

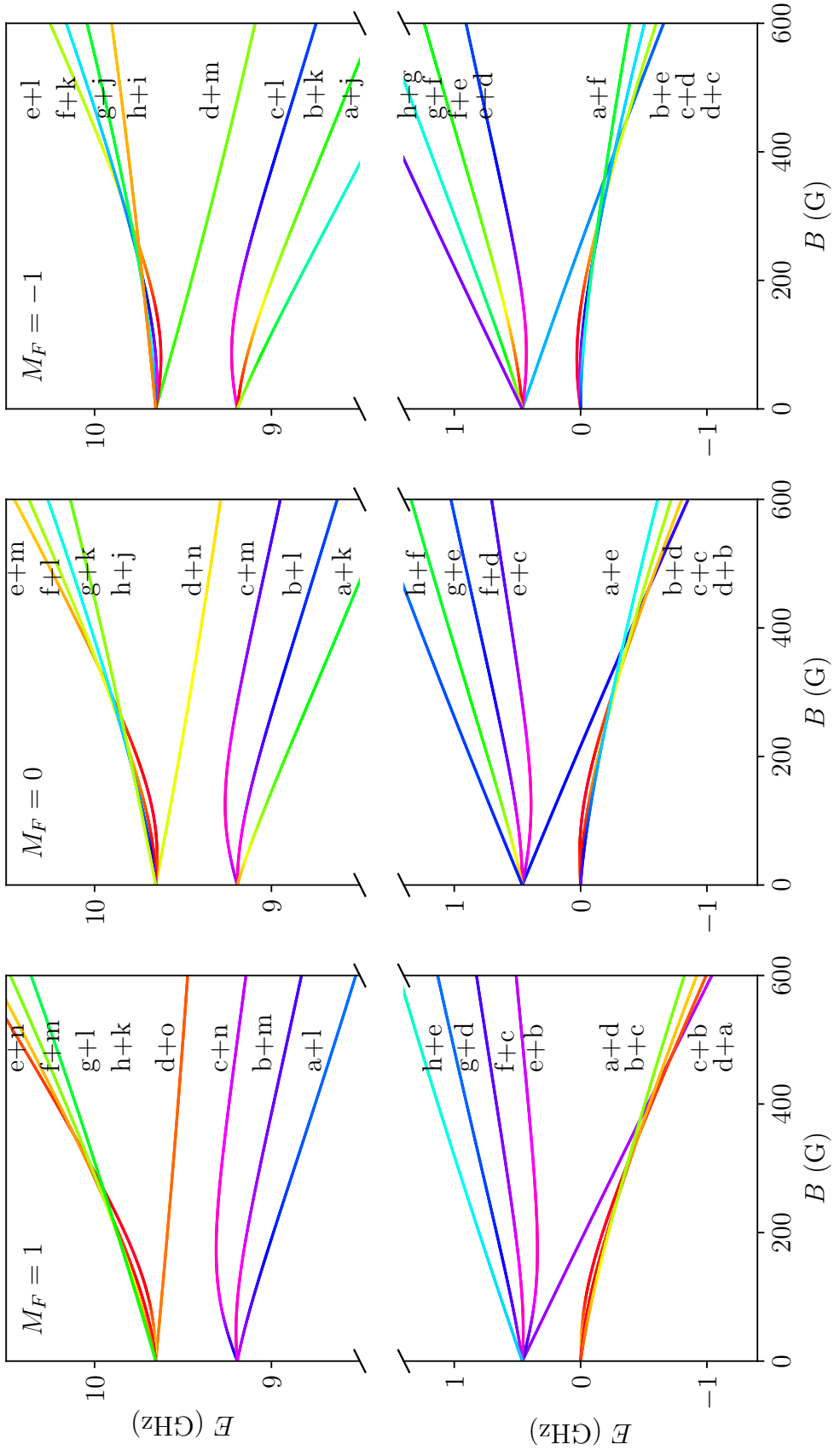


Figure 3.3: $^{39}$K+$^{133}$Cs pair states with $m_F = 1, 0$, and $-1$ as a function of magnetic field. The color of the pair states encodes their singlet fractions. Pink corresponds to $F_s = 0.5$ and red corresponds to $F_s = 0.0$ as is shown by the inset in Figure 3.2.

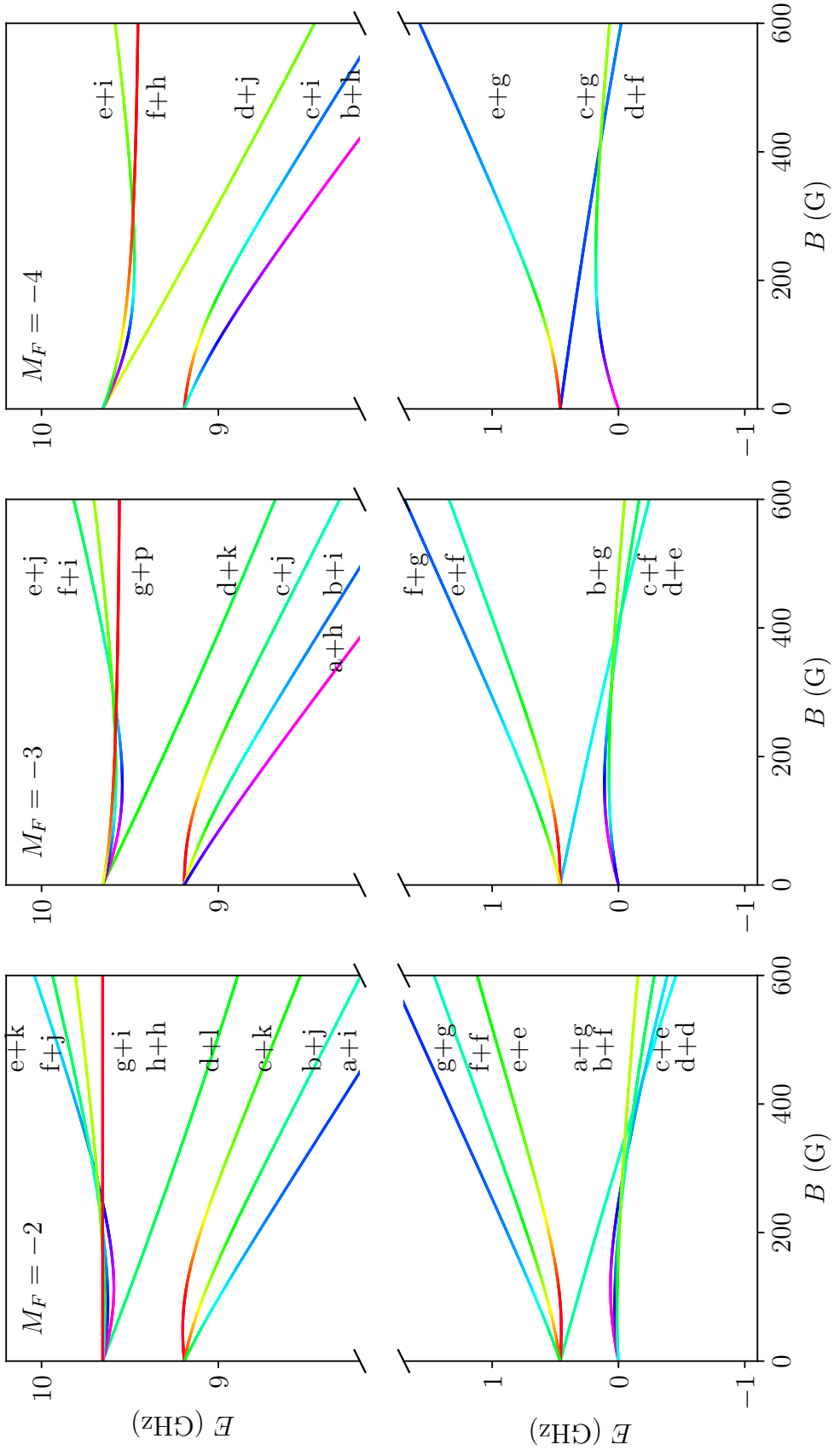


Figure 3.4: $^{39}$K+$^{133}$Cs pair states with $m_F = -2, -3$, and $-4$ as a function of magnetic field. The color of the pair states encodes their singlet fractions. Pink corresponds to $F_s = 0.5$ and red corresponds to $F_s = 0.0$ as is shown by the inset in Figure 3.2.

Table 3.1: Available basis sets for alkali-metal atom + alkali-metal atom calculations in BOUND, FIELD, and MOLSCAT.

| | |
|---|---|
| Uncoupled basis | $\|s_{\rm A}, m_{s,{\rm A}}\rangle\|i_{\rm A}, m_{i,{\rm A}}\rangle\|s_{\rm B}, m_{s,{\rm B}}\rangle\|i_{\rm B}, m_{i,{\rm B}}\rangle\|L, M_L\rangle$ |
| Partially coupled basis | $\|(s_{\rm A}, i_{\rm A})f_{\rm A}, m_{f,{\rm A}}\rangle\|(s_{\rm B}, i_{\rm B})f_{\rm B}, m_{f,{\rm B}}\rangle\|L, M_L\rangle$ |
| Fully coupled basis | $\|(f_{\rm A}, f_{\rm B})F, M_F\rangle\|L, M_L\rangle$ |
| SIF basis | $\|(s_{\rm A}, s_{\rm B})S, M_S\rangle\|(i_{\rm A}, i_{\rm B})I, M_I\rangle\|L, M_L\rangle$ |

### 3.2.2 Calculations of Bound States and Scattering

To obtain bound-state eigenvalues and values of the scattering length from the multichannel Schrödinger Equation we use the BOUND, FIELD and MOLSCAT programs [84, 85]. Chapter 2 contains a detailed discussion of coupled-channel theory and numerical propagation. In this section we summarize the basis sets available for alkali-metal atom + alkali-metal atom calculations and briefly give details of the calculations undertaken in this chapter.

A variety of basis sets are implemented in the BOUND, FIELD, and MOLSCAT program packages for alkali-metal atom + alkali-metal atom calculations. These basis sets are direct products of functions that span the space of $\hat{H}_{\rm intl}$ and $\hat{L}^2$ in Equation 2.13. They are used to expand the multichannel wavefunction (Equation 2.14) and to construct the coupling matrix (Equation 2.16) for coupled-channel calculations. These basis sets are tabulated in Table 3.1. The derivation of the coupling-matrix elements in the uncoupled representation is standard and given elsewhere [38]. The derivation of the coupling-matrix elements in the partially coupled, fully coupled, and SIF basis sets can be obtained with angular momentum theory [114, 115]. The work presented in this chapter used a variety of these basis sets. We included all electron and nuclear spins. The value of the end-over-end angular momentum is specified where appropriate. The majority of the calculations undertaken here used $L = 0$.

For the scattering calculations undertaken in MOLSCAT, Manolopoulos' LDMD propagator [116] was used to propagate the log-derivative matrix from $R_{\rm min} = 5.6\ a_0$ to $R_{\rm mid} = 20.0\ a_0$ with a step size of $0.001\ a_0$. The variable-step size Airy propa-

gator [117, 118] was used from $R_{\mathrm{mid}}$ to $R_{\mathrm{max}} = 3000\ a_0$. The collision energy was around 1 pK. For the bound-state calculations undertaken in BOUND, Manolopoulos' LDMD propagator was used from $R_{\mathrm{min}} = 5.6\ a_0$ to $R_{\mathrm{mid}} = 15.0\ a_0$ with a step size of $0.001\ a_0$. The variable-step size Airy propagator was used from $R_{\mathrm{mid}}$ to $R_{\mathrm{max}} = 5000\ a_0$.

The FIELD program is very closely related to the BOUND program [84]. Whereas BOUND calculated a bound-state energy for a given value of magnetic field, FIELD calculates the magnetic field at which a state with specified energy exists. Our FIELD calculations used the same propagation parameters as our BOUND calculations.

We have calculated the singlet/triplet fractions of each the near-threshold bound states. BOUND is able to calculate the expectation value of an operator for a state with a finite-difference approach [119]. Having located a bound state with energy, $E_n^{(0)}$, a modified energy, $E_n(a)$, is obtained by applying a small perturbation, $a$, to the Hamiltonian such that $E_n(a) = E_n^{(0)} + a\langle\hat{A}\rangle_n + \mathcal{O}(a^2)$, where $\langle\hat{A}\rangle_n$ is the expectation value of operator $A$. The finite-difference approximation to the expectation value is

$$\langle\hat{A}\rangle_n = \frac{E^{(0)} - E_n(a)}{a}. \tag{3.6}$$

We use this capability to obtain values of the singlet and triplet fraction i.e. the expectation value of the singlet and triplet terms in the interaction potential for a particular bound state. The singlet fraction of a bound state varies as a function of energy and field. When we have calculated singlet fractions we have used values of energy and field at which the gradients of the states are constant. These calculations used the same propagation parameters as other BOUND calculations, which are given in this section.

### 3.2.3 $^{39}$K$^{133}$Cs Interaction Potential

The collision dynamics of alkali-metal atoms at ultracold temperatures are governed by the ground singlet and triplet electronic states, $X^1\Sigma^+$ and $a^3\Sigma^+$. These arise from the interplay of electron-electron repulsion at short range and attractive dispersion interactions at long range. The potential-energy operator is

$$\hat{V}(R) = \hat{V}_0\hat{\mathcal{P}}^{(0)} + \hat{V}_1\hat{\mathcal{P}}^{(1)} + \hat{V}^{\mathrm{d}}(R), \tag{3.7}$$

where $V_0(R)$ and $V_1(R)$ are the potential-energy curves for $X^1\Sigma^+$ and $a^3\Sigma^+$, and $\hat{\mathcal{P}}^{(0)}$ and $\hat{\mathcal{P}}^{(1)}$ are projection operators [19]. There also exist small anisotropic terms that arise from second-order spin-orbit coupling and the anisotropic dipole-dipole interaction of the electron spins on the separate atoms. These appear in the $\hat{V}^{\mathrm{d}}$ term. In this section we take the opportunity to introduce the mathematical functions that can be used to model the singlet and triplet curves. We also give details of the F2013 and G2017 potentials.

The models typically employed for the isotropic singlet and triplet surfaces in theories of the collisions of alkali-metal atoms at ultracold temperatures contain three segments. These segments are divided by $R_{\mathrm{SR},S}$ and $R_{\mathrm{LR},S}$ where $S = 0$ and 1 for the respective singlet and triplet curves [39, 110, 120]. Ferber et al. used $R_{\mathrm{SR},0} = 3.22$ Å, $R_{\mathrm{SR},1} = 5.23$ Å, $R_{\mathrm{LR},0} = 12.00$ Å, and $R_{\mathrm{SR},1} = 12.01$ Å [108]. These values were not modified by Gröbner et al. in 2017. The short-range segment can be represented with an inverse-power term,

$$V_{\mathrm{SR},S}(R) = A_{\mathrm{SR},S} + \frac{B_{\mathrm{SR},S}}{R^{N_S}}, \tag{3.8}$$

the potential between $R_{\mathrm{SR},S}$ and $R_{\mathrm{LR},S}$ is constructed with a finite-power series in a dimensionless radial variable,

$$V_{\mathrm{mid},S}(R) = \sum_{i=0}^{n_S} a_{i,S}\left(\frac{R - R_{\mathrm{m},S}}{R + b_S R_{\mathrm{m},S}}\right)^i, \tag{3.9}$$

and the long-range region of the potential is

$$V_{\mathrm{LR},S}(R) = -C_6/R^6 - C_8/R^8 - C_{10}/R^{10} - (-1)^S V_{\mathrm{ex}}(R). \tag{3.10}$$

The dispersion coefficients used in the model of the long-range segment of the potential model are the same for both the singlet and triplet potentials. The F2013 and G2017 potential used values of the $C_6, C_8$, and $C_{10}$ coefficients calculated with relativistic ab initio calculations augmented with experimental data [121, 122]. These values have not been altered during any of the efforts to refine the KCs interaction potential. The exchange term is equal to $A_{\mathrm{ex}} R^{\gamma} \exp(-\beta R)$ [123]. $A_{\mathrm{ex}}$, $\gamma$, and $\beta$ were obtained in 2013 by Ferber et al. and were not refined in 2017 by Gröbner et al.

In the middle segment of the potential the parameter $a_{i,S}$ is varied to ensure $V_{\mathrm{mid},S}(R) = V_{\mathrm{LR},S}(R)$ at $R_{\mathrm{LR},S}$. $R_{\mathrm{m},S}$ is chosen to be close to the equilibrium distance. These values were first obtained by Ferber et al. and have not been modified in any efforts to refit the potential since.

The short-range function contains two terms $A_{\mathrm{SR},S}$ and $B_{\mathrm{SR},S}$ that are selected to ensure that $V_{\mathrm{mid},S}(R) = V_{\mathrm{SR},S}(R)$ at $R_{\mathrm{SR},S}$ and that $V_S(R)$ has a continuous derivative. Ferber et al. found values of $A_{\mathrm{SR},S}$ and $B_{\mathrm{SR},S}$ that ensured their potential met these two conditions for a preliminary fit. Then they kept $B_{\mathrm{SR},S}$ fixed as they further refined $A_{\mathrm{SR},S}$. As such the F2013 potential displays a derivative discontinuity. Gröbner et al. repeated the determination of $A_{\mathrm{SR},S}$ and $B_{\mathrm{SR},S}$ for every iteration of their potential, so that their final triplet potential has no derivative discontinuity at $R_{\mathrm{SR},1}$. $N_S$ was first obtained in 2013 during Ferber et. al.'s fit to experimental data. Gröbner et al. varied all three parameters for the triplet potential in 2017 when attempting to correct deficiencies in the F2013 potential [110]. $N_1$ was changed from 10.25168 to 6.9(1) and $A_{\mathrm{SR},S}$ and $B_{\mathrm{SR},S}$ were varied in turn to ensure that the function remained continuous. Gröbner et al. did not modify the singlet potential and used Ferber et al.'s value of $N_0 = 6.84881$.

The anisotropic term in the interaction potential, $\hat{V}^{\mathrm{d}}$, is responsible for spin-relaxation processes, whereby states with different end-over-end angular momentum

are weakly coupled to one another, and Feshbach resonances caused by $L = 2$ bound states. This term contains a contribution from the dipole-dipole-like interaction of the two electron spins, that goes as $1/(R/a_0)^3$, and the second-order spin-orbit coupling that has the same angular dependence as the electron-electron interaction, but a more complex radial dependence [19]. Ferber et al. were unable to ascertain any information regarding $\hat{V}^{\mathrm{d}}$ and did not attempt to generate a model of it. Patel et al. needed to include $\hat{V}^{\mathrm{d}}$ and generated an approximation of it based on the same functions used in $^{87}$Rb$^{133}$Cs calculations [31]. Gröbner et al. did not refine Patel et al.'s approximation of $\hat{V}^{\mathrm{d}}$.

There exist other functions that can be employed in models of interaction potentials [124–126]. We take this opportunity to introduce an alternative functional form for $V_{\mathrm{SR},S}(R)$ developed by the Hutson group[1]. Ihm et al. proposed a model of the short-range repulsion in van der Waals-type systems inspired by the overlap of two separate charge distributions [127]. Hutson et al. used this result to develop

$$V_{\mathrm{SR}}(R) = A_{\mathrm{SR}} + B_{\mathrm{SR}} e^{-\alpha R}. \tag{3.11}$$

Ihm et al. had found $\alpha \approx 0.85\beta$, where $\beta$ is the average of $\sqrt{8E_{\mathrm{I}}}$ for the two atoms and $E_{\mathrm{I}}$ is the ionization energy in atomic units. This functional form offers an intuition and approximation of $\alpha_S$. The Hutson Group found that Equation 3.11 gives a good representation of short-range potentials for pairs of alkali-metal atoms. $A_{\mathrm{SR},S}$ and $B_{\mathrm{SR},S}$ are varied to match $V_{\mathrm{SR},S}$ with $V_{\mathrm{mid},S}$ and to ensure that the derivative of $V_S(R)$ remains continuous.

### 3.2.4 Scattering Observables and the Interaction Potential

The parameters in the various functions introduced in Section 3.2.3 influence calculations of observables from bound states and scattering in different ways. We review these relationships here. Brookes and Hutson refined the interaction potential for NaCs in 2022 and published a detailed discussion of the sensitivity of different ob-

[1]This unpublished work was undertaken by Z. Chrome, M. D. Frye, and J. M. Hutson in 2021.

servables for ultracold scattering and spectroscopy to different parameters in models of the interaction potential [39]. They had access to a variety of measurements that included bound-state energies and Feshbach resonance positions. Their analysis proved useful in the development of the thoughts and analysis presented here.

It is difficult to overstate the importance of the singlet and triplet scattering lengths in describing and understanding the collisions of ultracold alkali-metal atoms. These scattering lengths are determined by the singlet and triplet interaction potentials. When fitting $V_1(R)$ to experimental measurements of Feshbach resonance positions Gröbner et al. found they needed to reduce the triplet scattering length, $a_\mathrm{t}$, from 82.24 $a_0$ to 74.88(9) $a_0$. This was achieved by changing $N_1$ in $V_{\mathrm{SR},1}$ from 10.25168 to 6.9(1), while holding the mid-range and long-range regions of the potential constant.

The combination of the singlet and triplet scattering lengths determines the overall scattering length and therefore the energies of near-threshold bound states. Measurements of bound-state energies are therefore very useful when calibrating models of interaction potentials. The energy of a bound state and its variation with magnetic field determine the position of any Feshbach resonances that state causes. Therefore measurements of Feshbach resonance positions are useful for refining the singlet and triplet scattering lengths.

It is important to understand the sensitivity of bound-state energies and resonance properties to the singlet and triplet interaction potentials. To optimize the singlet and triplet curves at short range, in an effort to obtain accurate singlet and triplet scattering lengths, a minimum of two Feshbach resonance positions are needed. These Feshbach resonances must be caused by states with different sensitivities to the singlet and triplet potential curves. The six Feshbach resonance positions measured by Gröbner et al. in 2017 and used in their fit to obtain the interaction potential are included in Table 3.2. We calculated the singlet fractions of the states that caused these resonances and it is clear that they were caused by states with similar values of $F_\mathrm{s}$.

Table 3.2: Feshbach resonance positions used by Gröbner et al. in 2017 to refine the KCs interaction potential. The threshold at which the resonance occurred, the position of the resonance as measured in experiment, and the singlet fraction of the state that causes the resonance are given.

| Threshold | $B_{\mathrm{res}}^{\mathrm{exp}}$ (G) | $\mathrm{F_s}$ |
|---|---|---|
| a+a | 361.1 | 0.378 |
| a+a | 442.59 | 0.482 |
| b+a | 419.3 | 0.360 |
| b+a | 513.12 | 0.478 |
| c+a | 491.5 | 0.394 |
| c+a | 559.32 | 0.479 |

We have stated that bound-state energies and Feshbach resonance positions are determined by $a_{\mathrm{s}}$, $a_{\mathrm{t}}$, and the overall scattering length. The difference between $a_{\mathrm{s}}$ and $a_{\mathrm{t}}$ also determines the variation of a state's energy with magnetic field near-threshold. Bound states curve away from the thresholds they cross. The extent of this curvature determines the widths of Feshbach resonances. Measurements of Feshbach resonance positions do not offer any information on the width of the resonance or the curvature of the bound state beneath it. Measurements of bound-state energy are able to capture this effect and therefore offer information on the difference between the singlet and triplet scattering lengths.

A variety of different states can cross the lowest threshold and cause a Feshbach resonance. Measuring the positions of resonances caused by near-threshold states with different vibrational quanta is advantageous when refitting the $C_6$ coefficient. The $C_6$ coefficient determines the outer turning point of the potential well near threshold. In our work we use the quantum number $n$ to label vibrational states; $n = -1$ is reserved for the least-bound state and $n$ decreases for successively deeper states.

Thus far we have implicitly been discussing observables that are related to $L = 0$ states. Any attempts at refining $\hat{V}^{\mathrm{d}}$ will require measurements of observables related to $L = 2$ states. The $\hat{V}^{\mathrm{d}}$ term determines the strength of interactions between states with different end-over-end angular momentum. Measurements of bound-state energies around avoided crossings between $L = 0$ and $L = 2$ states are useful

for determining the strength of the interaction between those states and allowing the parameters in $\hat{V}^{\mathrm{d}}$ to be refined [128].

We have discussed a number of experimental observables and how they are useful in fitting models of interaction potentials. This analysis helped us as we analyzed the near-threshold bound states of KCs and attempted to identify measurements that would allow us to refine our model of the potential. This discussion is presented in Section 3.3.1.

### 3.2.5 Least-Squares Fitting

When optimizing a theoretical model the goal is to obtain a set of accurate model parameters. The degree to which a model is accurate can be gauged partly from that model's ability to return accurate predictions of measured quantities. In the context of interaction potentials those measured quantities are experimental observables such as the binding energy of a state or the position of a Feshbach resonance. In order to optimize our model of the KCs interaction potential we undertook an interactive non-linear least-squares analysis with the I-NoLLS program [129].

The least-squares problem is defined as minimizing the sum of squares,

$$\chi^2 = \sum_{i=1}^{n} \left( \frac{1}{\sigma_i} \left( y_i^{\mathrm{obs}} - y_i^{\mathrm{calc}}(p_1 ... p_m) \right) \right)^2 . \tag{3.12}$$

The sum of squares is a sum over $n$ measured data points where the inverse of the uncertainty associated with measurement $i$, $\sigma_i$, is multiplied by the difference between the observed, $y_i^{\mathrm{obs}}$, and calculated values, $y_i^{\mathrm{calc}}(p_1 ... p_m)$. The calculated value is a function of the $m$ parameters that are to be fitted in the model. We have used the notation of Law and Hutson, and their discussion of non-linear least-squares analysis, throughout this section [129].

There are a number of different algorithms that can be used in the minimization of $\chi^2$, and the optimization of the model, which have been implemented in the I-NoLLS program. These include the Gauss-Newton and Levenberg-Marquardt

algorithms, both of which require the calculation of the Jacobian matrix. This $n \times m$ matrix contains the first-order partial derivatives of the calculated values with respect to the model parameters;

$$J_{ij} = \frac{\partial y_i^{\text{calc}}}{\partial p_j}. \tag{3.13}$$

A key feature of the I-NoLLS program is that it calculates a super-Jacobian and a sub-Jacobian matrix. The super-Jacobian matrix contains all the calculated values that may be included in the fit and their variation with all parameters in the model that are being fit. The sub-Jacobian matrix contains a subset of these values and parameters. This distinction affords a greater degree of control when undertaking the fit. That the user of the program can include and exclude different datum and parameters for specific iterations of the fit is one element of the interactive fitting I-NoLLS empowers. The program also allows researchers to employ and test different algorithms in order to minimize $\chi^2$ while leading the fit. Interactive fitting is important when the parameters in a model are correlated to one another and is advantageous when the calculations needed to generate $y_i^{\text{calc}}$ are expensive.

The Jacobian matrix appears in the Taylor series expansion of the vector $y^{\text{calc}}$, with $i$ elements, in parameter space,

$$y^{\text{calc}}(p + x) = y^{\text{calc}}(p) + Jx + ... \quad , \tag{3.14}$$

where the vector $x$ is a small variation of the parameters. When undertaking a least-squares analysis we are attempting to find a value of $x$, i.e. a step in parameter space, that will return the optimum set of parameters. It is typical to assume that $y^{\text{calc}}(p)$ is linear in $p$ such that higher-order terms in the Taylor series expansions can be neglected. By defining a diagonal matrix with elements $G_{ii} = 1/\sigma_i$ and inserting the first two terms in the Taylor series expansion into Equation 3.12, the

least-squares problem can be reexpressed as minimizing

$$||Ax - b||_2^2. \tag{3.15}$$

The notation $||...||_2$ indicates the square root of the sum of squares of a vector's elements. $A = GJ$ and $b = Gd$ where $d$ is a vector containing the differences between the measured and calculated values of the observables, $y^{\text{obs}} - y^{\text{calc}}$. It should be noted that this formulation of the problem assumes a linear variation of the calculated values with the parameters.

The Gauss-Newton and Levenberg-Marquardt algorithms are best expressed in terms of the singular-value decomposition (SVD) of the matrix $A$. The SVD is a generalization of the eigenvalue decomposition of a square matrix. The matrix $A$ is expressed as $UKV^{\text{T}}$ where $U$ and $V^{\text{T}}$ are $n \times n$ and $m \times m$ orthogonal matrices. $K$ is a matrix that contains the singular values of the decomposition. Each singular value corresponds to a direction in parameter space; each singular direction is uncorrelated from one another. Large singular values correspond to well defined singular directions and small singular values correspond to poorly defined singular directions. The SVD of $A$ can be inserted into 3.15. Multiplication of this expression by $U^{\text{T}}$ yields a problem that has a solution vector $q$ with elements $q_j = g_j/s_j$, where the elements $g_j$ are from the matrix $g = U^{\text{T}}b$ and $s_j$ are the singular values, such that the ideal step through parameter space is $x = Vq$. This is the Gauss-Newton algorithm.

The Levenberg-Marquardt algorithm affords greater control than the Gauss-Newton algorithm with respect to the step taken in parameter space to minimize $\chi^2$ and refine the model. Equation 3.15 is reformulated such that it is equal to

$$\left|\left| \begin{pmatrix} A \\ \lambda I_m \end{pmatrix} x - \begin{pmatrix} b \\ \lambda 0 \end{pmatrix} \right|\right|_2^2, \tag{3.16}$$

where $I_m$ is the identity matrix and $\lambda$ is a scalar quantity. The Levenberg-Marquardt

algorithm is called, alternatively, damped least-squares and works by introducing the current parameters of the model into the Jacobian matrix as data points. By doing this the parameter step taken during the fitting can be varied by altering $\lambda_m$. If $\lambda_m$ is small the step along the direction associated with the smallest singular value is damped.

We have discussed the complications that arise from parameter correlation in the context of finding a minimum in $\chi^2$. Parameter correlation also complicates the interpretation of the uncertainties associated with refined model parameters and theoretical calculations of the measured observables used in the least-squares analysis. We have used correlated uncertainties when analyzing our fit of the B2024 potential in Section 3.3.2. We believe it is important to report correlated uncertainties because the correlation between parameters determines the uncertainties associated with the parameters.

## 3.3 Results and Discussion

Section 3.2 describes the background of $^{39}$K+$^{133}$Cs collisions. Our attention now turns to describing the work undertaken in collaboration with the Nägerl Group. We present an analysis of the near-threshold bound states and the Feshbach resonances that occur in ultracold $^{39}$K + $^{133}$Cs collisions. Our analysis of scattering observables and our understanding of the bound states allowed us to suggest a number of measurements for our collaborators to undertake. These results allowed us to refine the interaction potential. We discuss the B2024 potential and then use it to characterize a number of Feshbach resonances that exist in collisions of $^{39}$K + $^{133}$Cs.

### 3.3.1 Part I: Near-threshold Bound States and Scattering Resonances

#### Bound States

We study the $L = 0$ bound states that are likely to cause broad Feshbach resonances at the lowest collision thresholds. We used the G2017 potential for these calculations.

The a+a threshold ($M_F = 4$) is the lowest threshold. Figure 3.5 shows that a single bound state runs approximately parallel to the a+a threshold and undergoes avoided crossings with two bound states that come up from lower energy as a function of $B$. The shallower of these two states has a singlet fraction of 0.378 and the other state has a singlet fraction of 0.482. These values of the singlet fraction were obtained with BOUND. The calculations were undertaken for values of field and binding energy where the states' gradients were constant and are indicated in Figure 3.5 by the position of the labels of the singlet fractions. The multichannel wavefunctions of these states, in an $(S, I, F)$ basis, are shown in Figure 3.6 and confirm that the deeper of the two is more sensitive to the singlet potential.

The two deeper bound states in Figure 3.5 approach threshold as a function of the magnetic field. Prior to crossing threshold, these states avoided cross with the least-bound state beneath the a+a threshold. The state that crosses threshold may be a mixture of the two states, but the position of the Feshbach resonance is ultimately determined by the deeper state and the variation of its energy as a function of magnetic field. We often use the concept of a 'bare' bound state when building an understanding of the near-threshold bound states. These bare states are hypothetical states and would exist if the interactions between states were switched off. The true bound states and the bare bound states are the same away from the threshold and any avoided crossings between states. Feshbach resonance positions are ultimately determined by these bare bound states, the energy of which is determined by the scattering length. From the bound-state spectra in Figure 3.5 it is clear that there are two Feshbach resonances caused by $L = 0$ states at the a+a

threshold.

The state that runs parallel to the a+a threshold, in Figure 3.5, will most likely have the character, and properties, of that threshold. We elect to label the thresholds and bound states with the quantum numbers that are appropriate at higher fields. The state running parallel to threshold is labeled by $(-1(-\frac{1}{2},\frac{3}{2})(3,3)\mathrm{s})$ where we have used the notation $(n(m_{s,\mathrm{K}},m_{i,\mathrm{K}})(f_{\mathrm{Cs}},m_{f,\mathrm{Cs}})L)$. For KCs the bin boundaries are 0, 0.398, 2.754, 8.800, 20.239 GHz. The least-bound state is approximately 70 MHz beneath its threshold. As the first bin ends at 398 MHz this bound state lies comfortably in the first bin and is labeled $n = -1$. A similar analysis allows $(-2(\frac{1}{2},\frac{3}{2})(3,2)\mathrm{s})$ and $(-2(\frac{1}{2},\frac{1}{2})(3,3)\mathrm{s})$ to be assigned to the states, which at $B =$ 0 G, are bound by approximately 900 MHz and 1150 MHz. These two deeper states are supported by the h+b and g+a thresholds displayed in Figure 3.2. It is clear from Figure 3.2 that the h+b and g+a thresholds have moderate and large singlet fractions, respectively, which agree with the singlet fractions calculated using BOUND.

Our attention now turns to the bound states beneath the $L = 0$ thresholds with $M_F = 3$. For $B > 267$ G the lowest threshold is the b+a threshold. For $B < 267$ G the lowest threshold is the a+b threshold. It is evident from Figure 3.7 that five $L = 0$ bound states with $M_F = 3$ exist in the ranges of energy and magnetic field we have studied. Two of these states are $n = -1$ states that run parallel to the two lowest thresholds. At $B \approx 0$ G the shallower of the two is $(-1(-\frac{1}{2},\frac{1}{2})(3,3)\mathrm{s})$. The other is $(-1(-\frac{1}{2},\frac{3}{2})(3,2)\mathrm{s})$. From Figure 3.2 it is clear that we do not expect either of these states to have high singlet fractions. The remaining three states, that at zero field are bound by approximately 830, 900, and 1090 MHz, approach the lowest two thresholds as a function of the magnetic field. These five states are responsible for four Feshbach resonances in the b+a channel, beneath 600 G. The positions of the first three resonances are determined by the deeply bound states. These states are found to have singlet fractions of 0.290, 0.360, and 0.478 respectively. Due to the gradients of the states, their depth, and their singlet fractions, it is clear these

are states with $n = -2$ supported by the f+a, g+b, and h+c thresholds. The fourth resonance is caused by a shallow state i.e. the least-bound state of the a+b threshold crossing the b+a threshold.

The lowest panel in Figure 3.8 shows the bound states and scattering at thresholds with $m_F = 2$. There are several more bound states compared to Figures 3.5 and 3.7. The three lowest thresholds with $m_F = 2$ each support a bound state with $n = -1$. Two of these three shallow states cause Feshbach resonances in the c+a threshold at $\approx 460$ G and $\approx 610$ G. There are four deeply bound states, the first of which causes a Feshbach resonance at the the b+b threshold. The remaining three deeply bound states cause Feshbach resonances at the c+a threshold. The four deeper bound states have singlet fractions, calculated with BOUND, equal to 0.190, 0.299, 0.394, and 0.479.

Studying the singlet fractions reported in Figures 3.5, 3.7, and 3.8 confirm a number of the expectations we built from studying the singlet fractions of the atom-pair states. Bound states, and by extension the $L = 0$ thresholds, that have the highest singlet fractions exhibit a low variation of their energy with magnetic field. In 2017, when the last attempt was made at fitting the interaction potential, Gröbner et al. measured the position of the two resonances in the a+a, the resonances at 419.3 G and 513.12 G at the b+a threshold, and the resonances at 491.5 G and 559.32 G at the c+a threshold. These were all caused by states with $n = -2$ approaching threshold. The singlet fraction of these states ranged from 0.360 to 0.482. The measurements used in 2017 did not have the range of sensitivity needed to refine both potentials. The bound states or Feshbach resonance positions that would be useful in our attempts to refine the potential would be those that occur at lower fields. These are caused by states with higher values of $dE/dB$ and lower singlet fractions.

The bound states with $M_F = 1$ and $M_F = 0$ display similarities to those with $M_F = 2$. There exist a number of states that run approximately parallel to the lowest thresholds. From Figure 3.2.1 we expect these shallow states to have low

singlet fractions similarly to the shallow states in Figures 3.5, 3.7, and 3.8. It is evident from Figures 3.9 and 3.10 that a threshold with excited $f_{\mathrm{K}} = 2$ approaches and crosses the lower thresholds over a range of magnetic field. These are the respective d+a and d+b thresholds. These support a shallow bound state with $n = -1$ that can be seen to 'enter' the bound-state spectrum at just over 300 G. Five deeper states exist with $M_F = 1$ and $M_F = 0$. Four of these approach threshold as a function of magnetic field. The deepest of the five states in Figures 3.9 and 3.10 have negative gradients.

It is also evident from Figures 3.9 and 3.10 that the bound states with lower $m_F$ values have smaller singlet fractions. This observation is confirmed by Figures 3.2 and 3.2.1 and can be explained by the higher gradients of the energies of the states in Figures 3.9 and 3.10 with magnetic field. Bound states that do not vary much with magnetic field, i.e. have small gradients, display the highest singlet fractions. Gaining a deeper understanding of the bound states at lower energies is key. Figure 3.11 displays the bound states with different values of $m_F$ which we included in the preceding figures. It is evident that, as $B \to 0$ G, bound states with different values of $m_F$ coalesce to discrete energies. These are the bound-state energies with different values of the total angular momentum, $F$, which is the conserved quantity at $B = 0$ G. These zero-field states were studied and assigned by Gröbner et al [110]. The three states at approximately $-100$ MHz are states with total angular momentum $F = 4, 3, 2$ which arise as the resultant of $f_K = 1$ and $f_{Cs} = 3$. The states at $-700$ MHz to $-1100$ MHz have $F = 1, 2, 3, 4, 5$ which arise as the resultants of $f_{\mathrm{K}} = 2$ and $f_{\mathrm{Cs}} = 3$.

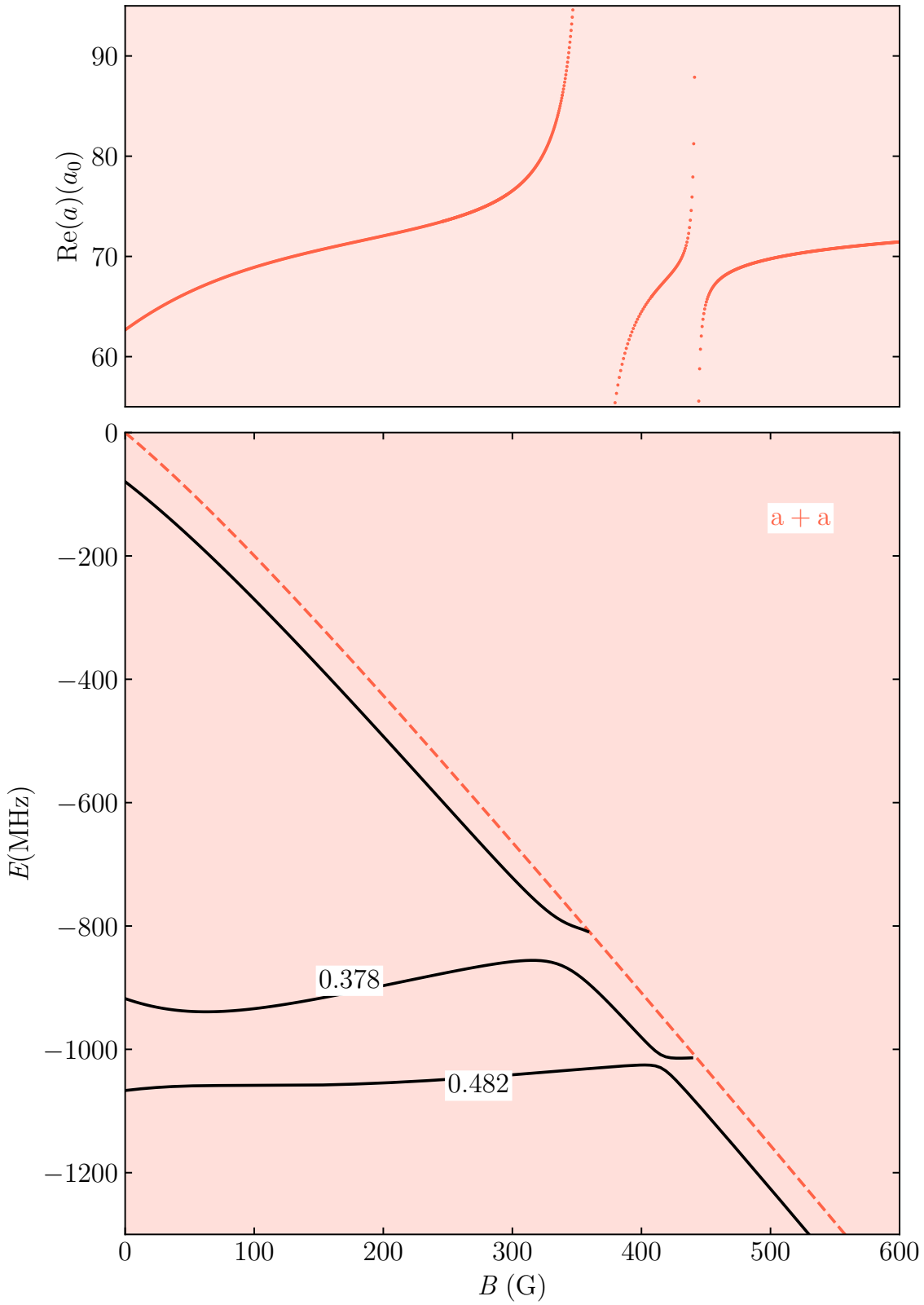


Figure 3.5: Energies of bound states with $m_F = 4$ (lower panel) and the scattering length (upper panel) for the a+a threshold. Singlet fractions of deeply bound states are printed in the lower panel.

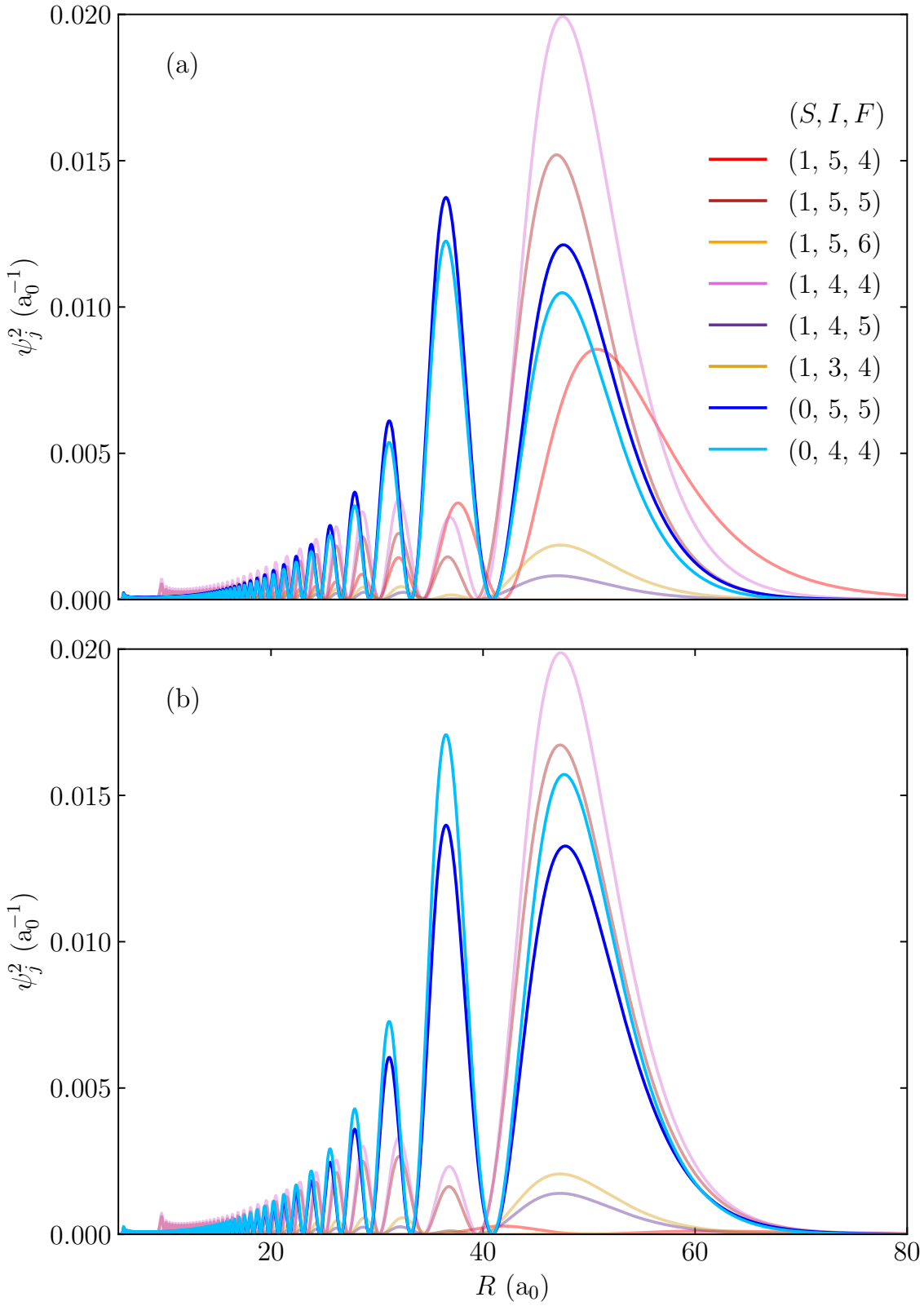


Figure 3.6: Square of the radial channel functions that constitute the multichannel wavefunctions of the states that appear in Figure 3.5. Panel (a) corresponds to the state in Figure 3.5 with a singlet fraction of 0.378 and panel (b) corresponds to the state with a singlet fraction of 0.482.

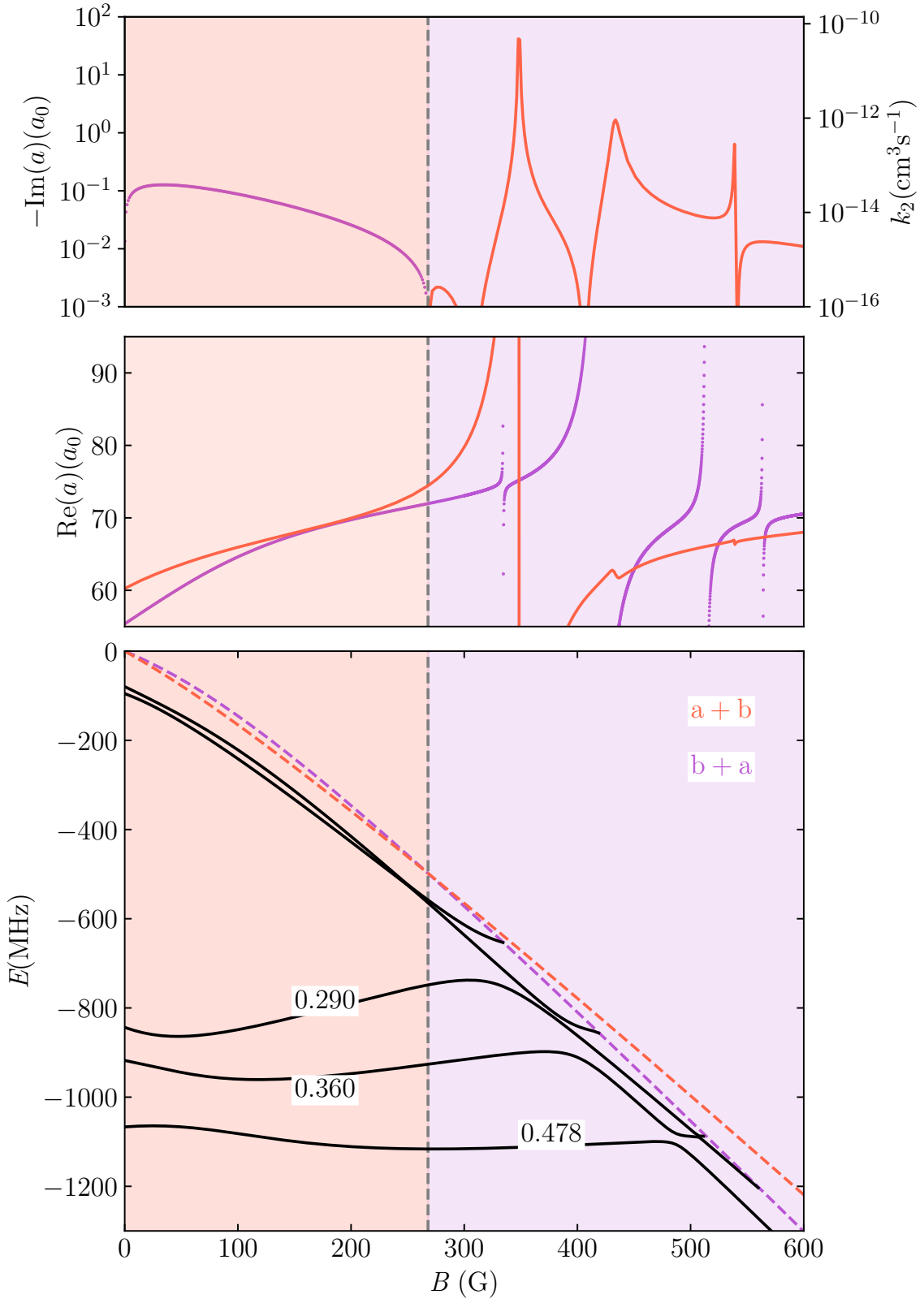


Figure 3.7: Energies of bound states with $m_F = 3$ (lower panel), the real part of scattering length for the a+b and b+a thresholds (middle panel), and the imaginary part of the scattering length with the loss coefficient at limitingly low energy (upper panel). Singlet fractions of deeply bound states are printed in lower panel.

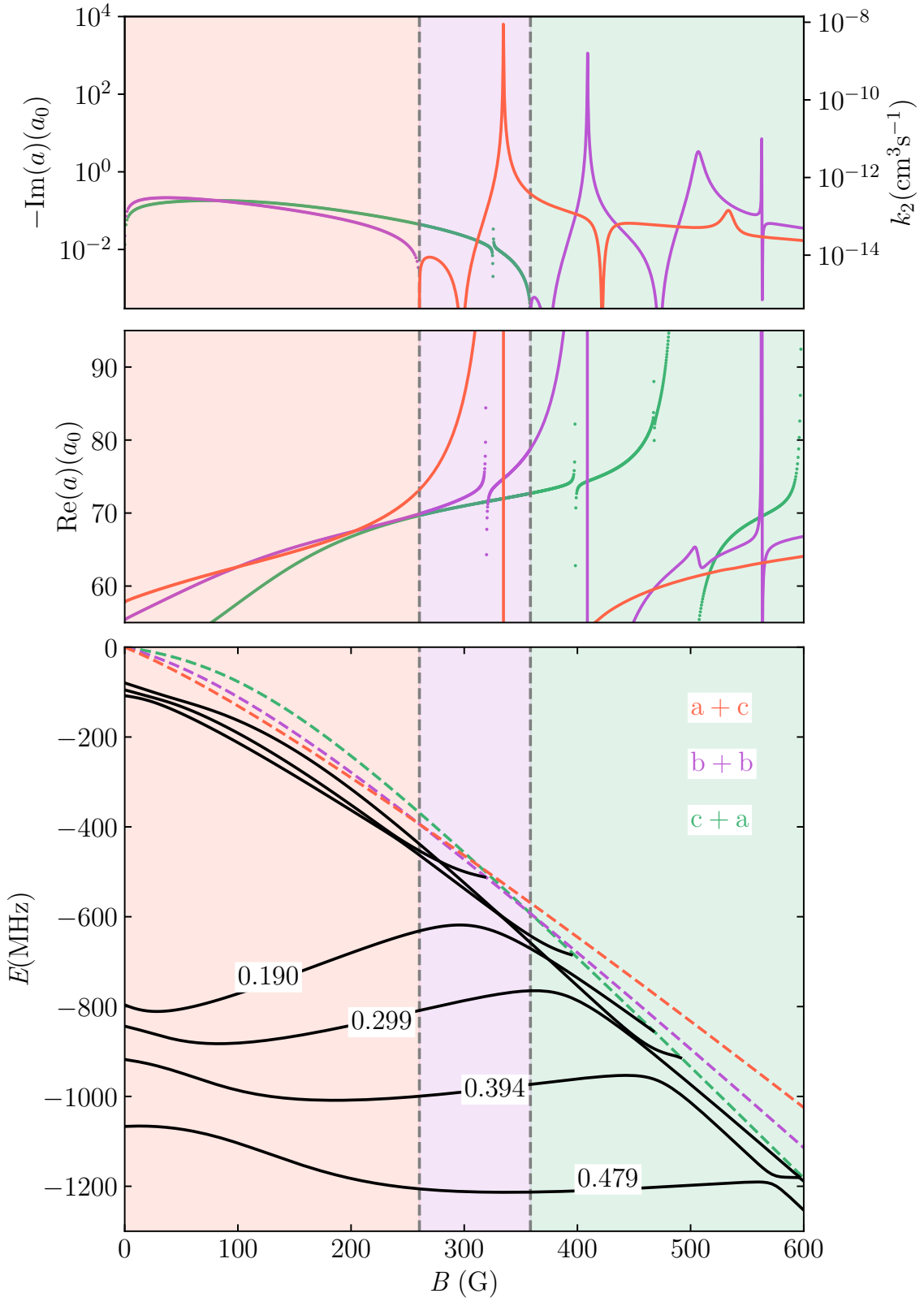


Figure 3.8: Energies of bound states with $m_F = 2$ (lower panel), the real part of scattering length for the a+c, b+b, and c+a thresholds (middle panel), and the imaginary part of the scattering length with the loss coefficient at limitingly low energy (upper panel). Singlet fractions of deeply bound states are printed in lower panel.

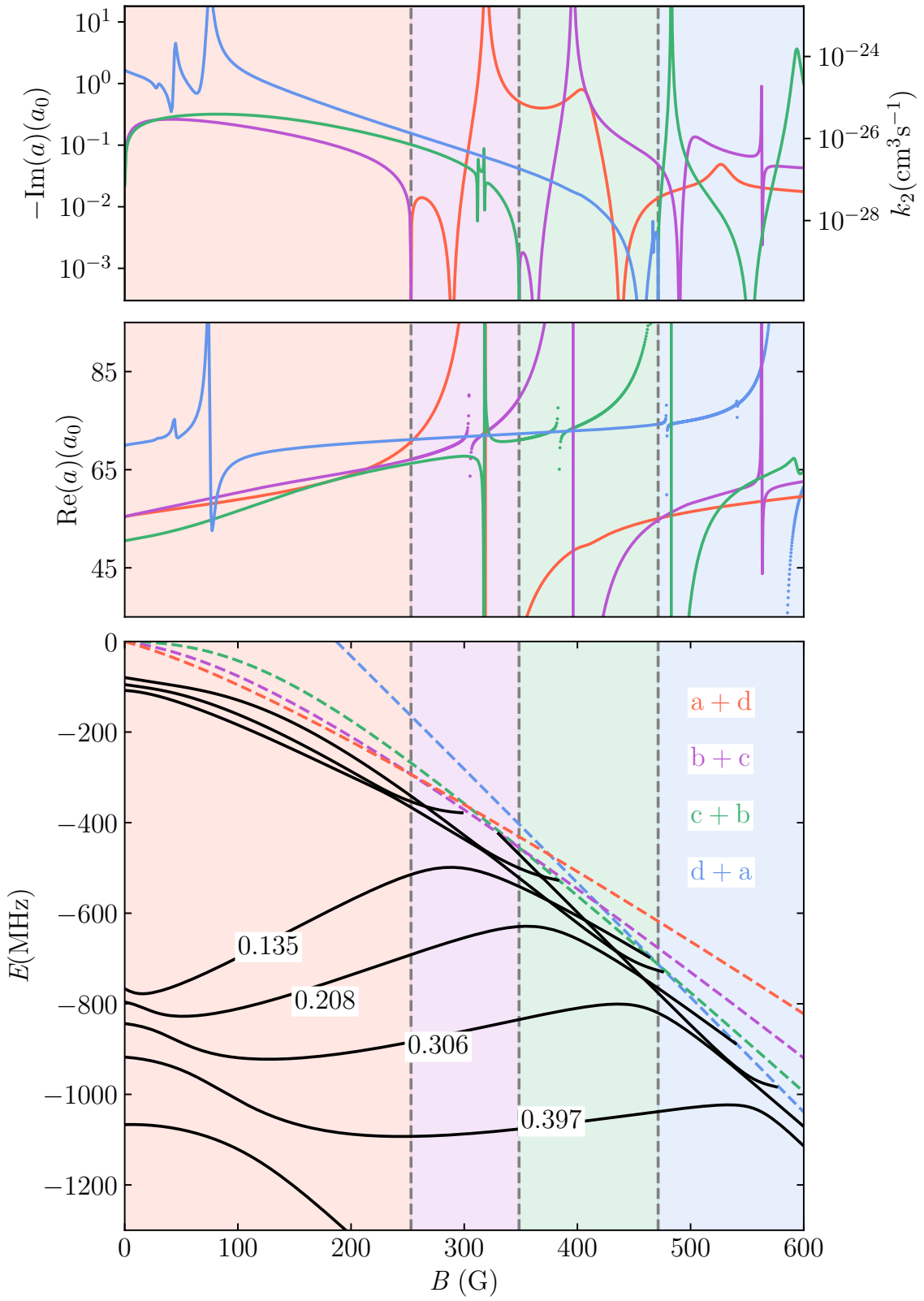


Figure 3.9: Energies of bound states with $m_F = 1$ (lower panel), the real part of scattering length for the a+d, b+c, c+b, and d+a thresholds (middle panel), and the imaginary part of the scattering length with the loss coefficient at limitingly low energy (upper panel). Singlet fractions of deeply bound states are printed in lower panel.

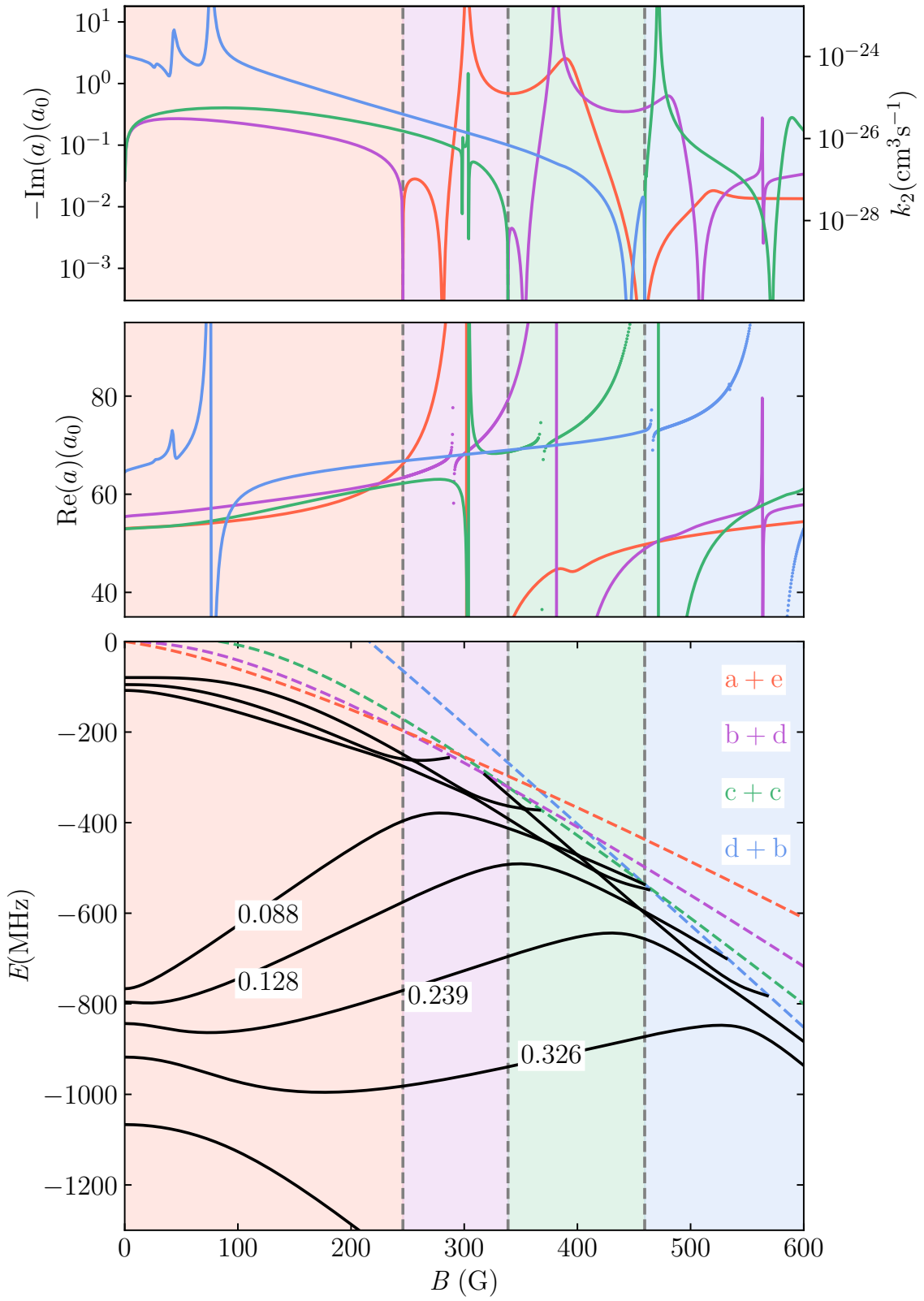


Figure 3.10: Energies of bound states with $m_F = 0$ (lower panel), the real part of scattering length for the a+e, b+d, c+c, and d+b thresholds (middle panel), and the imaginary part of the scattering length with the loss coefficient at limitingly low energy (upper panel). Singlet fractions of deeply bound states are printed in lower panel.

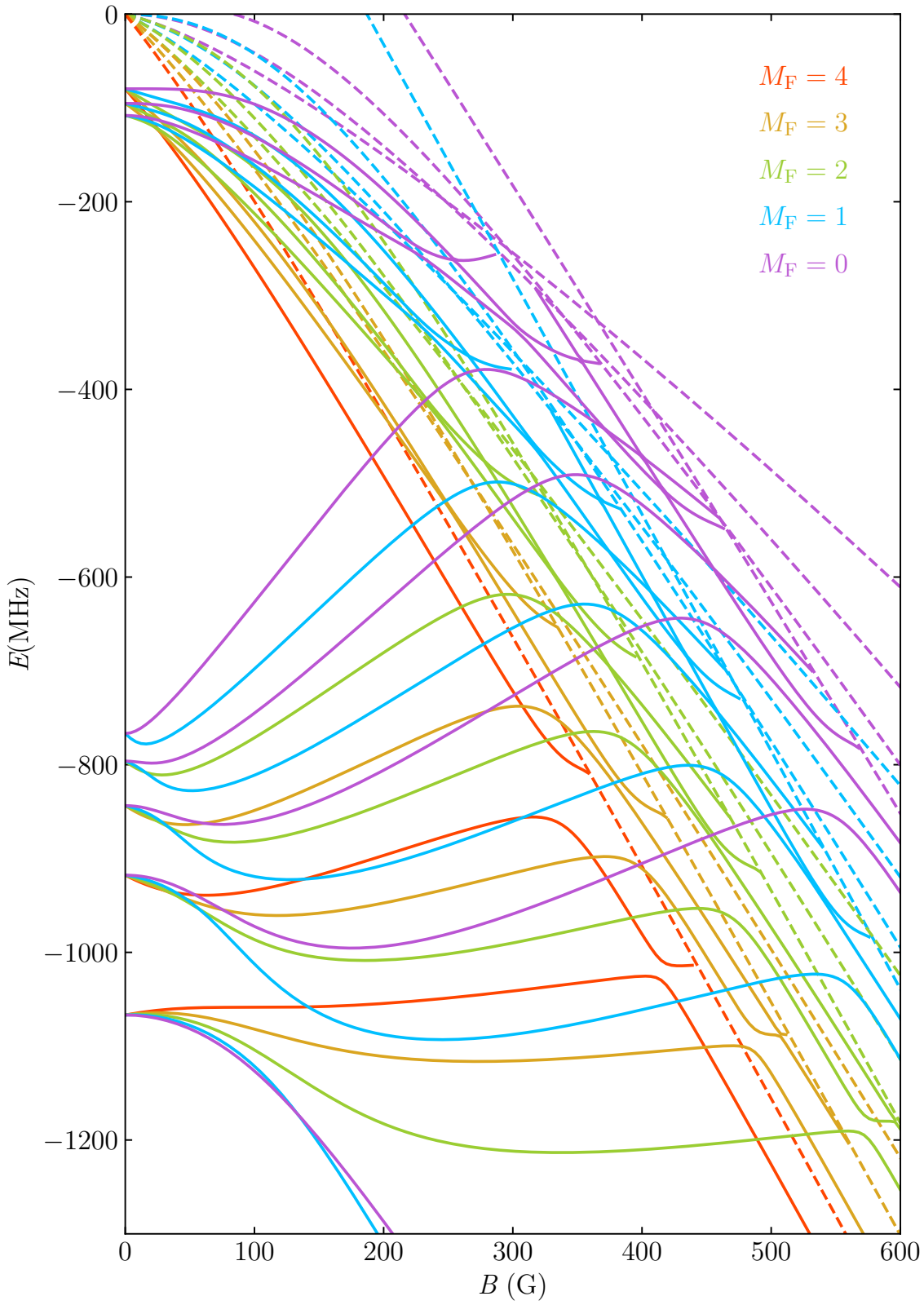


Figure 3.11: Energies of KCs near-threshold bound-states with $M_F$ = 4, 3, 2, 1, and 0.

Table 3.3: $B_{\rm res}$ (B), $\Delta$ (G), and $a_{\rm bg}$ ($a_0$) for the s-wave Feshbach resonances caused by states with low singlet fractions. The thresholds these resonances occur at are given.

| Threshold | $B_{\rm res}$ (G) | $\Delta$ (G) | $a_{\rm bg}$ ($a_0$) | $F_s$ |
|---|---|---|---|---|
| b+b | 319.341 | 0.0466 | 73.39 | 0.190 |
| b+c | 304.623 | 0.0549 | 71.05 | 0.135 |
| b+d | 290.267 | 0.0484 | 67.24 | 0.088 |

**Scattering Resonances**

With the analysis detailed in the previous section we suggested a number of Feshbach resonance positions for the Nägerl Group to measure. Here we characterize and discuss the resonances suggested using a series of MOLSCAT calculations and the G2017 potential.

In order to refine both the singlet and triplet scattering lengths the positions of several Feshbach resonances are needed. These resonances need to be caused by states with a range of singlet fractions that is wider than 0.360 to 0.482. In order to obtain this range a number of additional resonances need to be measured. These are tabulated in Table 3.3 and have been characterized with $L = 0$ calculations.

These resonances have moderate widths, are at relatively low fields, and should be easy to measure. Characterizing these resonances as elastic resonances is valid so far as they occur at the lowest threshold, for their respective values of $M_F$, and cannot be decayed via spin-exchange processes. We undertook a series of $L = 2$ calculations in order to confirm that spin-relaxation processes did not decay the resonance substantially. These calculations confirmed that all three resonances were inelastic resonances with weak background inelasticity. For example, the resonance at the b+b threshold had low background inelasticity, as demonstrated by $\beta_{\rm bg} = 7.45 \times 10^{-4}\ a_0$ and a symmetric peak in $\beta$ with its maximum at $a_{\rm res} = 885.12\ a_0$. This resonance had $\Gamma_B^{\rm inel} = -7.73 \times 10^{-3}$ G. The resonance width was not modified by spin-relaxation processes. The resonance at the b+c threshold was very similar. The resonance had $\beta_{\rm bg} = 1.08 \times 10^{-3}\ a_0$, $a_{\rm res} = 935.86\ a_0$, and $\Gamma_B^{\rm inel} = -8.35 \times 10^{-3}$ G. The resonance width was not modified by spin-relaxation processes.

Table 3.4: $B_{\text{res}}$ (B), $\Delta$ (G), and $a_{\text{bg}}$ ($a_0$) for s-wave Feshbach resonances caused by states with $n = -1$. The thresholds at which these resonances occur are given.

| Threshold | $B_{\text{res}}$ (G) | $\Delta$ (G) | $a_{\text{bg}}$ ($a_0$) |
|---|---|---|---|
| b+a | 563.74 | 0.0742 | 69.797 |
| c+a | 467.67 | 0.0061 | 82.560 |
| d+a | 478.85 | 0.0114 | 74.366 |
| d+b | 466.01 | 0.0266 | 73.000 |

In the preceding section a number of bound states with $n = -1$ that cause Feshbach resonances were highlighted. These would be useful, in combination with the positions of Feshbach resonances caused by states with $n = -2$, in refining the $C_6$ parameter. These resonances are characterized with $L = 0$ calculations in Table 3.4. These resonances are not decayed via spin-exchange processes.

### 3.3.2 Part II: Fitting the Interaction Potential

#### Experimental Data

When adjusting the interaction potential we had a number of experimental measurements available to us; our collaborators in the Nägerl Group measured a number of the resonances we suggested in the previous section. We collate them here and discuss the various advantages they have in the context of our refitting.

We utilized the measurements, reproduced in Table 3.2, undertaken by Gröbner et al in 2017. These measurements do not posses the variety of singlet fractions needed to refine both the singlet and triplet potentials.

The Nägerl Group attempted to locate the positions of several other resonances with Feshbach spectroscopy. We briefly summarize the procedure outlined by Gröbner et al. [110]. In the vicinity of a Feshbach resonance between $^{39}$K and $^{133}$Cs the loss of $^{39}$K from the trap increases due to three-body processes. The magnetic field is ramped from 0 G to a value in the vicinity of a Feshbach resonance. The magnetic field is held constant for a period of time. The magnetic field is then ramped back to approximately 0 G. Absorption imaging is used to detect the remaining fraction of $^{39}$K atoms. Repeating this process for a series of magnetic field values across

the range of field a Feshbach resonance is expected to exist in, allows plots of the remaining fraction of $^{39}$K atoms to be plotted as a function of field. It is typical to fit the loss feature with a Lorentzian. The minimum of the Lorentzian, and the fraction $^{39}K$ atoms remaining, is taken to be the position of the resonance, $B_{\text{res}}^{\text{exp}}$.

The Nägerl group identified two loss features with Feshbach spectroscopy that we believe to be caused by states with low singlet fractions. The first loss feature was at 315.57 G at the b+b threshold and the second loss feature was at 299.58 G at the b+c threshold. We believed these loss features were caused by resonances which were caused by states with respective singlet fractions of 0.190 and 0.135. These two measurements, in addition to those measured in 2017, provide a set of observables that are sensitive to both the singlet and triplet potentials.

The uncertainties associated with the resonance positions obtained from Feshbach spectroscopy are not obvious. The Lorentzian functions used to fit the peaks obtained in 2024 had uncertainties of the order $10^{-3}$ G and $10^{-4}$ G. The same method for determining resonance positions was used by Gröbner et al. in 2017, though larger uncertainties of the order $10^{-3}$ G and $10^{-2}$ G were reported. In their least squares fit Gröbner et al. used uncertainties of 0.3 G and 0.4 G. We used these uncertainties in our least-squares analysis and potential refitting. For the recently measured resonance positions we used uncertainties of 0.2 G.

Several other Feshbach resonance positions were obtained from Feshbach spectroscopy. Minima in the fraction of $^{39}$K atoms were caused by states with $n = -1$ crossing threshold, and were therefore useful in any attempts to refit the $C_6$ coefficient. Loss minima were measured at 466.266 G, 478.051 G, and 464.595 G. These resonances were measured at the c+a, d+a, and d+b thresholds, respectively. An additional loss feature was found at 463.273 G at the c+a threshold. Our $L = 0$ calculations had not predicted another resonance here. We found that an $L = 2$ state crosses threshold 5 G beneath the additional loss feature. This resonance is discussed in detail in the following section.

We had access to measurements of the binding energy of the state that causes

a resonance at 361.1 G at the a+a threshold. These measurements range from −1300 kHz to −10 kHz in depth. These measurements are more accurate than resonance positions determined with Feshbach spectroscopy. Although we had a series of measurements (shown in Figure 3.12 as blue crosses) of the bound-state energy we used only two in our fit. The first of these measurements was $E_\mathrm{b} = 10.66$ kHz, where $E_\mathrm{b}$ is the binding energy, at 361.4995 G and the second was $E_\mathrm{b} = 1.28$ MHz at 359.566 G. We assigned these measurements uncertainties of 0.003 G and 0.002 G, respectively, in our fit. These two measurements were selected such that we had one near-threshold and another far away from threshold. These two points captured the energy of the unperturbed state, the deeper measurement, and the state near-threshold where its gradient has altered. The change in the state's gradient is exceptionally sensitive to the difference between the singlet and triplet scattering lengths. This was discussed in more detail in Section 3.2.4.

**Fitting Potential Parameters**

We refined the KCs interaction potential with a least-squares analysis and the I-NoLLS program. We found that the difference between the singlet and triplet scattering lengths was larger than previous models of the potential predicted. The model of the potential we developed gives $a_\mathrm{s} = -29.2 \pm 1.6\ a_0$ and $a_\mathrm{t} = 77.70 \pm 0.4\ a_0$. The uncertainties reported here are the correlated uncertainties ($2\sigma$) calculated within the I-NoLLS program. The G2017 potential predicted $a_\mathrm{s} = -18.37\ a_0$ and $a_\mathrm{t} = 74.88 \pm 0.09\ a_0$. We elected to use Equation 3.10 in our model of the short-range regions of the singlet and triplet curves and varied $\alpha_{S=0}$ and $\alpha_{S=1}$ in order to change $a_\mathrm{s}$ and $a_\mathrm{t}$. We used Equation 3.10 for our model of the short-range potential because it matches our physical intuition of the short-range repulsion that exists between atoms and may be more accurate in studies of higher-energy collisions. In Section 3.5 we stated that the accuracy of a model can be partly gauged from its ability to return accurate predictions of measured quantities. It is also important, however, that a model meets qualitative expectations built on elementary physical

principles.

Our model of the potential used $C_6 = 5129\ E_h a_0^6$. This value of $C_6$ was calculated by Derevianko et al. and was used in the F2013 and G2017 potentials. We obtained estimates of $\alpha_{S=0}$ and $\alpha_{S=1}$ using the ionization energies of K and Cs [130, 131], as detailed in Section 3.2.3. $a_\mathrm{s}$ and $a_\mathrm{t}$ are functions of $\alpha_{S=0}$, $\alpha_{S=1}$, $R^0_\mathrm{SR}$, and $R^1_\mathrm{SR}$. We selected values of $R^0_\mathrm{SR} = 3.5$ Å and $R^1_\mathrm{SR} = 5.25$ Å. These values of $R^0_\mathrm{SR}$ and $R^1_\mathrm{SR}$ ensured that small changes in $\alpha_{S=0}$ and $\alpha_{S=1}$ could vary the singlet and triplet scattering lengths across an appropriate range of values.

We scaled the parameters in our fit by their units and undertook two iterations of the Gauss-Newton algorithm to identify $\alpha_{S=0} = 1.70342 \pm 0.00235$ Å$^{-1}$ and $\alpha_{S=1} = 1.726 \pm 0.015$ Å$^{-1}$.

The observable quantities we included in our fit were two measurements of the bound-state energy beneath the 361.10 G resonance at the a+a threshold, the Feshbach resonance positions measured in 2017, and the Feshbach resonance positions measured in the last year. The Feshbach resonance positions measured with Feshbach spectroscopy and used in our fit are given in Table 3.5. Before discussing the Feshbach spectroscopy measurements we discuss the bound-state energy measurements. In our fit we gave the measurements of the bound-state energies the smallest uncertainty. This reflects the accuracy of the measurements, their experimental uncertainty was orders of magnitude lower than the measurements obtained with Feshbach spectroscopy, and the weight we wanted to give to these measurements in our fit. We have discussed how the variation of a state's gradient as it approaches threshold is sensitive to the difference between the singlet and triplet scattering lengths. At $361.500 \pm 0.002$ G the bound state had $E_\mathrm{b} = 10.66$ kHz. Our potential found the bound state to have this energy at $361.5 \pm 0.1$ G. At $359.566 \pm 0.003$ G the bound state had $E_\mathrm{b} = 1.28$ MHz. Our potential found the bound state to have this energy at $359.57 \pm 0.09$ G. Figure 3.12 shows our model of the potential (B2024) is able to accurately calculate the energy of the bound state (red line) beneath the 361.65 G resonance at the a+a threshold across a large range of energy (not just for

the two representative values included in our fit). We also included the calculation of this bound state with the G2017 potential (black line). It is clear that the previous potential was unable to predict the bound-state energy or Feshbach resonance position accurately. The F2013 and G2017 potentials had an inaccurate value of $a_s$ which gave an inaccurate difference between the singlet and triplet scattering lengths. The B2024 potential has a larger singlet and triplet difference and is therefore able to predict the energy of the bound state and its curvature near-threshold accurately.

The Feshbach spectroscopy undertaken by the Nägerl Group suggested that this resonance occurred at 361.10 G. Our potential, which is clearly able to calculate the energy of the underlying state, predicts the position of the resonance to be 361.7±0.1 G. This prediction lies outside the assigned uncertainty of 0.4 G and suggests that the error associated with Feshbach resonance positions determined from atom loss are greater than we believed.

Table 3.5 contains the measured Feshbach resonance positions used in our fit, the uncertainties of these measurements, and the resonance positions calculated from the B2024 potential. We report the correlated uncertainties calculated with I-NoLLS for our predictions of the resonance positions. There is a range of agreement between experiment and theory. This agreement is ultimately sufficient given the accuracy of the bound-state energy calculations. The only resonance that is indicative of a limitation of our model of the potential is the resonance at 599.32 G at the c+a threshold. Our potential predicts this resonance to occur at 597.78 G. Predicting the position of this resonance has the potential to be quite complex. There are two $L = 0$ resonances in close proximity to one another at around 600 G. The first is caused by a state with $n = -2$ and the second, which has since been measured at 610.1 G, is caused by a state with $n = -1$. These states undergo an avoided crossing before crossing threshold. The energies of the bare bound states, their variation with magnetic field, and the strength of the avoided crossing will all play a role in determining the position of the resonances.

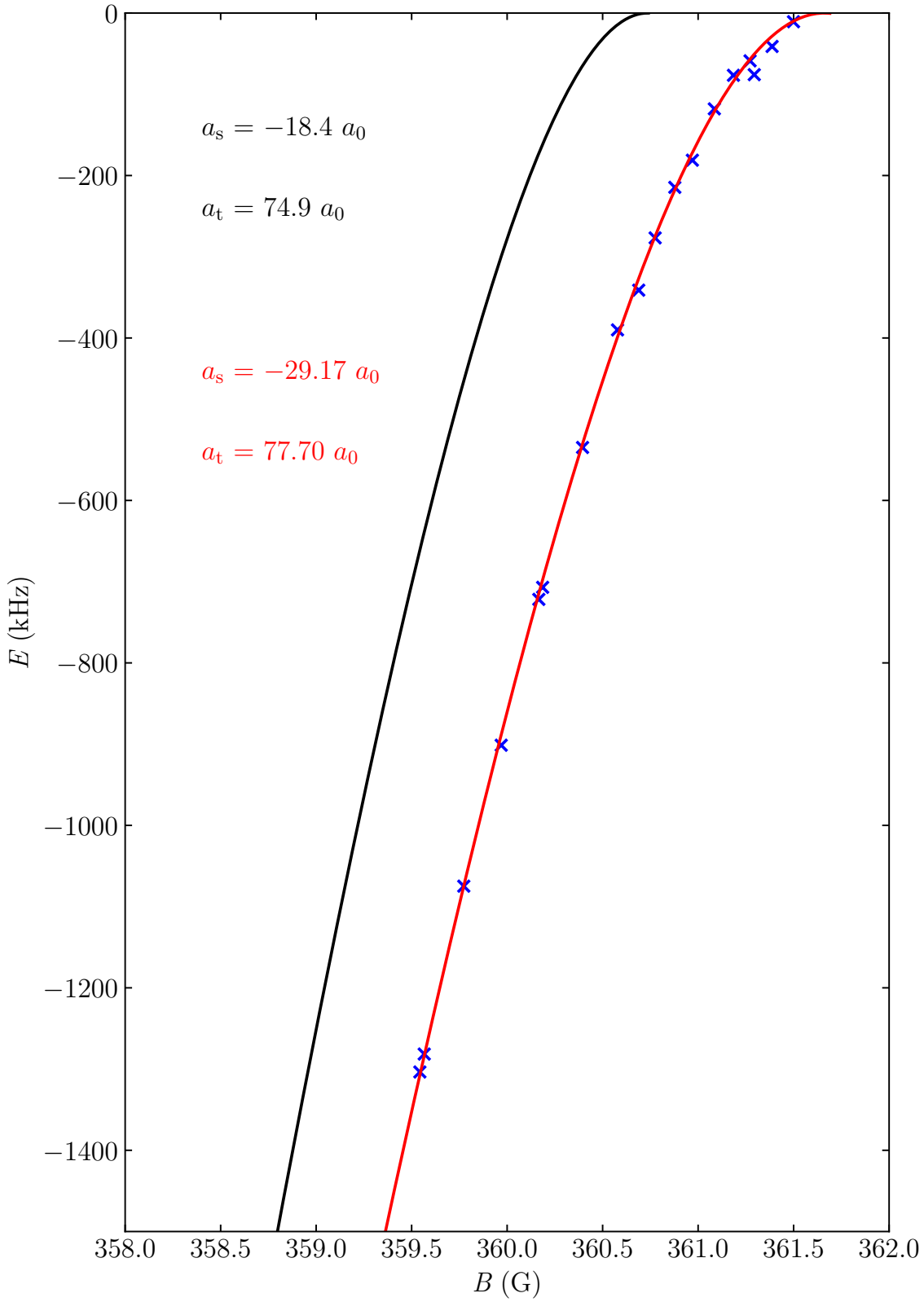


Figure 3.12: Bound-state energy measurements (blue crosses) in the vicinity of the Feshbach resonance at the a+a threshold. The bound-state energies calculated with the G2017 (black line) and B2024 (red line) potential are shown.

Table 3.5: Agreement between measured Feshbach resonance positions and those predicted with the B2024 potential. The thresholds these resonances occur at are given. The uncertainty of the measurement included in our fit and the $2\sigma$ value calculated from our fit are included.

| Threshold | $B_{\text{res}}^{\text{exp}}$ (G) | Uncertainty (G) | $B_{\text{res}}^{\text{calc}}$ (G) | $2\sigma$ (G) |
|---|---|---|---|---|
| b+c | 299.57 | 0.2 | 299.87 | 0.74 |
| c+a | 466.24 | 0.2 | 465.61 | 0.35 |
| b+b | 315.57 | 0.2 | 315.77 | 0.59 |
| d+a | 478.05 | 0.2 | 478.07 | 0.19 |
| d+b | 464.60 | 0.2 | 464.62 | 0.26 |
| c+a | 599.32 | 0.3 | 597.78 | 0.29 |
| c+a | 491.50 | 0.4 | 492.24 | 0.13 |
| b+a | 513.12 | 0.3 | 513.77 | 0.15 |
| b+a | 419.30 | 0.3 | 420.24 | 0.09 |
| a+a | 442.59 | 0.4 | 443.45 | 0.11 |

We attempted a fit of the potential that included $C_6$, in addition to $\alpha_{S=0}$ and $\alpha_{S=1}$. The aim of this fit was to see if changing $C_6$ could improve the discrepancy between our prediction and the measurement of the resonance at 599.32 G at the c+a threshold. The singular-value decomposition in this 3-parameter space yielded two well-defined singular values and a single poorly defined singular value. We scaled the parameters by their uncertainties and use the Levenberg-Marquardt algorithm to damp the step along the third poorly defined singular value. Similar agreement between the calculated values and the experimental measurements was obtained from a fit that found $\alpha_{S=0} = 1.7531 \pm 0.0311$ Å$^{-1}$, $\alpha_{S=1} = 2.19 \pm 0.19$ Å$^{-1}$, and $C_6 = 5189 \pm 18\ E_h a_0^6$ and the B2024 potential.

There were a number of limitations with the model of the potential we obtained when varying $C_6$ in our non-linear least-square fit. Firstly, changing $C_6$ was unable to correct for the error in the calculation of the resonance at the c+a threshold at 599.32 G. Secondly, the value of $\alpha_{S=1}$ was concerning; this value lay substantially outside the 95% limits we predicted in the fit of the B2024 potential. In addition, the difference between $\alpha_{S=0}$ and $\alpha_{S=1}$ did not meet our expectation that these values would be similar. Finally, our value of $C_6$ fell outside Derevianko et al.'s reported uncertainty. Derevianko et al. reported that the uncertainty ($1\sigma$) for their value of

Table 3.6: Broad resonances at lowest scattering thresholds characterized with $L = 0$ scattering calculations.

| Threshold | $B_{\rm res}$ (G) | $\Delta$ (G) | $a_{\rm bg}$ ($a_0$) |
|---|---|---|---|
| a+a | 361.66 | 5.23 | 74.65 |
| a+a | 443.45 | 0.41 | 70.08 |
| b+a | 332.23 | 0.03 | 77.60 |
| b+a | 420.24 | 4.80 | 74.74 |
| b+a | 513.77 | 0.58 | 71.29 |
| b+a | 553.58 | 0.09 | 71.47 |
| b+b | 315.77 | 0.07 | 76.60 |
| c+a | 396.36 | 0.03 | 77.05 |
| c+a | 465.61 | $7\times10^{-3}$ | 86.46 |
| c+a | 492.24 | 4.23 | 74.89 |
| c+a | 597.78 | 0.46 | 72.85 |
| c+a | 609.04 | 0.10 | 69.63 |
| b+c | 299.87 | 0.08 | 74.12 |
| c+b | 380.67 | 0.07 | 75.89 |
| d+a | 478.07 | 0.02 | 77.38 |
| d+a | 538.91 | $2 \times 10^{-3}$ | 81.87 |
| d+a | 578.88 | 3.66 | 75.23 |
| b+d | 284.43 | 0.07 | 69.90 |
| c+c | 364.58 | 0.09 | 73.41 |
| d+b | 464.63 | 0.04 | 76.12 |
| d+b | 534.03 | $2 \times 10^{-3}$ | 87.24 |
| d+b | 571.11 | 8.17 | 71.90 |

$C_6$ was $\pm 30\ E_h a_0^6$. As such our value and the value of Derevianko et al. lay within their mutual 95% confidence limits. The correlated uncertainty in our value of $C_6$ was smaller than the value calculated by Derevianko et al. The values of $a_{\rm s}$ and $a_{\rm t}$ we found when varying $\alpha_{S=0}$, $\alpha_{S=1}$, and $C_6$ were, respectively, $-31.72 \pm 3.1\ a_0$ and $77.60 \pm 0.45\ a_0$.

### Predictions with the B2024 Potential

With our new potential we undertook a series of calculations in order to aid researchers working on $^{39}$K + $^{133}$Cs collisions in the future.

We began by characterizing a number of Feshbach resonances at the lowest $^{39}$K+$^{133}$Cs collision thresholds caused by bound states with $L = 0$. We characterized these resonances with $B_{\rm res}$ (G), $\Delta$ (G), and $a_{\rm bg}$; our previous calculations confirmed these resonances are only weakly decayed via spin-relaxation processes.

We used $L = 0$ calculations. The thresholds and resonance parameters are given in Table 3.6.

At present the Nägerl Group have formed loosely-bound molecules with magnetoassociation and the Feshbach resonances at 361.65 G at the a+a threshold. They have begun to explore the bound states with $L = 0$ and $L = 2$ in the vicinity of this resonance. Their next aim is to identify a STIRAP scheme that will allow the efficient conversion of a loosely-bound state to the rovibrational-ground state. The most efficient scheme may not involve the state populated during magnetoassociation. As such we have calculated the $L = 0$ and $L = 2$ states in the vicinity of the Feshbach resonance at 361.65 G. These states are shown in Figure 3.13. It is clear that several $L = 2$ states avoided cross with the $L = 0$ bound state (labeled in red in Figure 3.13) that causes the broad $L = 0$ Feshbach resonance at the a+a threshold. It is possible to transfer the $L = 0$ state to one of these $L = 2$ states by approaching the crossing and varying the magnetic field over the crossing sufficiently slowly such that adiabatic passage occurs. In order to aid future experiments we have included the positions of the crossings and the strengths of these crossings in Figure 3.13. The strengths of the crossings, $2\Omega$, are obtained from a fit of the bound-state energies at the crossing position to the eigenvalues of a $2 \times 2$ matrix. $\Omega$ is the effective coupling matrix element and $2\Omega$ is the gap between the levels at the crossing position.

**Recent Insights**

The Nägerl group measured a loss feature in the fraction of $^{39}$K atoms at 463.27 G at the c+a threshold. With the G2017 potential we predicted that a bound state with $L = 2$ would cross the c+a threshold approximately 5 G to the left of the observed loss feature. Neither of our fits improved this discrepancy. The B2024 potential predicted this $L = 2$ resonance to occur at $459.13 \pm 0.29$ G and our fit that included $C_6$ predicted the resonance to occur at $459.10 \pm 0.18$ G. One limitation of our fit of the KCs interaction potential is that we have not included any observables which are sensitive to the energies of $L = 2$ states and their interaction with the $L = 0$ states.

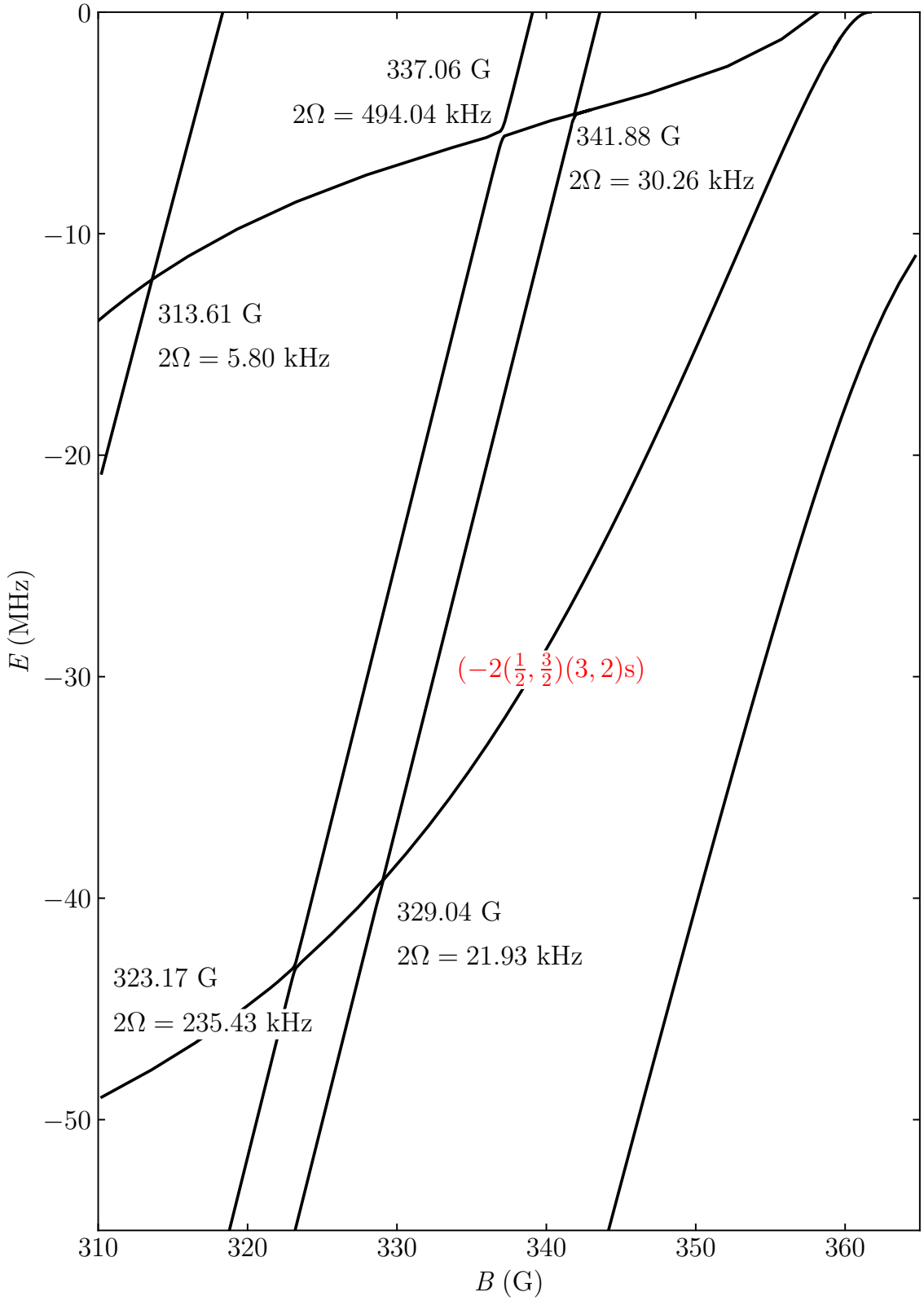


Figure 3.13: $L = 0$ and $L = 2$ bound states calculated in the vicinity of the resonance at the a+a threshold. The positions of avoided crossings between different states are included on the figure as are the strengths of these avoided crossings.

Recently we have had a series of new results from the Nägerl Group who have begun to explore the bound-state spectrum beneath the 361.65 G resonance. These bound states were discussed in the previous section and are shown in Figure 3.13. In Figure 3.13 it is clear that a $L = 2$ state crosses the $L = 0$ state at 329.04 G. The Nägerl Group have measured this crossing at 329.22 G. This suggests the B2024 potential will underestimate the positions of $L = 2$ resonances by approximately 0.2 G. This deficiency may be corrected by reducing the energies of the $L = 2$ bound states by approximately 0.3 MHz. We expect the B2024 potential to be consistent with respect to the error in calculations of the energies of the $L = 2$ states. As such it is unlikely that the observed loss feature at 463.27 G at the c+a threshold is caused by the $L = 2$ bound state we expect to cause a resonance at $459.13 \pm 0.29$ G. It is possible that this loss feature is caused by some element of the experiment and is not due to a Feshbach resonance. Cho et al. found that heating of an ultracold mixture of $^{87}$Rb and $^{133}$Cs occured due to two-photon Raman transitions and depended on the polarization of the lasers used to construct the dipole trap relative to the magnetic field [132].

## 3.4 Conclusions

Ultracold $^{39}$K + $^{133}$Cs collisions have been studied for several years now with a variety of techniques including Fourier-transform spectroscopy [108], Feshbach spectroscopy [133], and theoretical coupled-channel calculations [109, 133]. This work has been motivated by the goal of producing ultracold $^{39}$K$^{133}$Cs molecules in the rovibrational-ground state, and the need to understand these collisions and the underlying interatomic potential. Our work makes a large contribution to achieving these goals as we have been able to develop a more accurate model (B2024) of the KCs potential. With an interactive non-linear least-squares fit to a series of experimental measurements we have determined $a_{\mathrm{s}} = -29.71 \pm 1.6\ a_0$ and $a_{\mathrm{t}} = 77.70 \pm 0.4\ a_0$. Our results show that the difference between the singlet and triplet scattering lengths is larger than previously believed. This will improve theo-

retical predictions of resonance positions and widths and help calculate bound-state energies accurately.

We used coupled-channel calculations and the G2017 potential to study the singlet fractions of the near-threshold bound states that cause broad $L = 0$ Feshbach resonances at the lowest collision thresholds. We found that the states with lower singlet fractions caused resonances at lower values of magnetic field and that these resonances had widths ranging from approximately $6 \times 10^{-3}$ G to $7 \times 10^{-2}$ G. The Nägerl Group carried out a series of Feshbach spectroscopy experiments to determine the positions of these resonances. The Nägerl Group also performed a series of measurements on the bound state beneath the resonance at the a+a threshold. Measurements of bound-state energies are more accurate than measurements of Feshbach resonance positions, and are sensitive to the difference between $a_{\mathrm{s}}$ and $a_{\mathrm{t}}$.

The B2024 potential was developed by varying the short-range regions of the singlet and triplet curves. We used an exponential model of the short-range repulsion between the atoms that was previously investigated by the Hutson Group. We fit $\alpha_{S=0}$ and $\alpha_{S=1}$ to the measurements recently obtained by the Nägerl Group and the resonances measured in 2017 by Gröbner et al. We also attempted a fit of $\alpha_{S=0}$, $\alpha_{S=1}$, and $C_6$ although this potential was unable to resolve any of the issues we identified in the B2024 potential and had several issues. These issues included a value of $\alpha_{S=1}$ that was surprisingly different to $\alpha_{S=0}$, and a $C_6$ value that lay outside the uncertainty reported by Derevianko et al.

We used the B2024 potential in coupled-channel calculations of the $L = 0$ and $L = 2$ bound states in the vicinity of the a+a threshold. This has enabled the Nägerl Group to explore the bound states in the vicinity of the a+a threshold and assess various STIRAP schemes to produce ultracold $^{39}$K$^{133}$Cs molecules in the rovibrational-ground state.

# Chapter 4

# Resonances in collisions of Rb and CaF

This chapter is a reproduction of the following publication: R. C. Bird, M. R. Tarbutt and J. M. Hutson, *Physical Review Research*, 2023, **5**, 023184. J. M. Hutson supervised the theoretical work and M. R. Tarbutt contributed insights into potential experiments.

## 4.1 Introduction

Ultracold molecules have many applications that are now emerging, ranging from quantum simulation [134, 135], quantum computing [136–138] and the study of novel quantum phases [139, 140] to tests of fundamental physics [141–143]. Key to most of these applications are polar molecules, which can have long-range anisotropic interactions resulting from their permanent dipoles. Many such molecules have been produced at microkelvin temperatures by association of pairs of alkali-metal atoms, followed by laser transfer to the vibrational ground state [30–32, 144–150]. Another class of molecules, exemplified by CaF and SrF, have been cooled directly by magneto-optical trapping followed by sub-Doppler laser cooling [151–156].

Elastic and inelastic collisions are at the heart of ultracold physics. For ultracold atoms, it is often possible to control ultracold collisions by adjusting an applied magnetic field close to a zero-energy Feshbach resonance [21]. Such a resonance occurs whenever a molecular bound state can be tuned across a scattering threshold as a function of applied field. The s-wave scattering length then passes through a pole as a function of field, allowing the effective interaction strength to be tuned to any desired value. This control has been applied in many areas of ultracold physics, including condensate collapse [157], soliton creation [158], Efimov physics [159] and investigations of the BCS-BEC crossover in degenerate Fermi gases [8]. Feshbach resonances are also used for magnetoassociation, in which pairs of ultracold atoms are converted to weakly bound diatomic molecules by sweeping a magnetic field across the resonance [160, 161].

Much new physics will become accessible when atom-molecule collisions can be controlled with tunable Feshbach resonances. Control of the s-wave scattering length

may allow sympathetic cooling of molecules to quantum degeneracy, and the formation of atom-molecule mixtures with novel properties. It may also be possible to form polyatomic molecules by magnetoassociation. Feshbach resonances have now been observed in collisions between ultracold $^{40}$K atoms and $^{23}$Na$^{40}$K molecules in singlet states [150, 162–165] and between $^{23}$Na atoms and $^{6}$Li$^{23}$Na molecules in triplet states [166]. These systems have also been investigated theoretically [162, 166–168]. Resonances have not yet been observed in collisions of laser-cooled molecules such as CaF and SrF, with $^2\Sigma$ ground states, but we have recently succeeded in making ultracold mixtures of CaF molecules and Rb atoms, and studied their inelastic collisions in both magnetic traps [169] and magneto-optical traps [170]. Several laser-coolable molecules have been cooled to 5 $\mu$K [154, 155] and confined in optical traps [153] and optical tweezers [171], opening the way to experiments in controlled magnetic fields.

The purpose of the present paper is to investigate the resonances that are expected in collisions between molecules in $^2\Sigma$ states and alkali-metal atoms. These systems have strong similarities to pairs of alkali-metal atoms, particularly for the long-range states that are most likely to cause magnetically tunable Feshbach resonances. We show that there is a high probability that tunable Feshbach resonances will exist at magnetic fields below 1000 G, and that they will be broad enough to control collisions and form triatomic molecules by magnetoassociation. There are additional complications and additional resonances that arise from the rotational structure of the molecule and the anisotropy of the interaction potential, but we find that these are unlikely to affect the general features of the scattering. We focus on $^{87}$Rb+$^{40}$Ca$^{19}$F as a prototype system, but many of the features are transferable to other molecules such as SrF and other alkali-metal atoms. In the following we mostly omit isotopic masses and write Rb+CaF for $^{87}$Rb+$^{40}$Ca$^{19}$F.

The structure of this chapter is as follows. Section 4.2 describes the underlying theory, including monomer Hamiltonians, interaction potentials, and computational methods. Section 4.3.1 describes the near-threshold levels that can exist for Rb+CaF

and the Feshbach resonances they can cause, using a simple model that omits rotational degrees of freedom. Section 4.4 considers the effects of CaF rotation and potential anisotropy. Section 4.5 considers the possible effects of quantum chaos at short range. Section 4.6 presents conclusions and offers perspectives for future work to take advantage of the resonances.

## 4.2 Theory

### 4.2.1 Monomer Hamiltonians and Levels

The Hamiltonian of an alkali-metal atom A in its ground $^2$S state is

$$\hat{h}_{\mathrm{A}} = \zeta_{\mathrm{A}} \hat{\boldsymbol{i}}_{\mathrm{A}} \cdot \hat{\boldsymbol{s}}_{\mathrm{A}} + \left( g_{s,\mathrm{A}} \hat{s}_{\mathrm{A},z} + g_i \hat{i}_{\mathrm{A},z} \right) \mu_{\mathrm{B}} B, \tag{4.1}$$

where $\hat{\boldsymbol{s}}_{\mathrm{A}}$ and $\hat{\boldsymbol{i}}_{\mathrm{A}}$ are vector operators for the electron and nuclear spin, $\hat{s}_{\mathrm{A},z}$ and $\hat{i}_{\mathrm{A},z}$ are their components along the $z$ axis defined by the magnetic field $B$, $\zeta_{\mathrm{A}}$ is the hyperfine coupling constant, and $g_{s,\mathrm{A}}$ and $g_{i,\mathrm{A}}$ are the g-factors for the electron and nuclear spins [1]. The nuclear spins vary from 1 for $^6$Li to 9/2 for $^{40}$K, and the hyperfine splittings $A_{\mathrm{hfs}} = \zeta_{\mathrm{A}}(i_{\mathrm{A}} + \frac{1}{2})/h$ vary from 228 MHz for $^6$Li to 9.19 GHz for $^{133}$Cs. We focus here on $^{87}$Rb, $i = 3/2$ and $A_{\mathrm{hfs}} \approx 6.83$ GHz. At zero field the levels are labeled by total angular momentum $f_{\mathrm{Rb}} = 1$ and 2. When a field is applied, each level splits into $2f_{\mathrm{Rb}} + 1$ sublevels, color-coded in Fig. 4.1 according to the projection $m_{f,\mathrm{Rb}}$. At sufficiently high field, pairs of levels with $f_{\mathrm{Rb}} = 1$ and 2 but the same value of $m_{f,\mathrm{Rb}}$ mix sufficiently that the levels are better described by $m_{s,\mathrm{Rb}}$ and $m_{i,\mathrm{Rb}}$ than by $f_{\mathrm{Rb}}$. For $^{87}$Rb this transition is still incomplete at 2000 G, but it occurs at much lower fields for alkali-metal atoms with small hyperfine splittings, such as Li and Na.

The CaF or SrF molecule may be treated at different levels of complexity. The

[1] In writing basis sets for pairs of atoms, it is necessary to distinguish between quantum numbers for the individual atoms and those for the pair. We adopt the widely used convention of using lower-case letters for the individual atoms and upper-case letters for the pair.

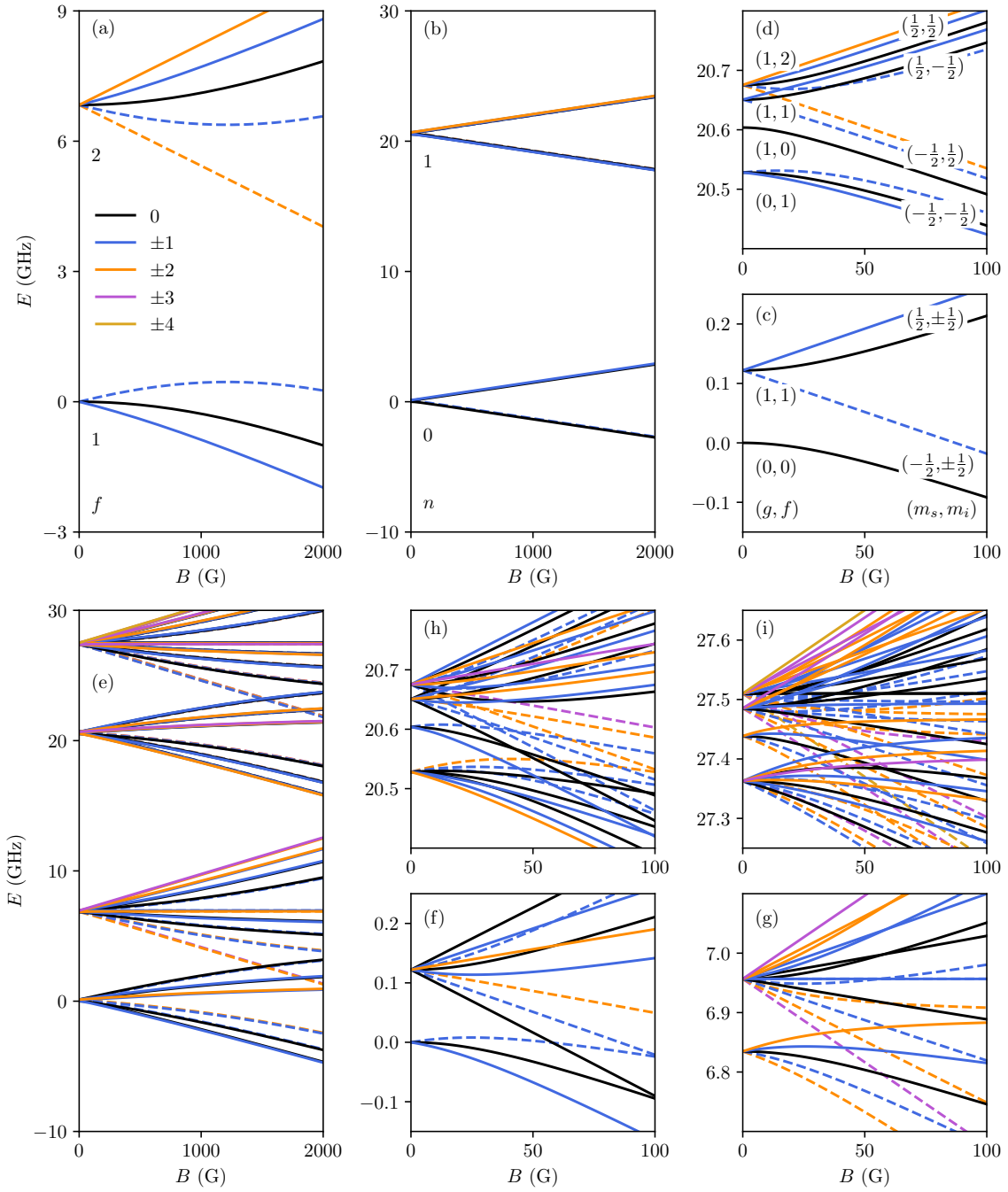


Figure 4.1: Energies as a function of magnetic field for (a) $^{87}$Rb atom in ground $^2$S state; (b) Lowest two rotational levels of CaF, with expanded views of $n = 0$ and 1 in (c) and (d), respectively; (e) Scattering thresholds of $^{87}$Rb+CaF, with expanded views of $(f_{\mathrm{Rb}}, n) = (1, 0)$, (2,0), (1,1) and (2,1) in (f) and (g), (h) and (i), respectively. All level energies are shown relative to the ground state at zero field and are color-coded as shown in the legend according to $m_{f,\mathrm{Rb}}$, $m_{f,\mathrm{CaF}}$ or $M_F = m_{f,\mathrm{Rb}} + m_{f,\mathrm{CaF}}$, as appropriate; negative values are indicated by dashed lines.

stable isotopes $^{40}$Ca, $^{88}$Sr, $^{86}$Sr and $^{84}$Sr all have zero nuclear spin, while $^{87}$Sr has $i = 9/2$; only the spin-zero isotopes will be considered here. The simplest useful approximation is to neglect the molecular rotation, and in this case the molecular Hamiltonian $\hat{h}^{n=0}_{\mathrm{CaF}}$ is the same as Eq. 4.1, with $i_{\mathrm{F}} = 1/2$ for $^{19}$F in CaF. However, when rotation is included, several extra rotation-fine-hyperfine (rfhf) terms are needed. The ones important here are

$$\hat{h}^{\mathrm{rfhf}}_{\mathrm{CaF}} = b_0 \hat{\boldsymbol{n}}^2 + \gamma \hat{\boldsymbol{s}}_{\mathrm{CaF}} \cdot \hat{\boldsymbol{n}} + t\sqrt{6} T^2(C) \cdot T^2(\hat{\boldsymbol{i}}_{\mathrm{F}}, \hat{\boldsymbol{s}}_{\mathrm{CaF}}), \tag{4.2}$$

where $\hat{\boldsymbol{n}}$ is the vector operator for the molecular rotation. The first term represents the rotational energy of a molecule in its vibrational ground state, treated as a rigid rotor. The second term represents the electron spin-rotation interaction, and the third accounts for the anisotropic interaction between electron and nuclear spins: $T^2(\hat{\boldsymbol{i}}, \hat{\boldsymbol{s}})$ is the rank-2 spherical tensor formed from $\hat{\boldsymbol{i}}$ and $\hat{\boldsymbol{s}}$, and $T^2(C)$ is a spherical tensor whose components are the Racah-normalized spherical harmonics $C^2_q(\theta, \phi)$ involving the orientation of the molecular axis. Values of $b_0/h \approx 10.3$ GHz, $\gamma/h \approx 40$ MHz, $\zeta_{\mathrm{F}}/h \approx 120$ MHz and $t/h \approx 14$ MHz are taken from ref. [172] [2]. A more complete version of Eq. 4.2, including additional contributions of the order of kHz that are unimportant here, has been given in ref. [174].

The full Hamiltonian for CaF is $\hat{h}_{\mathrm{CaF}} = \hat{h}^{n=0}_{\mathrm{CaF}} + \hat{h}^{\mathrm{rfhf}}_{\mathrm{CaF}}$. The resulting level diagram is shown as a function of magnetic field in Fig. 4.1(b), with expanded views for $n = 0$ and 1 in Figs. 4.1(c) and (d). There are only very small matrix elements that are off-diagonal in $n$, so the levels for $n = 0$ are very similar to those of an alkali-metal atom with $i_{\mathrm{F}} = 1/2$. The hyperfine splitting is small, so $i_{\mathrm{F}}$ and $s_{\mathrm{CaF}}$ are mostly decoupled by 50 G. At higher field, the states are well described by $m_{s,\mathrm{CaF}}$ and $m_{i,\mathrm{F}}$.

In a rotating molecule at low field, $i_{\mathrm{F}}$ and $s_{\mathrm{CaF}} = 1/2$ couple to give a resultant $g = 0$ or 1, and $g$ couples to the rotational angular momentum $n$ to produce the

[2] Ref. [172] uses the notation of Frosch and Foley [173], where our $b_0$, $\gamma$, $\zeta_{\mathrm{F}}$ and $t$ are $B$, $\gamma$, $b + c/3$ and $c/3$, respectively.

total molecular angular momentum $f_{\mathrm{CaF}}$. For $n = 1$, there are zero-field levels with $f_{\mathrm{CaF}} = 0$, 1, 1, 2, as labeled on Fig. 4.1(d). The lower level with $f = 1$ is predominantly $g = 0$ and the remaining three are predominantly $g = 1$. In a magnetic field, however, $i_{\mathrm{F}}$, $s_{\mathrm{CaF}}$ and $n$ are again mostly decoupled by 50 G; at higher fields, the states are better described by $m_{s,\mathrm{CaF}}$, $m_{i,\mathrm{F}}$ and $m_n$ than by $g$ and $f_{\mathrm{CaF}}$. States of different $m_{s,\mathrm{CaF}}$ are well separated; within the group for a particular value of $m_{s,\mathrm{CaF}}$, there are 2 subgroups with $m_{i,\mathrm{F}} = \pm\frac{1}{2}$, with splitting about $\zeta/2 = 60$ MHz, and each subgroup is further divided into states with different $m_n$, with adjacent states separated by about $\gamma/2 = 20$ MHz. The projection quantum numbers are not fully conserved, but these qualitative arguments help to understand the general patterns at high field.

### 4.2.2 Calculations of Bound States and Scattering

The Hamiltonian for an alkali-metal atom interacting with a CaF molecule is

$$\hat{H} = \frac{\hbar^2}{2\mu}\left(-R^{-1}\frac{d^2}{dR^2}R + \frac{\hat{\boldsymbol{L}}^2}{R^2}\right) + \hat{h}_{\mathrm{A}} + \hat{h}_{\mathrm{CaF}} + \hat{V}_{\mathrm{int}}, \tag{4.3}$$

where $R$ is the intermolecular distance, $\mu$ is the reduced mass, $\hat{\boldsymbol{L}}^2$ is the operator for relative rotation of the pair and $\hat{V}_{\mathrm{int}}$ is the interaction operator described below. We carry out calculations of both bound states and scattering using coupled-channel methods [19, 21, 175]. The total wavefunction is expanded as

$$\Psi(R,\xi) = R^{-1}\sum_j \Phi_j(\xi)\psi_j(R). \tag{4.4}$$

Here $\{\Phi_j(\xi)\}$ is a set of basis functions that span all coordinates except $R$, including the relative rotation; these coordinates are collectively designated $\xi$. In the coupled-channel calculations described in Sec. 4.3.1, $\xi$ includes only electron and nuclear spins. However, in more complete treatments, it may also include basis functions for overall rotation of the collision complex and rotation and vibration of CaF.

Substituting the expansion (4.4) into the total Schrödinger equation produces a set of coupled differential equations that are solved by propagation with respect to the internuclear distance $R$. The coupled equations are identical for bound states and scattering, but the boundary conditions are different.

Scattering calculations are performed with the MOLSCAT package [85, 176]. Such calculations produce the scattering matrix $\boldsymbol{S}$, for a single value of the collision energy and magnetic field each time. The complex s-wave scattering length $a(k_0)$ is obtained from the diagonal element of $\boldsymbol{S}$ in the incoming channel, $S_{00}$,

$$a(k_0) = \frac{1}{ik_0}\left(\frac{1 - S_{00}(k_0)}{1 + S_{00}(k_0)}\right), \tag{4.5}$$

where $k_0$ is the incoming wavenumber, related to the collision energy $E_{\mathrm{coll}}$ by $E_{\mathrm{coll}} = \hbar^2 k_0^2/(2\mu)$. The scattering length $a(k_0)$ becomes constant at sufficiently low $E_{\mathrm{coll}}$, with limiting value $a$. In the present work, s-wave scattering lengths are calculated at $E_{\mathrm{coll}}/k_{\mathrm{B}} = 10$ nK, which is low enough to neglect the dependence on $k_0$.

A zero-energy Feshbach resonance occurs where a bound state of the atom-molecule pair (triatomic molecule) crosses a scattering threshold as a function of applied field. At the lowest threshold, or in the absence of inelastic processes, the scattering length is real. Near a resonance, $a(B)$ passes through a pole, and is approximately

$$a(B) = a_{\mathrm{bg}}\left(1 - \frac{\Delta}{B - B_{\mathrm{res}}}\right), \tag{4.6}$$

where $B_{\mathrm{res}}$ is the position of the resonance, $\Delta$ is its width, and $a_{\mathrm{bg}}$ is a slowly varying background scattering length. In the presence of inelastic processes, $a(B)$ is complex and the pole is replaced by an oscillation [177]. MOLSCAT can converge on Feshbach resonances automatically and characterize them to obtain $B_{\mathrm{res}}$, $\Delta$ and $a_{\mathrm{bg}}$ (and the additional parameters needed in the presence of inelasticity) as described in ref. [107].

Coupled-channel bound-state calculations are performed using the packages BOUND and FIELD [84, 178], which converge upon bound-state energies at fixed field, or

bound-state fields at fixed energy, respectively. The methods used are described in ref. [17].

In the present work, the coupled equations for both scattering and bound-state calculations are solved using the fixed-step symplectic log-derivative propagator of Manolopoulos and Gray [179] from $R_{\mathrm{min}} = 3\ a_0$ to $R_{\mathrm{mid}} = 15\ a_0$, with an interval size of 0.001 $a_0$, and the variable-step Airy propagator of Alexander and Manolopoulos [118] between $R_{\mathrm{mid}}$ and $R_{\mathrm{max}}$, where $R_{\mathrm{max}} = 300\ a_0$ for BOUND and FIELD and $3,000\ a_0$ for MOLSCAT.

### 4.2.3 The Interaction Operator

Rb($^2$S) and CaF($^2\Sigma$) interact to give two electronic surfaces of $^1\mathrm{A}'$ and $^3\mathrm{A}'$ symmetry. These are to some extent analogous to the singlet and triplet curves of alkali-metal dimers: the singlet surface is expected to be deep, and the triplet surface much shallower. The surfaces have not been characterized in any detail, either experimentally or theoretically, but both of them are expected to be strongly anisotropic at short range. We designate them $V^S(R,\theta)$, with $S = 0$ for the singlet and $S = 1$ for the triplet. Here $\theta$ is the angle between the CaF bond and the intermolecular axis in Jacobi coordinates. The interaction operator is

$$\hat{V}_{\mathrm{int}} = V^0(R,\theta)\hat{\mathcal{P}}^0 + V^1(R,\theta)\hat{\mathcal{P}}^1 + \hat{V}^{\mathrm{d}}, \tag{4.7}$$

where $\hat{\mathcal{P}}^0$ and $\hat{\mathcal{P}}^1$ are projection operators onto the singlet and triplet spin spaces, respectively, and $\hat{V}^{\mathrm{d}}$ is a small electron spin-spin term described below.

The Feshbach resonances of interest here depend mostly on the properties of near-threshold states. These are bound by amounts comparable to the hyperfine and Zeeman splittings of Rb and CaF and (to a lesser extent) the low-lying rotational states of CaF. The most important states are those with binding energies less than about 30 GHz below their respective thresholds; this is considerably less than 0.1% of the expected singlet well depth. The binding energies of these states are dependent

mostly on long-range dispersion and induction forces, which are the same for the singlet and triplet surfaces. The leading term is of the form

$$V^S(R,\theta) = \left[-C_6^{(0)} - C_6^{(2)} P_2(\cos\theta)\right] R^{-6}, \tag{4.8}$$

with $C_6^{(0)} \approx 3084\ E_\mathrm{h} a_0^6$ [180]. For $C_6^{(2)}$ there is substantial cancelation between the dispersion and induction contributions; we estimate $C_6^{(2)} \approx 100(20)\ E_\mathrm{h} a_0^6$. For Rb+CaF, the outer turning point at a binding energy of 30 GHz is near 30 $a_0$.

Potential terms that are the same for the singlet and triplet surfaces cannot cause couplings between orthogonal spin states. They are therefore unlikely to cause magnetically tunable Feshbach resonances. The most important interactions that mix different spin states are spin-exchange interactions, due to the difference between the singlet and triplet surfaces. Julienne *et al.* [20] have shown that, for a pair of atoms, spin-exchange interactions can cause nonadiabatic transitions between coupled channels at distances $R_\mathrm{X}$ where the interaction approximately matches the asymptotic energy difference between the channels concerned. For $^{87}$Rb this occurs around 22 $a_0$ [20]. The strength of the interaction is modulated by overall phases due to the short-range parts of the potentials for the channels concerned, and (if the long-range potentials are identical from $R_\mathrm{X}$ to $\infty$) is smallest when the two channels have the same scattering length.

There is also a spin-spin term $\hat{V}^\mathrm{d}$ in the interaction operator that results from magnetic dipole-dipole interactions between the electron spins on Rb and CaF, supplemented at short range by second-order spin-orbit terms that have the same overall dependence on spin coordinates. This term is important for heavy alkali-metal atoms such as Cs [181], and may cause additional weak resonances in Rb+CaF as discussed below, but its effect is not considered in detail in the present work.

### 4.2.4 Thresholds

Figure 4.1(e) shows the scattering thresholds for $^{87}$Rb+CaF, which are simply sums of energies of Rb and CaF. Figures (f) to (i) show expanded views of each group. The thresholds are color-coded according to $M_F = m_{f,\mathrm{Rb}} + m_{f,\mathrm{CaF}}$, because this quantity is conserved in collisions if anisotropic terms in $V_{\mathrm{int}}$ are neglected.

The importance of the thresholds lies in the fact that near-threshold levels lie approximately parallel to them, within well-defined energy intervals known as bins. These bins were introduced in Section 2. This concept will be used extensively in discussing the patterns of near-threshold levels and the resulting resonances in the following sections.

### 4.2.5 Near-threshold Levels

Each scattering threshold $j$ supports a series of levels of the collision complex that have binding energies $E^{\mathrm{b}}_{j\eta}(B)$ below the threshold concerned. Here $\eta$ is a vibrational quantum number, defined so that the least-bound rotationless state below each threshold is labelled $\eta = -1$ and successively deeper levels are labeled $-2$, $-3$, etc. To a first approximation, the near-threshold levels retain the character of the threshold that supports them. Because of this, each level lies approximately parallel to the threshold that supports it and may be described in a single-channel approximation. There are nevertheless interactions between levels supported by different channels $j$, which cause $B$-dependent shifts and avoided crossings between levels. These interactions, and the strengths of the resulting avoided crossings, generally become larger as $|\eta|$ increases; these will be discussed below.

For a single-channel system with an asymptotic potential $-C_6R^{-6}$, the least-bound s-wave state (with $L = 0$ and $\eta = -1$) lies within $\sim 36\bar{E}$ of threshold, where $\bar{E} = \hbar^2/(2\mu\bar{a}^2)$ and $\bar{a}$ is the mean scattering length of Gribakin and Flambaum [102], $\bar{a} = (2\mu C_6/\hbar^2)^{1/4} \times 0.4779888\ldots$. We refer to this energy interval as the top bin. The position of the bound state within this bin depends on the background scattering length $a_{\mathrm{bg}}$ for the channel concerned, neglecting resonances (which themselves arise

from couplings between channels). Each subsequent level ($\eta = -2$, $-3$, etc.) lies within its own bin, with successive bins becoming wider and bin boundaries at energies roughly proportional to $(|\eta| + \frac{1}{8})^3$ [103, 182]. For Rb+CaF, $\bar{a} = 67.3\ a_0$, $\bar{E}/h = 11.4$ MHz, and the first 5 bin boundaries are at about 410, 2900, 9100, 21000 and 40000 MHz. These values may be shifted by the influence of terms beyond $-C_6R^{-6}$. In general, the levels lie near the top of their bins when $a_{\rm bg} \gg \bar{a}$ and towards the bottom of the bins for $a_{\rm bg} \ll \bar{a}$.

## 4.3 Bound States and Resonances in the Absence of Anisotropy

### 4.3.1 Bound States Below the Lowest Threshold

The coupling between CaF rotational levels is fairly small at long range. It is driven mostly by the anisotropic part of the long-range interaction potential, characterized by $C_6^{(2)}$. The effects of the anisotropy will be considered in Section 4.4. In this section we will consider a simpler model, with the anisotropy neglected. This is expected to be a reasonably good approximation for collisions involving CaF ($n = 0$), though it will neglect some additional resonances considered later.

If anisotropy is neglected, the scattering is largely controlled by the isotropic dispersion coefficient $C_6^{(0)}$ and by scattering lengths $a_{\rm s}$ and $a_{\rm t}$ that characterize overall phases due to the short-range parts of the singlet and triplet potentials. These scattering lengths are completely unknown for Rb+CaF, so we explore the pattern of near-threshold bound states, and the resulting Feshbach resonances, for a representative sample of values of them.

Scattering lengths take values from $-\infty$ to $+\infty$, but some values are more likely than others [102]. The most likely value is the mean scattering length $\bar{a}$ defined above, and for a randomly chosen potential curve that decays as $-C_6R^{-6}$ at long range there is a 50% probability of a scattering length between 0 and $2\bar{a}$. To a

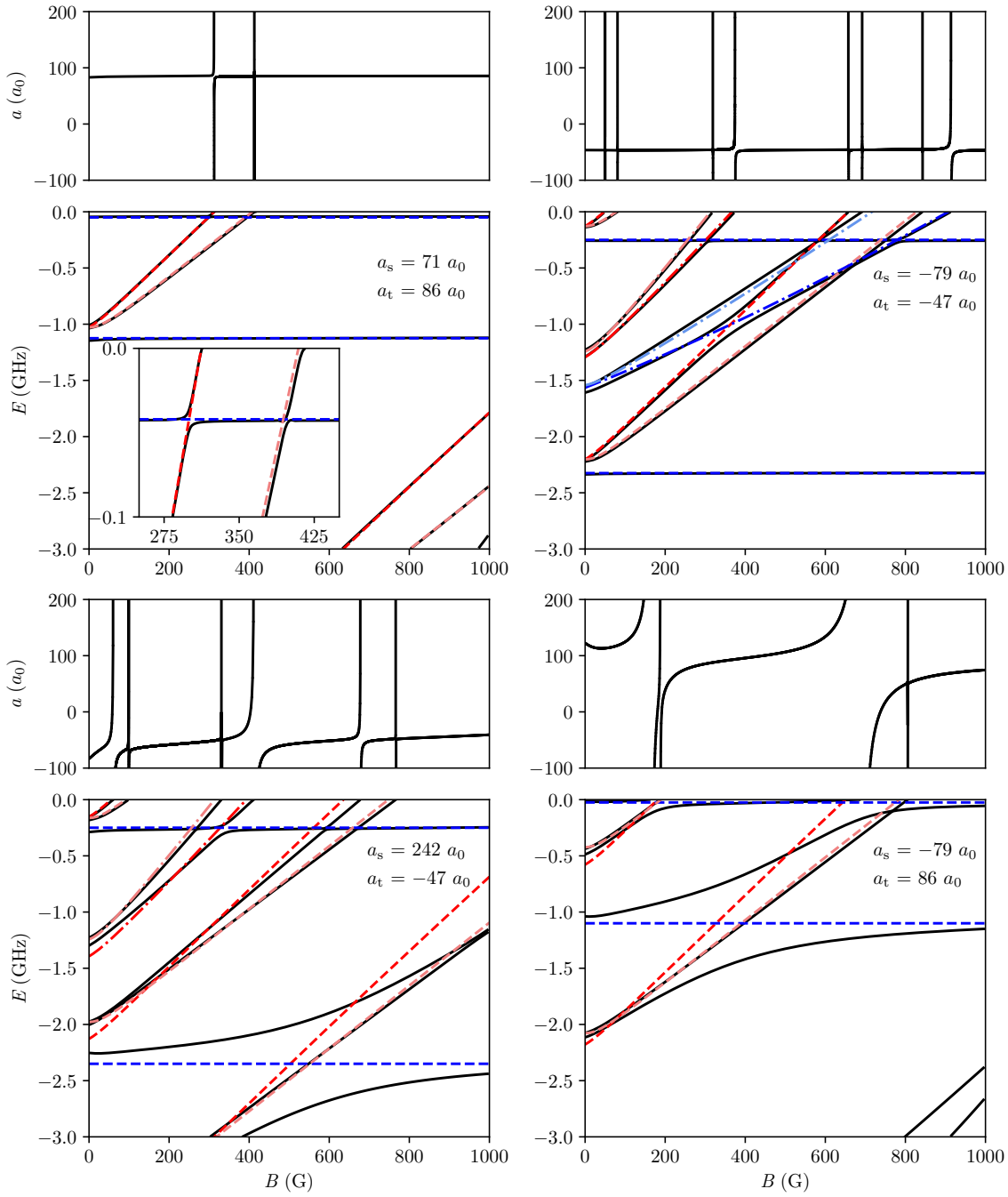


Figure 4.2: Near-threshold levels of Rb+CaF with $M_F = 1$, neglecting anisotropy, shown relative to the energy of the lowest threshold, for four representative combinations of the singlet and triplet scattering lengths. Solid black lines show results from coupled-channel calculations. Dashed (dot-dashed) lines show uncoupled states parallel to thresholds with $f_{\mathrm{Rb}} = 1$ (2). Values of $m_{s,\mathrm{CaF}}$ are encoded with red (blue) for $\frac{1}{2}$ $(-\frac{1}{2})$, with darker (lighter) colors for $m_{i,\mathrm{F}} = \frac{1}{2}$ $(-\frac{1}{2})$. $m_{f,\mathrm{Rb}}$ is given by $M_F - m_{s,\mathrm{CaF}} - m_{i,\mathrm{F}}$. Above each plot of energies is the corresponding plot of scattering length, with Feshbach resonances where states cross threshold.

good approximation, different interaction potentials that produce the same $a_s$ and $a_t$, and have the same value of $C_6$, have the same low-energy scattering properties and near-threshold bound states.

We use singlet and triplet potential curves based on those for Cs [181], but with the value of $C_6$ replaced with $C_6^{(0)}$ for Rb+CaF. These potentials are then adjusted at short range to give the desired scattering length as described in ref. [181]. As an initial sample, we pick 3 values $a_s = -79$, 71 and 242 $a_0$ and $a_t = -47$, 86 and 297 $a_0$. These are purposely not exact multiples of $\bar{a}$, because such values can produce shape resonances at atypically low energy, and are slightly different for $a_s$ and $a_t$, because $a_s = a_t$ is a special case that produces unusually weak interchannel couplings [20]. We consider all 9 combinations of these values of $a_s$ and $a_t$.

The solid lines in Figure 4.2 shows the near-threshold energy levels for 4 combinations of $a_s$ and $a_t$, obtained from coupled-channel calculations using the package BOUND. In this case we use a basis set of fully uncoupled functions [98], including only rotationless functions, $n = 0$ and $L = 0$. All energies are shown with respect to the (field-dependent) energy of the lowest threshold, which has approximate quantum numbers $(f_{\mathrm{Rb}}, m_{f,\mathrm{Rb}}, m_{s,\mathrm{CaF}}, m_{i,\mathrm{F}}) = (1, 1, -\frac{1}{2}, \frac{1}{2})$ at fields above 50 G. All states shown have $M_F = 1$, which is the same as the lowest threshold, because spin-exchange interactions cannot change $M_F$. Also shown are dashed and dot-dashed lines, parallel to thresholds but offset from them: these represent hypothetical states that would exist in the absence of interchannel couplings; the real states may be interpreted in terms of these, but with shifts and avoided crossings of various strengths due to the couplings.

The simplest case is that in Fig. 4.2 for which $a_s = 71$ $a_0$ and $a_t = 86$ $a_0$. Here the real states lie close to the uncoupled ones, with only small shifts and weak avoided crossings. $a_s$ and $a_t$ are close to one another, so the interchannel coupling is weak, and they are comparable to $\bar{a}$, so each state lies fairly high in its bin. The near-horizontal states are those supported by the lowest threshold in the first and second bins. There is also a pair of states that originate near $-1.0$ GHz at

zero field; the thresholds that support these have approximate quantum numbers $(1, 0, \frac{1}{2}, \frac{1}{2})$ (upper) and $(1, 1, \frac{1}{2}, -\frac{1}{2})$ (lower). In first order the spin-exchange coupling can change $f_{\mathrm{Rb}}$, $m_{f,\mathrm{Rb}}$ and $m_{s,\mathrm{CaF}}$ by $\pm 1$ while conserving $m_{f,\mathrm{Rb}} + m_{s,\mathrm{CaF}}$, but cannot change $m_{i,\mathrm{F}}$. There is therefore a much wider avoided crossing between the near-threshold horizontal state and the upper state of the sloping pair, which is predominantly $m_{i,\mathrm{F}} = \frac{1}{2}$, than with the lower one, which is predominantly $m_{i,\mathrm{F}} = -\frac{1}{2}$.

A case with somewhat stronger coupling is shown in Fig. 4.2(b), for $a_{\mathrm{s}} = -79\ a_0$ and $a_{\mathrm{t}} = -47\ a_0$. Here $a_{\mathrm{s}}$ and $a_{\mathrm{t}}$ are negative, so the states lie much deeper in their bins than in (a). The real states still lie close to the uncoupled ones, but there is a strong avoided crossing between the states shown as red dashed and blue dot-dashed lines. States approximately parallel to the thresholds with $f_{\mathrm{Rb}} = 1$ can again be identified, with the states in the second bin now originating from around $-2.3$ GHz at zero field. These are echoed by similar states in the top bin. However, there are two further pairs of states; these are supported by thresholds with $f_{\mathrm{Rb}} = 2$, and lie in the third bin beneath their thresholds. The pair originating near $-1.6$ GHz have approximate quantum numbers $(2, 1, -\frac{1}{2}, \frac{1}{2})$ (lower, involving ground-state CaF but excited Rb) and $(2, 2, -\frac{1}{2}, -\frac{1}{2})$ (upper), while the pair originating near $-1.2$ GHz have $(2, 0, \frac{1}{2}, \frac{1}{2})$ (lower) and $(2, 1, \frac{1}{2}, -\frac{1}{2})$ (upper). Once again the strong avoided crossings are those between states with the same values of $m_{i,\mathrm{F}}$.

Figs. 4.2(c) and (d) show further examples for cases with much stronger coupling, with $a_{\mathrm{s}}$ and $a_{\mathrm{t}}$ substantially different. For these cases the identification of the dashed and dotted lines is less certain, because real states are substantially shifted from the uncoupled states by interchannel couplings. Plausible assignments are shown with the same coding as in (a) and (b).

Additional bound states exist with $M_F \neq 1$. These are not connected to the lowest incoming threshold by spin-exchange coupling. However, there are additional small couplings due to the spin-spin interaction $\hat{V}^{\mathrm{d}}$. This has matrix elements off-diagonal in $f_{\mathrm{Rb}}$, $m_{f,\mathrm{Rb}}$ and $m_{s,\mathrm{CaF}}$ by $\pm 1$, but can change $m_{f,\mathrm{Rb}} + m_{s,\mathrm{CaF}}$ by up to $\pm 2$,

with $M_L$ changing by up to $\mp 2$ to conserve $M_{\rm tot} = M_F + M_L$. Rotationally excited states with $L = 2$ and $M_F$ from $-1$ to 3 can therefore cause additional resonances at the lowest threshold. These are expected to be narrow, and are not included in the present calculations because there is no information available on the strength of second-order spin-orbit coupling for Rb+CaF. States with other values of $L$ and $M_F$ might in principle cause resonances, but with higher-order coupling via $\hat{V}^{\rm d}$, so the resonances will be even narrower.

### 4.3.2 Resonances

Each bound state with $M_F = 1$ causes a magnetically tunable Feshbach resonance where it crosses threshold as a function of $B$. For all the cases considered, several such resonances exist at fields below 1000 G. However, their widths vary greatly. Figure 4.2 includes a panel above each energy-level plot that shows the variation of scattering length with magnetic field. In addition, we have characterized the resonances to extract $B_{\rm res}$, $\Delta$ and $a_{\rm bg}$ for all resonances below 1000 G for all 9 of our representative combinations of $a_{\rm s}$ and $a_{\rm t}$, using the method of ref. [107], and the results are given in Table 4.1.

The resonance widths may be rationalized using the same arguments about interchannel couplings used to interpret the strength of avoided crossings in Section 4.3.1. First, the resonances are generally broadest in cases where $a_{\rm s}$ and $a_{\rm t}$ are substantially different, providing strong spin-exchange coupling. Secondly, for any given combination of $a_{\rm s}$ and $a_{\rm t}$, the strongest resonances are those where the bound state causing the resonance has a substantial component with the same value of $m_{i,\rm F}$ as the incoming channel, which for the lowest threshold is dominated by $m_{i,\rm F} = \frac{1}{2}$ at fields above 50 G. The specific uncoupled states that cause the widest resonances are $(1, 0, \frac{1}{2}, \frac{1}{2})$ $(2, 1, -\frac{1}{2}, \frac{1}{2})$ and $(2, 0, \frac{1}{2}, \frac{1}{2})$, though in some cases their character is spread across more than one real state.

It is noteworthy that, even when $a_{\rm s} \approx a_{\rm t}$ and spin-exchange coupling is weak, there are resonances that are wide enough to use to control collisions or form tri-

atomic molecules by magnetoassociation.

## 4.4 The Role of CaF Rotation

There can also be resonances due to states supported by rotationally excited thresholds. This section will consider the structure of such states and the likelihood that they produce resonances at experimentally accessible fields.

The thresholds for CaF ($n = 1$) are from 20 to 30 GHz above the lowest threshold, so states that can cause Feshbach resonances must be bound by about this amount. The outer turning point at this depth is at around $R = 30\ a_0$. The potential anisotropy at this distance, due to dispersion and induction, is around 1 GHz. This is substantially less than the CaF rotational spacing, so will cause only weak mixing between different CaF rotational states at this distance. However, it is substantially larger than the rotational constant of the triatomic complex, $B = \hbar^2/(2\mu R^2)$, which is about 60 MHz at this distance. It is also larger than the spin-rotation coupling constant, $\gamma \approx 40$ MHz. The long-range anisotropy is thus sufficient to quantize $n$ along the intermolecular axis, with projection $K$, instead of along the axis of the field. This is exactly analogous to the situation for Van der Waals complexes in coupling case 2 [183].

For each CaF rotational level $(n, K)$ there will be a set of spin states, labeled at fields above 50 G by $(f_{\mathrm{Rb}}, m_{f,\mathrm{Rb}}, m_{s,\mathrm{CaF}}, m_{i,\mathrm{F}})$. Each such set $(n, K)$ will sample the short-range singlet and triplet potentials over a different range of Jacobi angles $\theta$, so each group will be characterized by different singlet and triplet scattering lengths $a_{\mathrm{s}}(n, K)$ and $a_{\mathrm{t}}(n, K)$. These will probably be unrelated to the corresponding quantities for the channels with $n = 0$, $a_{\mathrm{s}}(0, 0)$ and $a_{\mathrm{t}}(0, 0)$ (designated simply $a_{\mathrm{s}}$ and $a_{\mathrm{t}}$ in Sec. 4.3.1). For a particular interaction potential, the sets of spin states for $n > 0$ may therefore lie at quite different depths within their bins from those for $n = 0$. The patterns of levels will nevertheless be characterized by $a_{\mathrm{s}}(n, K)$ and $a_{\mathrm{t}}(n, K)$ and by quantum numbers $(f_{\mathrm{Rb}}, m_{f,\mathrm{Rb}}, m_{s,\mathrm{CaF}}, m_{i,\mathrm{F}})$, in a similar way to those for the states with $n = 0$ described above.

Table 4.1: Feshbach resonance positions, widths and background scattering lengths for different combinations of $a_s$ and $a_t$. The approximate quantum numbers of the uncoupled state that causes the resonance are given in each case. Asterisks indicate cases where this uncoupled state is substantially mixed with the least-bound state in the incoming channel where it crosses threshold.

| $a_s$ ($a_0$) | $a_t$ ($a_0$) | $B_{res}$ (G) | $\Delta$ (G) | $a_{bg}$ ($a_0$) | $f_{Rb}$ | $m_{f,Rb}$ | $m_{s,CaF}$ | $m_{i,F}$ | $\eta$ | |
|---|---|---|---|---|---|---|---|---|---|---|
| −79 | −47 | 50 | $-6.8\times10^{-4}$ | −47 | 1 | 0 | $\frac{1}{2}$ | $\frac{1}{2}$ | −1 | |
| | | 81 | $-2.3\times10^{-4}$ | −47 | 1 | 1 | $\frac{1}{2}$ | $-\frac{1}{2}$ | −1 | |
| | | 319 | $-8.2\times10^{-3}$ | −46 | 2 | 1 | $\frac{1}{2}$ | $-\frac{1}{2}$ | −3 | |
| | | 375 | $-4.8\times10^{-1}$ | −46 | 2 | 0 | $\frac{1}{2}$ | $\frac{1}{2}$ | −3 | |
| | | 658 | $-1.7\times10^{-2}$ | −46 | 1 | 0 | $\frac{1}{2}$ | $\frac{1}{2}$ | −2 | |
| | | 692 | $-1.0\times10^{-2}$ | −46 | 2 | 2 | $-\frac{1}{2}$ | $-\frac{1}{2}$ | −3 | |
| | | 843 | $-8.6\times10^{-4}$ | −45 | 1 | 1 | $\frac{1}{2}$ | $-\frac{1}{2}$ | −2 | |
| | | 914 | −1.1 | −46 | 2 | 1 | $-\frac{1}{2}$ | $\frac{1}{2}$ | −3 | |
| −79 | 86 | 164 | 16 | 112 | 1 | 0 | $\frac{1}{2}$ | $\frac{1}{2}$ | −2 | * |
| | | 188 | 3.3 | 27 | 1 | 1 | $\frac{1}{2}$ | $-\frac{1}{2}$ | −2 | |
| | | 688 | 49 | 87 | 1 | 0 | $\frac{1}{2}$ | $\frac{1}{2}$ | −3 | * |
| | | 806 | $3.0\times10^{-2}$ | 51 | 1 | 1 | $\frac{1}{2}$ | $-\frac{1}{2}$ | −3 | |
| −79 | 297 | 124 | 1.8 | 273 | 1 | 1 | $\frac{1}{2}$ | $-\frac{1}{2}$ | −1 | |
| | | 599 | 88 | 383 | 1 | 0 | $\frac{1}{2}$ | $\frac{1}{2}$ | −2 | * |
| | | 725 | $5.7\times10^{-2}$ | 117 | 1 | 1 | $\frac{1}{2}$ | $-\frac{1}{2}$ | −2 | |
| | | 934 | $9.5\times10^{-2}$ | 294 | 2 | 1 | $\frac{1}{2}$ | $-\frac{1}{2}$ | −3 | |
| | | 953 | $3.8\times10^{-1}$ | 292 | 2 | 0 | $\frac{1}{2}$ | $\frac{1}{2}$ | −3 | |
| 71 | −47 | 99 | −32 | −83 | 1 | 0 | $\frac{1}{2}$ | $\frac{1}{2}$ | −1 | |
| | | 134 | $-2.4\times10^{-1}$ | −144 | 1 | 1 | $\frac{1}{2}$ | $-\frac{1}{2}$ | −1 | |
| | | 343 | $-1.9\times10^{-1}$ | −49 | 2 | 1 | $\frac{1}{2}$ | $-\frac{1}{2}$ | −2 | |
| | | 455 | −27 | −51 | 2 | 0 | $\frac{1}{2}$ | $\frac{1}{2}$ | −2 | |
| | | 689 | −3.2 | −50 | 1 | 0 | $\frac{1}{2}$ | $\frac{1}{2}$ | −2 | |
| | | 776 | $-3.9\times10^{-2}$ | −49 | 1 | 1 | $\frac{1}{2}$ | $-\frac{1}{2}$ | −2 | |
| 71 | 86 | 312 | $1.1\times10^{-1}$ | 85 | 1 | 0 | $\frac{1}{2}$ | $\frac{1}{2}$ | −2 | |
| | | 413 | $9.4\times10^{-4}$ | 85 | 1 | 1 | $\frac{1}{2}$ | $-\frac{1}{2}$ | −2 | |
| 71 | 297 | 172 | 18 | 202 | 1 | 0 | $\frac{1}{2}$ | $\frac{1}{2}$ | −2 | * |
| | | 285 | $9.5\times10^{-2}$ | 185 | 1 | 1 | $\frac{1}{2}$ | $-\frac{1}{2}$ | −2 | |
| | | 860 | $2.9\times10^{-2}$ | 279 | 2 | 1 | $\frac{1}{2}$ | $-\frac{1}{2}$ | −3 | |
| | | 952 | $3.2\times10^{-1}$ | 294 | 2 | 0 | $\frac{1}{2}$ | $\frac{1}{2}$ | −3 | |
| 242 | −47 | 61 | −2.8 | −65 | 1 | 0 | $\frac{1}{2}$ | $\frac{1}{2}$ | −1 | |
| | | 99 | $-1.8\times10^{-1}$ | −67 | 1 | 1 | $\frac{1}{2}$ | $-\frac{1}{2}$ | −1 | |
| | | 331 | $-9.6\times10^{-2}$ | −50 | 2 | 1 | $\frac{1}{2}$ | $-\frac{1}{2}$ | −3 | |
| | | 413 | −10 | −54 | 2 | 0 | $\frac{1}{2}$ | $\frac{1}{2}$ | −3 | |
| | | 678 | −1.4 | −50 | 1 | 0 | $\frac{1}{2}$ | $\frac{1}{2}$ | −2 | |
| | | 766 | $-4.4\times10^{-2}$ | −48 | 1 | 1 | $\frac{1}{2}$ | $-\frac{1}{2}$ | −2 | |
| 242 | 86 | 248 | 4.0 | 93 | 1 | 0 | $\frac{1}{2}$ | $\frac{1}{2}$ | −2 | * |
| | | 302 | $1.4\times10^{-1}$ | 86 | 1 | 1 | $\frac{1}{2}$ | $-\frac{1}{2}$ | −2 | |
| 242 | 297 | 134 | $3.3\times10^{-3}$ | 300 | 1 | 0 | $\frac{1}{2}$ | $\frac{1}{2}$ | −2 | |
| | | 187 | $1.9\times10^{-4}$ | 300 | 1 | 1 | $\frac{1}{2}$ | $-\frac{1}{2}$ | −2 | |
| | | 838 | $7.8\times10^{-4}$ | 302 | 2 | 1 | $\frac{1}{2}$ | $-\frac{1}{2}$ | −3 | |
| | | 951 | $1.3\times10^{-1}$ | 301 | 2 | 0 | $\frac{1}{2}$ | $\frac{1}{2}$ | −3 | |
| | | 990 | $1.8\times10^{-4}$ | 300 | 1 | 0 | $\frac{1}{2}$ | $\frac{1}{2}$ | −3 | |

For Rb+CaF, the spin-exchange interaction may be characterized in terms of an anisotropic surface $V^-(R,\theta)$ that is half the difference between the singlet and triplet surfaces,

$$V^-(R,\theta) = \tfrac{1}{2}\left[V^0(R,\theta) - V^1(R,\theta)\right]. \tag{4.9}$$

This may be expanded in Legendre polynomials,

$$V^-(R,\theta) = \sum_\lambda V_\lambda^-(R) P_\lambda(\cos\theta). \tag{4.10}$$

Such a potential is diagonal in $K$, but each term in the expansion can couple $(n,K) = (0,0)$ to $(\lambda,0)$. The term $V_1^-(R)$ can thus couple an incoming state at the lowest threshold to states with $(n,K) = (1,0)$. The spin selection rules are the same as for $n = 0$, so the strongest resonances will be those due to states dominated by $m_{i,\mathrm{F}} = \frac{1}{2}$. As for $n = 0$, there are 3 such uncoupled states, with quantum numbers $(f_{\mathrm{Rb}}, m_{f,\mathrm{Rb}}, m_{s,\mathrm{CaF}}, m_{i,\mathrm{F}}) = (1,0,\frac{1}{2},\frac{1}{2})$ $(2,1,-\frac{1}{2},\frac{1}{2})$ and $(2,0,\frac{1}{2},\frac{1}{2})$. $V^-(R,\theta)$ is strongly anisotropic at short range, so there will always be some intermolecular distance $R$ where it matches the separation between the incoming and resonant thresholds, where nonadiabatic couplings can occur by extension of the theory of ref. [20].

For a potential with long-range form $-C_6R^{-6}$, the binding energy of a state that lies below the top bin is approximately proportional to $(|\eta| + \frac{1}{8})^3$ [102, 182]. Here $\eta$ is a noninteger vibrational quantum number, with integer values at the bin boundaries. For an unknown potential of sufficient depth, the fractional part of $\eta$ may be regarded as a uniform random variable. Since there is one state in each bin, this allows calculation of the probability that there is a state within any particular range of energies.

As seen in Sec. 4.3.1, the states that can cause strong resonances traverse about 3 GHz of binding energy between zero field and 1000 G. Since the thresholds with $(n, f_{\mathrm{Rb}}) = (1,1)$ lie about 20 GHz above $(0,1)$, the zero-field binding energy of a state must be between 20 and 23 GHz if it is to cause a Feshbach resonance below

1000 G. For an unknown potential, there is only about a 19% probability that there is a state with a binding energy in this range. The corresponding probability for $n = 2$ is about 9%, and the probabilities decrease for successively higher $n$, because the bins are correspondingly wider at the required binding energy.

The overall conclusion of this section is that there *may* be resonances due to states involving rotationally excited CaF, but that they will occur at fields below 1000 G for a fairly small subset of possible interaction potentials. In any case, the mixing between rotational states of CaF due to long-range anisotropy is weak enough that it will not affect the likelihood of resonances due to the ground rotational state.

## 4.5 Potential Effects of Chaos

The interaction potentials for Rb+CaF are very strongly anisotropic at short range, and provide strong coupling between CaF rotational and vibrational states. It is quite likely that Rb+CaF will possess short-range states that exhibit quantum chaos, in the same way as alkali-metal 3-atom [167, 184] and 4-atom systems [185, 186]. The onset of chaos has also been studied in Li+CaH and Li+CaF [187].

For Rb+CaF, the density of short-range singlet vibrational states at the energy of the lowest threshold has been estimated as 4 $K^{-1}$ [169], corresponding to a mean spacing of 5 GHz. If these states are fully chaotic, it is likely to produce structure in the singlet scattering length on this energy scale. However, the hyperfine couplings in singlet states will be small, probably dominated by nuclear electric quadrupole couplings of no more that a few MHz, which is tiny compared to the state separations. Furthermore, Zeeman shifts are very small for singlet states, though they do differ from those for the incoming threshold. At most, the presence of chaos at short range might make the singlet scattering length different for collisions involving Rb($f = 1$) and Rb($f = 2$). This would affect the details of the level structure, but not the probabilities of observing Feshbach resonances.

The density of short-range triplet states at threshold is likely to be much smaller, perhaps by an order of magnitude. This corresponds to a mean spacing of order

50 GHz. The difference arises because the density of states for an atom-diatom system scales approximately with $D^{3/2}$ [167], where $D$ is the well depth, and the triplet surface of Rb+CaF is expected to be substantially shallower than the singlet surface, as for the alkali-metal dimers. The hyperfine couplings for triplet states will be comparable to those for the separated atom and molecule (6.8 GHz for Rb, 120 MHz for CaF) but these are still substantially smaller than the likely spacings between short-range triplet states. Zeeman effects are also much larger for triplet states than for singlet states, but are still only a few GHz at fields below 1000 G, so will not cause substantial mixings between short-range triplet states.

It thus appears that the qualitative arguments in this paper about the patterns of energy levels and likelihood of Feshbach resonances will remain valid even if the short-range levels of Rb+CaF exhibit quantum chaos.

## 4.6 Conclusions

We have investigated magnetically tunable Feshbach resonances that may be expected in collisions between molecules in $^2\Sigma$ states and alkali-metal atoms, focussing on the prototype system Rb+CaF. The details of the short-range interaction potential are unknown, but expected to have minor influence, except to determine singlet and triplet scattering lengths $a_\mathrm{s}$ and $a_\mathrm{t}$. We have carried out coupled-channel calculations of the near-threshold bound states and scattering properties for a variety of values of these scattering lengths. We find that the large majority of plausible interaction potentials produce multiple resonances at magnetic field below 1000 G, which are likely to be experimentally accessible. In each case, at least some of these resonances are wide enough to be experimentally useful for tuning scattering lengths or for forming triatomic molecules by magnetoassociation.

The patterns of bound states may be understood in terms of underlying uncoupled states that lie parallel to atom-molecule thresholds as a function of magnetic field. There are varying degrees of coupling between these states, which depend on the values of $a_\mathrm{s}$ and $a_\mathrm{t}$. The coupling is weakest when $a_\mathrm{s}$ and $a_\mathrm{t}$ are similar. The

widths of the resonances may be explained in terms of the nature of the states that cross threshold, together with effects due to the scattering lengths.

We have considered the effect of potential anisotropy, which causes coupling between CaF rotational states. This coupling is very strong at short range. Even at long range, it is sufficient to quantize the CaF rotation along the intermolecular axis instead of along the magnetic field. It is likely that each rotational state of CaF will be characterized by different values of the singlet and triplet scattering lengths. We have found that there is a small but significant probability of additional wide resonances due to states supported by rotationally excited thresholds. We have also considered the potential influence of chaotic behavior for short-range states of Rb+CaF. We expect that, even if present, it will have limited effects on the long-range states that are principally responsible for the resonances and will not change the qualitative conclusions.

This work indicates that atom-molecule systems such as Rb+CaF will have a rich spectrum of magnetically tunable Feshbach resonances at experimentally accessible magnetic fields. The resonances can be used to form a more detailed understanding of the atom-diatom potential energy surfaces. Much new physics will be accessible when these resonances are located. For example, a resonance can be used to tune the s-wave scattering length for interspecies collisions. In this way we can expect to find favorable conditions for sympathetic cooling, which can greatly increase the phase-space density of the molecular gas. The resonances may also be used to form polyatomic molecules by magnetoassociation. Many applications have already been identified for such molecules. They have unique advantages for probing interactions beyond the Standard Model that violate time-reversal symmetry [188, 189] and for testing theories of ultralight dark matter [190]. Their usefulness for quantum information processing has been highlighted [191, 192], and the very large number of stable, accessible internal states make them interesting as qudits [193]. They can also be used to explore a rich diversity of many-body phenomena such as quantum magnetism [194].

## 4.7 Recent Perspectives

The results presented in this chapter were published in June 2023 and several relevant studies have been reported since. Thus far this chapter has been a direct reproduction of our paper. However, the opportunity is now taken to review these recent advances and assess the extent to which they support our insights.

Park et al. and Karman et al., two papers comprising a joint experimental and theoretical study, addressed the magnetically tunable Feshbach resonances in $^{23}$Na($^2$S) + $^{23}$Na$^6$Li($^3\Sigma$) collisions, were published in August 2023 [195, 196]. This work constituted an important step forward in studies of the collisions of alkali-metal atoms with alkali-metal dimers. Previously, systems such as $^{40}$K + $^{23}$Na$^{40}$K had been studied, where it was possible to assign various Feshbach resonances to long-range states whose nature was not complicated by the highly anisotropic nature of the interaction potential at short range [162]. Park et al. and Karman et al. addressed Feshbach resonances governed by the anisotropy of the interaction potential. The upper and lower spin stretched states of $^{23}$Na ($^2$S) + $^{23}$Na$^6$Li ($^3\Sigma$) were prepared by Park et al. in their experiment. Collisions at both thresholds occur primarily on the quartet potential, which does not allow chemical reactions. There also exists a reactive doublet potential. At the upper threshold 8 Feshbach resonances were observed beneath 1400 G. At the lower threshold 17 Feshbach resonances were observed beneath 1400 G. Theoretical analysis suggested that more Feshbach resonances exist at the upper threshold, but they are sufficiently decayed such that they couldn't be found in the experiment. These resonances decayed to either the lower spin-stretched threshold or the doublet potential. It was found that the resonance states, for both thresholds, were supported by the quartet potential and had excited mechanical angular momentum. The anisotropic spin-spin interaction and, to a notably lesser extent, the spin-rotation coupling in the $^{23}$Na$^6$Li molecule were responsible, in combination with the anisotropy of the potential, for coupling the resonant states to the incoming channel. It was found that the theoretical predication of the resonance positions depended very strongly on the anisotropy of the

interaction potential. It should be noted that the coupling mechanism observed and studied by Park et al. and Karman et al. is specific to $^3\Sigma$ molecules on account of the intramolecular spin-spin interaction and the role it plays in the atom-molecule collision dynamics.

Morita et al. studied Rb($^2$S) + SrF($^2\Sigma$) collisions using numerically exact coupled channel calculations that accounted for the hyperfine structure of the colliding species and the rotational structure of the molecule [197]. They employed anisotropic potential energy surfaces for the singlet and triplet electronic states that were calculated with ab initio electronic structure methods. Due to uncertainties in the calculated potential energy surface Morita et al. did not expect to predict the positions of Feshbach resonances accurately, although they expected to be able to predict the pattern and density of resonances. This work is a very useful lens in which to consider our results for Rb + CaF as the underlying mechanisms that can couple bound states to the continuum are the same. Morita et al. adopted a different philosophy, compared to us, with which to approach the problem. Whereas we made a series of judgments in order to boil down the problem to its most essential and simple features Morita et al. included all possible detail. This difference arises due to differing motivations. Our aim was to assess if there would be enough broad Feshbach resonances at the lowest threshold, caused by a single coupling mechanism (spin-exchange interactions between states with no excited rotational motion), in order to motivate an experiment. Morita et al. worked to include all possible complexity using various recently developed capabilities [198].

Morita et al. calculated elastic and inelastic cross sections at excited scattering thresholds. An average of five Feshbach resonances per 1000 G were reported. A number of these resonances were found to be caused by low-lying excited rotational states. In Section 4.4 we argued that states bound by the long-range portion of the interaction potential would cause such resonances. Morita et al. believed these to be caused by short-range states. Several resonances appeared to be caused by spin-exchange interactions between states with no excited rotational motion. These

are the resonances we studied quantitatively with a variety of model potentials in Section 4.3.2. By scaling the short-range interaction potential Morita et. al. demonstrated that the density and positions of resonances caused by states with excited molecular rotation were sensitive to the anisotropy of the potential, as expected. It was apparent, however, that the positions of several resonances were insensitive to the short-range region of the potential. The results published by Morita et al. were mostly in line with our expectations. It should be reiterated that the singlet and triplet scattering lengths are exceptionally important quantities that offer insight into the collision physics of ultracold species. Morita et al. did not provide any information regarding the scattering lengths returned by their potentials. As such, it is unclear which of the nine potentials we explored is closest to their potential. Furthermore, it should be noted that Morita et al. made no mention of how they assessed the number of Feshbach resonances. Plotting cross sections to find Feshbach resonances is likely to prove erroneous as narrow resonances could easily not be identified depending on the selected grid size. Anisotropic dipole-dipole interactions arising from the two electric spins on the different collision partners were found to have little effect on the number of Feshbach resonances. These resonances, however, are often exceptionally narrow and are likely not to be visible on large grids.

Since the publication of our paper, a number of important discoveries and observations have been made regarding the Feshbach resonances in atom+molecule collisions that depend on the short-range anisotropic region of the interaction potential. Morita et al. studied the collisions of a $^2$S atom and a $^2\Sigma$ molecule, similarly to us. They employed a radically different approach. The results published by Morita et al. are unable to discredit our predictions of spin-exchange interactions between rotationless states or our expectations regarding the role of CaF rotation. It is exceptionally hard to compare results as it is not clear what the properties, pertaining to the near-threshold physics, of their interaction potential are.

# Chapter 5

# Mergoassociation with Optical Tweezers: Part I

This chapter is a reproduction of the following publication: R. C. Bird, C. R. Le Sueur and J. M. Hutson, *Physical Review Research*, 2023, **5**, 043086. J. M. Hutson supervised the project. C. R. Le Sueur performed the algebra needed to separate the relative and center-of-mass motions, and derived the radial coefficients for the expansion of the trap potential in spherical polar coordinates.

Bird et al., and the work presented in this chapter, followed our collaboration and publication with the Cornish Group (Durham University): D. K. Ruttley, A. Guttridge, S. Spence, R. C. Bird, C. R. Le Sueur, J. M. Hutson and S. L. Cornish, *Physical Review Letters*, 2023, **130**, 223401. Ruttley et al. observed and studied a novel method for producing ultracold molecules, mergoassociation. C. R. Le Sueur, J. M. Hutson, and I contributed to Ruttley et al. by developing a coupled-channel method for calculating the energy levels of the relative motion for two atoms in two separate spherical traps. We studied the effect of trap strength on the avoided crossing responsible for mergoassociation. These results are briefly discussed in this chapter. The coupled-channel method developed here extended the method developed in Ruttley et al. by including trap anisotorpy.

## 5.1 Introduction

Ultracold molecules have recently been formed in optical tweezers by mergoassociation [199]. The process begins with two atoms in separate tweezer traps, which are then merged. The atom pair is converted into a molecule by the merging process, with no further action required.

The energy levels involved in mergoassociation are shown schematically in Figure 5.1. As a function of trap separation, there is an avoided crossing between the lowest motional state of the atom pair and a weakly bound molecular state. If the merging is carried out slowly enough to follow the crossing adiabatically, the atom pair is converted into a weakly bound molecule. A major advantage of this approach is that it can work even for unstructured atoms, and does not require a magnetically tunable Feshbach resonance. It thus opens the way to creating ultracold molecules

from atom pairs without Feshbach resonances at experimentally accessible magnetic fields. It also offers possibilities for constructing two-qubit gates for quantum logic operations [200].

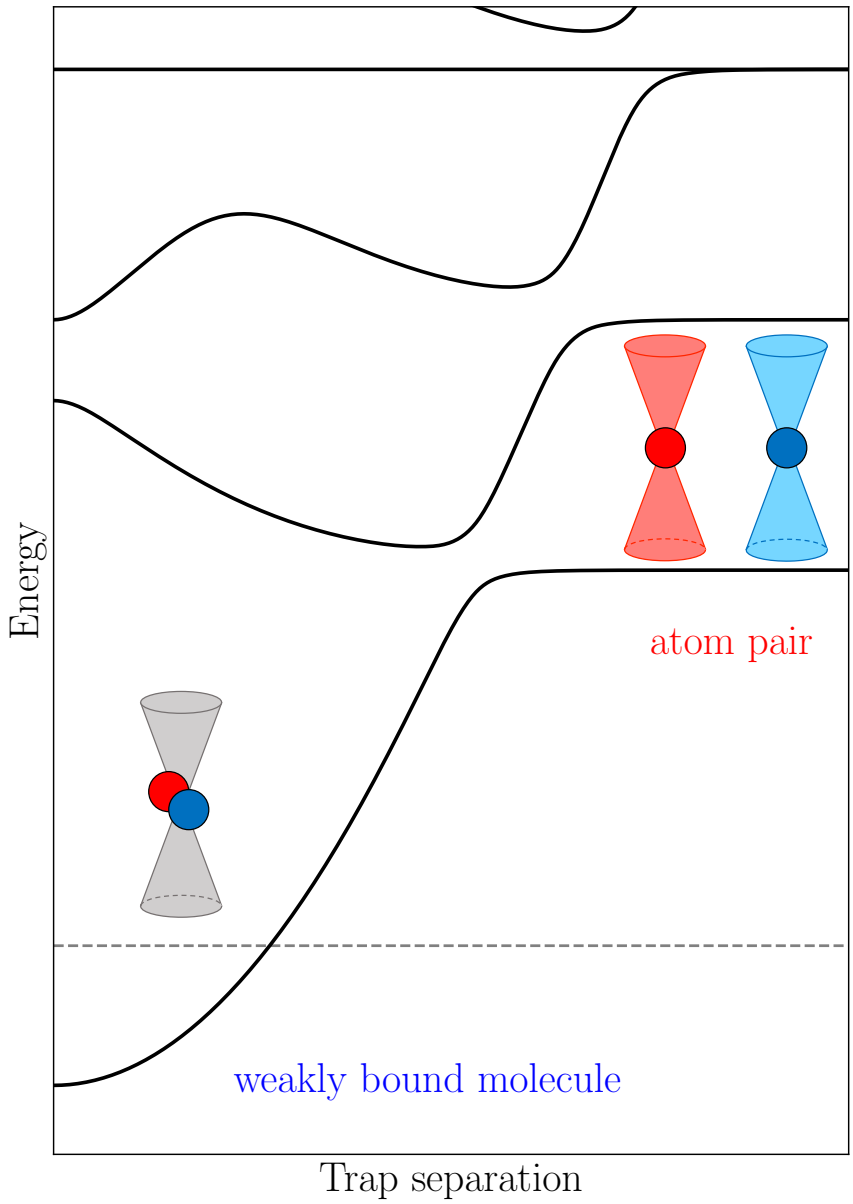


Figure 5.1: Schematic representation of the energy levels involved in mergoassociation, as a function of trap separation $z_0$. The molecular level (approximately quadratic as a function of $z_0$) has avoided crossings with motional states of the atom pair (approximately horizontal at large $z_0$). Mergoassociation occurs when an atom pair in the lowest motional state is transferred into the molecular state by adiabatic passage over the lowest avoided crossing.

Avoided crossings between atomic and molecular states as a function of trap separation were first studied by Stock et al. [201, 202], who considered the case of two atoms initially in identical spherical traps. Other authors have investigated similar situations for ions and molecules in spherical or quasi-1d traps [203, 204]. However, optical tweezers for ultracold atoms are usually formed in the high-intensity region at the waist of a focused laser beam [205]. Such tweezers are strongly anisotropic, usually with much weaker confinement along the laser beam than perpendicular to it. In ref. [199], the ratio of the corresponding harmonic frequencies was about 1:6. The spherical model we developed to model the mergoassociation process in this experiment, the results of which are presented in this chapter, performed suprisingly well.

Following the development and utilization of the aforementioned spherical model we developed the theory of merging nonidentical nonspherical traps. In Section 5.2 we derive the separation between the relative and center-of-mass motions for separated traps, including the coupling term between them. In Section 5.3, we develop a numerically exact coupled-channel approach to handle the relative motion of two atoms in nonspherical traps, including the case of traps that are not coaligned. In Section 5.4, we solve the coupled equations and present energy-level diagrams for merging of two cylindrically symmetric tweezers as a function of their aspect ratios. We focus on the strength of the lowest avoided crossing, which is the key quantity for mergoassociation, and show that it depends strongly on aspect ratio. In this section we also present the results of our spherical calculation which were used in [199]. We are able to explain the success of the spherical approximation in ref. [199]. In Section 5.5 we develop an approximate method based on a basis-set approach, which qualitatively reproduces the coupled-channel results and gives insight into the dependence of avoided-crossing strength on aspect ratio. Finally, in Section 5.6 we present conclusions and perspectives for future work.

## 5.2 Separation of Relative and Center-of-Mass Motion

We consider two atoms independently confined in adjacent optical traps. Atom $i$ has mass $m_i$ and position $\boldsymbol{R}_i$ and is confined in a trap centered at $\boldsymbol{R}_i^0$. The motion may be factorized approximately into terms involving the relative and center-of-mass coordinates of the pair, $\boldsymbol{R}$ and $\boldsymbol{\mathcal{R}}$ respectively. The 2-atom kinetic energy operator is exactly separable,

$$\begin{aligned} -\frac{\hbar^2}{2m_1}\nabla_1^2 - \frac{\hbar^2}{2m_2}\nabla_2^2 &= -\frac{\hbar^2}{2\mathcal{M}}\nabla_{\mathcal{R}}^2 - \frac{\hbar^2}{2\mu}\nabla_R^2 \\ &= \hat{T}_{\rm com} + \hat{T}_{\rm rel}, \end{aligned} \tag{5.1}$$

where

$$\boldsymbol{\mathcal{R}} = \left(m_1\boldsymbol{R}_1 + m_2\boldsymbol{R}_2\right)/\mathcal{M}; \tag{5.2}$$

$$\boldsymbol{R} = \boldsymbol{R}_2 - \boldsymbol{R}_1; \tag{5.3}$$

$$\mathcal{M} = m_1 + m_2; \tag{5.4}$$

$$\mu = m_1 m_2/\mathcal{M}. \tag{5.5}$$

### 5.2.1 Spherical Traps

If each trap is harmonic and spherical, the total potential energy due to the traps is

$$V^{\rm trap} = \tfrac{1}{2}m_1\omega_1^2|\boldsymbol{R}_1 - \boldsymbol{R}_1^0|^2 + \tfrac{1}{2}m_2\omega_2^2|\boldsymbol{R}_2 - \boldsymbol{R}_2^0|^2, \tag{5.6}$$

where $\omega_i$ is the harmonic frequency for atom $i$. This may be written

$$\begin{aligned} &\tfrac{1}{2}\mu\omega_{\rm rel}^2|\boldsymbol{R} - \boldsymbol{R}_0|^2 + \tfrac{1}{2}\mathcal{M}\omega_{\rm com}^2|\boldsymbol{\mathcal{R}} - \boldsymbol{\mathcal{R}}_0|^2 \\ &\qquad + \mu\Delta\omega^2(\boldsymbol{\mathcal{R}} - \boldsymbol{\mathcal{R}}_0)\cdot(\boldsymbol{R} - \boldsymbol{R}_0), \end{aligned} \tag{5.7}$$

where

$$\boldsymbol{R}_0 = \boldsymbol{R}_2^0 - \boldsymbol{R}_1^0; \tag{5.8}$$

$$\omega_{\rm rel}^2 = \left(m_2\omega_1^2 + m_1\omega_2^2\right)/\mathcal{M}; \tag{5.9}$$

$$\boldsymbol{\mathcal{R}}_0 = \left(m_1\boldsymbol{R}_1^0 + m_2\boldsymbol{R}_2^0\right)/\mathcal{M}; \tag{5.10}$$

$$\omega_{\rm com}^2 = \left(m_1\omega_1^2 + m_2\omega_2^2\right)/\mathcal{M}; \tag{5.11}$$

$$\Delta\omega^2 = \omega_2^2 - \omega_1^2. \tag{5.12}$$

This is a generalization of the result of Stock et al. [201], who dealt with the case $m_1 = m_2$ and $\omega_1 = \omega_2$, so that the coupling term vanished. The separation is similar to that for two nonidentical atoms in a single trap [206], except that the coupling term here involves $(\boldsymbol{\mathcal{R}} - \boldsymbol{\mathcal{R}}_0)\cdot(\boldsymbol{R} - \boldsymbol{R}_0)$ instead of $\boldsymbol{\mathcal{R}}\cdot\boldsymbol{R}$. The relative and center-of-mass motions are uncoupled if the trap frequencies for the two atoms are the same. The coupling is generally not important if both atoms are in the motional ground state, but can be significant when trap states that are excited in the relative and center-of-mass motions are nearly degenerate.

### 5.2.2 Nonspherical Traps

If the individual traps are harmonic but non-spherical, each trap has three principal axes perpendicular to one another. Eq. 5.7 generalizes to

$$\begin{aligned} V^{\rm trap} = {} & \tfrac{1}{2}\mu[\boldsymbol{R} - \boldsymbol{R}_0]^T\boldsymbol{\omega}_{\rm rel}^2[\boldsymbol{R} - \boldsymbol{R}_0] \\ & + \tfrac{1}{2}\mathcal{M}[\boldsymbol{\mathcal{R}} - \boldsymbol{\mathcal{R}}_0]^T\boldsymbol{\omega}_{\rm com}^2[\boldsymbol{\mathcal{R}} - \boldsymbol{\mathcal{R}}_0] \\ & + \mu[\boldsymbol{\mathcal{R}} - \boldsymbol{\mathcal{R}}_0]^T\Delta\boldsymbol{\omega}^2[\boldsymbol{R} - \boldsymbol{R}_0], \end{aligned} \tag{5.13}$$

where $\boldsymbol{\omega}_{\rm rel}^2$, $\boldsymbol{\omega}_{\rm com}^2$ and $\Delta\boldsymbol{\omega}^2$ are second-rank tensors. We choose Cartesian axes along the principal axes of $\boldsymbol{\omega}_{\rm rel}^2$, so that it may be represented as a diagonal matrix,

$$\boldsymbol{\omega}_{\rm rel}^2 = \begin{pmatrix} \omega_{{\rm rel},x}^2 & 0 & 0 \\ 0 & \omega_{{\rm rel},y}^2 & 0 \\ 0 & 0 & \omega_{{\rm rel},z}^2 \end{pmatrix}. \tag{5.14}$$

If the two traps are coaligned, meaning that they share the same set of principal axes, $\boldsymbol{\omega}_{\rm com}^2$ and $\Delta\boldsymbol{\omega}^2$ are also diagonal matrices, defined similarly; if not, they are nondiagonal symmetric matrices. $\boldsymbol{R}$, $\boldsymbol{R}_0$, $\boldsymbol{\mathcal{R}}$ and $\boldsymbol{\mathcal{R}}_0$ are column vectors,

$$\boldsymbol{R} = \begin{pmatrix} x \\ y \\ z \end{pmatrix} = R \begin{pmatrix} \sin\theta\cos\phi \\ \sin\theta\sin\phi \\ \cos\theta \end{pmatrix} \tag{5.15}$$

and similarly for $\boldsymbol{R}_0$, $\boldsymbol{\mathcal{R}}$ and $\boldsymbol{\mathcal{R}}_0$. The components of $\boldsymbol{R}$ and $\boldsymbol{\mathcal{R}}$ are denoted $x$, $y$, $z$ and $X$, $Y$, $Z$, respectively, and similarly for $\boldsymbol{R}_0$ and $\boldsymbol{\mathcal{R}}_0$. If the traps are anharmonic, the potentials for motion in $\boldsymbol{R}$ and $\boldsymbol{\mathcal{R}}$ are also anharmonic. The coupling term is then more complicated, but is still zero if either $\boldsymbol{R} = \boldsymbol{R}_0$ or $\boldsymbol{\mathcal{R}} = \boldsymbol{\mathcal{R}}_0$. In the remainder of this chapter, we neglect the coupling term and focus on the relative motion. In Chapter 6 we include the coupling term. We restrict the discussion in Chapters 5 and 6 to the case where the two traps are coaligned, so that the tensors $\boldsymbol{\omega}_1^2$, $\boldsymbol{\omega}_2^2$, $\boldsymbol{\omega}_{\rm rel}^2$, $\boldsymbol{\omega}_{\rm com}^2$ and $\Delta\boldsymbol{\omega}^2$ all have the same principal axes and $\Delta\boldsymbol{\omega}^2 = (\boldsymbol{\omega}_1 + \boldsymbol{\omega}_2)(\boldsymbol{\omega}_2 - \boldsymbol{\omega}_1)$.

## 5.3 Coupled-Channel Formulation for Relative Motion

### 5.3.1 The Trap Potential

Even if the two traps are not coaligned, the potential for relative motion is harmonic. It has three principal axes perpendicular to one another, which are used to define

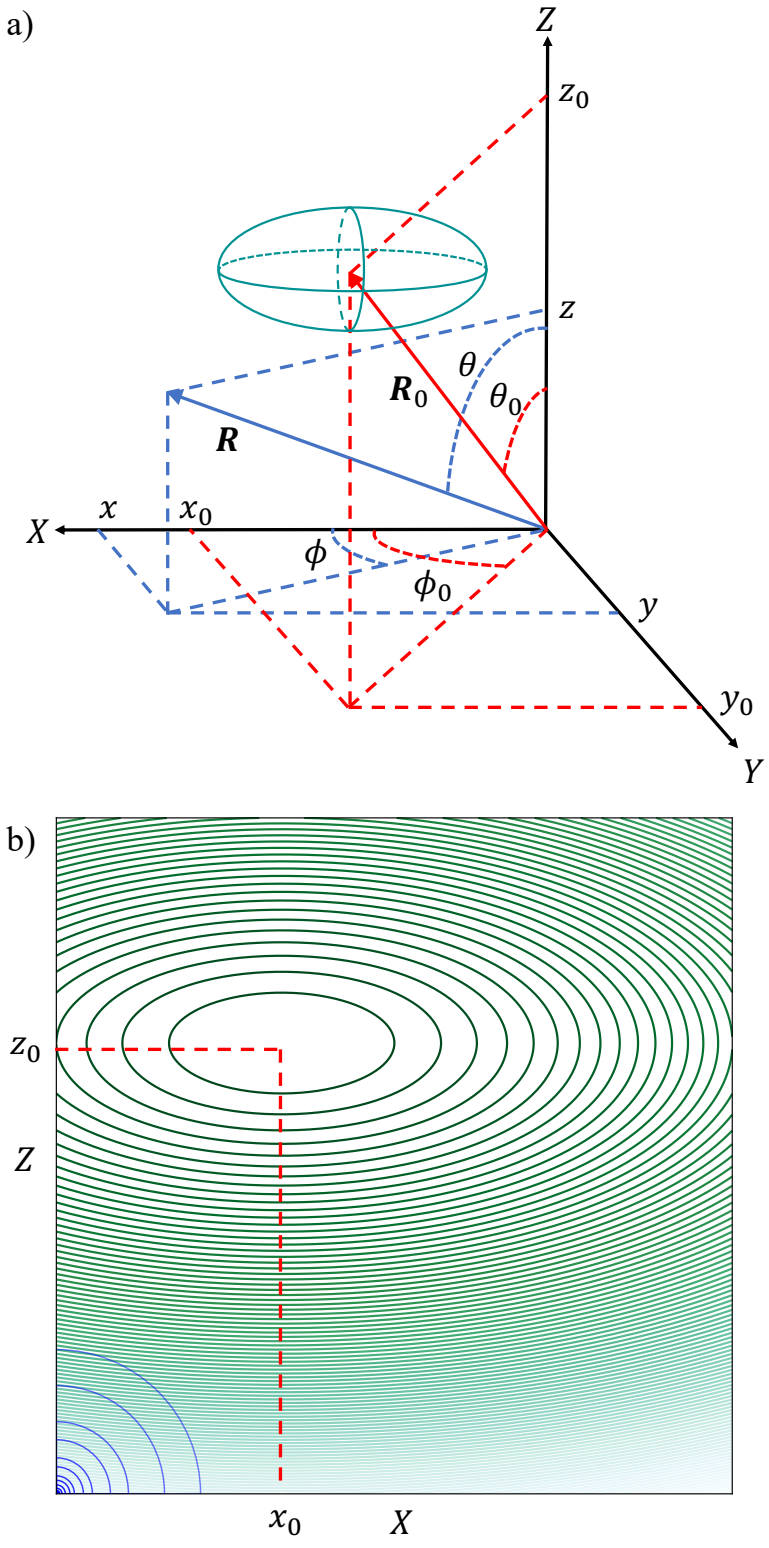


Figure 5.2: (a) Coordinate system for relative motion. The ellipsoid is a schematic representation of the shape of the trap potential for relative motion, and the Cartesian axes are aligned along its principal axes. (b) A cut through the potential for relative motion for $y = 0$, showing the contours of the harmonic trap centered at $\boldsymbol{R}_0$ (green) and a shorter-range atom-atom potential centered at the origin (blue).

Cartesian axes as above. The resulting coordinate system is shown in Fig. 5.2(a). The potential for relative motion may be written

$$V_{\rm rel}^{\rm trap}(\boldsymbol{R}) = \tfrac{1}{2}\mu[\boldsymbol{R}-\boldsymbol{R}_0]^T\boldsymbol{\omega}_{\rm rel}^2[\boldsymbol{R}-\boldsymbol{R}_0], \tag{5.16}$$

with a minimum at the trap separation $\boldsymbol{R} = \boldsymbol{R}_0$. A cut through this is shown in green in Fig. 5.2(b).

For calculations in spherical polar coordinates, it is convenient to expand the potential for relative motion as

$$V_{\rm rel}^{\rm trap}(\boldsymbol{R}) = \sum_{\lambda\kappa} V_{\lambda\kappa}(R)C_{\lambda\kappa}(\theta,\phi), \tag{5.17}$$

where $C_{\lambda\kappa}(\theta,\phi) = [4\pi/(2\lambda+1)]^{1/2}Y_{\lambda\kappa}(\theta,\phi)$ are Racah-normalized spherical harmonics. For the potential (5.16), the only non-zero terms in the expansion are

$$V_{00}(R) = \tfrac{1}{2}\mu\bar{\omega}_{\rm rel}^2R^2 + \tfrac{1}{2}\mu\boldsymbol{R}_0^T\boldsymbol{\omega}_{\rm rel}^2\boldsymbol{R}_0; \tag{5.18}$$

$$V_{10}(R) = -\mu\omega_{{\rm rel},z}^2 z_0 R; \tag{5.19}$$

$$V_{1\pm1} = \mp\tfrac{1}{\sqrt{2}}\mu(\omega_{{\rm rel},x}^2x_0 - i\omega_{{\rm rel},y}^2y_0)R; \tag{5.20}$$

$$V_{20}(R) = \tfrac{1}{6}\mu(2\omega_{{\rm rel},z}^2 - \omega_{{\rm rel},x}^2 - \omega_{{\rm rel},y}^2)R^2; \tag{5.21}$$

$$V_{2\pm2}(R) = \tfrac{1}{2\sqrt{6}}\mu(\omega_{{\rm rel},x}^2 - \omega_{{\rm rel},y}^2)R^2, \tag{5.22}$$

where

$$\bar{\omega}_{\rm rel}^2 = \tfrac{1}{3}\left(\omega_{{\rm rel},x}^2 + \omega_{{\rm rel},y}^2 + \omega_{{\rm rel},z}^2\right). \tag{5.23}$$

The constant term in $V_{00}(R)$ involving $\boldsymbol{R}_0^T\boldsymbol{\omega}_{\rm rel}^2\boldsymbol{R}_0$ is chosen to place the minimum of the combined trap at zero energy. It is often convenient to express the trap potential in terms of harmonic lengths for relative motion. $\beta_{{\rm rel},\alpha} = [\hbar/(\mu\omega_{{\rm rel},\alpha})]^{1/2}$.

There are two special cases of the expansion that are of particular interest. If the traps are cylindrically symmetrical around the intertrap vector $\boldsymbol{R}_0$, $z$ may be chosen to lie along $\boldsymbol{R}_0$. Terms with $\kappa \neq 0$ are then zero and the expansion may be

replaced by a simpler one in terms of Legendre polynomials $P_\lambda(\cos\theta)$,

$$V_{\rm rel}^{\rm trap}(\boldsymbol{R}) = \sum_\lambda V_{\lambda 0}(R) P_\lambda(\cos\theta). \tag{5.24}$$

If the individual traps are spherical, the term $V_{20}(R)$ is also zero. This is the case handled by Stock et al. [201] and Ruttley et al. [199].

The expansion (5.17) remains valid for anharmonic potentials, but in this case the expansion does not terminate and the coefficients $V_{\lambda\kappa}(R)$ must usually be evaluated by numerical quadrature.

### 5.3.2 The Interaction Potential

The interaction potential $V_{\rm int}(\boldsymbol{R})$ between the two atoms may be represented at various levels of complexity. For unstructured atoms, it is isotropic, $V_{\rm int}(R)$. When all the harmonic lengths $\beta_{{\rm rel},\alpha}$ are large compared to the range of the potential, it may be sufficient to represent $V_{\rm int}(\boldsymbol{R})$ as a point contact potential [207],

$$V_{\rm int}(\boldsymbol{R}) = \frac{2\pi\hbar^2 a(E)}{\mu}\delta(\boldsymbol{R})\frac{\partial}{\partial R}R, \tag{5.25}$$

where the scattering length $a(E)$ may depend on energy if required. Such a contact potential may be implemented in coupled-channel calculations as a boundary condition on the log-derivative of the s-wave component of the wavefunction,

$$\frac{d\psi_{00}}{dR}[\psi_{00}(R)]^{-1} = -1/a(E) \tag{5.26}$$

at $R = 0$. A contact potential affects only states with non-zero density at $R = 0$, which here occurs only for states with a component in $M = 0$.

More complicated treatments might include atoms or molecules with additional coordinates $\xi$ for internal structure, such as alkali-metal atoms including electron and nuclear spin and Zeeman effects. The interaction potential then depends on $\xi$ as well as $\boldsymbol{R}$ and $V_{\rm int}(\boldsymbol{R},\xi)$ may itself be anisotropic. The total wavefunction would

then be expanded in a basis set that includes functions for $\xi$, as for calculations on untrapped atom pairs [98].

### 5.3.3 Coupled-channel Equations

The Schrödinger equation for relative motion is

$$\left[\frac{\hbar^2}{2\mu}\left(-R^{-1}\frac{d^2}{dR^2}R+\frac{\hat{L}^2}{R^2}\right)+V(\boldsymbol{R})-E\right]\Psi(R,\theta,\phi)=0, \tag{5.27}$$

where $\hat{L}^2$ is the angular momentum operator for relative motion of the atoms and $E$ is the total energy. The total potential energy is $V(\boldsymbol{R})=V_{\rm rel}^{\rm trap}(\boldsymbol{R})+V_{\rm int}(\boldsymbol{R})$. To solve Eq. 5.27, we expand the wavefunction as

$$\Psi(R,\theta,\phi)=R^{-1}\sum_{LM}\psi_{LM}(R)Y_{LM}(\theta,\phi), \tag{5.28}$$

where $Y_{LM}(\theta,\phi)$ are spherical harmonics normalized to unity. Substituting the expansion (5.28) into Eq. 5.27 gives a set of coupled equations for the channel functions $\psi_{LM}(R)$,

$$\frac{d^2\psi_{LM}}{dR^2}=\sum_{L'M'}\left[W_{LM,L'M'}(R)-\mathcal{E}\delta_{LL'}\delta_{MM'}\right]\psi_{L'M'}(R), \tag{5.29}$$

where $\delta_{ij}$ is the Kronecker delta, $\mathcal{E}=2\mu E/\hbar^2$ and

$$\begin{aligned}W_{LM,L'M'}(R)&=\frac{L(L+1)}{R^2}\delta_{LL'}\delta_{MM'}\\&+\frac{2\mu}{\hbar^2}\int_0^{2\pi}\int_0^{\pi}Y_{LM}^*(\theta,\phi)V(R,\theta,\phi)Y_{L'M'}(\theta,\phi)\sin\theta\,d\theta\,d\phi.\end{aligned} \tag{5.30}$$

The contribution of $V_{\rm rel}^{\rm trap}(\boldsymbol{R})$ to $W_{LM,L'M'}(R)$ is

$$\begin{aligned}&\frac{2\mu}{\hbar^2}\sum_{\lambda\kappa}V_{\lambda\kappa}(R)(-1)^M[(2L+1)(2L'+1)]^{1/2}\\&\qquad\times\begin{pmatrix}L&\lambda&L'\\-M&\kappa&M'\end{pmatrix}\begin{pmatrix}L&\lambda&L'\\0&0&0\end{pmatrix}.\end{aligned} \tag{5.31}$$

If $\boldsymbol{R}_0$ lies along one of the principal axes of the traps, chosen as $Z$, the potential (5.17) is symmetric with respect to a proper rotation $C_2(Z)$, so the quantity $(-1)^M$ is conserved and separate calculations may be performed for even and odd $M$. In addition, basis functions for $M \neq 0$ are symmetrized,

$$\Phi_{LM}(\theta,\phi) = \tfrac{1}{\sqrt{2}}\left[Y_{LM}(\theta,\phi) \pm (-1)^M Y_{L-M}(\theta,\phi)\right] \tag{5.32}$$

and separate calculations are carried out for + and − symmetry. Only the functions of + symmetry for $M \neq 0$ are coupled to those for $M = 0$. Parity is not conserved, so functions for both even and odd $L$ must be included. If in addition $V_{\rm rel}^{\rm trap}(\boldsymbol{R})$ is cylindrically symmetric about the $z$ axis, the sum over $\kappa$ is limited to $\kappa = 0$. The coupled equations are then diagonal in $M$.

### 5.3.4 Solution of Coupled Equations

We solve the coupled equations to find bound states using the package BOUND [84, 178]. This propagates solutions of the coupled-channel equations for a trial energy from short range and from long range to a matching point $R_{\rm match}$ in the classically allowed intermediate region. It then converges upon energies at which the wavefunction and its derivative are continuous at $R_{\rm match}$, using the methods described in ref. [17] and Chapter 2. The coupled equations are propagated from $R = 0$ to $R_{\rm match} \approx R_0$ using the fixed-step symplectic log-derivative propagator of Manolopoulos and Gray [179] with a step size of 25 Å and from $R_{\rm max}$ to $R_{\rm match}$ using the variable-step Airy propagator of Alexander and Manolopoulos [118]. The outer limit of integration is chosen as

$$R_{\rm max} = \left[\sum_{\alpha=x,y,z} (\alpha_0 + \rho\beta_{{\rm rel},\alpha})^2\right]^{1/2}, \tag{5.33}$$

where $\rho$ is typically 4.

The present coupled-channel approach differs from the treatment of Stock et al. [201] in that it does not need basis sets for the interatomic distance $R$, which

is handled efficiently by the propagation. The $R$-dependent coupling matrices in our formulation are much smaller than the Hamiltonian matrix in a basis set that includes functions for $R$.

The size of the spherical-harmonic basis set required depends on $R_0$ and the trap geometry, and is discussed below.

It would be straightforward to apply the coupled-channel method with a realistic atom-atom potential $V_{\rm int}(R)$ in place of the contact potential. This would require a much smaller step size for the short-range part of the propagation, but the method would be otherwise unchanged.

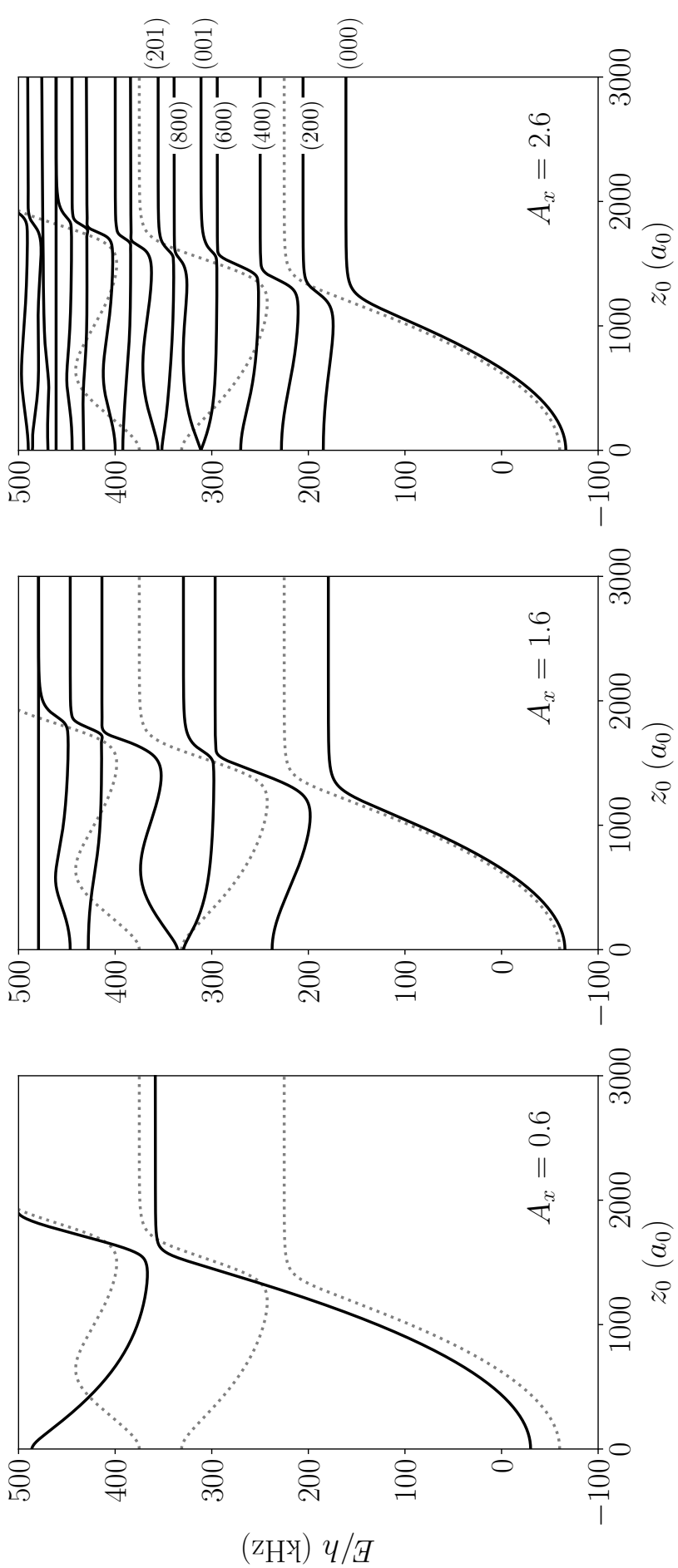


Figure 5.3: Energies of two atoms in separate tweezers as a function of trap separation, obtained from coupled-channel calculations. Each panel is for a different aspect ratio $A_x$, for $\beta_{\mathrm{rel},z} = \beta_{\mathrm{rel},y} \approx 677\ a_0$, corresponding to $\omega_{\mathrm{rel},z} = \omega_{\mathrm{rel},y} = 150$ kHz. The grey dotted lines correspond to the spherical case with $A_x = A_y = 1$.

## 5.4 Coupled-Channel Results

In this section we present coupled-channel results for a pair of cylindrically symmetric traps that approach one another along an axis perpendicular to their symmetry axis. This is close to the configuration that has been used experimentally to achieve mergoassociation of Rb and Cs atoms to form a weakly bound RbCs molecule [199]. It differs from the case considered in ref. [208], where the traps approach along their symmetry axis. We choose the axis $Z$ along the direction of approach and $X$ as the symmetry axis of the traps, with $\omega_{\mathrm{rel},y} = \omega_{\mathrm{rel},z}$. The separation of the traps is thus $z_0$, with $x_0 = y_0 = 0$. We represent the atom-atom interaction with a contact potential of the form (5.25), with a scattering length $a = 645\ a_0$ [128] appropriate for RbCs. This contact potential gives a binding energy $E_\mathrm{b} = 83$ kHz for the least-bound state of RbCs; this somewhat underestimates the true value $E_\mathrm{b} = 100 \pm 20$ kHz [128], because the universal binding-energy formula $E_\mathrm{b} = \hbar^2/(2\mu a^2)$ starts to break down at this depth [209]. Since a contact potential affects only states with a component of $M = 0$, we carry out calculations only for even $M$ and + symmetry.

We define aspect ratios $A_x = \beta_{\mathrm{rel},x}/\beta_{\mathrm{rel},z} = (\omega_{\mathrm{rel},z}/\omega_{\mathrm{rel},x})^{1/2}$ and $A_y = \beta_{\mathrm{rel},y}/\beta_{\mathrm{rel},z} = (\omega_{\mathrm{rel},z}/\omega_{\mathrm{rel},y})^{1/2}$. For the coupled-channel calculations in this section, with cylindrically symmetric traps, $A_y = 1$.

The size of the basis set required depends on the trap geometry and also increases with $R_0$. For the majority of the calculations described here, including functions up to $L_\mathrm{max} = 24$ gives convergence of the energies to 6 significant figures for the largest $R_0$ considered here. Calculations for $A_x \ll 1$ required $L_\mathrm{max} = 40$.

Figure 5.3 shows the energy levels for relative motion of two atoms in adjacent traps, as a function of trap separation, for various values of the aspect ratio $A_x$. In all cases, $\omega_{\mathrm{rel},z} = 150$ kHz. The dotted lines show the corresponding levels for a pair of spherical traps. At large separation, the energy levels of the trap states are those

of a 3-dimensional harmonic oscillator in the relative motion. These are

$$E_{n_x n_y n_z} = \hbar[(n_x + \tfrac{1}{2})\omega_{\mathrm{rel},x} + (n_y + \tfrac{1}{2})\omega_{\mathrm{rel},y} + (n_z + \tfrac{1}{2})\omega_{\mathrm{rel},z}]. \tag{5.34}$$

The energies shown are those for states that feel the influence of the contact potential, which are those with non-zero density at $R = 0$; for the trap states, this corresponds to limiting $n_x$ and $n_y$ to even values. The quantum numbers are shown for $A_x = 2.6$ in Fig. 5.3; this corresponds to $\omega_{\mathrm{rel},z} = 6.76\,\omega_{\mathrm{rel},x}$, so trap levels with $(n_x, n_y, n_z) = (2,0,0)$, (4,0,0) and (6,0,0) all lie below (0,0,1) at large $z_0$. For small separation ($z_0 \lesssim \beta_{\mathrm{rel},z}$), the trap states have substantial amplitude at $R = 0$, so they are significantly shifted by $V_{\mathrm{int}}(\boldsymbol{R})$. In the limit $z_0 = 0$, they correspond to the levels for two atoms in a cylindrically symmetric trap [210, 211].

Cutting through the trap states is a molecular level that is shifted quadratically by the trap potential at $R = 0$, which here is $\frac{1}{2}\mu\omega_{\mathrm{rel},z}^2 z_0^2$. There is an additional shift due to the curvature of the trap potential, as described in Sec. 5.5 below; this exists even at $z_0 = 0$. There are avoided crossings wherever the shifted molecular level would cross one of the trap levels. It is the lowest of these avoided crossings that allows mergoassociation to form a weakly bound molecule from a pair of atoms; this occurs when traps containing atoms in their relative motional ground state are merged slowly enough to traverse the avoided crossing adiabatically.

The lowest crossing occurs at $z_0 = z_0^{\mathrm{X}}$, where the shifted molecular level has the same energy as the lowest level of the trap. When the atom-atom interaction is represented as a contact potential, this is approximately

$$z_0^{\mathrm{X}} \approx \beta_{\mathrm{rel},z} \left(1 + A_x^{-2} + A_y^{-2} + A_a^{-2}\right)^{1/2}, \tag{5.35}$$

where $A_a = a/\beta_{\mathrm{rel},z}$. We locate this crossing numerically using the state energies from coupled-channel calculations and then determine its precise position and effective coupling matrix element $\Omega_{\mathrm{eff}}$ by a local fit of the energies near $z_0 = z_0^{\mathrm{X}}$ to the

eigenvalues of a $2 \times 2$ matrix

$$\begin{pmatrix} E_{\rm X} + d_{\rm mol}(z_0 - z_0^{\rm X}) & \Omega_{\rm eff} \\ \Omega_{\rm eff} & E_{\rm X} + d_{\rm at}(z_0 - z_0^{\rm X}) \end{pmatrix}, \tag{5.36}$$

where $E_{\rm X}$ is the central energy of the avoided crossing and $d_{\rm at}$ and $d_{\rm mol}$ are the gradients of the atom-pair and molecular states near $z_0^{\rm X}$. To a first approximation, $d_{\rm at} = 0$ and

$$d_{\rm mol} = \mu\omega_{{\rm rel},z}^2 z_0^{\rm X} = \frac{\hbar^2 z_0^{\rm X}}{\mu\beta_{{\rm rel},z}^4}. \tag{5.37}$$

This procedure accurately determines the point of closest approach between the two states, and interprets their separation at that point as $2\Omega_{\rm eff}$; however, it neglects effects due to other nearby states, so the resulting value of $\Omega_{\rm eff}$ can be an underestimate of the true matrix element between the two states when other avoided crossings overlap the lowest one, as seen for $A_x = 2.6$ in Fig. 5.3.

Figure 5.4 shows the resulting values of $\Omega_{\rm eff}$ as a function of aspect ratio $A_x$ for various values $\beta_{{\rm rel},z}$. The general form of $\Omega_{\rm eff}$ for any value of $\beta_{{\rm rel},z}$ is that it reaches a maximum at a value of $A_x$ near 1.3, corresponding to $\omega_{{\rm rel},z}/\omega_{{\rm rel},x} \approx 2$. There is a sharp dropoff in $\Omega_{\rm eff}$ at smaller values of $A_x$, and $\Omega_{\rm eff} \to 0$ as $A_x \to 0$. There is a much gentler dropoff at larger values of $A_x$. The origins of this behavior will be discussed in Section 5.5.

The semiclassical probability of traversing the avoided crossing adiabatically and thus forming a molecule may be calculated by numerical solution of the time-dependent Schrödinger equation. In a full treatment, this requires a derivative coupling matrix that may be obtained from the eigenstates as a function of $z_0$, which are available from the present calculation. A simple approximation to this is provided in the 2-state case by the Landau-Zener formula,

$$P_{\rm LZ} = \exp\left(\frac{-2\pi\Omega_{\rm eff}^2}{\hbar\,|(d_{\rm mol} - d_{\rm at})\,dz_0/dt|}\right), \tag{5.38}$$

where $dz_0/dt$ is the speed of relative motion of the traps at $z_0^{\rm X}$. In initial experimental

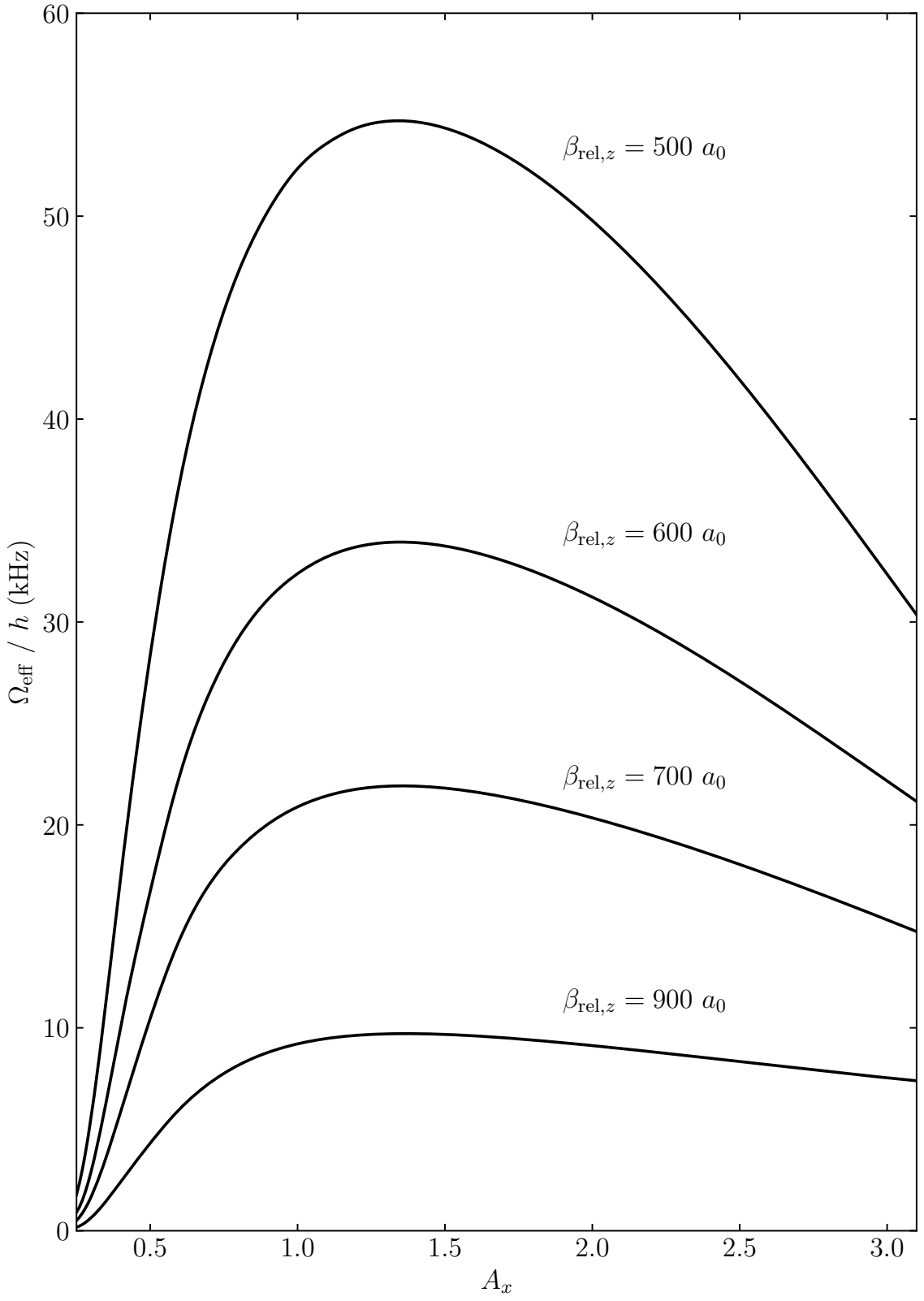


Figure 5.4: Effective matrix element $\Omega_{\mathrm{eff}}$ for the lowest avoided crossing, from coupled-channel calculations, as a function of aspect ratio $A_x$ for $A_y = 1$ and various values of $\beta_{\mathrm{rel},z}$.

work, Ruttley et al. [199] measured the probability of mergoassociation over the range $600\,a_0 \lesssim \beta_{\mathrm{rel},z} \lesssim 1500\,a_0$. They used tweezers with $A_x \approx 2.6$, but nevertheless found that the probabilities were well reproduced using theoretical crossing strengths calculated for spherical traps ($A_x = 1$). Figure 5.4 explains this result: the strength of the avoided crossing dies off only slowly for $A_x > 1.3$, and aspect ratios $1.5 < A_x < 2.6$ give crossing strengths qualitatively similar to those for $A_x = 1$.

## 5.5 Approximate Model

In this section we develop an approximate model that reproduces the main features of the coupled-channel results. This method can include both the relative and center-of-mass motions. Details of the entire method can be found in the Appendix. Our discussion of the center-of-mass levels is given in Chapter 6.

The Hamiltonian for relative motion may be written

$$\begin{aligned}\hat{H}_{\mathrm{rel}} &= \hat{T}_{\mathrm{rel}} + V_{\mathrm{rel}}^{\mathrm{trap}}(\boldsymbol{R}) + V_{\mathrm{int}}(\boldsymbol{R}) \\ &= \hat{H}_{\mathrm{rel}}^{\mathrm{trap}} + V_{\mathrm{int}}(\boldsymbol{R}) = \hat{H}_{\mathrm{int}} + V_{\mathrm{rel}}^{\mathrm{trap}}(\boldsymbol{R}),\end{aligned} \tag{5.39}$$

where $\hat{T}_{\mathrm{rel}}$ is the kinetic energy operator, $\hat{H}_{\mathrm{rel}}^{\mathrm{trap}}$ is the Hamiltonian for the nonspherical harmonic trap and $\hat{H}_{\mathrm{int}}$ is the Hamiltonian for the untrapped atom pair. If $V_{\mathrm{int}}(\boldsymbol{R})$ is represented as a contact potential as in Eq. 5.25, and $a > 0$, $\hat{H}_{\mathrm{int}}$ has a single molecular bound state, with eigenfunction

$$\psi_a = (2\pi a)^{-1/2} R^{-1} \exp(-R/a), \tag{5.40}$$

and eigenvalue

$$E_a = -\hbar^2/(2\mu a^2). \tag{5.41}$$

The eigenfunctions of $\hat{H}_{\mathrm{rel}}^{\mathrm{trap}}$ are products of harmonic-oscillator functions in $x$, $y$ and $z$,

$$\psi_{n_x n_y n_z}(x, y, z) = \psi_{n_x}(x - x_0)\psi_{n_y}(y - y_0)\psi_{n_z}(z - z_0), \tag{5.42}$$

where

$$\psi_n(\alpha) = (2^n n! \beta_{\mathrm{rel},\alpha})^{-1/2} \pi^{-1/4} H_n(\alpha/\beta_{\mathrm{rel},\alpha}) \times \exp(-\tfrac{1}{2}(\alpha/\beta_{\mathrm{rel},\alpha})^2) \tag{5.43}$$

and $H_n(q)$ is a Hermite polynomial. The corresponding eigenvalues are given by Eq. 5.34.

We consider a nonorthogonal basis set formed by the functions (5.40) and (5.42) and construct Hamiltonian and overlap matrices. The functions are normalized, so the diagonal elements of the overlap matrix **S** are all 1. The only non-zero off-diagonal elements are those between the bound-state function (5.40) and the harmonic-oscillator functions (5.42),

$$\begin{aligned} S_{a,n_x n_y n_z} &= \langle a | n_x n_y n_z \rangle \\ &= \int_0^{2\pi} \int_0^{\pi} \int_0^{\infty} \psi_a \psi_{n_x n_y n_z} r^2 dr \, \sin\theta d\theta \, d\phi. \end{aligned} \tag{5.44}$$

These are evaluated by 3-dimensional numerical quadrature, using Gauss-Laguerre quadrature for $r$, Gauss-Legendre quadrature for $\theta$ and equally spaced and weighted points for $\phi$.

The diagonal elements of the Hamiltonian matrix for the harmonic-oscillator functions are

$$H_{n_x n_y n_z, n_x n_y n_z} = E_{n_x n_y n_z} + \langle n_x n_y n_z | V_{\mathrm{int}}(\boldsymbol{R}) | n_x n_y n_z \rangle, \tag{5.45}$$

where for a contact potential

$$\langle n_x n_y n_z | V_{\mathrm{int}}(\boldsymbol{R}) | n_x n_y n_z \rangle = (2\pi\hbar^2 a/\mu) |\psi_{n_x}(x_0) \psi_{n_y}(y_0) \psi_{n_z}(z_0)|^2. \tag{5.46}$$

For the molecular function,

$$H_{aa} = E_a + \langle a|V_{\rm rel}^{\rm trap}(\boldsymbol{R})|a\rangle, \tag{5.47}$$

where

$$\langle a|V_{\rm rel}^{\rm trap}(\boldsymbol{R})|a\rangle = V_{\rm rel}^{\rm trap}(\boldsymbol{R}_0) + \frac{A_a^2}{12}\hbar\omega_{{\rm rel},z}(1 + A_x^{-4} + A_y^{-4}). \tag{5.48}$$

The second term accounts for the curvature of the trap potential. It is usually relatively small for $A_a \lesssim 1$, but is independent of $\boldsymbol{R}_0$, and is responsible for the shift of the molecular state at $z_0 = 0$ seen in Fig. 5.3, particularly at $A_x = 0.6$.

The off-diagonal elements of the Hamiltonian between harmonic-oscillator functions are

$$\begin{aligned} H_{n'_x n'_y n'_z, n_x n_y n_z} = {} & (2\pi\hbar^2 a/\mu)\psi_{n_x}(x_0)\psi_{n_y}(y_0)\psi_{n_z}(z_0) \\ & \times\psi_{n'_x}(x_0)\psi_{n'_y}(y_0)\psi_{n'_z}(z_0), \end{aligned} \tag{5.49}$$

while those between the harmonic-oscillator functions and the molecular function are

$$\begin{aligned} H_{a,n_x n_y n_z} = {} & E_{n_x n_y n_z} S_{a,n_x n_y n_z} \\ & - (\hbar^2/\mu)(2\pi/a)^{1/2}\psi_{n_x}(x_0)\psi_{n_y}(y_0)\psi_{n_z}(z_0). \end{aligned} \tag{5.50}$$

The equations above may be used in two ways. First, they may be used to produce complete energy-level diagrams as a function of $R_0$ or other parameters. For this, matrices **H** and **S** are evaluated using a substantial number of harmonic-oscillator basis functions, and then used to solve a generalized matrix eigenvalue problem $\mathbf{HC} = \mathbf{SCE}$ to produce eigenvectors **C** and a diagonal matrix of eigenvalues **E**. We illustrate this with the case investigated in Section 5.4, with two cylindrically symmetric traps and the intertrap vector perpendicular to the symmetry axis of the

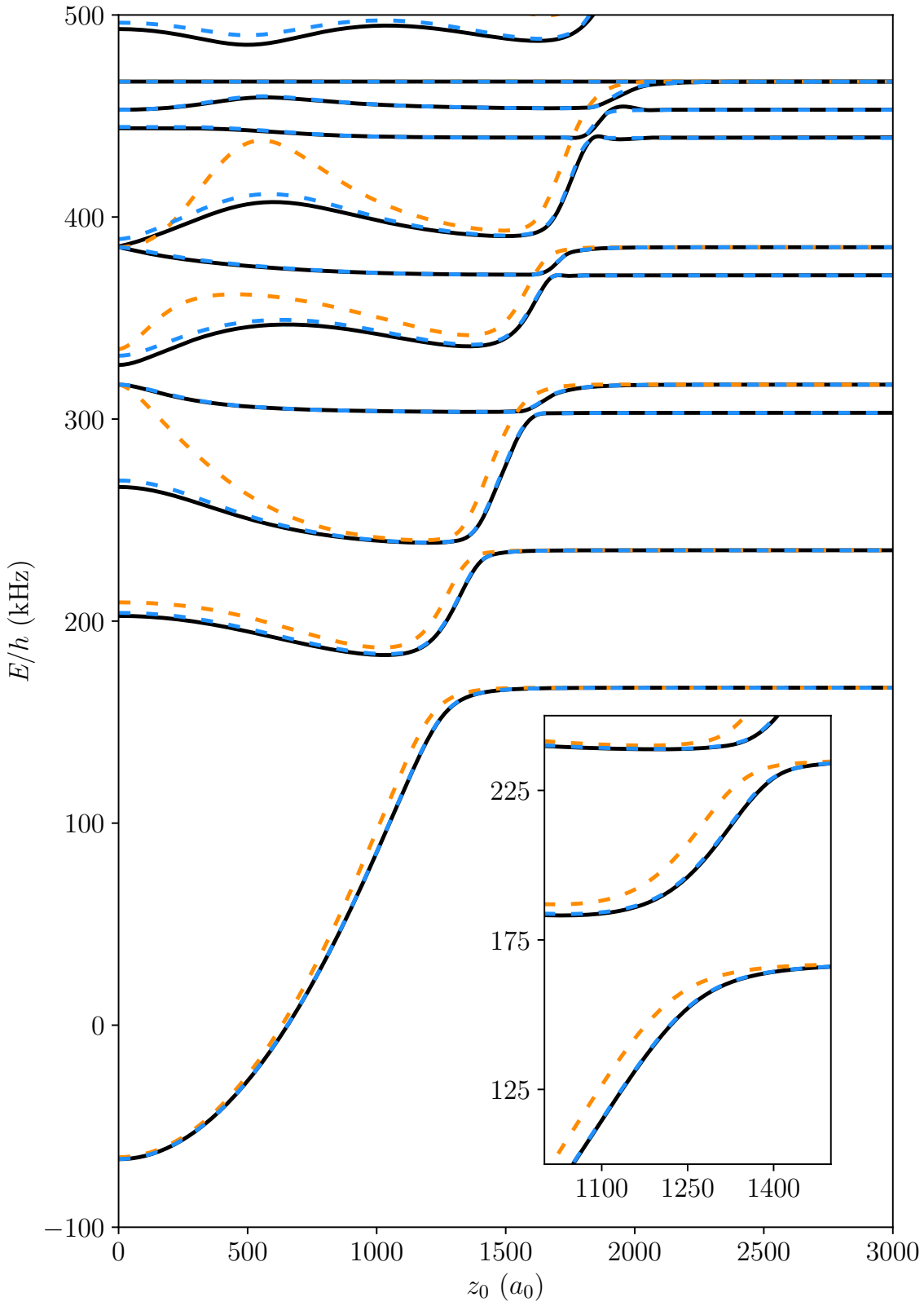


Figure 5.5: Energies of two atoms in separate tweezers as a function of trap separation for $A_x = 2.1$. Black lines show the results of coupled-channel calculations, while orange and blue dashed lines show basis-set calculations with $n_x, n_y, n_z \leq 2$ and 10, respectively. Other parameters are as in Fig. 5.3.

traps. Figure 5.5 shows the levels for $A_x = 2.1$, using harmonic-oscillator basis sets with $n_x, n_y, n_z \leq 2$ and 10, compared with the results of coupled-channel calculations. It may be seen that the basis-set approach gives qualitatively correct results even for a small basis set. However, it is not fully converged for small $z_0$ even for a large basis set. This arises because the true wavefunctions have cusps at $\boldsymbol{R} = 0$, due to the contact potential, and these cusps are poorly represented by an expansion in harmonic functions. They can be handled in spherical coordinates using parabolic cylinder functions in place of harmonic-oscillator functions [201], but such functions are inefficient for well-separated traps.

A much simpler application of the basis-set approach is to the strengths of avoided crossings that predominantly involve only the molecular state and a single harmonic-oscillator function. As in Sec. 5.4, we focus on the crossing between the molecular state and the lowest harmonic-oscillator state. Under these circumstances, the off-diagonal matrix element of the Hamiltonian between the two functions is

$$H_{a,000} = E_{000} S_{a,000} + \langle a | V_{\rm int}(\boldsymbol{R}) | 000 \rangle, \tag{5.51}$$

where

$$\langle a | V_{\rm int}(\boldsymbol{R}) | 000 \rangle = -\frac{\hbar^2}{\mu} \left( \frac{2 \exp[-\frac{1}{2}(z_0^{\rm X}/\beta_{{\rm rel},z})^2]}{\sqrt{\pi} a \beta_{{\rm rel},x} \beta_{{\rm rel},y} \beta_{{\rm rel},z}} \right)^{1/2}. \tag{5.52}$$

If $z_0^{\rm X}$ is taken from Eq. 5.35, this may be written

$$-\hbar\omega_{{\rm rel},z} \left( \frac{2 \exp[-\frac{1}{2}(1 + A_x^{-2} + A_y^{-2} + A_a^{-2})]}{\sqrt{\pi} A_x A_y A_a} \right)^{1/2}. \tag{5.53}$$

If the overlap integral $S_{a,000}$ is neglected, Eq. 5.53 provides an analytic first approximation to the effective matrix element $\Omega_{\rm eff}$, as shown by the dotted lines in Fig. 5.6. It also shows that the sharp dropoff in $\Omega_{\rm eff}$ at small values of $A_x$ occurs because $z_0^{\rm X}$ increases sharply as $A_x$ decreases, due to the term involving $A_x^{-2}$ in Eq. 5.35. Conversely, the much slower dropoff at large $A_x$ occurs because of the

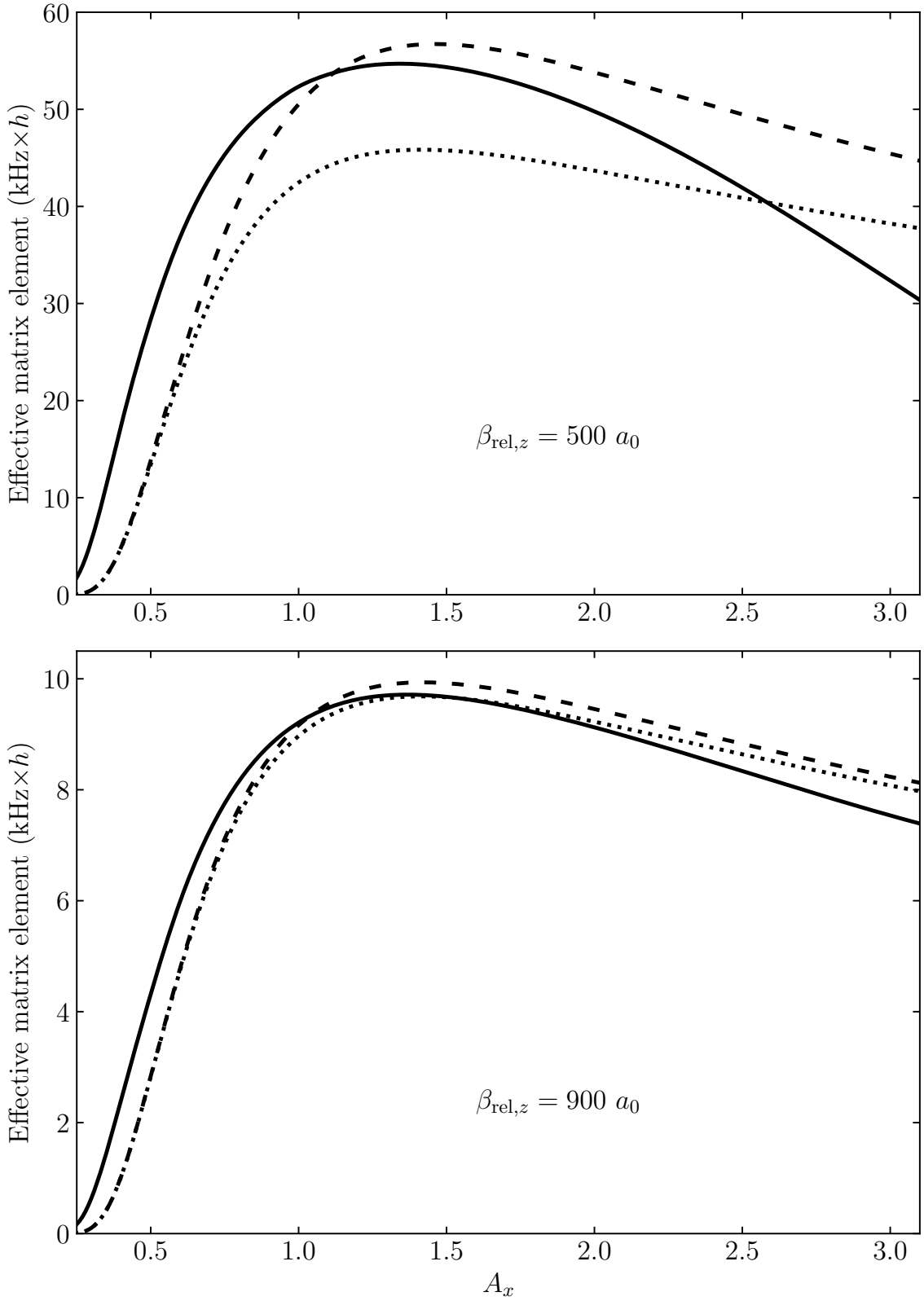


Figure 5.6: Effective matrix element for the lowest avoided crossing as a function of aspect ratio $A_x$ for $A_y = 1$ and two values of $\beta_{\mathrm{rel},z}$; results shown are $\Omega_{\mathrm{eff}}$ from coupled-channel calculations (black), $|\langle a|V_{\mathrm{int}}(\boldsymbol{R})|000\rangle|$ from Eq. 5.53 (dotted), and $|\Omega_{\mathrm{eff}}^{2\times2}|$ from Eq. 5.55 (dashed).

harmonic-oscillator normalization factor involving $\beta_{\mathrm{rel},x}^{-1/2}$ in Eq. 5.52.

Equations 5.52 and 5.53 are derived here for a contact potential. More generally, however, the wavefunction for a molecular state with binding energy $E_\mathrm{b}$ is asymptotically of the form $R^{-1}\exp(-kR)$, where $k = (2\mu E_\mathrm{b}/\hbar^2)^{1/2}$ and $k^{-1}$ plays the role of an effective scattering length. This is valid even when $E_\mathrm{b}$ is too large to be represented by Eq. 5.41 with the true scattering length $a$. For fixed $A_x$ and $A_y$, the quantity $\Omega_\mathrm{eff}^2$ that appears in the Landau-Zener formula (5.38) is thus approximately proportional to

$$\omega_{\mathrm{rel},z}^2 \tilde{E}_\mathrm{b}^{1/2} \exp(-\tilde{E}_\mathrm{b}), \tag{5.54}$$

where $\tilde{E}_\mathrm{b} = E_\mathrm{b}/(\hbar\omega_{\mathrm{rel},z})$. The strength of the avoided crossing decreases sharply for $\tilde{E}_\mathrm{b} \gg 1$, and the binding energies of the molecules that can be formed by mergoassociation are likely to be limited by the trap frequencies that can be achieved.

It may be noted that, for the case $A_y = 1$ and neglecting overlap, Eq. 5.53 predicts that the maximum value of $\Omega_\mathrm{eff}$ appears at $A_x = \sqrt{2}$ for all values of $\beta_{\mathrm{rel},z}$. This agrees remarkably well with the coupled-channel results in Fig. 5.4. The analytic expression shows a maximum for $A_x = \sqrt{2}$, qualitatively explaining the maximum near $A_x = 1.3$ found from coupled-channel calculations.

If the effects of wavefunction overlap are included, the half-separation between the eigenvalues of the $2 \times 2$ generalized eigenvalue problem at the point of closest approach is

$$\Omega_\mathrm{eff}^{2\times2} = \frac{\langle a|V_\mathrm{int}(\boldsymbol{R})|000\rangle - \langle 000|V_\mathrm{int}(\boldsymbol{R})|000\rangle S_{a,000}}{1 - S_{a,000}^2}. \tag{5.55}$$

This is nonanalytic, because the overlap integral $S_{a,000}$ must be evaluated by numerical quadrature. Nevertheless, the evaluation is straightforward. The values of $\Omega_\mathrm{eff}^{2\times2}$ from Eq. 5.55 are shown by the dashed lines in Fig. 5.6.

Figure 5.6 shows that Eq. 5.53 provides a qualitatively reasonable approximation to $\Omega_\mathrm{eff}$ at large $\beta_{\mathrm{rel},z}$, but that the approximation breaks down for smaller $\beta_{\mathrm{rel},z}$, particularly for large $A_x$. Eq. 5.55 improves the agreement when the overlap is moderate. However, both equations underestimate $\Omega_\mathrm{eff}$ for $A_x < 1$. This is due

mainly to approximating $z_0^{\mathrm{X}}$ by Eq. 5.35, which neglects the second term in Eq. A.8 and thus overestimates $z_0^{\mathrm{X}}$. There are also remaining discrepancies at high $A_x$, particularly for smaller $\beta_{\mathrm{rel},z}$. These arise because, for $z_0 \lesssim 2\beta_{\mathrm{rel},z}$ and $A_a \gtrsim 1$, the trap states are strongly shifted and mixed by $V_{\mathrm{int}}(\boldsymbol{R})$. For $A_x^{-2} + A_a^{-2} \lesssim 1$, $z_0^{\mathrm{X}}$ from Eq. 5.35 is small enough that this mixing is important and the lowest crossing is not well characterized by $H_{a,000}$ and $S_{a,000}$ alone. Under these circumstances it is necessary to use a larger basis set, rather than the $2 \times 2$ approximation implicit in Eqs. 5.52 and 5.55.

An important point to note is that, for a contact potential, the results may be expressed in dimensionless form, with all lengths (including $a$) expressed with respect to a single length scale ($\beta_{\mathrm{rel},z}$ here) and all energies expressed with respect to a corresponding energy scale $\hbar\omega_{\mathrm{rel},z}$. The results from both coupled-channel calculations and the basis-set approach are "universal" for given values of $A_x$, $A_y$ and $A_a$ when expressed in these units. Results for values of $a$ that differ from $a = 645\ a_0$ used here may thus be obtained by appropriate scalings of the harmonic lengths and energies, without additional calculations.

The coupled-channel approach of Sec. 5.3 can be applied for any interaction potential $V_{\mathrm{int}}(\boldsymbol{R})$. However, the basis-set approach cannot be applied for interaction potentials that are non-integrable near $R = 0$, as is the case for most realistic atom-atom potentials. It also cannot be applied for contact potentials corresponding to $a < 0$, because the molecular function (5.40) then cannot be normalized. Furthermore, it requires very large basis sets of harmonic-oscillator functions when $A_a \gg 1$ and $R_0 \lesssim \beta_{\mathrm{rel},z}$.

### 5.5.1 Errors in Approximations to $\Omega_{\mathrm{eff}}$

This section constitutes a detailed discussion of all the various approximations to, and errors in our calculation of, $\Omega_{\mathrm{eff}}$. With an appropriately sized basis set, and converged propagation parameters, the results of the coupled-channel calculations are exact. Our procedure for obtaining $\Omega_{\mathrm{eff}}$ from these converged coupled-channel

calculations, the results presented in Figure 5.4, assumes that the avoided crossing between the least bound state and the lowest trap state is isolated from excited trap states. As explained in Section 5.4, a local fit to the $2 \times 2$ matrix in Equation 5.36 is used to extract $\Omega_{\text{eff}}$. We expect this procedure to break down for $A_x \gg 1$ when the energy separation between the states of the trap is small. More advanced $N \times N$ fits could improve this limitation. This particular procedure doesn't rely on any approximation to $z_0^X$.

The basis-set method, by contrast, is not numerically exact. The non-orthogonal basis set is particularly poor for $z_0 \to 0$. Furthermore, for $z_0 \gg 0$ the Hamiltonian matrix we calculate has large off-diagonal matrix elements, and the excited trap states are strongly coupled to the loosley bound molecular state and lowest trap state. We have already showed, in Figure 5.5, that restricting the basis set in our method leads to unconverged results. We don't expect the basis set method's inaccuracy at $z_0 \approx 0$ to impact any approximation made to $\Omega_{\text{eff}}$, which is almost always calculated at many hundreds of bohr. However, it is likely that using the basis-set method as well as a $2 \times 2$ approximation will, in certain limits, introduce quite large errors into approximations of $\Omega_{\text{eff}}$.

Using the basis set method we obtain the $2 \times 2$ matrix representation of the relative-motion Hamiltonian,

$$\begin{pmatrix} E_{\text{b}} + \langle a|\hat{V}_{\text{harm}}|a\rangle & E_{n_x n_y n_z} S_{a,n_x n_y n_z} + \langle n_x n_y n_z|\hat{V}_{\text{int}}|a\rangle \\ E_{n_x n_y n_z} S_{a,n_x n_y n_z} + \langle n_x n_y n_z|\hat{V}_{\text{int}}|a\rangle & E_{\text{harm}} + \langle n_x n_y n_z|\hat{V}_{\text{int}}|n_x n_y n_z\rangle \end{pmatrix}. \quad (5.56)$$

When using Equation 5.56 to approximate $\Omega_{\text{eff}}$ we are no longer converging on a value of $z_0^X$, it is approximated with Equation 5.35. A simple equality is used in the derivation of Equation 5.35; at some value of $z_0$, $z_0^X$, the energies of the molecular state must equal the energy of the first trap state. The energy of the trap state is the ground state of the harmonic trap. The energy of the molecular state is approximated as $E_{\text{b}} + \mu\omega_{\text{rel},z}^2 z_0^2/2$. The approximations made to the effective-matrix element in the previous section, Figure 5.6, using Equation 5.56 are either the full

$2 \times 2$ eigenvalues or $\langle n_x n_y n_z | \hat{V}_{\text{int}} | a \rangle$.

Consider an artificial system with a scattering length of 250 $a_0$ and the same reduced mass as RbCs. In this model scenario two traps with $\beta_{\text{rel,z}} = 500$ $a_0$ are being mergoassociated.

Figure 5.7 shows that our approximation to $z_0^X$ (vertical dashed line) is reasonably accurate for $A_a \approx 0.5$ and $A_x \geq 1$. It is clear that in case of $A_x = 0.4$ our approximation of $z_0^X$ is an overestimation. As such any approximation made to $\Omega_{\text{eff}}$ with Equation 5.56 will be an overestimation because the gap between the molecular state and the trap state is inflated. The $2 \times 2$ approximation also overestimates the binding energy of the molecular state at $z = 0$ for $A_x = 0.4$. Consequently, in the $2 \times 2$ case the avoided crossing appears at larger values. The top right panel in Figure 5.7 shows a substantial shift in binding energy at $z_0 = 0$ due to the first order $\langle a | \hat{V}_{\text{harm}} | a \rangle$ term. Such a large correction does not occur for $A_x > 1$. This term is evaluated numerically in our implementation of the basis set method but is equal to

$$\frac{\mu \omega_z^2}{12} \left(1 + A_x^{-4} + A_y^{-4}\right) a^2, \tag{5.57}$$

at $z_0 = 0$. The black dot on the RHS panels of Figure 5.7 is the shift in $E_{\text{b}}$ we expect from $\langle a | \hat{V}_{\text{harm}} | a \rangle$, obtained with the converged calculations. The first-order correction to this shift is clearly an overestimation. This suggests that there are higher order corrections to $E_{\text{b}}$ that mitigate the first order effects. We previously commented on the large off-diagonal elements between excited trap states in light of the qualitative conclusions concerning basis set size drawn from Figure 5.5. We hypothesised that it may be advantageous to include the analytical expression for $\langle a | \hat{V}_{\text{harm}} | a \rangle$ in our approximation of $z_0^X$, in the hope that we would gain a more accurate estimation of the crossing position. It should be noted that such a step would only be valuable if it were to accurately reproduce the binding energy of the molecular state for $A_x < 1$, this particular problem is not relevant to $A_x \geq 1$. However, in light of the effect of neglecting the higher order terms, including $\langle a | \hat{V}_{\text{harm}} | a \rangle$ will not be sufficient. This correction will simply just over correct the

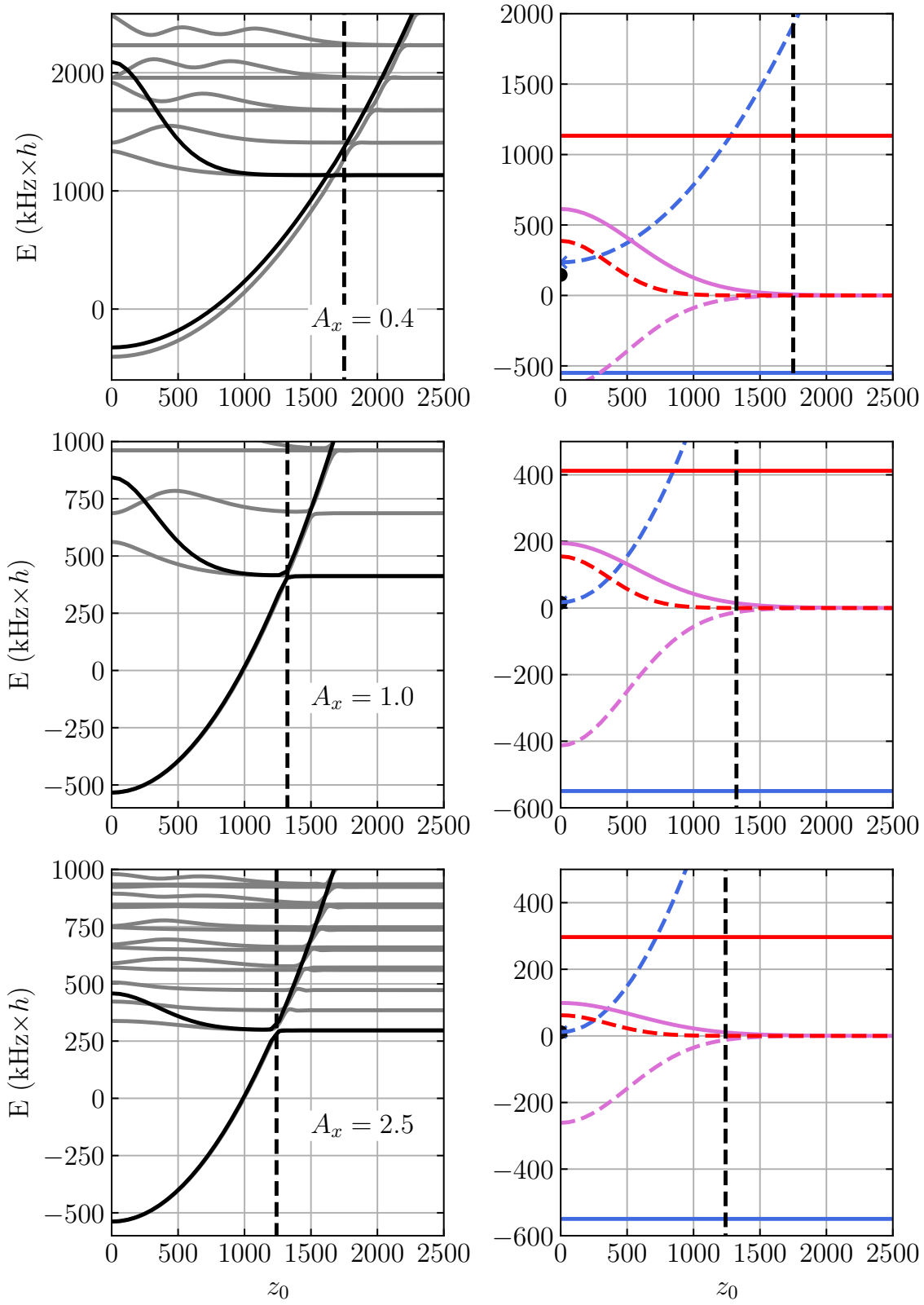


Figure 5.7: LHS: bound state spectra for $a = 250.0$ a$_0$, $\beta_{\mathrm{rel,z}} = 500$ a$_0$, and a series of different aspect ratios. Eigenvalues from 2×2 (black) and $397 \times 397$ (grey) calculation are shown. RHS: terms featuring in 5.56. The blue solid (dashed) line is $E_{\mathrm{b}}$ ($\langle a|\hat{V}_{\mathrm{harm}}|a\rangle$). Black dot is the 'actual' shift of molecular state due to the trap.

current estimate and therefore give us a similar, if not worse prediction of $z_0$.

Mergoassociation is most effective when the scattering length is large compared to the length of the trap. Understanding the poor performance of our approximations to $\Omega_{\text{eff}}$ in this scenario is therefore important. Consider the RbCs system with a scattering length of 645 $a_0$, being mergoassociated in traps with $\beta_{\text{rel,z}} = 500$ $a_0$. This example is identical to parameters given for the results presented in the top panel of Figure 5.6. The following discussion explains errors in our approximations to $\Omega_{\text{eff}}$ when $a \geq \beta_{\text{rel,z}}$.

Figure 5.8 shows that the approximations made in our basis-set method break down much more dramatically for the case where $a > \beta_{\text{rel,z}}$. This is to be expected as the length scale of the interaction, the scattering length, exceeds the magnitude of our trap potential. The harmonic oscillator functions in our basis do not meet the boundary condition required by the contact potential operator. For each aspect ratio the position of the lowest avoided crossing is poorly approximated by 5.35. This is because the zero-order binding energy is substantially shifted by the harmonic oscillator trap potential.

It is immediately clear from Figure 5.8 that the $2 \times 2$ Hamiltonian matrix (black lines) does a poor job at capturing the features of the converged bound state spectrum (grey lines) for all aspect ratios when $a > \beta_{\text{rel,z}}$. This is markedly different to Figure 5.7 where there are only, relatively small, errors for the $A_x = 0.4$ case. It is also evident from Figure 5.8 that our estimate of $z_0^X$ is poorer when $a > \beta_{\text{rel,z}}$. In practice this results in any evaluation of Equation 5.56, in order to approximate $\Omega_{\text{eff}}$, will be inflated as eigenvalues to the right of the avoided crossing will have been used. With a larger scattering length more serious errors are introduced to $\langle a|\hat{V}_{\text{harm}}|a\rangle$. As show by comparing the black dot on the RHS of Figure 5.8 to the blue dashed line the neglect of higher-order terms leads to a serious overestimation of the shift in the binding energy of the loosley bound molecular state due to the expectation value of its wavefunction over the trap potential.

We have also taken the chance to reanalyse our findings using reduced units.

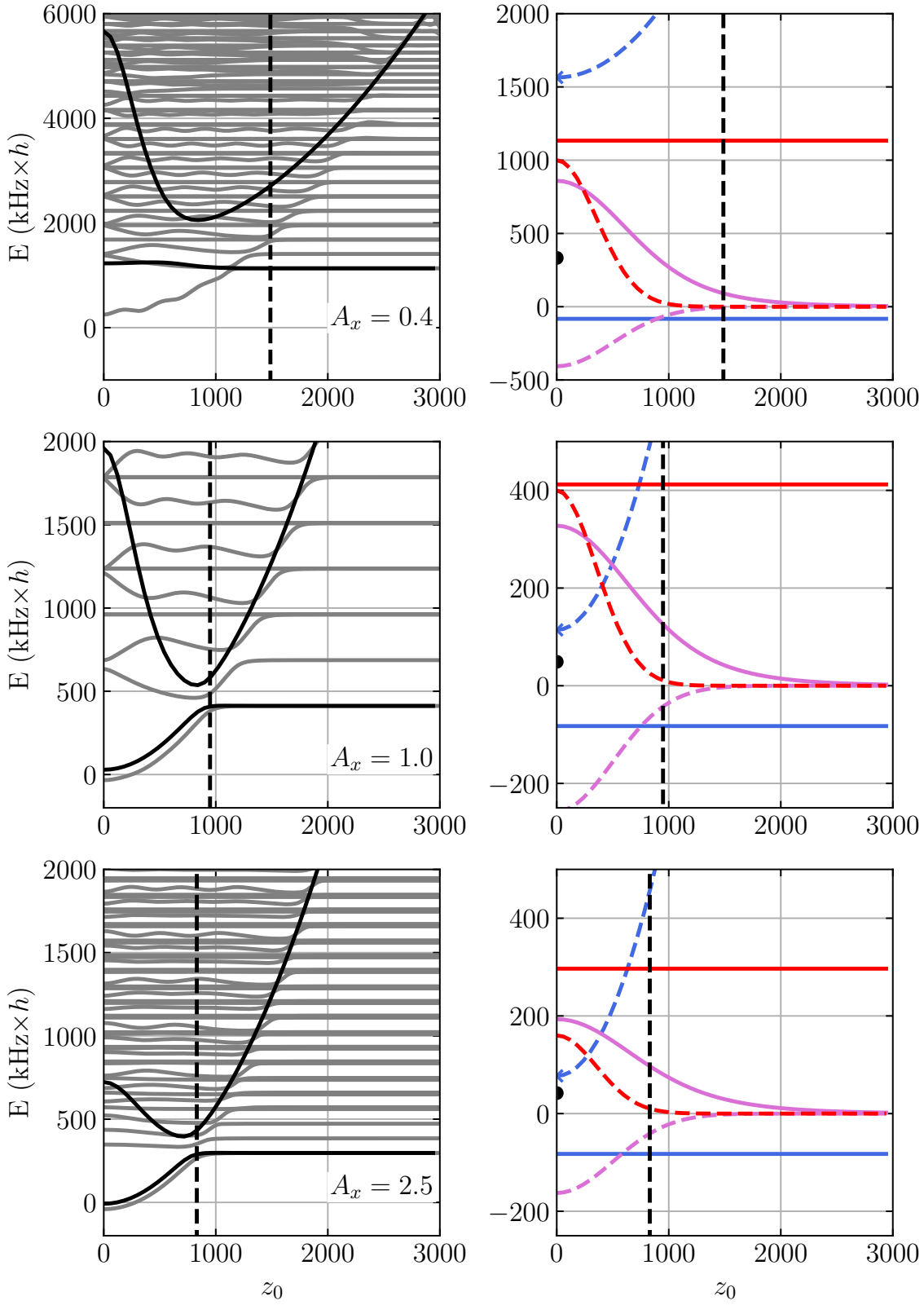


Figure 5.8: LHS: bound state spectra for $a = 645.0$ a$_0$, $\beta_{\mathrm{rel,z}} = 500$ a$_0$, and a series of different aspect ratios. Eigenvalues from 2×2 (black) and $397 \times 397$ (grey) calculation are shown. RHS: terms featuring in 5.56. The blue solid (dashed) line is $E_{\mathrm{b}}$ ($\langle a|\hat{V}_{\mathrm{harm}}|a\rangle$). Black dot is the 'actual' shift of molecular state due to the trap.

The previous two examples were designed to offer a more practical analysis that can easily be mapped onto certain system. The following is designed to help disentangle the break down of our various approximations with $A_a$ and $A_x$, reframe the previous discussion with respect to reduced units, and conclude the analysis presented in this section.

The calculations presented in Figure 5.9 used $\beta_z = 500$ $a_0$ ($\omega_z \approx 277$ kHz). Several values of $A_a = 0.5, 1.0, 1.5$ were used in an attempt to cover various scenarios where the ratio of the scattering length to the trap length are small to large. Two values of $A_x = 0.5$ and $A_x = 2.5$ are used for each value of $A_a$, so we are in the limits of very small aspect ratio and very large aspect ratio. Dimensionless units are used throughout, as such these results are applicable to all systems. From Figure 5.9 we see that our approximation of $z_0^X$ is bad for $A_x \ll 1$. As such using the $2 \times 2$ Hamiltonian to approximate $\Omega_{\text{eff}}$ will result in an overestimation for all $A_a$, and scattering lengths. Our estimation of $z_0^X$ is good for $A_x \gg 1$. At the values of $z_0$ of interest, i.e. $z_0^X$, the $2 \times 2$ Hamiltonian captures the eigenvalues of the molecular and lowest trap state to varying levels of accuracy, that depends on the interplay between $A_a$ and $A_x$. For large $A_a$ the eigenvalues are erroneous, the magnitude of this error is more sever at $A_x \gg 1$, although it is also poor for $A_x \ll 1$.

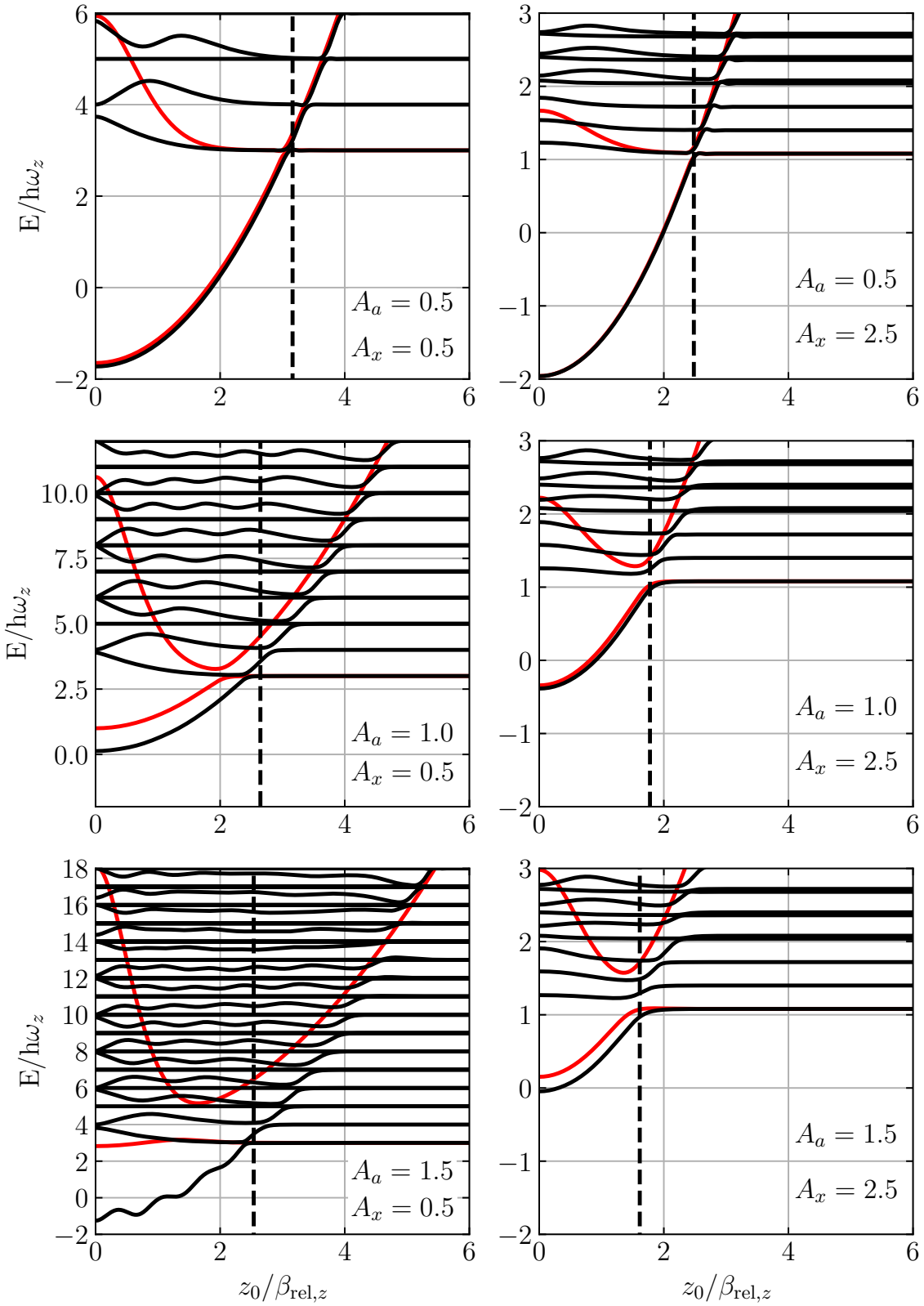


Figure 5.9: Comparison of eigenvalues obtained with $2 \times 2$ (red) and $397 \times 397$ (black) Hamiltonian for different combinations of $A_a$ and $A_x$. Dashed vertical lines show approximation of $z_0^X$ obtained with Equation 5.35

## 5.6 Conclusions

We have developed the theory of pairs of atoms in adjacent nonspherical traps. This is important for understanding mergoassociation [199], in which weakly bound molecules are formed during the merging of two optical tweezers or cells of an optical lattice. For harmonic traps, we find that the separation of relative and center-of-mass motion is similar to that for two atoms in a single trap [206], but with a different coupling term between the motions.

We have developed a coupled-channel approach that can be used for the relative motion of atom pairs in harmonic traps with arbitrary anisotropy and arbitrary relative orientation. We have solved the coupled equations for pairs of coaligned nonspherical traps, as a function of trap separation. We approximate the atom-atom interaction here by a contact potential, but the method can be readily extended to handle other interaction potentials. If the molecule formed from the two atoms has a weakly bound state, it undergoes avoided crossings, as a function of trap separation, with the states of the trapped atom pair. Merging two traps that each contain an atom in its lowest motional state can thus form a molecule by adiabatic passage across the lowest-energy avoided crossing. This is mergoassociation.

We focus on the case important for mergoassociation with optical tweezers, where two traps that are individually cylindrical are merged along an axis $Z$ perpendicular to their symmetry axis $X$. The confinement along these axes is characterized by harmonic lengths $\beta_{\mathrm{rel},z}$ and $\beta_{\mathrm{rel},x}$, respectively, with aspect ratio $A_x = \beta_{\mathrm{rel},x}/\beta_{\mathrm{rel},z}$. The strength of the avoided crossing depends strongly on the aspect ratio: for fixed $\beta_{\mathrm{rel},z}$, it has a maximum near $A_x = 1.3$. In initial experimental work on mergoassociation [199], it was found that experiments with $A_x \approx 2.6$ were well reproduced by theory based on spherical traps ($A_x = 1$). This is coincidental: $A_x = 1$ and 2.6 give similar crossing strengths simply because they lie on opposite sides of the maximum.

We have developed an approximate model of the energy levels for separated traps. This uses a nonorthogonal basis set that combines a single molecular function with

a set of Cartesian harmonic-oscillator functions for the trap states. The model gives reasonably accurate energy levels near the avoided crossing that is important for mergoassociation, though the harmonic-oscillator basis set converges slowly for small trap separations. In its simplest form, with only a single harmonic-oscillator function, the model gives an analytic expression for the crossing strength if overlap between the molecular and harmonic-oscillator functions is neglected. The analytic expression shows a maximum for $A_x = \sqrt{2}$, qualitatively explaining the maximum near $A_x = 1.3$ found from coupled-channel calculations.

The methods developed in this paper will help understand and predict the efficiency of mergoassociation, both with optical tweezers and with transport in an optical lattice. This will allow efficient conversion of atom pairs into molecules for systems with weakly bound states, even if they do not possess resonances suitable for magnetoassociation. It may also be possible to extend mergoassociation to more complex systems, involving molecules or Rydberg atoms. The avoided crossing characterized here also offers opportunities for high-fidelity two-qubit quantum logic operations with atom pairs [200–202].

# Chapter 6

# Mergoassociation with Optical Tweezers: Part II

This chapter is a reproduction of the following publication: R. C. Bird and J. M. Hutson, *Making molecules by mergoassociation: the role of center-of-mass motion*, 2024. The above is a preprint available from arXiv:2411.13393, and is currently being reviewed for publication. J. M. Hutson supervised theoretical work.

## 6.1 Introduction

Recent experiments [199] have shown that two ultracold atoms, confined in separate optical traps or tweezers, may combine to form a weakly bound molecule when the traps are merged. The process occurs because the energies of high-lying molecular states cross the energy of the atom pair as a function of trap separation. Coupling between the atom-pair and molecular states generates an avoided crossing between the states. Atom pairs can thus be converted into molecules by adiabatic passage as the traps are merged. The process is known as *mergoassociation* and has great potential for creating ultracold molecules that are inaccessible with other methods. The levels involved are discussed in the previous chapter.

The levels produced when two traps merge were first studied by Stock et al. [201, 202]. They considered two atoms that are identically trapped. Under these circumstances, with harmonic traps, there is an exact separation of the motions in the relative and center-of-mass coordinates. Their calculations dealt entirely with the relative motion and with spherical traps. Following the experimental work [199], which was carried out with Rb and Cs atoms in nonidentical optical tweezers with large anisotropy, we extended the formal theory to handle nonidentical, anisotropic traps. However, the numerical calculations presented in the previous chapter were still limited to the relative motion, neglecting coupling to the motion of the center of mass.

The purpose of the present paper is to investigate the influence of center-of-mass motion on the energy levels involved in mergoassociation and to consider their implications for experiments. Idziaszek et al. [203] briefly considered the coupling between the relative and center-of-mass motions for atom-ion interactions in one

dimension and commented that certain avoided crossings were weaker. However, the problem has not been considered in 3 dimensions and the dependence of the level patterns on the coupling strength has not been explored. The influence of coupling between the relative and center-of-mass motions on the levels that arise for two interacting particles in a single trap has been studied more extensively [206, 212–216].

The structure of this paper is as follows. Section 6.2 introduces the problem and describes the methods we use, including an important modification of the molecular basis functions that dramatically improves convergence. Section 6.3 uses the example of RbCs to explore the effects of the coupling between relative and center-of-mass motions for both weak and strong coupling (Sections 6.3.1 and 6.3.2). We consider the consequences of the coupling for mergoassociation starting from atoms either in their motional ground states or in motionally excited states. This section also explores mergoassociation for other systems, considering the examples of RbSr, RbYb and CsYb (Section 6.3.3), the effect of the strong anisotropy of the tweezer traps used in current experiments (Section 6.3.4), and the potential use of moveable traps to construct quantum logic gates (Section 6.3.5). Finally, Section 6.4 presents our conclusions.

## 6.2 Theoretical Methods

In the previous chapter we developed a theory of mergoassociation for pairs of non-identical nonspherical traps and a basis-set approach that gives accurate results for the energy levels of relative motion for separated traps. This uses a nonorthogonal basis set made up of 3-dimensional harmonic-oscillator functions centered at $\boldsymbol{R} = \boldsymbol{R}_0$, supplemented with a single function $\psi_a$ for the molecular state. The

Hamiltonian for relative motion may be written

$$\begin{aligned}\hat{H}_{\rm rel} &= \hat{T}_{\rm rel} + V_{\rm rel}^{\rm trap}(\boldsymbol{R}) + V_{\rm int}(\boldsymbol{R}) \\ &= \hat{H}_{\rm rel}^{\rm trap} + V_{\rm int}(\boldsymbol{R}) = \hat{H}_{\rm int} + V_{\rm rel}^{\rm trap}(\boldsymbol{R}),\end{aligned} \tag{6.1}$$

where $\hat{H}_{\rm rel}^{\rm trap}$ is the Hamiltonian for the nonspherical harmonic trap and $\hat{H}_{\rm int}$ is the Hamiltonian for the untrapped atom pair. If $V_{\rm int}(\boldsymbol{R})$ is represented as a contact potential at the origin [207] that corresponds to scattering length $a > 0$, $\hat{H}_{\rm int}$ has a single molecular bound state, with eigenfunction $\psi_a = (2\pi a)^{-1/2} R^{-1} \exp(-R/a)$, and eigenvalue $E_a = -\hbar^2/(2\mu a^2)$. The elements of the Hamiltonian and overlap matrices for relative motion are summarized in the Appendix.

Here we extend this approach to take account of motion in the center-of-mass coordinate $\boldsymbol{\mathcal{R}}$. The full Hamiltonian is

$$\hat{H} = \hat{H}_{\rm rel} + \hat{H}_{\rm com}^{\rm trap}(\boldsymbol{\mathcal{R}}) + V_{\rm cpl}^{\rm trap}(\boldsymbol{R}, \boldsymbol{\mathcal{R}}), \tag{6.2}$$

where $\hat{H}_{\rm com}^{\rm trap}(\boldsymbol{\mathcal{R}}) = \hat{T}_{\rm com} + V_{\rm com}^{\rm trap}(\boldsymbol{\mathcal{R}})$.

### 6.2.1 Direct-Product Approach

The simplest approach is to multiply each function in the basis set for relative motion with a set of 3-dimensional harmonic-oscillator functions in the center-of-mass coordinate. The harmonic functions are all eigenfunctions of $\hat{H}_{\rm com}^{\rm trap}(\boldsymbol{\mathcal{R}})$, which are centered at $\boldsymbol{\mathcal{R}} = \boldsymbol{\mathcal{R}}_0$. The resulting direct-product functions are represented by Dirac kets $|n_x n_y n_z N_X N_Y N_Z\rangle$ or $|a N_X N_Y N_Z\rangle$, and the resulting matrix elements are given in the Appendix. For spherical traps or traps displaced along $z$, the basis set may be factorized into 4 symmetry blocks with $n_x + N_x$ and $n_y + N_Y$ either even (E) or odd (O), and calculations are carried out for each block separately.

Figure 6.1 shows an example of energy levels for Rb and Cs in separated spherical traps as a function of $z_0$. These are calculated with a scattering length $a = 554\ a_0$; this corresponds to a bound-state energy $E_a/h \approx -112$ kHz, suitable for RbCs at

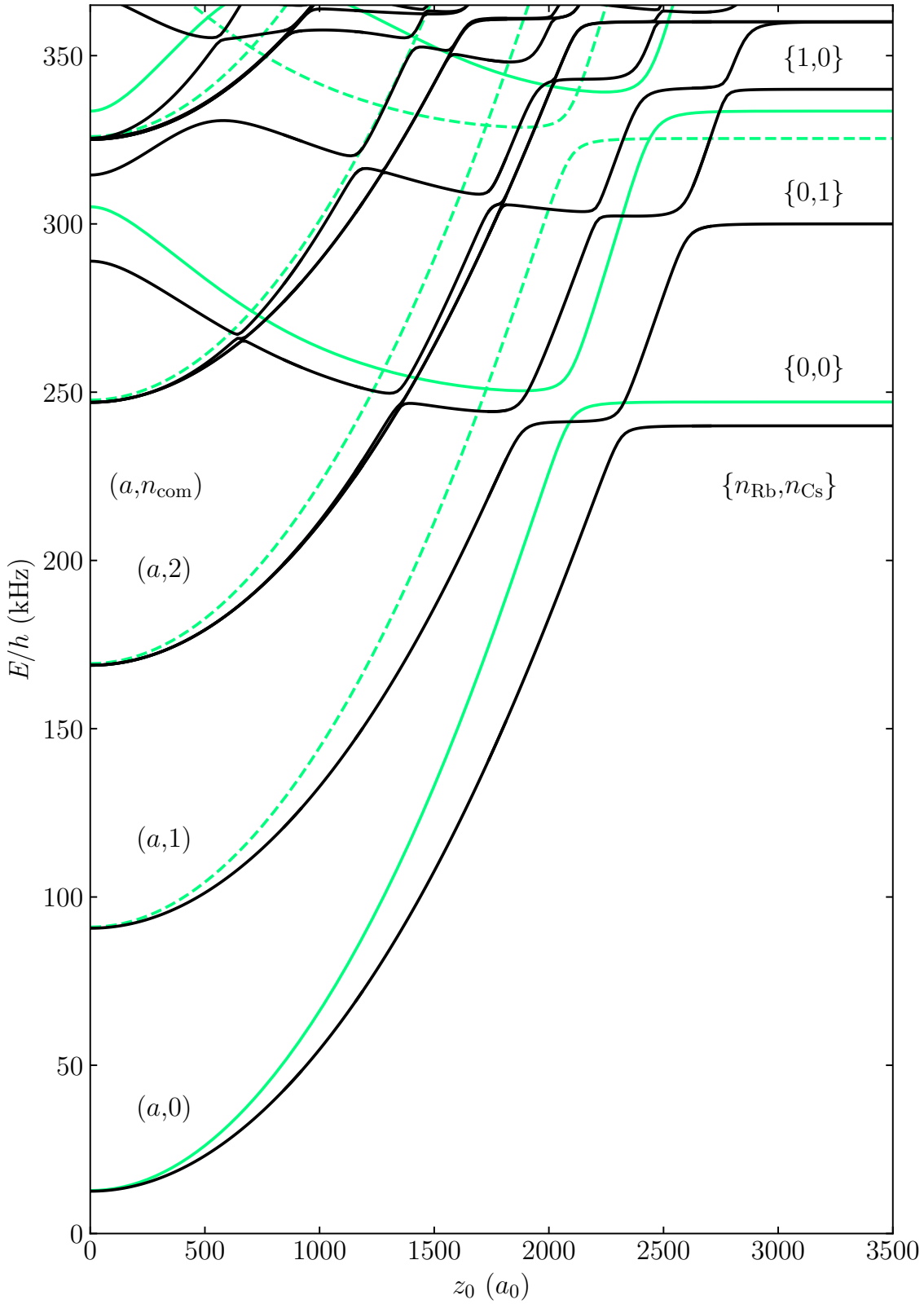


Figure 6.1: Levels of Rb and Cs atoms in separated spherical traps as a function of separation $z_0$, with $\omega_{\mathrm{Rb}} = 100$ kHz and $\omega_{\mathrm{Cs}} = 60$ kHz. Solid green lines show the levels for pure relative motion, while dashed green lines show levels excited in the center-of-mass coordinate but neglecting coupling between relative and center-of-mass motions. Black lines show the results of the full coupled calculation using a direct-product basis set (444)(444). Only levels with EE symmetry are shown.

the magnetic field used for mergoassociation in ref. [199]. The black lines are obtained with a large direct-product basis set with $(n_x^{\max} n_y^{\max} n_z^{\max})(N_X^{\max} N_Y^{\max} N_Z^{\max}) = (444)(444)$. This basis set contains 4270 functions for EE symmetry. The near-horizontal levels are those of pairs of trapped atoms that at large separation are in separate traps; they show single-atom trap excitations of frequency 60 and 100 kHz. They are labeled by the principal quantum numbers $\{n_{\mathrm{Rb}}, n_{\mathrm{Cs}}\}$ of the individual 3d harmonic traps. Their wavefunctions are not simply expressed in terms of relative and center-of-mass motions. The levels that vary quadratically with $z_0$ are molecular states and are labeled $(a, n_{\mathrm{com}})$, where $n_{\mathrm{com}}$ is the principal quantum number for center-of-mass motion. These two sets of levels undergo avoided crossings with one another.

Figure 6.1 compares these results with an approximation (green lines) that neglects the coupling $V_{\mathrm{cpl}}^{\mathrm{trap}}(\boldsymbol{R}, \boldsymbol{\mathcal{R}})$ between relative and center-of-mass motions. The uncoupled levels for the ground state of center-of-mass motion are shown as solid green lines, with levels excited in center-of-mass motion parallel to them and shown as dashed green lines. In this approximation, the atom-pair levels have incorrect energies governed by $\omega_{\mathrm{rel}}$ and $\omega_{\mathrm{com}}$. In addition, the coupled molecular levels are shifted upwards from the uncoupled ones by an amount that varies with $z_0$.

### 6.2.2 Shifted-Molecule Approach

The direct-product basis set has the disadvantage that there are non-zero matrix elements of the form

$$\langle a N_X' N_Y' N_Z' | V_{\mathrm{cpl}}^{\mathrm{trap}}(\boldsymbol{R}, \boldsymbol{\mathcal{R}}) | a N_X N_Y N_Z \rangle. \tag{6.3}$$

These matrix elements are diagonal in $a$ but off-diagonal in $N_X$, $N_Y$ or $N_Z$ by 1 when the trap separation $\boldsymbol{R}_0$ has components along $X$, $Y$ or $Z$, respectively. They are due to the term $\mu[\boldsymbol{\mathcal{R}} - \boldsymbol{\mathcal{R}}_0]^{\intercal} \Delta\boldsymbol{\omega}^2 \boldsymbol{R}_0$ in Eq. 5.13, which shifts the minimum in the potential for center-of-mass motion away from $\boldsymbol{\mathcal{R}}_0$ for molecular states. As a

result, convergence with respect to the basis set for center-of-mass motion is poor when $\Delta\boldsymbol{\omega}^2\boldsymbol{R}_0$ is substantial.

To circumvent this issue, we use a modified basis set where the functions for motion in $\boldsymbol{\mathcal{R}}$ are shifted for the molecular state. They are still harmonic-oscillator functions with the same frequency, but are centered at $\tilde{\boldsymbol{\mathcal{R}}}_0 = \boldsymbol{\mathcal{R}}_0 - \Delta\boldsymbol{\mathcal{R}}$, where

$$\Delta\boldsymbol{\mathcal{R}} = \frac{\mu}{\mathcal{M}}[\boldsymbol{\omega}^2_{\rm com}]^{-1}\Delta\boldsymbol{\omega}^2\boldsymbol{R}_0. \tag{6.4}$$

The resulting shifted-molecule functions are represented by Dirac kets $|a\tilde{N}_X\tilde{N}_Y\tilde{N}_Z\rangle$. The kets $|n_xn_yn_zN_XN_YN_Z\rangle$ are retained unmodified, centered on $\boldsymbol{\mathcal{R}}_0$. The matrix elements in the shifted-molecule basis set are given in the Appendix.

The most important effect of the shifted-molecule basis set is that the diagonal matrix elements for all molecular functions are shifted in energy by

$$\Delta E_a = -\frac{\mu}{2}\boldsymbol{R}_0^{\intercal}\Delta\boldsymbol{\omega}^2\Delta\boldsymbol{\mathcal{R}} = -\frac{\mu^2}{2\mathcal{M}}\boldsymbol{R}_0^{\intercal}[\boldsymbol{\omega}^2_{\rm com}]^{-1}[\Delta\boldsymbol{\omega}^2]^2\boldsymbol{R}_0. \tag{6.5}$$

This explains the shift of the molecular states seen in Fig. 6.1. It shows that the shift is quadratic in the trap separation $z_0$ and is the same for all molecular states. When coupling to center-of-mass motion is included, the quadratic term in the energies of the molecular states is $\frac{1}{2}\mu\boldsymbol{R}_0^{\intercal}\boldsymbol{\omega}^2_{\rm mol}\boldsymbol{R}_0$, where

$$\boldsymbol{\omega}^2_{\rm mol} = [\boldsymbol{\omega}^2_{\rm com}]^{-1}\boldsymbol{\omega}_1^2\boldsymbol{\omega}_2^2. \tag{6.6}$$

This compares with $\frac{1}{2}\mu\boldsymbol{R}_0^{\intercal}\boldsymbol{\omega}^2_{\rm rel}\boldsymbol{R}_0$ when coupling to center-of-mass motion is neglected.

Figure 6.2 compares results using small direct-product and shifted-molecule basis sets (with $(n_x^{\rm max}n_y^{\rm max}n_z^{\rm max})(N_X^{\rm max}N_Y^{\rm max}N_Z^{\rm max}) = (444)(222)$) with those using a much larger shifted-molecule basis set (444)(444); the latter gives nearly converged results. The small shifted-molecule basis set gives very accurate results for all the molecular states and for the singly excited atom-pair states; its only visible deficiency in Fig.

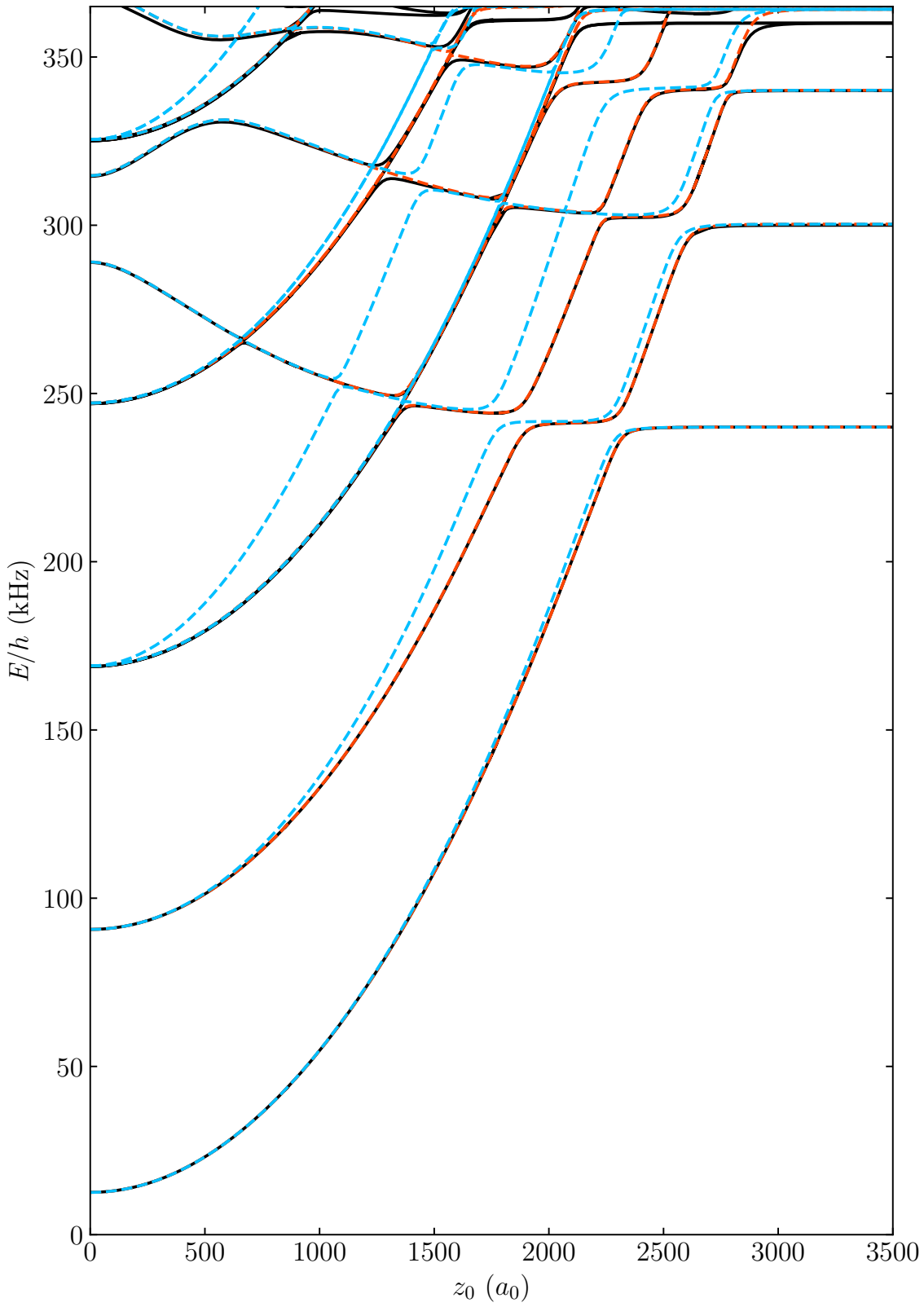


Figure 6.2: Levels of Rb and Cs atoms in separated spherical traps, as in Fig. 6.1, using different approaches. Black lines show results using a large shifted-molecule basis set (444)(444). Blue (or red) lines show results with smaller basis sets (444)(222) using the direct-product (or shifted-molecule) approach.

6.2 is for the atom-pair states with $(n_{\mathrm{Rb}}, n_{\mathrm{Cs}}) = (0, 2)$, which are unconverged with the smaller basis set of center-of-mass functions. The avoided crossings involving the ground and first-excited atom-pair states are all very accurately reproduced. The small direct-product basis set, by contrast, is substantially in error for several of the molecular states and their avoided crossings.

Comparison of Figs. 6.1 and 6.2 demonstrates that even the (444)(444) basis set is significantly unconverged for the direct-product approach, producing unphysical non-degeneracies for both molecular and atom-pair states with larger values of $N_X$ and/or $N_Y$. The shifted-molecule approach performs much better in this respect; the (444)(222) basis set is adequate for most purposes, and contains only 972 functions, so that diagonalization is computationally cheaper by about a factor of 80. This basis set is used in the remainder of the paper, except where otherwise stated.

## 6.3 Effects of Coupling Between Relative and Center-of-Mass Motion

Figure 6.3 shows the levels of different symmetries for Rb and Cs atoms in separated spherical traps with frequencies $\omega_{\mathrm{Rb}} = 110$ kHz and $\omega_{\mathrm{Cs}} = 90$ kHz. The levels of EE symmetry show complicated patterns of avoided crossings, which will be discussed further below. However, the levels of other symmetries are relatively simple. For spherical traps, the complete system has cylindrical symmetry, so levels of EO and OE symmetry are degenerate.

For spherical traps, the levels singly excited in either $\omega_{\mathrm{Rb}}$ or $\omega_{\mathrm{Cs}}$, with $n_{\mathrm{Rb}} = 1$ or $n_{\mathrm{Cs}} = 1$, are triply degenerate at large trap separations. Those with excitation along $x$ and $y$ have OE and EO symmetry, respectively. These two singly excited states show a $3 \times 3$ avoided crossing with a molecular state near 1800 $a_0$ and a narrower one near 1500 $a_0$. When the traps are merged adiabatically an atom pair with single excitation in $\omega_{\mathrm{Cs}}^{x(y)}$ (or more generally in the *lower* of $\omega_1^{x(y)}$ and $\omega_2^{x(y)}$) will undergo mergoassociation to form a motionally excited molecule with $n_{\mathrm{com}}^{x(y)} = 1$.

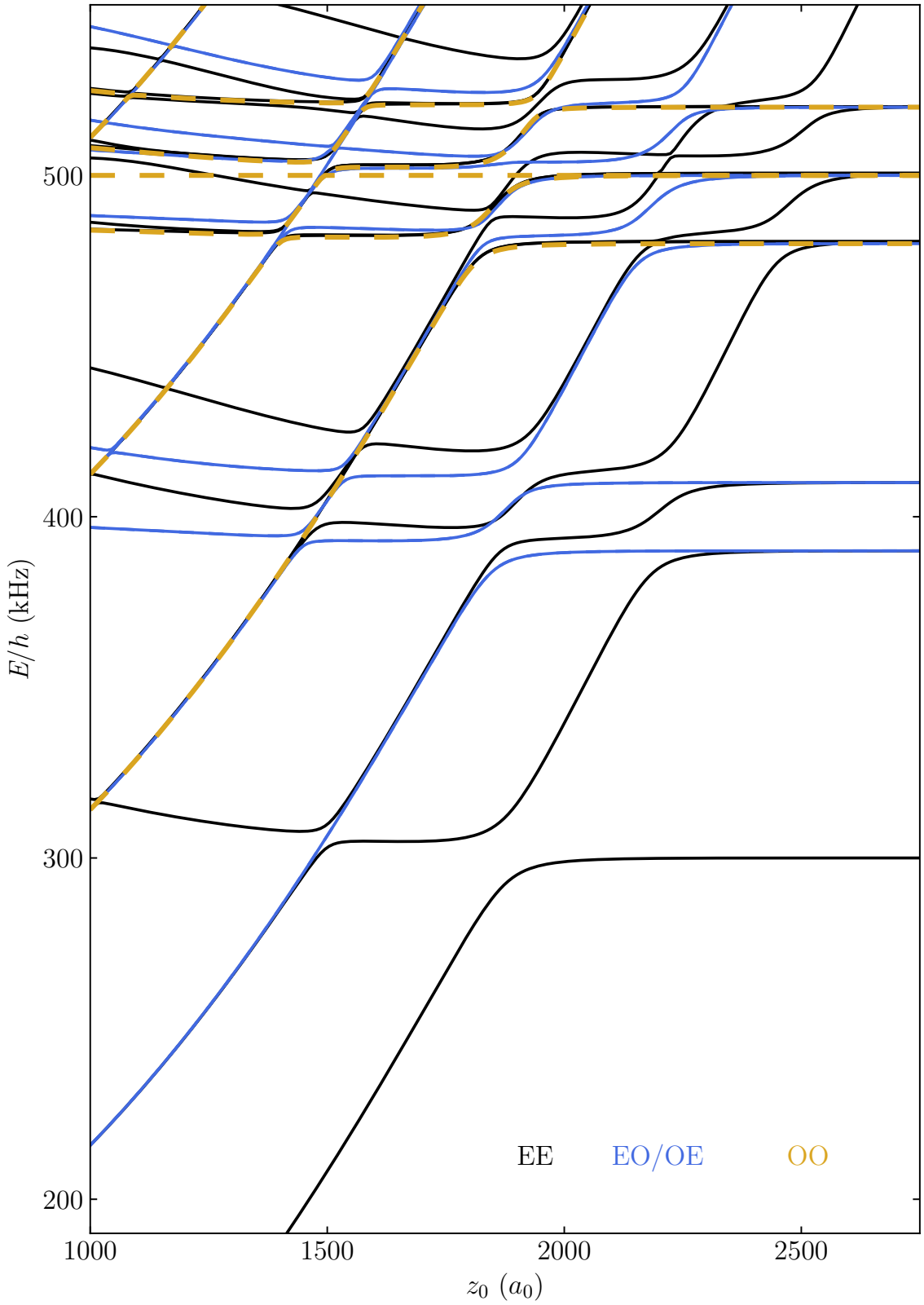


Figure 6.3: Levels of Rb and Cs atoms in separated spherical traps as a function of separation $z_0$, with $\omega_{\mathrm{Rb}} = 110$ kHz and $\omega_{\mathrm{Cs}} = 90$ kHz. Levels of EE, EO, OE, and OO symmetry are shown, but those of EO and OE symmetry are degenerate for spherical traps.

However, a pair with single excitation in $\omega_{\mathrm{Rb}}^{x(y)}$ (i.e. in the *higher* of $\omega_1^{x(y)}$ and $\omega_2^{x(y)}$) will be transferred to $n_{\mathrm{Cs}}^{x(y)} = 1$ at the two crossings near 1800 $a_0$; the pair may then pass either diabatically or adiabatically over the inner crossing; the former leaves the excitation in $n_{\mathrm{Cs}}$, while the latter forms a molecule with $n_{\mathrm{com}}^{x(y)} = 1$ and $n_{\mathrm{com}}^{z} = 1$.

The lowest atom-pair state with OO symmetry has $n_{\mathrm{Cs}}^{x} = 1$ and $n_{\mathrm{Cs}}^{y} = 1$. An atom pair in this state can again undergo mergoassociation to form a motionally excited molecule, now with $n_{\mathrm{com}}^{x} = 1$ and $n_{\mathrm{com}}^{y} = 1$. However, replacing one or both excitations with $\omega_{\mathrm{Rb}}^{x(y)}$ results in more complicated outcomes.

In the following, we focus on levels of EE symmetry, which are the most important for mergoassociation with well-cooled atoms.

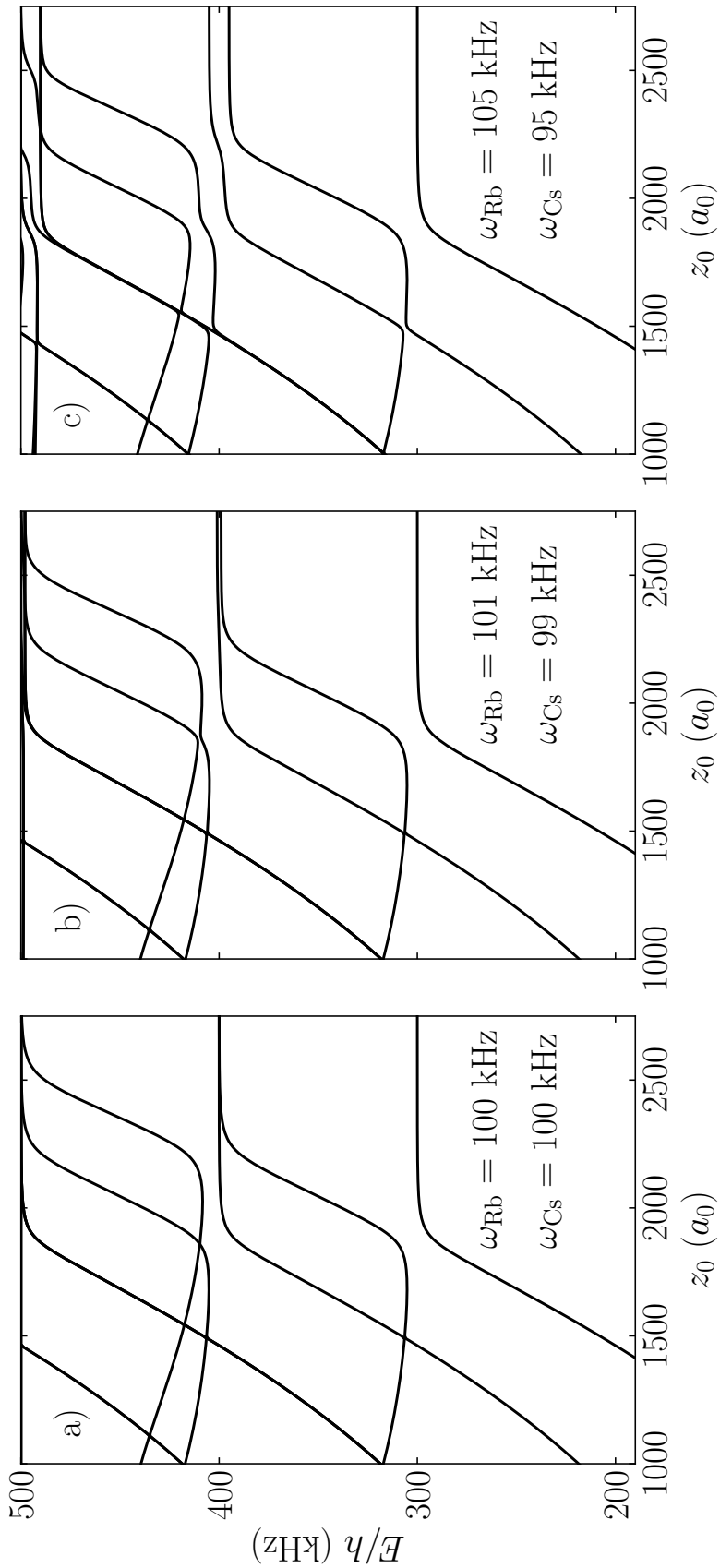


Figure 6.4: Levels of Rb and Cs in separated spherical traps as a function of separation $z_0$, with small differences between $\omega_1$ and $\omega_2$. Only levels of EE symmetry are shown.

### 6.3.1 Weak Coupling

When $\omega_1 = \omega_2$, the relative and center-of-mass motions are completely uncoupled. The levels and avoided crossings for EE symmetry are then as in Fig. 6.4(a). The lowest atom-pair state shows an avoided crossing with the molecular state with no center-of-mass motion, but there is an unavoided crossing with the molecular state that is motionally excited. There are 2 atom-pair states with 1 unit of motional excitation. One of them may be viewed as excited in the relative coordinate but not the center-of-mass coordinate, so shows an avoided crossing with the molecular state with no center-of-mass motion but an unavoided crossing with the one that is motionally excited. The other may be viewed as excited in the center-of-mass coordinate, so shows an avoided crossing with the molecular state that is motionally excited but does not interact with the lowest molecular state.

Only a small difference between $\omega_1$ and $\omega_2$ is needed to change this picture. Figure 6.4(c) shows a crossing diagram with approximately 10% difference between $\omega_1$ and $\omega_2$. Here the atom-pair states with 1 unit of motional excitation should be viewed at large separation as single-atom excitations for atom 1 and atom 2, respectively. This identification persists through the avoided crossings with both the ground and motionally excited molecular states. The molecular states, by contrast, remain best described as products of functions for relative and center-of-mass motion. Since the atom-pair states with excitation for a single atom are linear combinations of those with excitation in the relative and center-of-mass motions, there are strong avoided crossings between both atom-pair states and both molecular states.

Figure 6.4(b) shows an intermediate case with a 2% difference between $\omega_1$ and $\omega_2$. Here the atom-pair states with 1 unit of motional excitation again correspond to single-atom excitations at very large $z_0$, but these states mix as the two traps approach one another. At the values of $z_0$ where the atom-pair states cross molecular states, $z_0^{\mathrm{X}}$, this mixing is nearly complete and the levels are well described by quantum numbers for relative and center-of-mass motion. The diagram thus resembles Fig. 6.4(a): the lower singly-excited atom-pair state shows a strong avoided crossing

with the molecular state with no center-of-mass motion, but a weak avoided crossing with the molecular state that is motionally excited. The situation is reversed for the upper singly-excited atom-pair state, which is mostly excited in the center-of-mass coordinate.

### 6.3.2 Intermediate and Strong Coupling

Figure 6.5 shows level crossing diagrams for larger values of $\omega_{\mathrm{Rb}} - \omega_{\mathrm{Cs}}$. In this regime, the avoided crossings between atom-pair and molecular states are well isolated from one another and can each be characterized in terms of 2 interacting states.

#### Mergoassociation with atoms in Motional Ground States

For mergoassociation from atoms in their motional ground states, the most important quantity is the strength $\Omega_{\mathrm{eff}}$ of the lowest avoided crossing, near $z_0 = 2000\ a_0$ in Figs. 6.4 and 6.5. The strength of this crossing for RbCs is shown in Fig. 6.6(a) as a function of $\omega_{\mathrm{Rb}} - \omega_{\mathrm{Cs}}$. Here $\omega_{\mathrm{Rb}} + \omega_{\mathrm{Cs}}$ is held constant at 200 kHz, which keeps the energy of the lowest atom-pair state the same. However, the curvature of the molecular state is approximately proportional to $\omega_{\mathrm{mol}}$, given by Eq. 6.6. This generally decreases as $|\omega_{\mathrm{Rb}} - \omega_{\mathrm{Cs}}|$ increases (with $\omega_{\mathrm{Rb}} + \omega_{\mathrm{Cs}}$ held constant), though its maximum is slightly shifted from $\omega_{\mathrm{Rb}} = \omega_{\mathrm{Cs}}$ when $m_1 \neq m_2$. The crossing distance $z_0^{\mathrm{X}}$ thus increases with $|\omega_{\mathrm{Rb}} - \omega_{\mathrm{Cs}}|$. As shown in the previous chapter, the crossing strength depends principally on $\exp(-\frac{1}{2} z_0^{\mathrm{X}}/\beta_{\mathrm{rel}})$, so it decreases fast as $z_0^{\mathrm{X}}$ increases; here $\beta_{\mathrm{rel}} = (\hbar/\mu\omega_{\mathrm{rel}})^{\frac{1}{2}}$. The dashed blue line on Fig. 6.6(a) shows the result of the approximation from Eq. 55 in the previous chapter. The agreement is quite good, implying that the variation in $\Omega_{\mathrm{eff}}$ with $\omega_{\mathrm{Rb}} - \omega_{\mathrm{Cs}}$ is dominated by the variation in $\omega_{\mathrm{mol}}$ and hence in $z_0^{\mathrm{X}}$, rather than by the coupling between relative and center of mass motions, characterized by $\Delta\omega^2$.

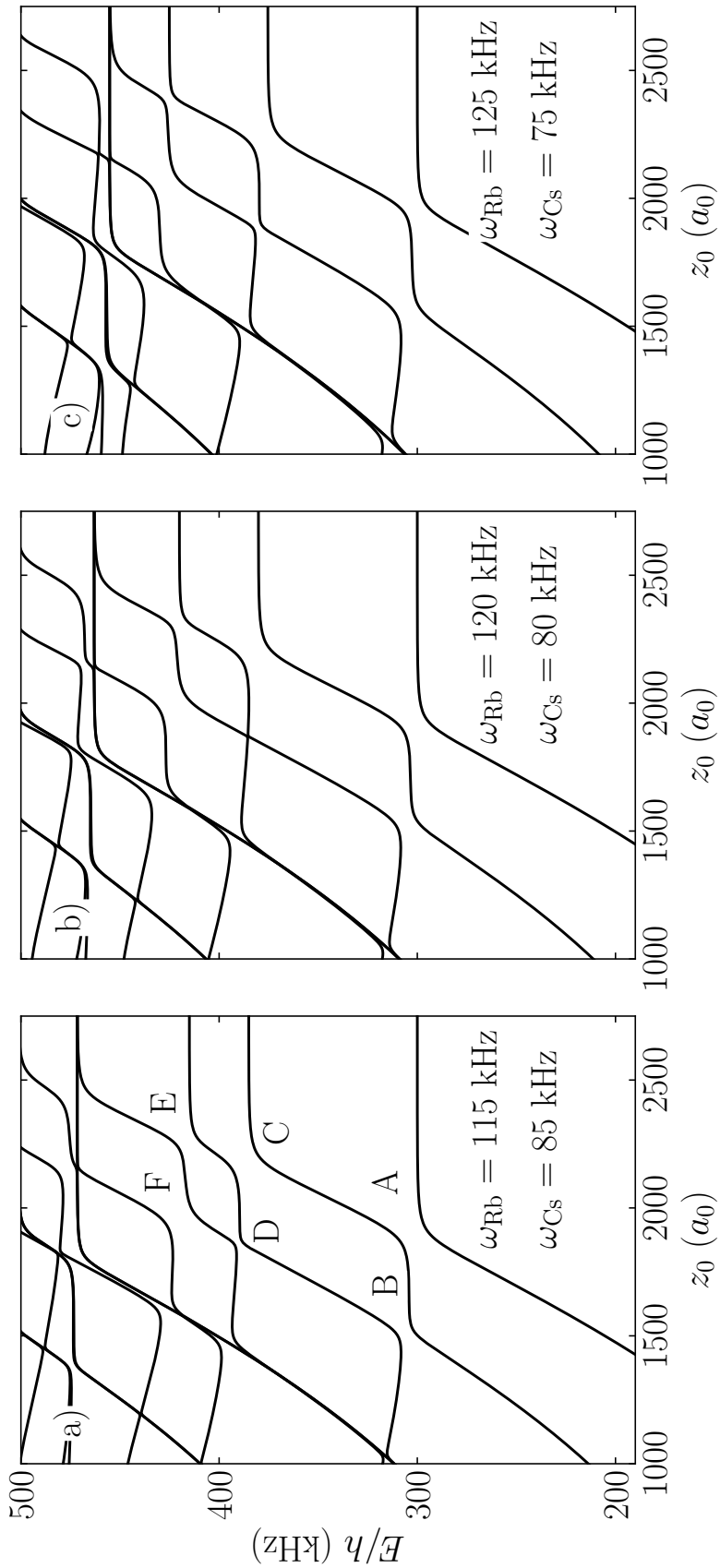


Figure 6.5: Levels of Rb and Cs in separated spherical traps as a function of separation $z_0$, with moderate differences between $\omega_1$ and $\omega_2$. Only levels of EE symmetry are shown.

**Mergoassociation with Motionally Excited Atoms**

It is important to understand what happens when traps containing motionally excited atoms are merged. Under these circumstances, there are several avoided crossings that can be involved, labeled A to F in Fig. 6.5(a). The probability of traversing an avoided crossing adiabatically is quantified by the Landau-Zener formula, with a sufficiently slow merge producing adiabatic passage. The critical merging speed is proportional to $\Omega_{\rm eff}^{-2}$, as is shown in the previous chapter.

There is interesting dependence of the strengths of the avoided crossings on $\omega_{\rm Rb} - \omega_{\rm Cs}$. As seen in section 6.3.2, the strength of crossing A peaks near $\omega_{\rm Cs} = \omega_{\rm Rb}$. Conversely, the strength of crossing B, shown in Fig. 6.6(b), is proportional to $|\omega_{\rm Cs} - \omega_{\rm Rb}|$ for small frequency differences; this arises because the relevant matrix element (Eq. A.18) includes a factor from the coupling between relative and center-of-mass motions. For larger frequency differences, the strength decreases for the same reasons as crossing A.

Crossings C, D, E, and F are more complicated. When $|\omega_{\rm Cs} - \omega_{\rm Rb}|$ is small, they involve the interaction of 3 states and do not lend themselves to simple characterization. This is again true when $\omega_{\rm Rb} \approx 2\omega_{\rm Cs}$ or $2\omega_{\rm Rb} \approx \omega_{\rm Cs}$, when the doubly excited state for one atom is close to the singly excited state for the other. Between these complicated regions, however, the crossing strengths may be characterized from a $2 \times 2$ model and are shown by the solid lines in Fig. 6.6. The grey dashed lines show interpolations through the regions where a $2 \times 2$ treatment breaks down; these are obtained by including a point at $\omega_{\rm Rb} = \omega_{\rm Cs}$, where the uncoupled problem can again be represented by a $2 \times 2$ matrix. The interpolations differ slightly from the solid curves in regions where a third state contributes significantly.

The separated atom-pair states involved in crossings C, D, E and F are characterized by quantum numbers $\{n_1, n_2\} = \{0, 1\}$ and $\{1,0\}$, and may be approximately represented as linear combinations of $(n_{\rm rel}, n_{\rm com}) = (1, 0)$ and (0,1). As a result, the matrix elements that govern their crossing strengths contain two terms, one proportional to $\omega_{\rm Cs} - \omega_{\rm Rb}$ and the other not. Because of this, the strengths of crossings D

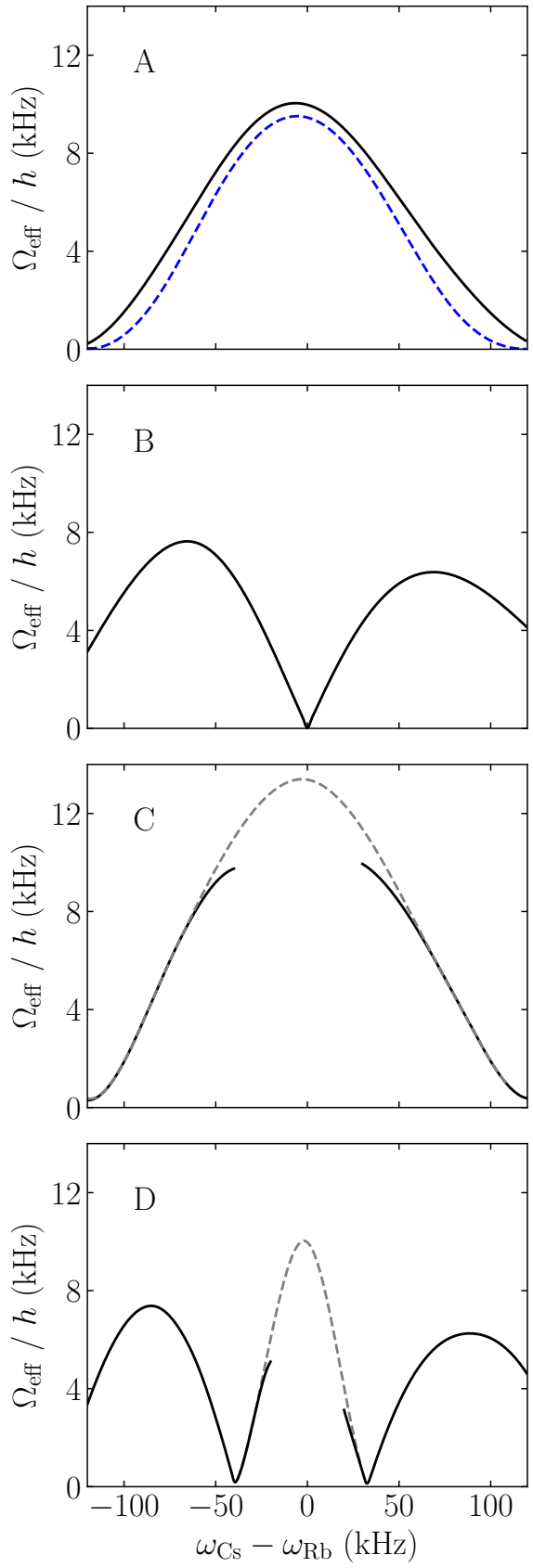


Figure 6.6: The strength of avoided crossings A to D as a function of $\omega_{\mathrm{Cs}} - \omega_{\mathrm{Rb}}$, with $\omega_{\mathrm{Rb}} + \omega_{\mathrm{Cs}}$ held constant at 200 kHz. The black lines show the crossing strengths from the shifted-molecule approach. The grey dashed lines show interpolations through regions where a $2 \times 2$ treatment breaks down, obtained as described in the text. The blue dashed line in (a) shows the result from Eq. 55 of ref. of the previous chapter.

and E have minima due to destructive interference as a function of $\omega_{\mathrm{Cs}} - \omega_{\mathrm{Rb}}$; the minima are not actual zeroes, because {0,1} and {1,0} contain some contributions from states other than (1,0) and (0,1).

If the atom with the *lower* trap frequency is motionally excited, it is possible to enter the state $(a, 0)$ at avoided crossing C. From this point there are several possibilities. First, it may be possible to traverse crossing A diabatically with a fast merge, producing a molecule in state $(a, 0)$ at small $z_0$. Alternatively, if crossing A is traversed adiabatically, the system will reach crossing B. For large frequency differences, crossing B can be traversed adiabatically, producing a motionally excited molecule in state $(a, 1)$. For small differences, however, crossing B is very weak and is likely to be traversed diabatically, producing a ground-state atom pair. Yet another possibility is to pause the merging around $z_0 \approx 2100\ a_0$ (for RbCs), which might allow optical transfer to a deeper state of the molecule.

If the atom with the *higher* trap frequency is motionally excited, it is possible to enter the state $(a, 0)$ at avoided crossing E. From this point there are many possible pathways based on different choices of adiabatic and diabatic traversals, controlled by merging speeds and trap frequencies. With a good understanding of the patterns of avoided crossings, it may be possible to devise sequences of merging and optical transfer that achieve efficient molecule formation even with motionally excited atoms.

### 6.3.3 Mergoassociation for Other Systems

Mergoassociation is potentially useful for many systems. As shown in the previous chapter, it is generally effective when the harmonic lengths of the traps or tweezers are comparable to (no more than a few times larger than) the scattering length. Otherwise, the lowest crossing occurs at large values of $z_0^{\mathrm{X}}/\beta_{\mathrm{rel}}$ and is too narrow to be useful. Mergoassociation is particularly promising for systems that lack Feshbach resonances, or where the Feshbach resonances are very narrow. Examples of this are systems of alkali-metal atoms with alkaline-earth atoms, where narrow

resonances have been predicted [217–221] and observed [222, 223] but not yet used for magnetoassociation. RbSr, RbYb and CsYb all have isotopic combinations with large positive scattering lengths: $^{87}$Rb$^{87}$Sr with $a = 1421(98)\ a_0$ [224], $^{87}$Rb$^{174}$Yb with $a = 880(120)\ a_0$ [225] and $^{133}$Cs$^{176}$Yb with $a = 798\ a_0$ [226].

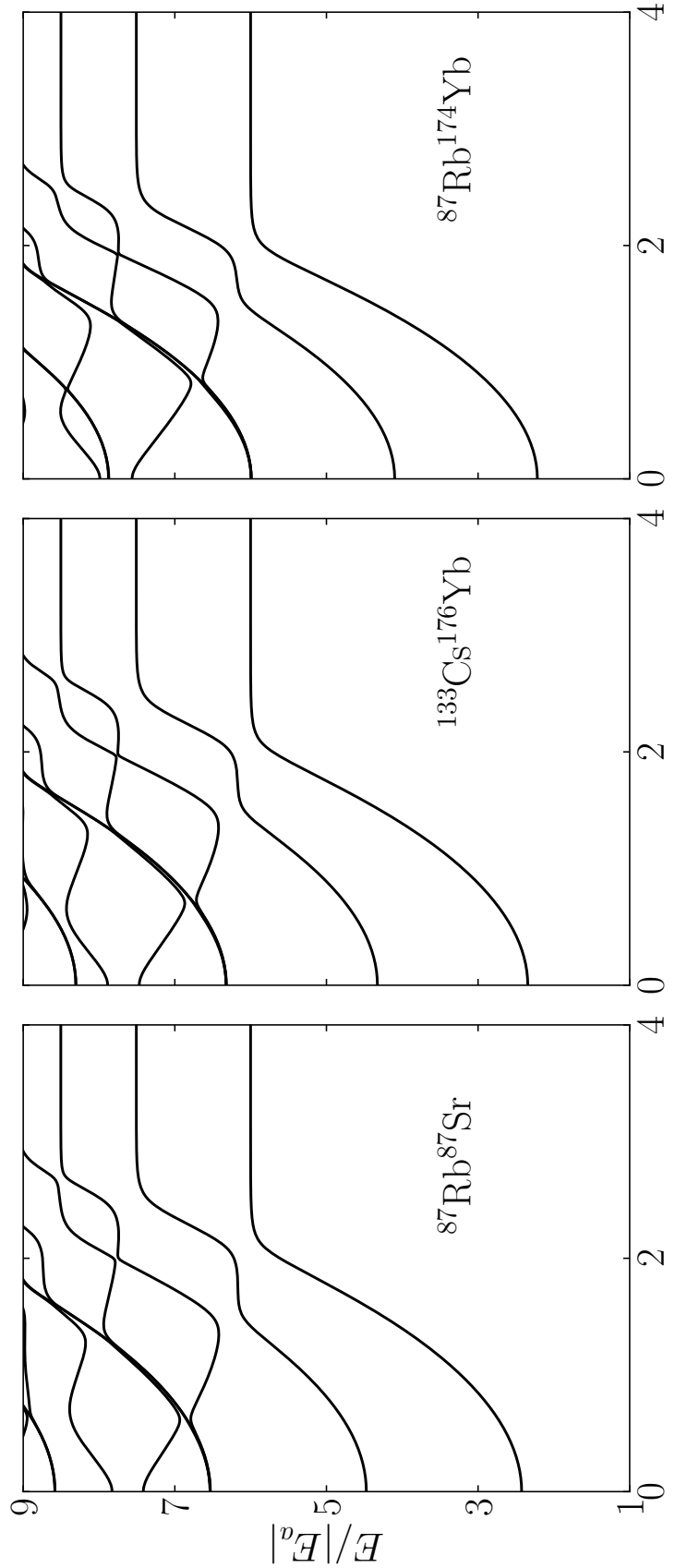


Figure 6.7: Level crossing diagrams for $^{87}$Rb$^{87}$Sr, $^{133}$Cs$^{176}$Yb and $^{87}$Rb$^{174}$Yb for $\hbar\omega_1 = 2.5|E_a|$ and $\hbar\omega_2 = 1.5|E_a|$. This corresponds to $(\omega_1, \omega_2) = (51.4, 30.9)$, (94.0, 56.4) and (100.5, 60.3) kHz for the three systems, respectively.

In the absence of coupling between relative and center-of-mass motions, the mergoassociation problem scales conveniently with lengths expressed in terms of the relative harmonic length for relative motion, $\beta_{\rm rel}$. This is the scaling we used in the previous chapter. However, in this representation, different scattering lengths $a$ produce a lowest avoided crossing for mergoassociation at different crossing distances $z_0^{\rm X}/\beta_{\rm rel}$. To compare systems with different $a$, it is more transparent to scale lengths according to $a$ and energies according to $|E_a| = \hbar^2/(2\mu a^2)$. In order to produce level crossing diagrams with molecular and atom-pair levels at approximately the same energies for different systems, we choose trapping frequencies that are the same multiple of $|E_a|$ for each system. This gives diagrams that are independent of $a$ and the mean atomic mass, but depend on the mass ratio $m_2/m_1$, which is close to 1 for RbSr, 1.3 for CsYb (compared to 1.53 for RbCs) and 2 for RbYb.

Figure 6.7 shows level crossing diagrams for $^{87}$Rb$^{87}$Sr, $^{133}$Cs$^{176}$Yb and $^{87}$Rb$^{174}$Yb with $\hbar\omega_1 = 2.5|E_a|$ and $\hbar\omega_2 = 1.5|E_a|$. It may be seen that the crossing diagrams differ in detail, but show fairly similar patterns of avoided crossings in all the cases shown, with only weak dependence on the mass ratio. The one difference of any significance is that crossing D, near $z_0/a = 2$ and $E/|E_a| = 8$, is substantially stronger for RbSr than for the other systems, because the position of the minimum in Fig. 6.6(d) depends on $m_2/m_1$. All three systems show substantial avoided crossings for pairs of atoms in a variety of motional states, so that mergoassociation is a promising method of molecule formation in all these systems.

### 6.3.4 Trap Anisotropy

Optical tweezers are often strongly anisotropic, with much weaker confinement along the laser propagation axis than perpendicular to it. The mergoassociation experiments of Ruttley et al. [199] were carried out on RbCs, using tweezers with frequency ratios $\omega_z/\omega_x \approx 1$ and $\omega_z/\omega_y \approx 6$ for both atoms. Figure 6.8 shows the energy levels that result for a representative set of parameters, including both anisotropy and coupling between the relative and center-of-mass motions. All four

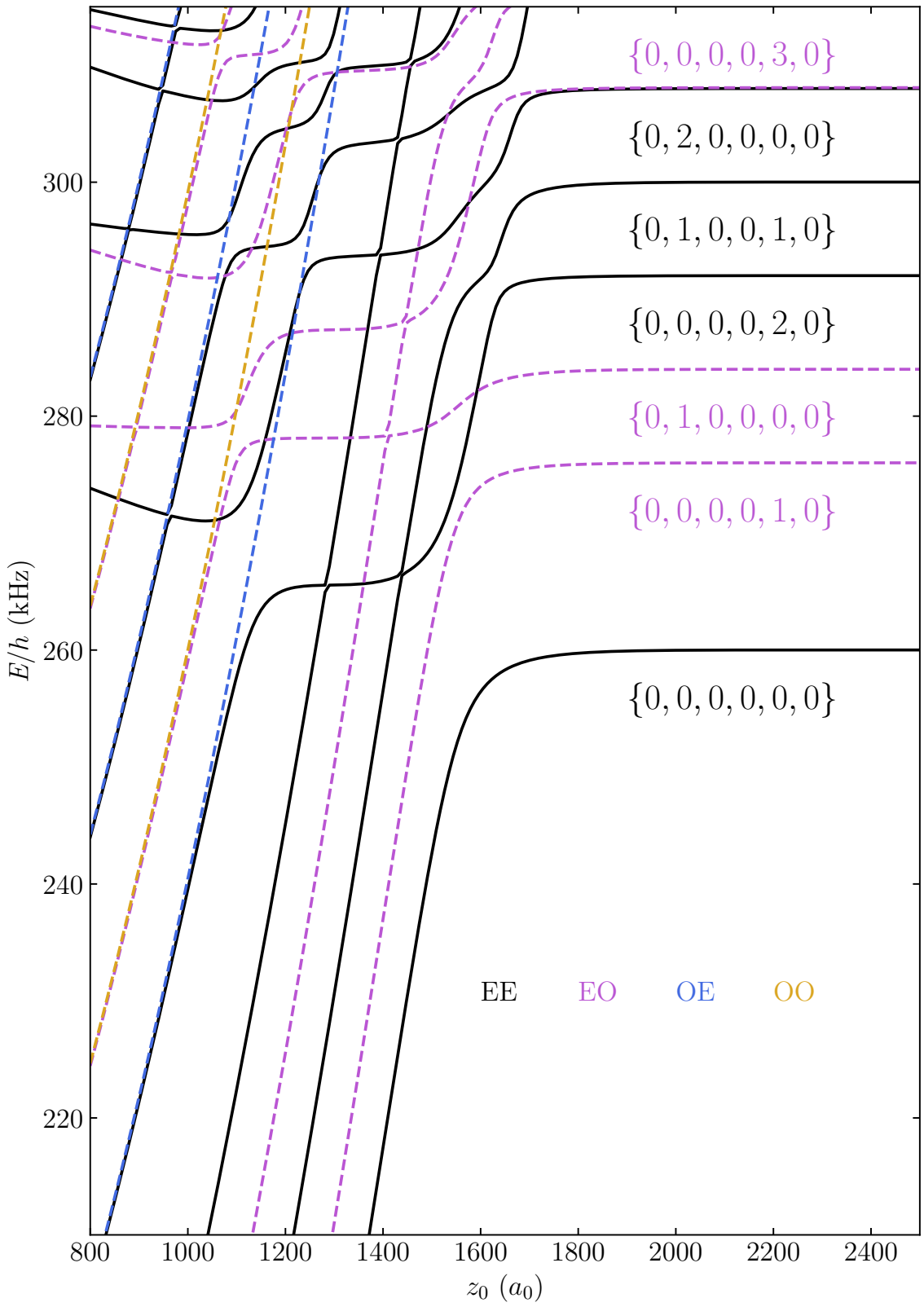


Figure 6.8: Levels of Rb and Cs atoms in separated anisotropic traps as a function of separation $z_0$, with $\{\omega_{\mathrm{Rb},x}, \omega_{\mathrm{Rb},y}, \omega_{\mathrm{Rb},z}\} = \{144, 24, 144\}$ kHz and $\{\omega_{\mathrm{Cs},x}, \omega_{\mathrm{Cs},y}, \omega_{\mathrm{Cs},z}\} = \{96, 16, 96\}$ kHz. Levels with EE, EO, OE, and OO symmetry are shown. The atom-pair states are labeled with quantum numbers $\{n_{\mathrm{Rb},x}, n_{\mathrm{Rb},y}, n_{\mathrm{Rb},z}, n_{\mathrm{Cs},x}, n_{\mathrm{Cs},y}, n_{\mathrm{Cs},z}\}$.

symmetries are shown. The calculations used a shifted-molecule basis set with $(n_x^{\max} n_y^{\max} n_z^{\max})(N_X^{\max} N_Y^{\max} N_Z^{\max}) = (444)(242)$. The details of the levels are complicated, and too specific to the individual case to justify detailed analysis here, but some important points are evident. First, the lowest crossing, involving atoms in their ground motional states, has a strength $\Omega_{\text{eff}} = 11.15$ kHz. This is similar to the strength obtained for spherical traps with frequencies chosen as $\omega_z$, which is $\Omega_{\text{eff}} = 11.84$ kHz. This justifies the spherical approximation used in ref. [199] to interpret the measured probabilities of diabatic and adiabatic crossing. If motional coupling is neglected, however, the crossing strength is 14.48 (15.61) kHz with anisotropy included (neglected). This demonstrates that the effects of motional coupling are significantly larger than those of anisotropy.

The avoided crossing involving the first-excited atom-pair state, with $n_{\text{Cs},y} = 1$, is only slightly weaker than the lowest crossing. Atom pairs in this state may also be converted to molecules when the traps are merged. However, most other avoided crossings are substantially weaker. As noted above, the critical merging speed for adiabatic passage is proportional to $\Omega_{\text{eff}}^{-2}$; at the merging speeds used in ref. [199], it is likely that these crossings would be traversed diabatically and fail to produce molecules.

### 6.3.5 Logic Gates

Merging traps may also have applications in quantum information processing [201]. The interactions that control the energy levels depend on the hyperfine state of the atoms involved, so they may be used to accumulate phase differences between pairs of atoms in different states. This allows the production of controlled entanglement and the construction of 2-particle quantum-logic gates.

An important general insight from the present work is that, for a particular mass ratio $m_2/m_1$, the patterns of levels are "universal" when lengths are expressed in terms of the scattering length and energies (and frequencies) are expressed in terms of the energy of the least-bound molecular state. Thus the key requirement

for achieving differential phase shifts is that the scattering lengths are significantly different for the different pairs of atomic states involved. This is satisfied for most alkali-metal pairs, but not for all; modeling it requires a good understanding of the interaction potentials and detailed coupled-channel calculations using them [39, 128, 133, 227].

The presence of coupling between relative and center-of-mass motions is a complicating factor for applications to logic gates. At the simplest level, such coupling modifies the trap separation at which the principal avoided crossing occurs, as described by Eq. 6.5. It is important to take this into account. Nevertheless, for interactions involving pairs of atoms in their motional ground states, this is simply a quantitative correction.

Another issue is the feasibility (or fidelity) of quantum logic operations at finite temperature, when not all atoms are in their motional ground states. In this context, it would be desirable if the potential curves for motionally excited atoms were parallel to those for ground-state atoms. This occurs when the trapping frequencies for the two atoms are exactly equal, but not when the difference between them is significant. One possible advantage arises in cases where the difference is very small: then, as seen in Fig. 6.4(b), the potential curve for an atom excited in the *higher* motional frequency is very similar to that for the absolute ground state, while that for an atom excited in the *lower* frequency is not. Thus, if one atom is less well cooled that the other, it may be helpful to ensure that its trapping frequency is slightly (but as little as possible) *higher* than that of its companion.

## 6.4 Conclusions

We have developed theoretical methods to calculate the energies of pairs of atoms in separated optical traps, taking account of both trap anisotropy and the coupling between relative and center-of-mass motions. The resulting levels are important both for molecule formation by mergoassociation and for potential applications in quantum information processing. We use basis sets based on Cartesian harmonic-

oscillator functions for both relative and center-of-mass motion. The functions for relative motion are supplemented with a single molecular function. The effective trap potential for center-of-mass motion that is felt by the molecular function is shifted from the minimum of the combined trap; taking account of this shift complicates the algebra, but produces a substantial reduction in the size of the basis set needed for convergence.

Both mergoassociation and applications to quantum-logic gates rely on adiabatic passage over avoided crossings between atom-pair states and molecular states as a function of trap separation. The strengths of these avoided crossings are thus particularly important. We have used the example of RbCs to explore the dependence of the level patterns and the crossing strengths on the frequency difference between the traps for the two atoms. The lowest crossing, which is crucial for both applications, shifts to larger trap separations and becomes significantly weaker when center-of-mass motion is accounted for. Other crossings, which are important when merging traps containing motionally excited atoms, show more complicated behavior.

We have extended our treatment to other systems. Mergoassociation is generally feasible for atom pairs with positive scattering lengths that are comparable to or larger than the harmonic lengths of the traps. This corresponds to binding energies (for the least-bound state) that are not more than a few times the trap frequencies. We have considered RbSr, RbYb and CsYb, which are resistant to magnetoassociation because their Feshbach resonances are so narrow and so sparse. All three systems have isotopic combinations with large positive scattering lengths. We have shown that, in units scaled by scattering lengths and binding energies, the level crossing diagrams are very similar for all three systems when the scaled trap freqencies are the same; they differ only because the ratio of atomic masses differs between systems. For all three systems, mergoassociation can form Feshbach molecules in the least-bound state with experimentally accessible trap frequencies.

Optical tweezer traps are usually strongly anisotropic, with much stronger confinement across the laser beam waist than along the beam. We have considered

the combined effects of anisotropy and coupling between relative and center-of-mass motions for RbCs, using trap frequencies typical of current experiments. We have found that the effect of anisotropy is weaker than that of motional coupling under these conditions. We have also explored the effect of motional coupling on the levels that might be used for quantum-logic gates. We have found that coupling between relative and center-of-mass motions can have substantial effects on the energy levels of separated traps. When merging traps containing atoms that are both in their motional ground states, the coupling leaves the general picture unchanged, but has significant effects that should be taken into account in quantitative work. However, when one or both atoms is in a motionally excited state, the coupling causes qualitative changes in the patterns of energy levels, which have important consequences for experimental outcomes.

# Chapter 7

# Conclusions

In this thesis we have explored molecule formation at ultracold temperatures. We studied two different approaches to ultracold molecule formation; magnetoassociation and mergoassociation. A variety of systems, including $^{39}$K$^{133}$Cs, $^{87}$Rb$^{40}$Ca$^{19}$F, $^{87}$Rb$^{133}$Cs, $^{87}$Rb$^{87}$Sr, $^{133}$Cs$^{176}$Yb, and $^{87}$Rb$^{174}$Yb, were considered. As such we have been able to capture some of the exciting variety in the field of ultracold molecular physics.

In Chapter 3 we explored the near-threshold bound states and Feshbach resonances that exist in ultracold $^{39}$K + $^{133}$Cs collisions. We used coupled-channel calculations to study the singlet fractions of the near-threshold bound states with $L = 0$ and found that the states that cross threshold at lower values of $B$ had lower singlet fractions. A number of the states that cross threshold were assigned as $n = -1$ states. We used $L = 0$ coupled-channel scattering calculations to find the positions and widths of the Feshbach resonances these states caused. The resonance widths ranged from approximately $6 \times 10^{-3}$ G to $7 \times 10^{-2}$ G. $L = 2$ coupled-channel calculations were used to confirm that these resonances were not strongly decayed via spin-relaxation processes. We found that spin-relaxation processes did not alter the widths found with our $L = 0$ calculations. The Nägerl Group carried out further experiments to determine resonance positions and bound-state properties, allowing us to undertake an interactive non-linear least-squares analysis of the KCs interaction potential. We found that the difference between the singlet and triplet scattering lengths to be larger than previously thought with $a_{\rm s} = -29.71 \pm 1.6\ a_0$ and $a_{\rm t} = 77.70 \pm 0.4\ a_0$. The most important measurements in our fit were the measurements of the bound state beneath the resonance at the a+a threshold. The variation of the gradient of a bound state as it approaches the threshold is intimately related with the difference between $a_{\rm s}$ and $a_{\rm t}$. We found that resonance positions measured with atom-loss spectroscopy were less accurate than previously thought. We used our new potential to study and characterize the resonances at the lowest thresholds beneath 600 G.

One set of the Feshbach resonances that will exist in the collisions between

alkali-metal atoms and $^2\Sigma$ molecules is analogous to the Feshbach resonances that exist between alkali-metal atoms. In Chapter 4 we used Rb+CaF as a prototype system and studied these resonances. We found that the density and widths of these resonances depend strongly on the singlet and triplet scattering lengths $a_\mathrm{s}$ and $a_\mathrm{t}$. These scattering lengths are currently unknown for Rb+CaF collisions. We undertook coupled-channel calculations with a variety of different potentials, that produced different values of $a_\mathrm{s}$ and $a_\mathrm{t}$, and found that it is likely multiple resonances will exist beneath 1000 G. We found that a number of these resonances will be sufficiently broad such that the s-wave scattering length may be tuned with a magnetic field in experiments and that triatomic molecules may be formed via magnetoassociation. Additional Feshbach resonances may be caused by states with excited CaF rotation. We discussed the nature and the likelihood of these resonances.

Chapters 3 and 4 are related to one another by the physics that underpins magnetoassociation; zero-energy magnetically tuneable Feshbach resonances. By considering these resonances in more simple atomic collisions and more complex atom-molecule collisions we have captured one of the current challenges for ultracold AMO physics; how to control the interactions between larger and more complex species and how to produce larger molecules with novel properties at ultracold temperatures.

Chapters 5 and 6 constitute an investigation into mergoassociation, a novel method used to produce ultracold molecules. Mergoassociation was first observed in an experiment in 2023 [199]. In mergoassociation two atoms are held in two separate traps, and the separation between the atoms is reduced. Molecule formation occurs at an avoided crossing between a molecular state and the lowest motional state of the atom pair. We developed coupled-channel methods to study the energy levels of the relative motion of two atoms confined in two separate harmonic traps. We quantified the effects of trap strength and trap anisotropy on the energy levels of mergoassociation and the avoided crossing responsible for molecule formation. To further our understanding of the mergoassociation process we developed a basis-set method. This method was computationally efficient and allowed us to derive a series

of approximations to the strength of the lowest avoided crossing and elucidate its dependence on trap strength and anisotropy.

Unlike our coupled-channel approach, the basis-set method was able to account for the relative and center-of-mass motions of two atoms confined in two separate traps. These motions are coupled when the traps have different frequencies. We used our basis-set method to explore the levels with excited center-of-mass motion, and the consequences of the coupling between the relative and center-of-mass motions in Chapter 6. We found that patterns of levels and the avoided crossings between levels showed a wide variety of behavior which was determined by the strength of the coupling. We discussed the consequences of mergoassociating motionally excited atoms and found that it is possible to design sequences of merging that will achieve efficient molecule formation. Our work primarily addressed RbCs, but we also explored mergoassociation for species that do not have broad Feshbach resonances that can be used to produce molecules with magnetoassociation. These molecules included $^{87}$Rb$^{87}$Sr, $^{133}$Cs$^{176}$Yb, and $^{87}$Rb$^{174}$Yb. Optical tweezer traps are typically anisotropic and we discussed the interplay of trap anisotropy and the coupling between the relative and center-of-mass motions.

By considering both magnetoassociation and mergoassociation we have explored two different approaches to molecule formation. The former is a well-established technique in ultracold AMO physics. The latter is novel and may prove useful in the future for generating molecules at ultracold temperatures. Mergoassociation will be particularly advantageous for generating species that do not exhibit broad Feshbach resonances in the collisions of their constituent particles.

The excitement around, and the importance of the physics that can be explored with, ultracold molecules shows no sign of fading. As more research is undertaken and more molecular systems are needed at ultracold temperatures having a variety of techniques to form molecules will be advantageous.

# Appendix A

# Matrix Elements for Mergoassociation Basis Set Method

The Hamiltonian used in the basis set method for the mergoassociation problem, addressed in Chapters 5 and 6, is

$$\hat{H} = \hat{T}_{\rm rel}(\boldsymbol{R}) + V_{\rm rel}^{\rm trap}(\boldsymbol{R}) + V_{\rm int}(\boldsymbol{R}) + \hat{H}_{\rm com}^{\rm trap}(\boldsymbol{\mathcal{R}}) + V_{\rm cpl}^{\rm trap}(\boldsymbol{R}, \boldsymbol{\mathcal{R}}). \tag{A.1}$$

The basis functions used here are products of functions in the relative coordinate $\boldsymbol{R}$ and functions in the center-of-mass coordinate $\boldsymbol{\mathcal{R}}$.

## A.1 Relative motion

For the relative coordinate, we use a nonorthogonal basis set formed from 3-dimensional harmonic-oscillator functions $|n_x n_y n_z\rangle = |n_x\rangle|n_y\rangle|n_z\rangle$, supplemented by a single molecular function $|a\rangle$. The harmonic-oscillator functions are

$$\psi_n(\alpha) = = (2^n n! \beta_{{\rm rel},\alpha})^{-1/2} \pi^{-1/4} H_n((\alpha - \alpha_0)/\beta_{{\rm rel},\alpha}) \exp(-\tfrac{1}{2}((\alpha - \alpha_0)/\beta_{{\rm rel},\alpha})^2), \tag{A.2}$$

where $\alpha = x$, $y$ or $z$, $\beta_{{\rm rel},\alpha} = [\hbar/(\mu\omega_{{\rm rel},\alpha})]^{1/2}$ and $H_n(q)$ is a Hermite polynomial. The corresponding eigenvalues are

$$E_{n_x n_y n_z} = \hbar\omega_{{\rm rel},x}(n_x + \tfrac{1}{2}) + \hbar\omega_{{\rm rel},y}(n_y + \tfrac{1}{2}) + \hbar\omega_{{\rm rel},z}(n_z + \tfrac{1}{2}). \tag{A.3}$$

For a contact potential, the molecular function $\psi_a = \langle R|a\rangle$ is given by Eq. 5.40 and its eigenvalue by Eq. 5.41.

The matrix elements for relative motion are as in the previous chapter. The functions are normalized, so the diagonal elements of the overlap matrix $\mathbf{S}$ are all 1. The only non-zero off-diagonal elements of $\mathbf{S}$ are those between the molecular function and the harmonic-oscillator functions,

$$S_{a,n_x n_y n_z} = \langle a|n_x n_y n_z\rangle = \int_0^{2\pi} \int_0^{\pi} \int_0^{\infty} \psi_a \psi_{n_x n_y n_z} R^2 dR \, \sin\theta d\theta \, d\phi. \tag{A.4}$$

These are evaluated by 3-dimensional numerical quadrature, using Gauss-Laguerre quadrature for $R$, Gauss-Legendre quadrature for $\theta$ and equally spaced and weighted points for $\phi$.

The elements of the Hamiltonian matrix for the harmonic-oscillator functions are

$$\langle n'_x n'_y n'_z | \hat{T}_{\rm rel}(\boldsymbol{R}) + V_{\rm rel}^{\rm trap}(\boldsymbol{R}) | n_x n_y n_z \rangle = E_{n_x n_y n_z} \delta_{n'_x n_x} \delta_{n'_y n_y} \delta_{n'_z n_z}, \tag{A.5}$$

$$\langle n'_x n'_y n'_z | V_{\rm int}(\boldsymbol{R}) | n_x n_y n_z \rangle = (2\pi\hbar^2 a/\mu) \psi_{n'_x}(x_0) \psi_{n_x}(x_0) \psi_{n'_y}(y_0) \psi_{n_y}(y_0) \psi_{n'_z}(z_0) \psi_{n_z}(z_0). \tag{A.6}$$

For the molecular function,

$$\langle a | \hat{T}_{\rm rel}(\boldsymbol{R}) + V_{\rm int}(\boldsymbol{R}) | a \rangle = E_a; \tag{A.7}$$

$$\langle a | V_{\rm rel}^{\rm trap}(\boldsymbol{R}) | a \rangle = V_{\rm rel}^{\rm trap}(\boldsymbol{R}_0) + \left( \frac{\mu a^2}{12} \right) (\omega_{{\rm rel},x}^2 + \omega_{{\rm rel},y}^2 + \omega_{{\rm rel},z}^2). \tag{A.8}$$

For a pure contact potential, $E_a = -\hbar^2/(2\mu a^2)$, but for real potentials this is accurate only for very large positive $a$ [209]; when this approximation breaks down, it is best to choose $a$ to reproduce $E_a$, rather than vice versa.

The off-diagonal elements between the harmonic-oscillator functions and the molecular function are

$$\langle a | \hat{T}_{\rm rel}(\boldsymbol{R}) + V_{\rm rel}^{\rm trap}(\boldsymbol{R}) | n_x n_y n_z \rangle = E_{n_x n_y n_z} S_{a, n_x n_y n_z};$$

$$\langle a | V_{\rm int}(\boldsymbol{R}) | n_x n_y n_z \rangle = -(\hbar^2/\mu)(2\pi/a)^{1/2} \psi_{n_x}(x_0) \psi_{n_y}(y_0) \psi_{n_z}(z_0). \tag{A.9}$$

## A.2 Center-of-mass motion

To include coupling to center-of-mass motion, we multiply each function in the basis set for relative motion with a set of 3-dimensional harmonic-oscillator functions in the center-of-mass coordinates, $|N_X N_Y N_Z\rangle = |N_X\rangle |N_Y\rangle |N_Z\rangle$, with functions $\Psi_\alpha(\alpha)$ defined by analogy with Eq. A.2. The matrix elements of $\hat{T}_{\rm rel}(\boldsymbol{R})$, $V_{\rm rel}^{\rm trap}(\boldsymbol{R})$, $V_{\rm int}(\boldsymbol{R})$

and the overlap matrix are simply multiplied by overlaps between center-of-mass functions. In the direct-product approach, these are

$$\langle N'_X N'_Y N'_Z | N_X N_Y N_Z \rangle = \delta_{N'_X N_X} \delta_{N'_Y N_Y} \delta_{N'_Z N_Z}. \tag{A.10}$$

The matrix elements of $\hat{H}^{\text{trap}}_{\text{com}}$ are thus

$$\langle n'_x n'_y n'_z N'_X N'_Y N'_Z | \hat{H}^{\text{trap}}_{\text{com}}(\boldsymbol{\mathcal{R}}) | n_x n_y n_z N_X N_Y N_Z \rangle = E_{N_X N_Y N_Z} \delta_{n'_x n_x} \delta_{n'_y n_y} \delta_{n'_z n_z} \delta_{N'_X N_X} \delta_{N'_Y N_Y} \delta_{N'_Z N_Z}; \tag{A.11}$$

$$\langle a N'_X N'_Y N'_Z | \hat{H}^{\text{trap}}_{\text{com}}(\boldsymbol{\mathcal{R}}) | a N_X N_Y N_Z \rangle = E_{N_X N_Y N_Z} \delta_{N'_X N_X} \delta_{N'_Y N_Y} \delta_{N'_Z N_Z}; \tag{A.12}$$

$$\langle a N'_X N'_Y N'_Z | \hat{H}^{\text{trap}}_{\text{com}}(\boldsymbol{\mathcal{R}}) | n_x n_y n_z N_X N_Y N_Z \rangle = E_{N_X N_Y N_Z} S_{a, n_x n_y n_z} \delta_{N'_X N_X} \delta_{N'_Y N_Y} \delta_{N'_Z N_Z}, \tag{A.13}$$

where

$$E_{N_X N_Y N_Z} = \hbar\omega_{\text{com},X}(N_X + \tfrac{1}{2}) + \hbar\omega_{\text{com},Y}(N_Y + \tfrac{1}{2}) + \hbar\omega_{\text{com},Z}(N_Z + \tfrac{1}{2}). \tag{A.14}$$

## A.3 Coupling between relative and center-of-mass motions

The matrix elements of $V_{\rm cpl}^{\rm trap}(\boldsymbol{R},\boldsymbol{\mathcal{R}})$ may be factorized

$$\langle n_x' n_y' n_z' N_X' N_Y' N_Z' | V_{\rm cpl}^{\rm trap}(\boldsymbol{R},\boldsymbol{\mathcal{R}}) | n_x n_y n_z N_X N_Y N_Z\rangle$$
$$= \mu \langle n_x' n_y' n_z' | (\boldsymbol{R}-\boldsymbol{R}_0)^{\intercal} | n_x n_y n_z\rangle \Delta\boldsymbol{\omega}^2 \langle N_X' N_Y' N_Z' | \boldsymbol{\mathcal{R}}-\boldsymbol{\mathcal{R}}_0 | N_X N_Y N_Z\rangle, \quad \text{(A.15)}$$

$$\langle a N_X' N_Y' N_Z' | V_{\rm cpl}^{\rm trap}(\boldsymbol{R},\boldsymbol{\mathcal{R}}) | a N_X N_Y N_Z\rangle$$
$$= \mu \langle a | (\boldsymbol{R}-\boldsymbol{R}_0)^{\intercal} | a\rangle \Delta\boldsymbol{\omega}^2 \langle N_X' N_Y' N_Z' | \boldsymbol{\mathcal{R}}-\boldsymbol{\mathcal{R}}_0 | N_X N_Y N_Z\rangle, \quad \text{(A.16)}$$

$$\langle a N_X' N_Y' N_Z' | V_{\rm cpl}^{\rm trap}(\boldsymbol{R},\boldsymbol{\mathcal{R}}) | n_x n_y n_z N_X N_Y N_Z\rangle$$
$$= \mu \langle a | (\boldsymbol{R}-\boldsymbol{R}_0)^{\intercal} | n_x n_y n_z\rangle \Delta\boldsymbol{\omega}^2 \langle N_X' N_Y' N_Z' | \boldsymbol{\mathcal{R}}-\boldsymbol{\mathcal{R}}_0 | N_X N_Y N_Z\rangle. \quad \text{(A.17)}$$

(A.18)

where

$$\langle a | \boldsymbol{R}-\boldsymbol{R}_0 | a\rangle = -\boldsymbol{R}_0. \quad \text{(A.19)}$$

Matrix elements involving $(\boldsymbol{R}-\boldsymbol{R}_0)|n_x n_y n_z\rangle$ are evaluated using the identity

$$(z-z_0)|n_z\rangle = 2^{-\frac{1}{2}}\beta_{{\rm rel},z}\left(\sqrt{n_z}\,|n_z-1\rangle + \sqrt{n_z+1}\,|n_z+1\rangle\right), \quad \text{(A.20)}$$

and similarly for other components. Thus

$$\langle a | z-z_0 | n_x n_y n_z\rangle = 2^{-\frac{1}{2}}\beta_{{\rm rel},z}\left(\sqrt{n_z}\,S_{a,n_x n_y n_z-1} + \sqrt{n_z+1}\,S_{a,n_x n_y n_z+1}\right) \quad \text{(A.21)}$$

$$\langle n_x' n_y' n_z' | z-z_0 | n_x n_y n_z\rangle = \delta_{n_x' n_x}\delta_{n_y' n_y} 2^{-\frac{1}{2}}\beta_{{\rm rel},z}\left(\delta_{n_z',n_z-1}\sqrt{n_z} + \delta_{n_z',n_z+1}\sqrt{n_z+1}\right), \quad \text{(A.22)}$$

with similar expressions for $x-x_0$, $y-y_0$. For the center-of-mass coordinates, the

analogous expressions are

$$\langle N'_X N'_Y N'_Z|Z - Z_0|N_X N_Y N_Z\rangle = \delta_{N'_X N_X}\delta_{N'_Y N_Y} 2^{-\frac{1}{2}}\beta_{\mathrm{com},Z}\left(\delta_{N'_Z,N_Z-1}\sqrt{N_Z} + \delta_{N'_Z,N_Z+1}\sqrt{N_Z+1}\right), \tag{A.23}$$

and similarly for $X - X_0$ and $Y - Y_0$.

## A.4 Shifted-molecule basis set

For the shifted-molecule basis set, the center-of-mass functions $|\tilde{N}_X\tilde{N}_Y\tilde{N}_Z\rangle$ are shifted in $\boldsymbol{\mathcal{R}}$ for functions containing $|a\rangle$ but not for those containing $|n_x n_y n_z\rangle$. This leaves Eqs. A.11 and A.16 unchanged, but Eqs. A.12 and A.17 are replaced by

$$\begin{aligned}&\langle a\tilde{N}'_X\tilde{N}'_Y\tilde{N}'_Z|\hat{H}^{\mathrm{trap}}_{\mathrm{com}}(\boldsymbol{\mathcal{R}}) + V^{\mathrm{trap}}_{\mathrm{cpl}}(\boldsymbol{R},\boldsymbol{\mathcal{R}})|a\tilde{N}_X\tilde{N}_Y\tilde{N}_Z\rangle \\ &\qquad = \left(E_{\tilde{N}_X\tilde{N}_Y\tilde{N}_Z} - \frac{\mu}{2}\boldsymbol{R}_0^{\intercal}\Delta\boldsymbol{\omega}^2\Delta\boldsymbol{\mathcal{R}}\right)\delta_{\tilde{N}'_X\tilde{N}_X}\delta_{\tilde{N}'_Y\tilde{N}_Y}\delta_{\tilde{N}'_Z\tilde{N}_Z}.\end{aligned} \tag{A.24}$$

The matrix elements (A.13) and (A.18) are also modified because $|N_X N_Y N_Z\rangle$ and $|\tilde{N}_X\tilde{N}_Y\tilde{N}_Z\rangle$ are nonorthogonal,

$$\begin{aligned}&\langle a\tilde{N}'_X\tilde{N}'_Y\tilde{N}'_Z|\hat{H}^{\mathrm{trap}}_{\mathrm{com}}(\boldsymbol{\mathcal{R}})|n_x n_y n_z N_X N_Y N_Z\rangle \\ &\qquad = E_{N_X N_Y N_Z} S_{a,n_x n_y n_z}\langle\tilde{N}'_X|N_X\rangle\langle\tilde{N}'_Y|N_Y\rangle\langle\tilde{N}'_Z|N_Z\rangle;\end{aligned} \tag{A.25}$$

$$\begin{aligned}&\langle a\tilde{N}'_X\tilde{N}'_Y\tilde{N}'_Z|V^{\mathrm{trap}}_{\mathrm{cpl}}(\boldsymbol{\mathcal{R}})|n_x n_y n_z N_X N_Y N_Z\rangle \\ &\qquad = \mu\langle a|(\boldsymbol{R} - \boldsymbol{R}_0)^{\intercal}|n_x n_y n_z\rangle\Delta\boldsymbol{\omega}^2\langle\tilde{N}'_X\tilde{N}'_Y\tilde{N}'_Z|\boldsymbol{\mathcal{R}} - \boldsymbol{\mathcal{R}}_0|N_X N_Y N_Z\rangle,\end{aligned} \tag{A.26}$$

where the overlap integrals between shifted and unshifted functions along each Cartesian axis $\alpha$ are [228]

$$\langle\tilde{m}|n\rangle = \left(\frac{m!}{2^{n-m}n!}\right)^{\frac{1}{2}}\rho_\alpha^{n-m}L_m^{n-m}(\rho_\alpha^2/2)\exp(-\rho_\alpha^2/4). \tag{A.27}$$

Here $\rho_\alpha = \Delta\mathcal{R}_\alpha/\beta_{\mathrm{com},\alpha}$, $n \geq m$ and $L_m^{n-m}$ is an associated Laguerre polynomial.

The matrix elements of $\boldsymbol{\mathcal{R}} - \boldsymbol{\mathcal{R}}_0$ in Eq. A.26 are expressed in terms of their

Cartesian components,

$$\langle \tilde{N}'_X \tilde{N}'_Y \tilde{N}'_Z | Z - Z_0 | N_X N_Y N_Z \rangle = \langle \tilde{N}'_X | N_X \rangle \langle \tilde{N}'_Y | N_Y \rangle 2^{-\frac{1}{2}} \beta_{\mathrm{com},Z} \times \left( \langle \tilde{N}'_Z | N_Z - 1 \rangle \sqrt{N_Z} + \langle \tilde{N}'_Z | N_Z + 1 \rangle \sqrt{N_Z + 1} \right) \tag{A.28}$$

and similarly for $X - X_0$ and $Y - Y_0$.

Finally, the non-zero off-diagonal elements of the overlap matrix are

$$\langle a \tilde{N}'_X \tilde{N}'_Y \tilde{N}'_Z | n_x n_y n_z N_X N_Y N_Z \rangle = S_{a,n_x n_y n_z} \langle \tilde{N}'_X | N_X \rangle \langle \tilde{N}'_Y | N_Y \rangle \langle \tilde{N}'_Z | N_Z \rangle. \tag{A.29}$$

# Bibliography


(1) L. D. Carr, D. DeMille, R. V. Krems and J. Ye, *New Journal of Physics*, 2009, **11**, 055049.

(2) G. Quéméner and P. S. Julienne, *Chemical Reviews*, 2012, **112**, 4949–5011.

(3) J. M. Hutson and P. Soldán, *International Reviews in Physical Chemistry*, 2006, **25**, 497–526.

(4) K. B. Davis, M. O. Mewes, M. R. Andrews, N. J. van Druten, D. S. Durfee, D. M. Kurn and W. Ketterle, *Phyical Review Letters*, 1995, **75**, 3969–3973.

(5) M. H. Anderson, J. R. Ensher, M. R. Matthews, C. E. Wieman and E. A. Cornell, *Science*, 1995, **269**, 198–201.

(6) W. Ketterle, *Reviews of Modern Physics*, 2002, **74**, 1131–1151.

(7) E. A. Cornell and C. E. Wieman, *Reviews of Modern Physics*, 2002, **74**, 875–893.

(8) I. Bloch, J. Dalibard and S. Nascimbène, *Nature Physics*, 2012, **8**, 267–276.

(9) S. Inouye, M. R. Andrews, J. Stenger, H. J. Miesner, D. M. Stamper-Kurn and W. Ketterle, *Nature*, 1998, **392**, 151–154.

(10) H. Feshbach, *Annals of Physics*, 1958, **5**, 357–390.

(11) Q. Zhang, Y. Wang, C. Zhu, Y. Wang, X. Zhang, K. Gao and W. Zhang, *Chinese Physics B*, 2020, **29**, 09203–09322.

(12) B. D. Marco and D. S. Jin, *Science*, 1999, **285**, 1703–1706.

(13) M. M. Parish, in *Quantum Gas Experiments*, Imperial College Press, 2014, pp. 179–197.

(14) L. Chomaz, I. Ferrier-Barbut, F. Ferlaino, B. Laburthe-Tolra, B. L. Lev and R. Pfau, *Reports on Progress in Physics*, 2023, **86**, 026401–026491.

(15) I. Bloch, J. Dalibard and W. Zwerger, *Reviews of Modern Physics*, 2008, **80**, 885–964.

(16) F. H. Mies, C. J. Williams, P. S. Julienne and M. Krauss, *Journal of Research of NIST*, 1996, **101**, 521.

(17) J. M. Hutson, *Computer Physics Communications*, 1994, **84**, 1–18.

(18) S. Green, *The Journal of Chemical Physics*, 1976, **64**, 3463–3473.

(19) H. T. C. Stoof, J. M. V. A. Koelman and B. J. Verhaar, *Physical Review B*, 1988, **38**, 4688–4697.

(20) P. S. Julienne, F. H. Mies, E. Tiesinga and C. J. Williams, *Physical Review Letters*, 1997, **78**, 1880–1883.

(21) C. Chin, R. Grimm, P. S. Julienne and E. Tiesinga, *Reviews Modern Physics*, 2010, **82**, 1225–1286.

(22) C. N. Cohen-Tannoudji, *Reviews of Modern Physics*, 1998, **70**, 707–719.

(23) S. Chu, *Reviews of Modern Physics*, 1998, **70**, 685–706.

(24) W. D. Phillips, *Reviews of Modern Physics*, 1998, **70**, 721–741.

(25) E. L. Raab, M. Prentiss, A. Cable, S. Chu and D. E. Pritchard, *Physical Review Letters*, 1987, **59**, 2631–2634.

(26) R. Grimm, M. Weidemüller and Y. Ovchinnikov, *Advances in Atomic, Molecular, and Optical Physics*, 2000, **42**, 95–170.

(27) K. B. Davis, M. O. Mewes, M. A. Joffe, M. R. Andrews and W. Ketterle, *Physical Review Letters*, 1995, **74**, 5202–5205.

(28) T. Langen, G. Valtolina, D. Wang and J. Ye, *Nature Physics*, 2024, **20**, 702–712.

(29) A. Das, P. D. Gregory, T. Takekoshi, L. Fernley, M. Landini, J. M. Hutson, S. L. Cornish and H.-C. Nägerl, *SciPost Phys.*, 2023, **15**, 220.

(30) K.-K. Ni, S. Ospelkaus, M. H. G. de Miranda, A. Pe'er, B. Neyenhuis, J. J. Zirbel, S. Kotochigova, P. S. Julienne, D. S. Jin and J. Ye, *Science*, 2008, **322**, 231.

(31) T. Takekoshi, L. Reichsöllner, A. Schindewolf, J. M. Hutson, C. R. Le Sueur, O. Dulieu, F. Ferlaino, R. Grimm and H.-C. Nägerl, *Physical Review Letters*, 2014, **113**, 205301.

(32) K. K. Voges, P. Gersema, M. Meyer zum Alten Borgloh, T. A. Schulze, T. Hartmann, A. Zenesini and S. Ospelkaus, *Physical Review Letters*, 2020, **125**, 083401.

(33) J. T. Zhang, Y. Yu, W. B. Cairncross, K. Wang, L. R. B. Picard, J. D. Hood, Y.-W. Lin, J. M. Hutson and K.-K. Ni, *Physical Review Letters*, 2020, **124**, 253401.

(34) M.-S. Heo, T. T. Wang, C. A. Christensen, T. M. Rvachov, D. A. Cotta, J.-H. Choi, Y.-R. Lee and W. Ketterle, *Physical Review A*, 2012, **86**, 021602(R).

(35) M. Guo, X. Ye, J. He, G. Quéméner and D. Wang, *Physical Review A*, 2018, **97**, 020501(R).

(36) F. Lang, K. Winkler, C. Strauss, R. Grimm and J. H. Denschlag, *Physical Review Letters*, 2008, **101**, 133005(4).

(37) J. G. Danzl, M. J. Mark, E. Haller, M. Gustavsson, R. Hart, A. Liem, H. Zellmer and H.-C. Nägerl, *New Journal of Physics*, 2009, **11**, 055036.

(38) J. M. Hutson, E. Tiesinga and P. S. Julienne, *Physical Review A*, 2008, **78**, 052703–052713.

(39) S. G. H. Brookes and J. M. Hutson, *Journal of Physical Chemistry A*, 2022, **126**, 3987–4001.

(40) V. Barbé, A. Ciamei, B. Pasquiou, L. Reichsöllner, F. S. P. S. Żuchowski and J. M. Hutson, *Nature Physics*, 2018, **14**, 881–884.

(41) T. Franzen, A. Guttridge, K. E. Wilson, J. Segal, M. D. Frye, J. M. Hutson and S. L. Cornish, *Physical Review Research*, 2022, **4**, 043072(7).

(42) S. Kotochigova, *Report on Progress in Physics*, 2014, **77**, 093901.

(43) J. Lim, J. R. Almond, M. A. Trigatzis, J. A. Devlin, N. J. Fitch, B. E. Sauer, M. R. Tarbutt and E. A. Hinds, *Physical Review Letters*, 2018, **120**, 123201(6).

(44) E. S. Shuman, J. F. Barry and D. DeMille1, *Nature*, 2018, **467**, 820–823.

(45) S. Truppe, H. J. Williams, M. Hambach, L. Caldwell, N. J. Fitch, E. A. Hinds, B. E. Sauer and M. R. Tarbutt, *Nature Physics*, 2017, **13**, 1173–1176.

(46) L. Anderegg, B. L. Augenbraun, Y. Bao, S. Burchesky, L. W. Cheuk, W. Ketterle and J. M. Doyle, *Nature Physics*, 2018, **14**, 890–893.

(47) S. Ding, Y. Wu, I. A. Finneran, J. J. Burau and J. Ye, *Physical Review X*, 2020, **10**, 021049(9).

(48) I. Kozyryev, L. Baum, K. Matsuda, B. L. Augenbraun, L. Anderegg, A. P. Sedlack and J. M. Doyle, *Physical Review Letters*, 2017, **118**, 173201(6).

(49) M. Brouard and C. Vallance, *Tutorials in Molecular Reaction Dynamics*, The Royal Society of Chemistry, 2010.

(50) Y. Liu, M. Hu, M. A. Nichols, D. Yang, D. Xie, H. Guo and K. K. Ni, *Nature*, 2021, **594**, 379–384.

(51) Y. Liu and K. K. Ni, *Annual Review of Physical Chemistry*, 2021, **73**, 4–28.

(52) B. Heazlewood and T. Softley, *Nature Reviews*, 2021, **5**, 125–140.

(53) M. T. Bell and T. P. Softley, *Molecular Physics*, 2009, **107**, 99–132.

(54) D. Mitra, K. H. Leung and T. Zelevinsky, *Physical Review A*, 2022, **105**, 040101.

(55) M. S. Safronova, D. Budker, D. DeMille, D. F. J. Kimball, A. Derevianko and C. W. Clark, *Reviews of Modern Physics*, 2018, **90**, 025008.

(56) N. J. Fitch, J. Lim, E. A. Hinds, B. E. Sauer and M. R. Tarbutt, *Quantum Science and Technology*, 2021, **6**, 014006.

(57) S. L. Cornish, M. R. Tarbutt and K. R. A. Hazzard, *Nature Physics*, 2024, **20**, 730–740.

(58) I. M. Georgescu, S. Ashhab and F. Nori, *Reviews of Modern Physics*, 2014, **86**, 153–186.

(59) J. A. Blackmore, L. Caldwell, P. D. Gregory, E. M. Bridge, R. Sawant, J. Aldegunde, J. Mur-Petit, D. Jaksch, J. M. Hutson, B. E. Sauer, M. R. Tarbutt and S. L. Cornish, *Quantum Science and Technology*, 2019, **4**, 014010.

(60) M. Ortner, A. Micheli, G. Pupillo and P. Zoller, *New Journal of Physics*, 2009, **11**, 055045.

(61) L. Pollet, J. D. Picon, H. P. Büchler and M. Troyer, *Physical Review Letters*, 2010, **104**, 125302–125306.

(62) A. Micheli, G. K. Brennen and P. Zoller, *Nature Physics*, 2006, **2**, 341–347.

(63) K. R. A. Hazzard, S. R. Manmana, M. Foss-Feig and A. M. Rey, *Physical Review Letters*, 2013, **110**, 075301–075307.

(64) G. Pupillo, A. Micheli, H. P. Büchler and P. Zoller, in *Cold Molecules: Theory, Experiment, Applications*, Taylor and Francis, 2009, ch. 1.

(65) T. H. Johnson, S. R. Clark and D. Jaksch, *EPJ Quantum Technology*, 2014, **1**.

(66) A. Montanaro, *npj Quantum Information*, 2016, **2**, 15023.

(67) R. Sewant, J. A. Blackmore, P. D. Gregory, J. Mur-Petit, D. Jaksch, J. Aldegunde, J. M. Hutson, M. R. Tarbutt and S. L. Cornish, *New Journal of Physics*, 2020, **22**, 013027(12).

(68) K. K. Ni, T. Rosenband and D. D. Grimes, *Chemical Science*, 2018, **9**, 6830–6838.

(69) D. Sardar, A. Christianen, H. Li and J. L. Bohn, *Physical Review A*, 2023, **107**, 032822(10).

(70) R. Bause, A. Christianen, A. Schindewolf, I. Bloch and X. Y. Luo, *Journal of Physical Chemistry A*, 2023, **127**, 729–741.

(71) M. Mayle, B. P. Ruzic and J. L. Bohn, *Physical Review A*, 2012, **85**, 062712(15).

(72) M. Mayle, G. Quéméner, B. P. Ruzic and J. L. Bohn, *Physical Review A*, 2013, **87**, 012709(8).

(73) P. D. Gregory, M. D. Frye, J. A. Blackmore, E. M. Bridge, R. Sawant, J. M. Hutson and S. L. Cornish, *Nature Comm.*, 2019, **10**, 3104.

(74) L. W. Cheuk, L. Anderegg, Y. Bao, S. Burchesky, S. S. Yu, W. Ketterle, K.-K. Ni and J. M. Doyle, *Physical Review A*, 2020, **125**, 043401(6).

(75) L. R. Li, J. D. Hood, Y. Yu, J. T. Zhang, N. R. Hutzler, T. Rosenband and K. K. Ni, *Science*, 2018, **360**, 900–903.

(76) W. B. Cairncross, J. T. Zhang, L. R. B. Pricard, Y. Yu, K. Wang and K. K. Ni, *Physical Review Letters*, 2021, **126**, 123402–12308.

(77) J. T. Zhang, L. R. B. Picard, W. B. Cairncross, K. Wang, Y. Yu, F. Fang and K.-K. Ni, *Quantum Science and Technology*, 2022, **7**, 035006.

(78) C. Karam, R. Vexiau, N. Bouloufa-Maafa, O. Dulieu, M. Lepers, M. M. zum Alten Borgloh, S. Ospelkaus and L. Karpa, *Physical Review Research*, 2023, **5**, 033074.

(79) T. Karman and J. M. Hutson, *Physical Review A*, 2019, **100**, 052704.

(80) B. Mukherjee, M. D. Frye, C. R. Le Sueur, M. R. Tarbutt and J. M. Hutson, *Physical Review Research*, 2023, **5**, 033097(16).

(81) P. D. Gregory, L. M. Fernley, A. L. Tao, S. L. Bromley, J. Stepp, Z. Zhang, S. Kotochigova, K. R. A. Hazzard and S. L. Cornish, *Nature Physics*, 2024, **20**, 415–421.

(82) A. J. Park, L. R. B. Picard, G. E. Patenotte, J. T. Zhang, T. Rosenband and K.-K. Ni, *Physical Review Letters*, 2023, **131**, 183401.

(83) N. Bigagli, W. Yuan, S. Zhang, B. Bulatovic, T. Karman, I. Stevenson and S. Will, *Observation of Bose-Einstein Condensation of Dipolar Molecules*, 2023.

(84) J. M. Hutson and C. R. Le Sueur, *Computer Physics Communications*, 2019, **241**, 1.

(85) J. M. Hutson and C. R. Le Sueur, *Computer Physics Communications*, 2019, **241**, 9.

(86) R. C. Bird, M. R. Tarbutt and J. M. Hutson, *Physical Review Research*, 2023, **5**, 023184.

(87) R. C. Bird, C. R. Le Sueur and J. M. Hutson, *Physical Review Research*, 2023, **5**, 043086.

(88) R. C. Bird and J. M. Hutson, *Making molecules by mergoassociation: the role of center-of-mass motion*, 2024.

(89) J. M. Hutson, in *Cold Molecules: Theory, Experiment, Applications*, Taylor & Francis, London, 2009, pp. 3–37.

(90) H. Friedrich, *Theoretical Atomic Physics*, Springer, 2017.

(91) M. S. Child, *Molecular Collision Theory*, Dover Publications ltd., 1997.

(92) G. Quéméner, *Ultracold collisions of molecules*, 2017.

(93) M. Abramowitz and I. A. Stegun, *Handbook of Mathematical Functions*, Dover Publications ltd., 1964.

(94) M. M. Woolfson and M. S. Woolfson, *Mathematics for Physics*, Oxford University Press, 2007.

(95) B. R. Johnson, *The Journal of Chemical Physics*, 1997, **64**, 4086–4093.

(96) B. R. Johnson, *The Journal of Chemical Physics*, 1978, **69**, 4678–4688.

(97) F. T. Smith, *Physical Review*, 1969, **179**, 111–123.

(98) J. M. Hutson, E. Tiesinga and P. S. Julienne, *Physical Review A*, 2008, **78**, 052703.

(99) W. H. Press, S. A. Teukolsky, W. T. Vetterling and B. P. Flannery, in Cambridge University Press, 1992, ch. 9, pp. 352–355.

(100) A. E. Thornley and J. M. Hutson, *Journal of Chemical Physics*, 1994, **101**, 5578–5584.

(101) O. Hinckelmann and L. Spruch, *Physical Review A*, 1971, **3**, 642–648.

(102) G. F. Gribakin and V. V. Flambaum, *Physical Review A*, 1993, **48**, 546–553.

(103) B. Gao, *Physical Review A*, 2000, **62**, 050702(4).

(104) B. Gao, *Physical Review A*, 2001, **64**, 010701(4).

(105) B. Gao, *Physical Review A*, 1998, **58**, 4222(4).

(106) B. Gao, *Physical Review A*, 1998, **58**, 1728(7).

(107) M. D. Frye and J. M. Hutson, *Physical Review A*, 2017, **96**, 042705.

(108) R. Ferber, O. Nikolayeva, M. Tamanis, H. Knöckel and E. Tiemann, *Physical Review A*, 2013, **88**, 012516(9).

(109) H. J. Patel, C. L. Blackley, S. L. Cornish and J. M. Hutson, *Physical Review A*, 2014, **90**, 032716(10).

(110) M. Gröbner, P. Weinmann, E. Kirilov, H. C. Nägerl, P. S. Julienne, C. R. Le Sueur and J. M. Hutson, *Physical Review A*, 2017, **95**, 022715(10).

(111) K. Bergmann, H. Theuer and B. W. Shore, *Rev. Mod. Phys.*, 1998, **70**, 1003–1025.

(112) T. G. Tiecke, Doctoral Dissertation, University of Amsterdam, 2009.

(113) D. A. Steck, *Cesium D Line Data*, `http://steck.us/alkalidata`, 2023.

(114) R. N. Zare, *Angular Momentum*, John Wiley & Sons, 1987.

(115) D. M. Brink and G. R. Satchler, *Angular Momentum*, Oxford University Press, 2nd, 1975.

(116) D. E. Manolopoulos, *Journal of Chemical Physics*, 1986, **85**, 6425–6429.

(117) M. H. Alexander, *Journal of Chemical Physics*, 1984, **81**, 4510–4516.

(118) M. H. Alexander and D. E. Manolopoulos, *Journal of Chemical Physics*, 1987, **86**, 2044.

(119) J. M. Hutson, 1988, **151**, 565–569.

(120) R. Ferber, I. Klincare, O. Nikolayeva, M. Tamanis, H. Knöckel, E. Tiemann and A. Pashov, *Physical Review A*, 2009, **80**, 062501.

(121) A. Derevianko, J. F. Babb and A. Dalgarno, *Physical Review A*, 2001, **63**, 052704.

(122) S. G. Porsev and A. Dalgarno, *Journal of Chemical Physics*, 2003, **119**, 844–850.

(123) B. M. Smirnov and M. I. Chibisov, *Soviet Physics JETP*, 1965, **21**, 624–628.

(124) R. J. Le Roy, N. S. Dattani, J. A. Coxon, A. J. Ross, P. Crozet and C. Linton, *Journal of Chemical Physics*, 2009, **131**, 204309.

(125) R. Coté, A. Dalgarno and M. J. Jamieson, *Physical Review A.*, 1994, **50**, 399.

(126) C. Linton, F. Martin, A. J. Ross, I. Russier, P. Crozet, A. Yiannopoulou, L. Li and A. M. Lyyra, *Journal of Molecular Spectroscopy*, 1999, **196**, 20–28.

(127) G. Ihm, M. W. Cole, F. Toigo and J. R. Klein, *Physical Review A*, 1990, **42**, 5244–5252.

(128) T. Takekoshi, M. Debatin, R. Rameshan, F. Ferlaino, R. Grimm, H.-C. Nägerl, C. R. Le Sueur, J. M. Hutson, P. S. Julienne, S. Kotochigova and E. Tiemann, *Physical Review A*, 2012, **85**, 032506.

(129) M. M. Law and J. M. Hutson, *Computer Physics Communications*, 1997, **102**, 252–268.

(130) J. Deiglmayr, H. Herburger, H. Saßmannshausen, P. Jansen, H. Schmutz and F. Merkt, *Physical Review A*, 2016, **93**, 013424.

(131) C.-J. Lorenzen and K. Niemax, *Physica Scripta*, 1983, **27**, 300.

(132) H.-W. Cho, D. J. McCarron, M. P. Köppinger, D. L. Jenkin, K. L. Butler, Paul S. Julienne, C. L. Blackley, C. R. Le Sueur, J. M. Hutson and S. L. Cornish, *Physical Review A*, 2013, **87**, 010703(R).

(133) M. Gröbner, P. Weinmann, E. Kirilov, H.-C. Nägerl, P. S. Julienne, C. R. Le Sueur and J. M. Hutson, *Physical Review A*, 2017, **95**, 022715.

(134) A. V. Gorshkov, S. R. Manmana, G. Chen, J. Ye, E. Demler, M. D. Lukin and A. M. Rey, *Physical Review Letters*, 2011, **107**, 115301.

(135) J. A. Blackmore, L. Caldwell, P. D. Gregory, E. M. Bridge, R. Sawant, J. Aldegunde, J. Mur-Petit, D. Jaksch, J. M. Hutson, B. E. Sauer, M. R. Tarbutt and S. L. Cornish, *Quantum Science and Technology*, 2019, **4**, 014010.

(136) D. DeMille, *Physical Review Letters*, 2002, **88**, 067901.

(137) C. M. Holland, Y. Lu and L. W. Cheuk, *Science*, 2023, **382**, 1143–1147.

(138) Y. Bao, S. S. Yu, L. Anderegg, E. Chae, W. Ketterle, K.-K. Ni and J. M. Doyle, *Science*, 2023, 1138–1143.

(139) B. Yan, S. A. Moses, B. Gadway, J. P. Covey, K. R. A. Hazzard, A. M. Rey, D. S. Jin and J. Ye, *Nature*, 2013, **501**, 521–525.

(140) J. R. Li, K. Matsuda, C. Miller, A. N. Carroll, W. G. Tobias, J. S. Higgins and J. Ye, *Nature*, 2023, **614**, 70–74.

(141) N. J. Fitch, J. Lim, E. A. Hinds, B. E. Sauer and M. R. Tarbutt, *Quantum Science and Technology*, 2021, **6**, 014006.

(142) L. Anderegg, N. B. Vilas, C. Hallas, P. Robichaud, A. Jadbabaie, J. M. Doyle and N. R. Hutzler, *Science*, 2023, 665–668.

(143) K. H. Leung, B. Iritani, E. Tiberi, I. Majewska, M. Borkowski, R. Moszynski and T. Zelevinsky, *Physical Review X*, 2023, **13**, 011047.

(144) W. B. Cairncross, J. T. Zhang, L. R. Picard, Y. Yu, K. Wang and K.-K. Ni, *Physical Review Letters*, 2021, **126**, 123402.

(145) P. K. Molony, P. D. Gregory, Z. Ji, B. Lu, M. P. Köppinger, C. R. Le Sueur, C. L. Blackley, J. M. Hutson and S. L. Cornish, *Physical Review Letters*, 2014, **113**, 255301.

(146) J. W. Park, S. A. Will and M. W. Zwierlein, *Physical Review Letters*, 2015, **114**, 205302.

(147) M. Guo, B. Zhu, B. Lu, X. Ye, F. Wang, R. Vexiau, N. Bouloufa-Maafa, G. Quéméner, O. Dulieu and D. Wang, *Physical Review Letters*, 2016, **116**, 205303.

(148) T. M. Rvachov, H. Son, A. T. Sommer, S. Ebadi, J. J. Park, M. W. Zwierlein, W. Ketterle and A. O. Jamison, *Physical Review Letters*, 2017, **119**, 143001.

(149) F. Seeßelberg, N. Buchheim, Z.-K. Lu, T. Schneider, X.-Y. Luo, E. Tiemann, I. Bloch and C. Gohle, *Physical Review A*, 2018, **97**, 013405.

(150) H. Yang, D.-C. Zhang, L. Liu, Y.-X. Liu, J. Nan, B. Zhao and J.-W. Pan, *Science*, 2019, **363**, 261–264.

(151) S. Truppe, H. J. Williams, M. Hambach, L. Caldwell, N. J. Fitch, E. A. Hinds, B. E. Sauer and M. R. Tarbutt, *Nature Physics*, 2017, **13**, 1173–1176.

(152) D. J. McCarron, M. H. Steinecker, Y. Zhu and D. DeMille, *Physical Review Letters*, 2018, **121**, 013202.

(153) L. Anderegg, B. L. Augenbraun, Y. Bao, S. Burchesky, L. W. Cheuk, W. Ketterle and J. M. Doyle, *Nature Physics*, 2018, **14**, 890–893.

(154) L. W. Cheuk, L. Anderegg, B. L. Augenbraun, Y. Bao, S. Burchesky, W. Ketterle and J. M. Doyle, *Physical Review Letters*, 2018, **121**, 083201.

(155) L. Caldwell, J. A. Devlin, H. J. Williams, N. J. Fitch, E. A. Hinds, B. E. Sauer and M. R. Tarbutt, *Physical Review Letters*, 2019, **123**, 033202.

(156) S. Ding, Y. Wu, I. A. Finneran, J. J. Burau and J. Ye, *Physical Review X*, 2020, **10**, 021049.

(157) J. L. Roberts, N. R. Claussen, S. L. Cornish, E. A. Donley, E. A. Cornell and C. E. Wieman, *Physical Review Letters*, 2001, **86**, 4211–4214.

(158) K. E. Strecker, G. B. Partridge, A. G. Truscott and R. G. Hulet, *New Journal of Physics*, 2003, **5**, 73.1–73.8.

(159) P. Naidon and S. Endo, *Reports on Progress in Physics*, 2017, **80**, 056001.

(160) J. M. Hutson and P. Soldán, *International Reviews in Physical Chemistry*, 2006, **25**, 497–526.

(161) T. Köhler, K. Góral and P. S. Julienne, *Reviews of Modern Physics*, 2006, **78**, 1311–1361.

(162) X.-Y. Wang, M. D. Frye, Z. Su, J. Cao, L. Liu, D.-C. Zhang, H. Yang, J. M. Hutson, B. Zhao, C.-L. Bai and J.-W. Pan, *New Journal of Physics*, 2021, **23**, 115010.

(163) Z. Su, H. Yang, J. Cao, X.-Y. Wang, J. Rui, B. Zhao and J.-W. Pan, *Physical Review Letters*, 2022, **129**, 033401.

(164) H. Yang, X.-Y. Wang, Z. Su, J. Cao, D.-C. Zhang, J. Rui, B. Zhao, C.-L. Bai and J.-W. Pan, *Nature*, 2022, **602**, 229–233.

(165) H. Yang, J. Cao, Z. Su, J. Rui, B. Zhao and J.-W. Pan, *Science*, 2022, **378**, 1009–1013.

(166) H. Son, J. J. Park, Y.-K. Lu, A. O. Jamison, T. Karman and W. Ketterle, *Science*, 2022, **375**, 1006.

(167) M. D. Frye and J. M. Hutson, *New Journal of Physics*, 2021, **23**, 125008.

(168) M. D. Frye and J. M. Hutson, *Physical Review Research*, 2023, **5**, 023001.

(169) S. Jurgilas, A. Chakraborty, C. J. H. Rich, L. Caldwell, H. J. Williams, N. J. Fitch, B. E. Sauer, M. D. Frye, J. M. Hutson and M. Tarbutt, *Physical Review Letters*, 2021, **126**, 153401.

(170) S. Jurgilas, A. Chakraborty, C. J. H. Rich, B. E. Sauer, M. D. Frye, J. M. Hutson and M. Tarbutt, *New Journal of Physics*, 2021, **23**, 075004.

(171) L. Anderegg, L. W. Cheuk, Y. Bao, S. Burchesky, W. Ketterle, K.-K. Ni and J. M. Doyle, *Science*, 2019, **365**, 1156–1158.

(172) W. J. Childs, G. L. Goodman and L. S. Goodman, *Journal of Molecular Spectroscopy*, 1981, **86**, 365–392.

(173) R. A. Frosch and H. M. Foley, *Physical Review*, 1952, **88**, 1337.

(174) L. Caldwell, H. J. Williams, N. J. Fitch, J. Aldegunde, J. M. Hutson, B. E. Sauer and M. R. Tarbutt, *Physical Review Letters*, 2020, **124**, 063001.

(175) A. M. Arthurs and A. Dalgarno, *Proceedings of the Royal Society A*, 1960, **256**, 540–551.

(176) J. M. Hutson and C. R. Le Sueur, MOLSCAT, BOUND *and* FIELD, *version 2020.0*, `https://github.com/molscat/molscat`, 2020.

(177) J. M. Hutson, *New Journal of Physics*, 2007, **9**, 152.

(178) J. M. Hutson and C. R. Le Sueur, `https://github.com/molscat/molscat`, 2022.

(179) D. E. Manolopoulos and S. K. Gray, *Journal of Chemical Physics*, 1995, **102**, 9214.

(180) J. Lim, M. D. Frye, J. M. Hutson and M. R. Tarbutt, *Physical Review A*, 2015, **92**, 053419.

(181) M. Berninger, A. Zenesini, B. Huang, W. Harm, H.-C. Nägerl, F. Ferlaino, R. Grimm, P. S. Julienne and J. M. Hutson, *Physical Review A*, 2013, **87**, 032517.

(182) R. J. Le Roy and R. B. Bernstein, *Journal of Chemical Physics*, 1970, **52**, 3869.

(183) J. M. Hutson, in *Advances in Molecular Vibrations and Collision Dynamics*, JAI Press, Greenwich, Connecticut, 1991, vol. 1A, pp. 1–45.

(184) M. Mayle, B. P. Ruzic and J. L. Bohn, *Physical Review A*, 2012, **85**, 062712.

(185) M. Mayle, G. Quéméner, B. P. Ruzic and J. L. Bohn, *Physical Review A*, 2013, **87**, 012709.

(186) A. Christianen, T. Karman and G. C. Groenenboom, *Physical Review A*, 2019, **100**, 032708.

(187) M. D. Frye, M. Morita, C. L. Vaillant, D. G. Green and J. M. Hutson, *Physical Review A*, 2016, **93**, 052713.

(188) I. Kozyryev and N. R. Hutzler, *Physical Review Letters*, 2017, **119**, 133002.

(189) N. R. Hutzler, *Quantum Science and Technology*, 2020, **5**, 044011.

(190) I. Kozyryev, Z. Lasner and J. M. Doyle, *Physical Review A*, 2021, **103**, 043313.

(191) Q. Wei, S. Kais, B. Friedrich and D. Herschbach, *Journal of Chemical Physics*, 2011, **135**, 154102.

(192) P. Yu, L. W. Cheuk, I. Kozyryev and J. M. Doyle, *New Journal of Physics*, 2019, **21**, 093049.

(193) R. Sawant, J. A. Blackmore, P. D. Gregory, J. Mur-Petit, D. Jaksch, J. Aldegunde, J. M. Hutson, M. R. Tarbutt and S. L. Cornish, *New Journal of Physics*, 2020, **22**, 013027.

(194) M. L. Wall, K. Maeda and L. D. Carr, *New Journal of Physics*, 2015, **17**, 025001.

(195) J. J. Park, H. Son, Y. Lu, T. Karman, M. Gronowski, M. Tomza, A. O. Jamison and W. Ketterle, *Physical Review X*, 2023, **13**, 031018.

(196) T. Karman, M. Gronowski, M. Tomza, J. J. Park, H. Son, Y. Lu, A. O. Jamison and W. Ketterle, *Physical Review A*, 2023, **108**, 023309.

(197) M. Morita, M. B. Kosicki, P. S. Żuchowski, P. Brumer and T. V. Tscherbul, *Physical Review A*, 2024, **110**, L021301.

(198) T. V. Tscherbul and J. P. D. Incao, *Physical Review A*, 2023, **108**, 053317–053332.

(199) D. K. Ruttley, A. Guttridge, S. Spence, R. C. Bird, C. R. Le Sueur, J. M. Hutson and S. L. Cornish, *Physical Review Letters*, 2023, **130**, 223401.

(200) D. Jaksch, H.-J. Briegel, J. I. Cirac, C. W. Gardiner and P. Zoller, *Physical Review Letters*, 1999, **82**, 1975(4).

(201) R. Stock, I. H. Deutsch and E. L. Bolda, *Physical Review Letters*, 2003, **91**, 183201.

(202) R. Stock and I. H. Deutsch, *Physical Review A*, 2006, **73**, 032701.

(203) Z. Idziaszek, T. Calarco and P. Zoller, *Physical Review A*, 2007, **76**, 033409.

(204) M. Sroczynska, A. Dawid, M. Tomza, Z. Idziaszek, T. Calarco and K. Jachymski, *New Journal of Physics*, 2022, **24**, 015001.

(205) A. M. Kaufman, B. J. Lester and C. A. Regal, *Physical Review X*, 2012, **2**, 041014.

(206) F. Deuretzbacher, K. Plassmeier, D. Pfannkuche, F. Werner, C. Ospelkaus, S. Ospelkaus, K. Sengstock and K. Bongs, *Physical Review A*, 2008, **77**, 032726.

(207) K. Huang and C. N. Yang, *Physical Review*, 1957, **105**, 767.

(208) M. Krych and Z. Idziaszek, *Physical Review A*, 2009, **80**, 022710.

(209) P. S. Julienne and J. M. Hutson, *Physical Review A*, 2014, **89**, 052715.

(210) E. L. Bolda, E. Tiesinga and P. S. Julienne, *Physical Review A*, 2003, **68**, 032702.

(211) E. L. Bolda, E. Tiesinga and P. S. Julienne, *Physical Review A*, 2006, **74**, 022712.

(212) J. Mentink and S. Kokkelmans, *Physical Review A*, 2009, **79**, 032709.

(213) K. Jachymski, Z. Idziaszek and T. Calarco, *Physical Review A*, 2013, **87**, 042701.

(214) K. Jachymski, *Journal of Physics B: Atomic, Molecular and Optical Physics*, 2016, **49**, 195204.

(215) K. Jachymski, *Journal of Physics B: Atomic, Molecular and Optical Physics*, 2020, **53**, 065302.

(216) J. D. Hood, Y. Yu, J. T. Zhang, K. Wang, L. R. Liu, B. Gao and K. K. Ni, *Physical Review Research*, 2020, **2**, 023108–023117.

(217) P. S. Żuchowski, J. Aldegunde and J. M. Hutson, *Physical Review Letters*, 2010, **105**, 153201.

(218) D. A. Brue and J. M. Hutson, *Physical Review Letters*, 2012, **108**, 043201.

(219) D. A. Brue and J. M. Hutson, *Physical Review A*, 2013, **87**, 052709.

(220) B. C. Yang, M. D. Frye, A. Guttridge, J. Aldegunde, P. S. Żuchowski, S. L. Cornish and J. M. Hutson, *Physical Review A*, 2019, **100**, 022704.

(221) B. Mukherjee, M. D. Frye and J. M. Hutson, *Physical Review A*, 2022, **105**, 023306.

(222) V. Barbé, A. Ciamei, B. Pasquiou, L. Reichsöllner, F. Schreck, P. S. Żuchowski and J. M. Hutson, *Nature Physics*, 2018, **14**, 881–884.

(223) T. Franzen, A. Guttridge, K. E. Wilson, J. Segall, M. D. Frye, J. M. Hutson and S. L. Cornish, *Physical Review Research*, 2022, **4**, 043072.

(224) A. Ciamei, J. J. Szczepkowski, A. Bayerle, V. Barbé, L. Reichsöllner, S. M. Tzanova, C.-C. Chen, B. Pasquiou, A. Grochola, P. Kowalczyk, W. Jastrzebski and F. Schreck, *Physical Chemistry Chemical Physics*, 2018, **20**, 26621.

(225) M. Borkowski, P. S. Żuchowski, R. Ciuryło, P. S. Julienne, D. Kedziera, L. Mentel, P. Tecmer, F. Münchow, C. Bruni and A. Görlitz, *Physical Review A*, 2013, **88**, 052708.

(226) A. Guttridge, M. D. Frye, B. C. Yang, J. M. Hutson and S. L. Cornish, *Physical Review A*, 2018, **98**, 022707.

(227) P. S. Julienne, *Faraday Discussions*, 2009, **142**, 361–388.

(228) I. S. Gradshteyn, I. M. Ryzhik, D. Zwillinger and V. Moll, *Table of Integrals, Series, and Products; 8th ed.* Academic Press, Amsterdam, 2015.